$^{9}Be^{+}$ ion qubit control using an optical frequency comb

Von der Fakultät für Mathematik und Physik
der Gottfried Wilhelm Leibniz Universität Hannover

zur Erlangung des akademischen Grades

Doktor der Naturwissenschaften
- Dr. rer. nat. -

genehmigte Dissertation von

Dipl.-Phys. Anna-Greta Paschke

2017

Referent:	Prof. Dr. Christian Ospelkaus Institut für Quantenoptik Leibniz Universität Hannover
Korreferent:	Prof. Dr. Piet Oliver Schmidt Institut für Quantenoptik Leibniz Universität Hannover
Tag der Promotion:	07.09.2017

Abstract

This thesis reports the first demonstration of $^9Be^+$ ion qubit control using an optical frequency comb. It covers a theoretical discussion of the requirements and the application range of coherent $^9Be^+$ ion control implemented by a pulsed laser, the development of an appropriate laser system as well as the experimental implementation and demonstration in a surface-electrode radio-frequency trap.
The use of a pulsed laser for coherent qubit control is motivated by the stringent requirements arising from a high-precision Penning trap experiment currently being designed and set up in our group. As part of the BASE collaboration, we aim to realize a test of CPT invariance based on a quantum logic inspired measurement and comparison of the proton's and antiproton's g-factor. Cooling, manipulation and the spin-state detection of a single trapped (anti-)proton will be implemented indirectly through interaction with a co-trapped beryllium ion. The essential manipulation of beryllium is carried out using two-photon stimulated Raman transitions. Because of the high required magnetic field of 5 T, which is mandatory for precise frequency measurements of the (anti-)proton, and the resulting large hyperfine qubit splitting of $^9Be^+$ near 140 GHz, the widely used continuous wave laser approach for the implementation of the Raman process is rather unprofitable. Instead, a pulsed Raman laser has been investigated in order to directly implement the necessary operations, where comb mode pairs coherently add up and provide the essential $^9Be^+$ ion qubit coupling.
Numerical simulations of the relevant processes in the $^9Be^+$ ion for various magnetic field regimes are presented, showing the importance of the comb's spectral properties. Due to the atomic level structure of beryllium, the spectral bandwidth and spectral shape must be precisely controlled in order to optimize the ratio between the Raman coupling strength and the scattering rate. The Raman laser system developed for this purpose is based on a customized femtosecond frequency comb operating near 626 nm. To selectively generate the required narrow-bandwidth ultraviolet pulses near 313 nm, a nonlinear spectral compression technique is implemented during the second-harmonic generation process. Here, for the first time, the significant influence of spatio-temporal couplings inside nonlinear BiBO crystals has been investigated. The nonlinear effects further allow a simple and efficient control of the comb's outer-lying frequency components. The implementation and demonstration of spin control and spin-motion coupling of a single $^9Be^+$ ion using the pulsed Raman system is reported for experiments carried out with a surface-electrode radio-frequency trap. The results convincingly validate the concept and exhibit a promising realization of the stringent requirements for beryllium qubit control in the high-field regime and further provides flexible applicability for qubit control in other field regimes.

Keywords: Coherent qubit control, UV frequency comb, nonlinear spectral pulse modification, trapped and laser-cooled ions, quantum logic spectroscopy

Kurzfassung

Im Rahmen dieser Dissertation wurde erstmalig die kohärente Kontrolle einzelner $^9Be^+$-Ionen mittels eines optischen Freqenzkamms realisiert. Die Arbeit umfasst eine theoretische Diskussion der Anforderungen, die Entwicklung eines geeigneten Lasersystems sowie den experimentellen Nachweis.
Die erstmalige Anwendung eines gepulsten Lasersystems für die kohärente Zustandsmanipulation von Beryllium-Ionen wurde aufgrund spezieller Anforderungen gewählt, die sich im Rahmen eines Hochpräzisions-Experiments in einer Penning-Falle ergeben. Ziel dieses Experiments ist ein Vergleich der g-Faktoren des Protons und des Antiprotons zur Überprüfung der CPT Symmetrie. Die Kühlung, Manipulation und Detektion des Spin-Zustandes einzelner gefangener (Anti-)Protonen sollen dabei erstmalig indirekt durch quantenmechanische Wechselwirkung mit einem Beryllium-Ion durchgeführt werden. Die dem Experimentprotokoll zugrunde liegende Manipulation des Beryllium-Ions erfolgt durch stimulierte Raman-Übergänge. Aufgrund des zur Manipulation des (Anti-)Protons erforderlichen, hohen Magnetfeldes von 5 T und der resultierenden großen atomaren Aufspaltung der Qubit Zustände von ungefähr 140 GHz, ist die weit verbreitete Verwendung eines Dauerstrich-Lasers für die Umsetzung des Raman Prozesses nicht überzeugend. Daher wurde im Rahmen dieser Arbeit die Implementierung notwendiger Operationen mittels eines optischen Frequenzkamms untersucht.
Die Dissertation zeigt und diskutiert numerische Simulationen der relevanten atomaren Prozesse in $^9Be^+$ für verschiedene Magnetfeldregimes. Um eine hohe Raman-Kopplungsstärke zu erzielen und gleichzeitig die Streurate zu unterdücken, ist es aufgrund der atomaren Struktur von Beryllium notwendig, die spektrale Breite und Form des Frequenzkamms präzise zu kontrollieren. Das zu diesem Zweck entwickelte Raman-Lasersystem basiert auf einem speziell angefertigten Frequenzkamm, welcher Femtosekunden-Pulse bei einer Wellenlänge von 626 nm emittiert. Zur selektiven Erzeugung schmalbandiger Pulse im ultravioletten Spektralbereich wurde eine nichtlineare spektrale Komprimierungs-Technik während der Frequenzverdopplung zu 313 nm implementiert. In diesem Zusammenhang ist erstmalig der signifikante Einfluss von räumlich-zeitlichen Kopplungen im nichtlinearen Medium BiBO untersucht worden. Die nichtlinearen Kopplungen ermöglichen zudem eine innovative und effiziente Manipulation der äußeren Frequenzkomponenten des optischen Kammes. Die Arbeit präsentiert darüber hinaus die experimentelle Implementierung der Kontrolle und Kopplung des Spin- und Bewegungs-Freiheitsgrades eines einzelnen $^9Be^+$-Ions unter Verwendung des gepulsten Raman-Systems. Die Ergebnisse der an einer Oberflächenfalle durchgeführten Experimente unterstreichen überzeugend das vorgestellte Konzept und stellen somit eine vielversprechende Umsetzung der speziellen Anforderungen an die kohärente Kontrolle $^9Be^+$-Ionen im Hochfeld-Regime dar.

Schlagwörter: Kohärente Zustandskontrolle, UV Frequenzkamm, spektrale Pulsmodifikation, gefangene und lasergekühlte Ionen, Quantenlogikspektroskopie

Contents

Chapter 1

Introduction

Since the development of ion traps [1, 2] a few decades ago, a remarkable growth in scientific and technological applications has taken place. The ability to study individual quantum systems and to precisely control all degrees of freedom of a single particle [3] under excellent environmental isolation has further revolutionized a wide range of modern research fields, such as atomic physics [4], high-precision experiments [5, 6, 7] and quantum information processing [8, 9, 10].

Penning traps [11, 12] have become one of the key instruments for high-precision experiments in atomic and nuclear physics [13, 14]. In such a trap, single particles and/or antiparticles are trapped by a superposition of electrostatic and magnetostatic fields. Due to the use of only static fields nearly no micro motion occurs and a high degree of isolation with virtually unlimited storage times is achieved. Further, the strong homogeneous magnetic field, typically on the order of several Tesla, enables high-precision measurements of the particle's cyclotron motion, which supports for example q/m, g-factor and mass measurements. The highly accurate determination of these atomic and nuclear properties provides stringent benchmarks for existing theoretical models and might lead to an improved understanding of fundamental interactions and symmetries.

Among the fundamental symmetries of nature is the invariance of physical processes under combined charge, parity and time reversal (CPT) within the Standard Model of particle physics [15]. While each single transformation (C,P,T) and the combinations of all pairs of two transformations is violated [16, 17, 18], the combination still holds [19]. This implies that fundamental properties of particles and antiparticles, such as their masses, their lifetimes, charges and magnetic moments should be identical, apart from the signs of the two latter. Even though our current understanding of physics is based on the Standard Model of particle physics and this model has

enormous proven predictive capabilities in many aspects, it is widely believed to require substitution by a more complete model. Several observations such as dark matter [20], dark energy [21] and the imbalance between matter and antimatter in the universe [22] are extremly difficult to explain within the Standard Model. Also, it has so far not been possible to implement gravity, as the last of four known fundamental interactions in nature, into the Standard Model by the formulation of an appropriate quantum field theory. This incompleteness motivates high-precision experiments to investigate CPT symmetry by comparing fundamental properties of particles and antiparticles, as possible physics beyond the Standard Model of particle physics might not require CPT invariance. A violation would have a meaningful impact on the foundations of our current understanding of physics, since it would be related to the really basic cornerstones of the Lorentz-invariant, local quantum field theories of the Standard Model [23].

g-factor comparisons between particles and antiparticles are one of the most sensitive (anti-)matter tests of possible CPT-violating effects [24, 25]. In the leptonic sector the electron's g-factor is indeed one of the most accurately measured and theoretically most precisely calculated quantities in modern physics. Based on Dehmelt's experiments comparing the electron's and the positron's g-factor [1] and ongoing work [26], CPT invariance is well tested for leptons with a current g-factor comparison uncertainty on the order of 10^{-12} [27, 28] and has so far not been found to be violated. In the baryonic sector, the situation is quite different. The experimental data is limited, although the g-factor anomaly of for example the (anti-)proton is three orders of magnitude larger than for the electron. The comparatively big anomaly arises because the (anti-)proton is a composite system, which at the same time prevents a precise calculation of the (anti-)proton's g-factor. As the g-factor anomaly would be strongly affected by a CPT violation, the comparison of the proton's and antiproton's g-factor provides one of the most stringent tests of CPT symmetry with baryons [29, 30]. Since a CPT violation would not have to occur in all sectors of the Standard Model to the same extent, the completion of high-precision measurements in the baryonic sector is of high interest. From an experimental point of view, the (anti-)proton's 1836-fold higher mass and 658-fold smaller magnetic moment compared to the electron complicates the precise determination of the g-factor. Currently mainly two efforts on (anti-)proton g-factor comparisons are carried out. One by the BASE (Baryon Antibaryon Symmetry Experiment) collaboration [31, 32, 33] and one by the ATRAP (Antihydrogen Trap) collaboration [34, 35], both operating antimatter experiments at an antiproton beamline at CERN's (french: Conseil Européen pour la Recherche Nucléaire) Antiproton Decelerator facility. The most accurate determination of the proton's g-factor by now has a relative precision of $3.3 \cdot 10^{-9}$ [7] and the antiproton's g-factor was recently published by BASE with a fractional precision of $0.8 \cdot 10^{-6}$ [36]. On this scale also no CPT violation has yet been found.

Despite the remarkable ongoing progress over the last years, precision experiments involving baryonic (anti-)matter, such as the (anti-)proton's g-factor measurement, are limited by the temperature of the particles [33]. Relevant improvements in precision would be provided by significantly lowering motional amplitudes. Unlike in other research fields, where the development of sophisticated cooling and manipulation techniques have brought substantial improvements over the last decades, these techniques have not yet or are just recently being started to be implemented in Penning traps. Exceptional progress has for example been made in the field of quantum information processing [8, 9, 10], which mostly relies on the possibility of achieving the motional ground state and on the ability to coherently manipulate single quantum states [37]. Ground-state cooling [38] and a series of techniques developed within quantum information processing have meanwhile been successfully applied to other research fields, such as high-precision spectroscopy. The prime example is quantum logic spectroscopy [39, 5], which has enabled atomic clocks of highest accuracy and the most accurate frequency standards to date with inaccuracies on the order of 10^{-18} [40]. The idea is that a well investigated and well controllable "logic" ion provides sympathetic laser cooling, state manipulation, and detection for a simultaneously trapped "spectroscopy" ion. Most work has however been focused on Paul traps [2], where charged particles are trapped in the center of an oscillating electric quadrupole field. The experimental overhead for implementing these techniques in Penning traps is considerably higher, due to technical complexities associated with the Penning trap environment, such as the high magnetic field. First results for motional ground-state cooling in a Penning trap on an optical transition in $^{40}Ca^{+}$ have just recently being published [41], demonstrating the general feasibility.

Our research group is part of and supported by the BASE collaboration. We aim to apply the cooling and manipulation techniques of quantum logic spectroscopy developed in the context of quantum information processing to high-precision g-factor experiments with trapped (anti-)protons in Penning traps. The ultimate goal is to boost the precision of ongoing tests of CPT symmetry. Following the proposals of Heinzen and Wineland [42, 43], the (anti-)proton will be coupled to a co-trapped atomic "logic" beryllium ion and sympathetically cooled, controlled and read out indirectly by using quantum logic operations. Beryllium is chosen due to its lightest mass among the commonly used qubit ions, which is highly desirable for the realization of the coupling scheme. The essential ground-state cooling and manipulation of $^{9}Be^{+}$ ions has so far not been demonstrated in Penning traps, mainly because of the lack of suitable laser systems. The high applied magnetic field in Penning traps provides large Zeeman ground-state splittings which requires special effort in terms of coherent qubit control. Subject of this thesis is the development and investigation of a laser system suitable for coherent control of

single beryllium ions trapped in the environment of an externally applied magnetic field of 5 T. This field strength is mandatory for precise frequency readout of the (anti-)proton and results in a beryllium qubit splitting near 140 GHz.

The essential quantum control of $^{9}Be^{+}$ will be carried out by two-photon stimulated Raman transitions [43], which in general requires two phase-coherent beams with frequency difference equal to the qubit splitting. For this typically continuous wave lasers are employed, where the two frequencies are provided by either phase locking two lasers or by a single laser modulated by acousto-optic or electro-optic modulators. Due to the lack of efficient high-frequency modulators and technical demands of phase locking two lasers with a frequency difference of 140 GHz, the continuous wave approach is rather unprofitable for implementation of the Raman process under given experimental conditions. Optical frequency combs [44] for this application in contrast offer the unique advantage of providing a broad spectrum with phase-coherent, regularly spaced sharp comb modes, which allows a direct and precise connection of also distant frequencies, without needing a second laser or inefficient high-frequency modulators, if the spectral bandwidth is larger than the qubit splitting. This feature allows to directly bridge the large qubit splitting in a controllable way, where pairs of comb modes coherently sum up and provide the Raman level coupling. So far only demonstrated for qubit control of $^{171}Yb^{+}$ ions for a qubit splitting near 10 GHz [45, 46], within this thesis, for the first time an optical frequency comb will be investigated for the implementation of $^{9}Be^{+}$ ion qubit control. The successful implementation might bring the technological breakthrough for ground-state laser cooling and state detection of single (anti-)protons, which may ultimately boost accuracies of current tests of CPT invariance based on g-factor comparisons. Further it may possibly contribute to a general impact on precision measurements, quantum logic and quantum simulations in Penning traps.

Outline

This thesis covers my doctoral research work, starting from the theoretical investigation of the application of an optical frequency comb for coherent qubit control of $^9Be^+$ ions under various experimental conditions, over the development and realization of an appropriate Raman laser system, to the first experimental demonstration of coherent qubit control of beryllium ions using an optical frequency comb carried out in a planar radio-frequency trap:

- Chapter 2 explains the quantum logic inspired g-factor measurement for single (anti-)protons. The measurement protocol, including the essential operations on the co-trapped beryllium ion, and key aspects of the implementation are discussed.

- Chapter 3 covers theoretical aspects of coherent qubit control. Besides general fundamentals on coherent laser control, this chapter gives insight into the physics of Raman transitions directly driven by an optical frequency comb. In addition it contains a comprehensive discussion of the specific requirements for qubit control of $^9Be^+$ ions using a pulsed Raman system.

- Chapter 4 describes the development of a narrow-bandwidth ultraviolet frequency comb for coherent qubit control of beryllium ions at magnetic fields of up to 5 T. The key parts are presented with special attention to the control of the comb's spectral properties.

- Chapter 5 presents the experimental implementation and demonstration of quantum control using the aforementioned Raman laser system. Results, obtained with a surface-electrode radio-frequency trap, demonstrating spin control and spin-motion coupling are shown and discussed.

- Chapter 6 concludes the experimental achievements and reviews them in the context of the planned (anti-)proton g-factor measurement experiment and beyond.

Chapter 2

Quantum logic enabled g-factor measurement of single (anti-)protons

As part of the BASE collaboration, our group aims to develop and implement novel laser-based, quantum logic inspired cooling and internal state detection techniques for single (anti-)protons. The ultimate goal is to support the most precise test of CPT symmetry in the baryonic sector of the Standard Model, based on a comparison of the proton's and antiproton's g-factor. The challenging spin state detection of the (anti-)proton required for g-factor measurement will be implemented indirectly through interaction with a co-trapped logic ion, following the proposals by Heinzen and Wineland [42, 43]. Where current efforts based on classical schemes are hurt by the slowness of state detection in combination with the inability to precisely control the motional states of the (anti-)proton, this quantum logic approach further allows for ground-state cooling of a single trapped (anti-)proton. This provides a boost in particle localization, allowing to speed-up detection times by potentially more than three orders of magnitude. It is expected that these improvements will contribute to further increases in the precision of g-factor measurements. In order to perform high precision g-factor measurements a single (anti-)proton will be trapped in a cryogenic Penning trap environment with static magnetic field of 5 T and brought into interaction with a single co-trapped $^9Be^+$ ion in a neighboring potential well. Experiments will be carried out in a multi-zone cylindrical Penning trap array partly adapted and extended from the BASE experiment. In order to perform different steps of the quantum logic cooling and detection procedure both particles will be shuttled between spatially separated zones. In this chapter the g-factor measurement protocol and key aspects of the implementation will be presented and discussed.

2.1 Determination of the g-factor

The g-factor is a dimensionless proportionality constant which denotes the relation between the (anti-)proton's spin $\vec{S}$ and its magnetic moment $\vec{\mu}_\mathrm{s}$ according to $\vec{\mu_\mathrm{s}} = g\frac{e}{2m_\mathrm{p}}\vec{S}$, where e/m_p is the charge-to-mass ratio of the (anti-)proton. Direct high-precision measurements of the g-factor are typically carried out in Penning traps, which provide an extraordinary degree of isolation and virtually unlimited storage times. A strong magnetic field in axial direction B_z radially confines the particle and a superimposed electric quadrupole field provides axial confinement. In such an environment the determination of the g-factor is based on the measurement of two frequencies from which the g-factor can be extracted according to:

$$g = 2\frac{\omega_\mathrm{L}}{\omega_\mathrm{c}} \tag{2.1}$$

Here $\omega_\mathrm{L} = g\frac{e}{2m_\mathrm{p}}B_\mathrm{z}$ is the Larmor frequency and $\omega_\mathrm{c} = \frac{e}{m_\mathrm{p}}B_\mathrm{z}$ is the free cyclotron frequency. Whereas both frequencies are field-dependent, the g-factor, given by the ratio of both frequencies, is field-independent.

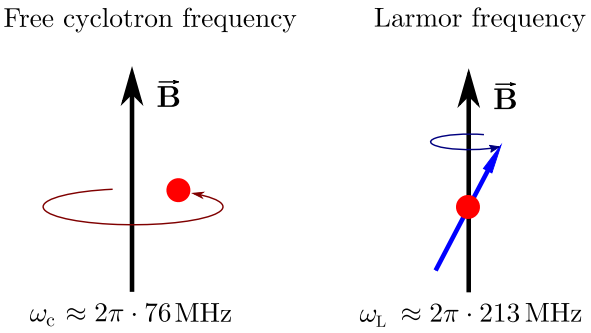

Figure 2.1: Schematical representation of the free cyclotron frequency for the case of zero axial velocity (left) and of the Larmor frequency (right). For a magnetic field of 5 T the (anti-)proton's free cyclotron frequency is $\omega_\mathrm{c} \sim 2\pi \cdot 76\,\mathrm{MHz}$ and describes the particle's circular trajectory around the magnetic field direction. The (anti-)proton's Larmor frequency at a magnetic field of 5 T is given by $\omega_\mathrm{L} \sim 2\pi \cdot 213\,\mathrm{MHz}$ and describes the precession of the particle's magnetic moment about the direction of the magnetic field.

Measurement of the free cyclotron frequency

The free cyclotron frequency ω_c describes the periodic motion a charged particle experiences in a homogeneous magnetic field due to the Lorentz-force. In case of zero axial velocity, its trajectory is constrained to a circular orbit perpendicular to

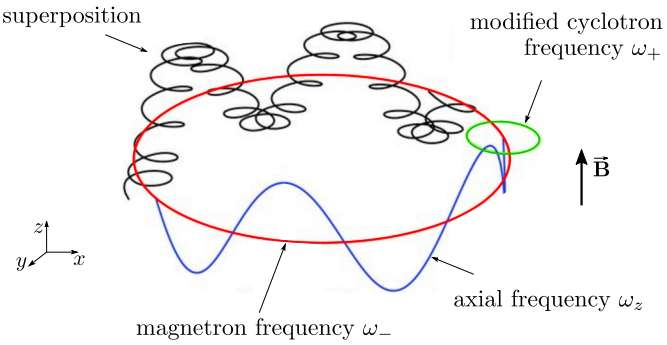

Figure 2.2: Schematical representation of the eigenfrequencies of a particle's motion occurring in a Penning trap environment. Its trajectory is composed of three decoupled harmonic oscillations: The modified cyclotron frequency ω_+, the magnetron frequency ω_- and the axial frequency ω_z.

the direction of the magnetic field, as schematically shown in Figure 2.1. Within the Penning trap environment the free cyclotron frequency can be determined by measuring the eigenfrequencies of the particle's oscillations and applying the Brown-Gabrielse invariance theorem [47]. The particle's trajectory in a Penning trap can be described by a superposition of three different decoupled harmonic oscillations, as schematically illustrated in Figure 2.2: The *modified cyclotron* motion ω_+ resulting from the free cyclotron frequency modified due to the additional electric fields, the *magnetron* frequency ω_- occurring due to the crossed magnetic and electrostatic potential and the *axial* motion ω_z resulting from the electrostatic quadrupole potential. The precise measurement of each frequency can be performed by detecting image currents in the trap electrodes using highly sensitive detection systems. The invariance theorem connects the experimentally accessible motional eigenfrequencies to the desired free cyclotron frequency according to $\omega_c^2 = \omega_+^2 + \omega_-^2 + \omega_z^2$, which allows a calculation even in presence of trap imperfections [11].

Measurement of the Larmor frequency

The Larmor frequency ω_L describes the precession frequency of the spin magnetic moment about the direction of an external magnetic field, as schematially shown in Figure 2.1. It corresponds to the energy that is required to change the (anti-) protons's spin state. The energy difference results from $E_s = -\mu_{s,z} \cdot B_z$ with two energy levels occurring for the (anti-)proton as spin 1/2 system, leading to $\Delta E_s = g\frac{e\hbar}{2m_p}B_z = \hbar\omega_L$. Since the Larmor precession is not accompanied by any extra physical motion of the particle, this frequency cannot be measured by simply detecting image currents. Instead, the Larmor frequency is determined by an

iterative process in which the spin flip probability is measured as a function of a radio-frequency (rf) drive field. The resulting resonance curve then allows to extract the desired Larmor frequency. This procedure requires to detect the spin state of the (anti-)proton for each applied rf frequency. The direct detection of a single (anti-)proton's spin-flip is the main experimental challenge and bottleneck in current experiments, based on classical measurement schemes.

Classical approach for spin detection

The established approach for detecting the spin orientation relies on the continuous Stern-Gerlach effect, which was first presented by Dehmelt and Ekström [48] for the g-factor measurement of the electron. It uses a magnetic inhomogenity to induce a coupling of the trapped particle's spin to its axial eigenfrequency. The spin transition causes a change in the axial frequency, which can be measured. Whereas the electron's g-factor is one of the most precisely measured quantities with this technique, it is hard to adopt to (anti-)protons due to their 1860-fold higher mass. This results in a 659-fold smaller magnetic moment, which in consequence requires a much stronger magnetic inhomogenity to be able to discriminate between different spin states. Current efforts therefore spatially separate the spin state analysis region with the strong magnetic inhomogenity from the region in which spin flips are driven and where the cyclotron frequency is measured to not degrade the spectroscopic signal [49]. In terms of cooling, the small cyclotron frequencies on the order of tens of MHz instead of hundreds of GHz resulting from the (anti-)proton's higher mass prevent cryogenic cooling to be able to reach the ground state of the cyclotron motion, which would be highly beneficial for the measurement protocol. In order to discriminate between spin flips through jumps in the axial frequency a stable cyclotron motion is required, which is best achieved for low temperatures. In current experiments cooling is achieved by coupling the (anti-)protons to a 4 K cryogenic resonator via image currents induced in trap electrodes [33, 50]. The achievable motional amplitudes of the (anti-)proton are critical because fluctuations in the ω_+ eigenmodes of their oscillations also induce a magnetic moment which couples to the inhomogenity of the magnetic field and causes a change in the axial eigenmode frequency being of the same order as the change due to a spin flip, which makes it extremely difficult to identify the spin state of the (anti-)proton. In combination with the long detection times on the order of several minutes, required to achieve sufficient Fourier resolution during detection, this brings extreme requirements on the stability of experimental parameters. Current experiments could therefore be strongly improved by cooling the (anti-)protons to the motional ground state and by speeding up the spin state detection procedure.

Quantum logic approach for cooling and state detection

To overcome the experimental challenges arising due to the high temperature and slow detection within the classical approach, our group aims to implement a completely different approach based on quantum logic operations. Cooling and state detection of a single (anti-)proton shall be realized indirectly through interaction with a co-trapped, well controllable "logic" ion following the proposals of Heinzen and Wineland from 1990 [42] and 1998 [43]. In particular the proposal from Wineland *et al.* from 1998 considers trapping both particles in separate, but near-by wells of a double-well potential, where the Coulomb interaction between them can be used for sympathetic cooling of the (anti-)protons. The proposed protocol for spin state detection relies on the same double well potential in combination with operations enabling spin state transfer via spin-motion coupling for the (anti-)proton and the atomic ion.

Sympathetic ground-state cooling

As first step of the sympathetic ground-state cooling of the single (anti-)proton, the atomic ion will be cooled to its motional ground state using resolved sideband cooling [43, 51]. This laser cooling technique requires the motional trap frequency to be much larger than the optical resonance linewidth, thereby satisfying the so-called strong-binding condition [52]. The ion will therefor be pre-cooled using Doppler laser cooling. Subsequently a sequence of motional subtracting sideband transitions will be applied, each providing a simultaneous spin flip and a reduction of the motional excitation by one quantum of motion (see chapter 3.1). By further implementing a dissipative repump process between each application, initializing the ion back into its initially prepared spin state, the motional excitation can successively be reduced until the motional ground state is achieved. In a second step the atomic ion and the (anti-)proton are brought to interact via the Coulomb force. In case of equal frequencies both particles will periodically exchange their energy, similar to classical pendulums being coupled via a spring. By interrupting the interaction after one exchange period, the kinetic energy of the (anti-)proton will have been transferred to the atomic ion. Subsequently re-cooling the atomic ion using sideband cooling again, both particles are brought in the absolute motional ground state. Compared to classical (anti-)proton g-factor experiments using only cryogenic cooling, the sympathetic cooling of the (anti-)proton will boost their localization from about $80\,\mu$m to 20 nm, being more than three orders of magnitude. This will have an important impact on reducing systematic errors in the measurement.

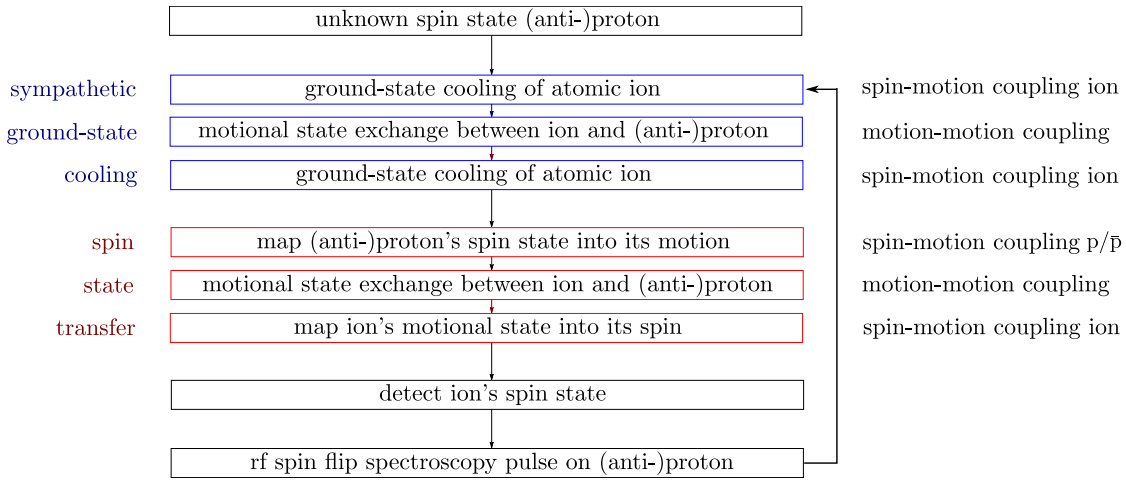

Figure 2.3: Quantum logic enabled measurement cycle for obtaining the Larmor frequency resonance as a function of a radio-frequency (rf) drive field. For each step of the sympathetic ground-state cooling and the spin state transfer the essential quantum logic operations are denoted on the right.

Spin state detection

The general idea for spin state detection is to transfer the unknown spin state of the (anti-)proton to the logic ion, where it can then easily and efficiently be read out using well established laser induced fluorescence detection. Assuming both particles have been cooled to the motional ground state, the procedure is based on three further key operations. First the unknown spin state of the (anti-)proton must be transferred into a conditional motional excitation. In a second step the (anti-)proton is coupled to the co-trapped atomic ion via the Coulomb interaction and their motional states are swapped. As a third step the conditional motional excitation of the logic ion must be converted back into a spin excitation. By this procedure the unknown spin state of the (anti-)proton has been transferred onto the atomic ion and can be easily detected for analysis. Using a state dependent fluorescence signal the final spin state of the logic ion can be determined, which allows to infer the intial spin state of the (anti-)proton. These operations can be performed within the range of milliseconds, therefore potentially boosting the (anti-)protons spin state detection time by three orders of magnitude, compared to classical schemes with state detection durations of several hundreds of seconds. The quantum logic state readout will therefore have a great impact on averaging times and studies of systematic effects.

Quantum logic enabled measurement cycle for the Larmor frequency

For a complete measurement of the Larmor resonance this cycle, including sympathetic ground-state cooling, spin transfer and detection, is then repeated once the (anti-)proton's spin state has been concluded and a spectroscopy pulse is applied to the (anti-)proton, as depicted in Figure 2.3. According to the proposals by Heinzen and Wineland the essential spin-motion coupling, as applied during several steps as denoted in the shown protocol, is suggested to be implemented by motional sideband transitions. Whereas the atomic ion provides an optical transition, allowing to use laser light for implementation (see chapter 3.1), the (anti-)proton does not exhibit an optical transition. The simultaneous spin flip and change in motional state will therefore be implemented on the spin flip transition at the Larmor frequency using radio-frequency radiation. For the essential coupling of the motional degrees of freedom, required for motional state exchange, the direct coupling of the atomic ion and the (anti-)proton in a double well potential, as suggested in 1998 [43], has the great advantage of being accessible for protons and antiprotons using the same atomic logic ion. Storing an antiproton in the same trap as the logic ion would alternatively require a negatively charged ion. This approach is being investigated in the group of Kellerbauer [53]. A third approach for achieving motional coupling was suggested in the first proposal of Wineland and Heinzen in 1990 by storing the two particles in different traps and coupling them through image charges induced in a shared trap electrode. This procedure is also being investigated in a different context in the groups of Rodriguez [54] and Häffner [55]. Here, we focus on the double well technique.

2.2 Implementation

In order to realize the sympathetic cooling and detection scheme, a segmented cylindrical Penning trap array consisting of different zones, partly adapted and extended from the BASE trap, has been designed within our group. Different steps of the quantum logic cooling and detection procedure will be carried out in spatially separate zones. Towards this end, the particles will be shifted between the zones by using time dependent voltages on trap electrodes. The transport must be performed within the motional ground state without significant heating. For achieving reasonably high Larmor frequencies a magnetic field of 5 T will be applied. Furthermore a cryogenic system will pre-cool the protons, which will presumably be loaded by irradiating organic material with electrons and then be resistively pre-cooled by a 4 K tank circuit. The cryostat, the magnet and outer vacuum system follow the design of the BASE setup at CERN. It consists of a large inner bore superconducting magnet and an independent science chamber, which is roughly the size of a large "can". This chamber has been extended and in addition to the CERN setup, the trap and

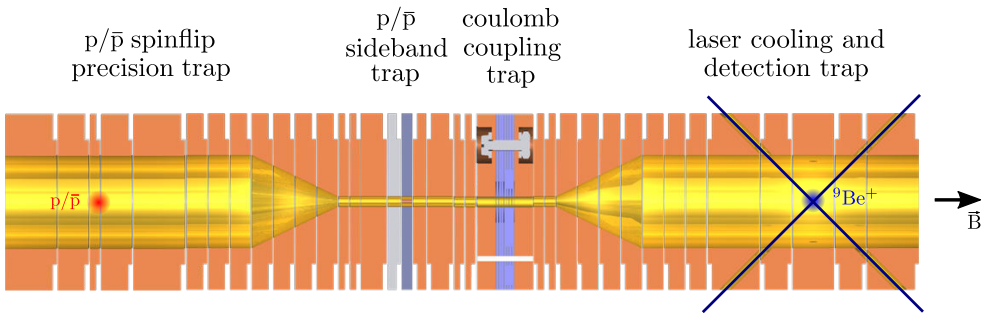

Figure 2.4: Sketch of a cut along the symmetry axis of the conceptual multi-zone Penning trap array. The coloured blocks represent the trap electrodes generating the electrostatic field providing axial confinement and allowing to shuttle the (anti-)particles between different zones. The design comprises four "modules", from left to right: The p/$\bar{\text{p}}$ spinflip precision trap, the p/$\bar{\text{p}}$ sideband trap, the double-well Coulomb coupling trap and the laser cooling and detection trap, which provides four laser ports at 45 ° with respect to the trap axis.

the apparatus will feature lasers and optical components for manipulating the logic ion. Once cooling and detection has been successfully demonstrated with protons in Hannover, the newly developed components shall be implemented at the BASE beamline at the Antiproton Decelerator (AD) at CERN, which is the only source of slow antiprotons. In current experiments, the kinetic energy of the antiprotons are further reduced by letting them pass a degrader foil attached in front of the trap "can", which allows trapping by applying voltages to the trap electrodes. The similarity of the two setups will support the challenging interchange of the experimental systems. Laser systems and optics will have to be adapted from the Hannover setup.

2.2.1 Trap setup and measurement protocol

Due to conflicting boundary conditions concerning trapping potentials and geometries, four spatially separate zones are designed for implementing different steps of the g-factor measurement protocol:

- (Anti-)proton spinflip precision trap
- (Anti-)proton sideband trap
- Double-well Coulomb coupling trap
- Laser cooling and detection trap

Figure 2.4 shows a cut along the symmetry axis of the conceptual multi-zone cylindrical Penning trap array. The trap is formed by multiple segmented wafers with differently sized inner holes stacked on top of each other with an insulating spacer inbetween. The first trap module, the (anti-)proton spinflip precision trap, is provided by our BASE collaborators from CERN. In this part motional and spin resonances of the single (anti-)proton will be probed. In the second part, the (anti-)proton sideband trap, the coupling of spin and motional degrees of freedom of the single (anti-)proton required for spin state transfer will be carried out. In the third trap, the Coulomb coupling trap, the double well potential for the single (anti-)proton and the single $^9Be^+$ ion will be provided, allowing to swap their motional states as required for sympathetic cooling and state transfer. The laser cooling and detection trap allows for spin-motion coupling, laser cooling and state readout of a single $^9Be^+$ ion. The trap design features four laser ports at 45 ° with respect to the trap axis. A detailed discussion of the specific requirements, of the trap design and the entire experimental apparatus can be found in [56].

Measurement protocol

To realize the entire spin state detection protocol, a single $^9Be^+$ ion will be loaded and trapped in the laser cooling and detection trap. Here it will be pre-cooled using Doppler cooling and then be cooled to its motional ground state using sideband cooling. The $^9Be^+$ ion will be prepared to the $|\uparrow\rangle$ state and motional subtracting blue sideband pulses will be applied, removing one quantum of motion and causing a spin flip to $|\downarrow\rangle$. After each pulse the ion will be dissipativly initialized back to the $|\uparrow\rangle$ level by pumping it to an excited state spontaneously decaying back into the initially prepared $|\uparrow\rangle$ state. This cycle will be repeated until the ion has reached its motional ground state. In the next step a pre-cooled (anti-)proton[1] and the ground state cooled atomic ion will both be shuttled to the double well trap in which they interact via the Coulomb force. Within one exchange period the motional states will have been swapped and the particles will be spatially separated again. Recooling the $^9Be^+$ ion to the ground state within the cooling and detection trap will bring both particles to their motional ground states. At this point the logic ion is assumed to be prepared in a well known spin state, in particular it will always be prepared in $|\uparrow\rangle$. The spin state of the proton is unknown within the first iteration loop, its position is within the (anti-)proton spinflip trap.
For implementing the state readout, the particles will then be separately shifted to the trap region performing the dedicated function. In order to realize the first key operation, the (anti-)proton will be shuttled to the sideband trap. Here a blue sideband radio-frequency pulse will be applied. This will flip the (anti-)proton's

[1] As preparation the trapped (anti-)protons will be pre-cooled by sympathetic Doppler cooling. This will be carried out analogous to sympathetic ground-state cooling using motional state transfer with a Doppler cooled $^9Be^+$ ion.

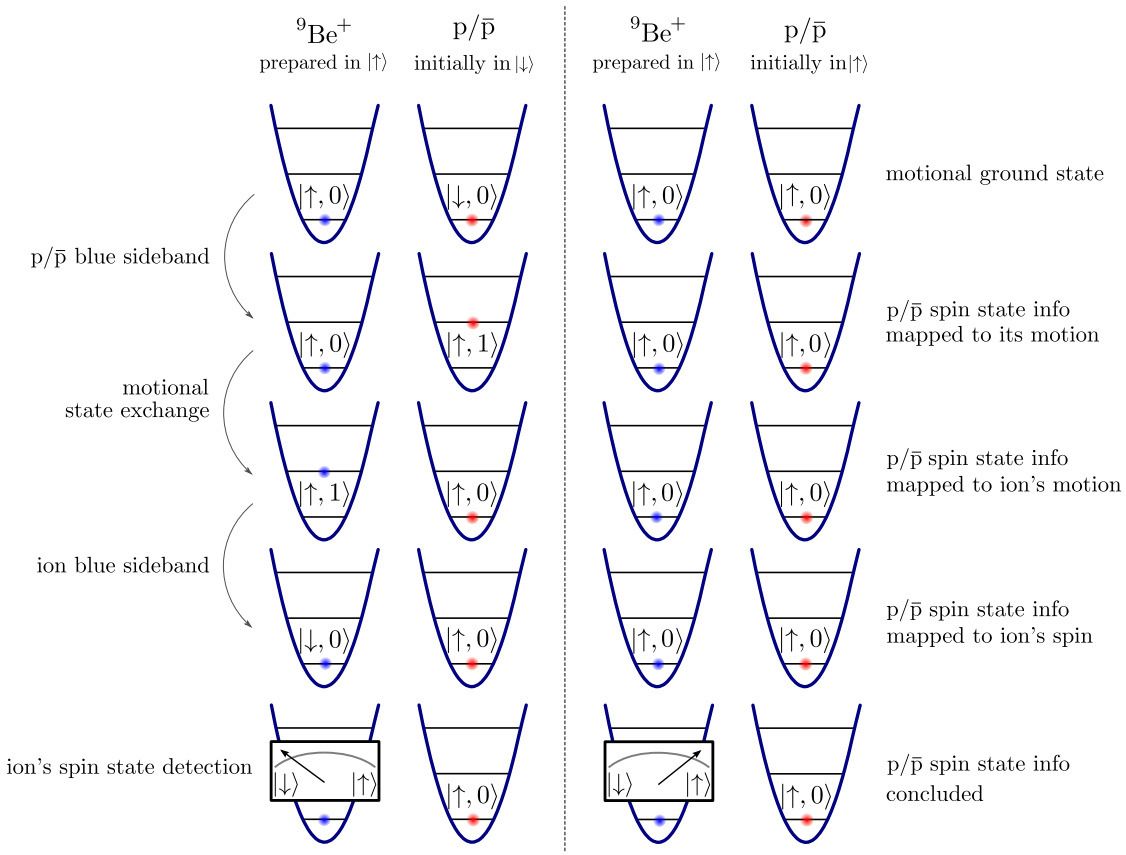

Figure 2.5: Quantum logic enabled measurement protocol for the spin state transfer and detection, assuming that the $^9Be^+$ ion and the (anti-)proton have been cooled to their motional ground states. The motional degree of freedom is visualized by the equidistant levels of a harmonic trapping potential, where the ground-state level corresponds to n=0 and the first motionally excited state to n=1. The left and the right column compare the cases of the (anti-)proton initially being in $|\downarrow\rangle$ (left) and the (anti-)proton initially being in $|\uparrow\rangle$ (right). The $^9Be^+$ ion is assumed to always be prepared in $|\uparrow\rangle$.

spin state and add one quantum of motion if and only if it was in $|\downarrow\rangle$ previously. In case of the (anti-)proton initially being in $|\uparrow\rangle$ no motional level exists to which a blue sideband pulse could couple and the ion remains unchanged in its internal and motional state. After this sideband pulse the spin state is therefore always $|\uparrow\rangle$ and the initially unknown spin state information has been mapped into the conditional motional excitation, where the information is given by whether the (anti-)proton is in the ground state (n=0) or in the first motionally excited state (n=1). This allows the second key operation to be performed. For this both particles are shuttled to the coupling trap. By keeping the trap frequencies equal for both particles over one exchange period, the conditional motional excitation of the (anti-)proton will

be transferred to the logic ion. After spatially separating the particles again and shuttling them back into their initial trap, the motional state of the logic ion now contains the information about the initial spin state of the (anti-)proton. It will be in n=1 if the (anti-)proton initially was in $|\downarrow\rangle$ and in n=0 otherwise. Within the cooling and detection trap the third key operation can then be performed on the logic ion. By applying a blue sideband transition the motional information will be mapped into the spin degree of freedom of the ion. The pulse will flip the ion's spin state and remove one quantum of motion if and only if it was motionally excited. It will remain unchanged if the ion was already in the motional ground state. By this procedure the spin state information of the (anti-)proton has been transferred to the logic ion's spin state, which can be read out by using state-dependent fluorescence detection. Shining in a laser beam being resonant on a closed-cycle transition from the $|\uparrow\rangle$ state will scatter photons which will be collected on a photomultiplier for data analysis. If the ion was is $|\downarrow\rangle$ the laser beam is far off-resonant and no photons will be scattered. The appearance of scattered photons hence indicates the spin state of the logic ion, allowing to deduce the initial spin state of the (anti-)proton. The measurement protocol for the spin state transfer and detection is summarized in Figure 2.5 for both possible initial spin states of the (anti-)proton.

2.2.2 Key operations

The successful realization of the quantum logic based cooling and state detection protocol requires the implementation and combination of three key operations, each of these alone being a challenging task to be overcome.

Proton and antiproton spin-motion coupling

Coupling the internal and motional degree of freedom of the (anti-)proton is challenging because no optical transitions exist allowing for laser based manipulation. The only available transition is the spin flip frequency, which for 5 T is on the order of 213 MHz. Coupling to a particle's motional state requires a spatial field variation over the size of a wavepacket [57], typically being on the order of tens of nm. Free space radio frequency fields with wavelengths on the order of meters do not bring sufficient variation and will therefore just flip the spin without affecting the motional state. This limitation has been overcome for atomic ions in the context of trapped-ion quantum information processing. Spin-motional couplings were achieved either by using a gradient in the near-field of dedicated conductors near-resonant with the ion's spin flip frequency [58, 59] or by applying a spin-dependent force induced by a static magnetic field gradient [60]. The latter approach will be applied for the first time to a single trapped (anti-)proton in the framework of this experiment, where the required field gradient will be obtained by a strong magnetic bottle in the dedicated sideband trap.

Motion-motion coupling between the (anti-)proton and the $^9Be^+$ ion

The second key operation is the motional coupling between the $^9Be^+$ ion and the (anti-)proton. The idea of direct Coulomb coupling two particles in a double well potential has already successfully been demonstrated for two atomic ions in the context of quantum information processing [61, 62]. Essential for the two particles to swap their motional excitation is that they have equal trap frequencies within their trapping potential. To achieve this, the ratio between the masses of the two particles must be equal to the ratio of their potential curvatures. As the coupling strength scales with the third power of the particle distance and larger ratios between the potential curvatures typically require a larger particle separation, the mass ratio should be kept as close to one as possible in order to achieve a strong coupling. For this reason $^9Be^+$ as the lightest readily laser cooled qubit ion was chosen for the experiment. The potential in which the $^9Be^+$ ion will be trapped must therefore provide a curvature about a factor $m(^9Be^+)/m(p) \approx 9$ higher than the potential curvature for the adjacently trapped (anti-)proton. Preliminary simulations yield a particle separation of $300\,\mu$m for an axial trap frequency of $2\pi \cdot 4\,$MHz, allowing to swap the motional states within 3.7 ms [33]. This double well Coulomb coupling including two particles of different mass trapped within a Penning trap is a unique feature of the project discussed within this thesis.

$^9Be^+$ ion spin-motion coupling

The third essential key operation is the coupling of the internal and motional degree of freedom of the $^9Be^+$ ion. Whereas coherent laser manipulation of atomic qubit ions is a standard process within trapped-ion quantum information processing, a substantial challenge arises from the high magnetic field of 5 T to be applied within this experiment. This field is required to achieve sufficently high frequencies for the (anti-)proton. For the $^9Be^+$ ion it leads to the drawback of causing a large ground-state splitting on the order of 140 GHz, which requires special effort in terms of qubit control. Implementing laser quantum control requires a Raman laser system with two phase-coherent beams with a frequency difference equal to the qubit splitting. Because of the large frequency gap, the widely used continuous wave laser approach is rather unprofitable. Instead, a pulsed laser system is investigated in order to directly implement the necessary operations, where pairs of comb teeth of the laser's spectrum coherently sum up and provide the desired coupling. This technique has so far only been demonstrated for $^{171}Yb^+$ ions at a level splitting near 10 GHz [45, 46]. The implementation for $^9Be^+$ ions is subject of this thesis and will bring out the first direct $^9Be^+$ ion qubit control using an optical frequency comb.

Chapter 3

Coherent qubit control

Our group aims to realize a precise test of CPT invariance with baryons based on a quantum logic inspired measurement and comparison of the proton's and antiproton's g-factor. Cooling, manipulation and spin state detection of a single trapped (anti-)proton will be implemented indirectly through interaction with a co-trapped beryllium ion using quantum logic operations. The essential manipulation of $^9Be^+$ will be carried out using two-photon stimulated Raman transitions. Because of the high required magnetic field of 5 T and the resulting large qubit splitting of $^9Be^+$ ions near 140 GHz, the widely used continuous wave laser approach is rather unprofitable. Instead, a pulsed Raman laser system is investigated to directly implement the necessary operations. In section 3.1, general basics on coherent laser control will be given. In section 3.2, a simplified model giving insight to the physics of Raman transitions driven by an optical frequency comb will be presented, while section 3.3 contains an accurate discussion of the specific requirements for qubit control of $^9Be^+$ ions using a pulsed Raman system.

3.1 Coherent laser control

The quantum logic inspired cooling and detection scheme presented in chapter 2 requires adressing and coupling of the internal and external degrees of freedom of the $^9Be^+$ ion. This can be achieved by performing certain transitions between a pair of long lived energy levels being identified as qubit states, as exemplarily shown in Figure 3.1. The spin qubit, representing the internal degree of freedom, possesses a lower state labeled $|\downarrow\rangle$ and an upper state labeled $|\uparrow\rangle$, separated by an energy $\hbar\omega_0$. Each of these states exhibits equidistant motional levels consecutively numbered by n, whose energies are determined by the harmonic trapping potential and whose splitting is given by the trap frequency ω_z. Spin-motion coupling can be

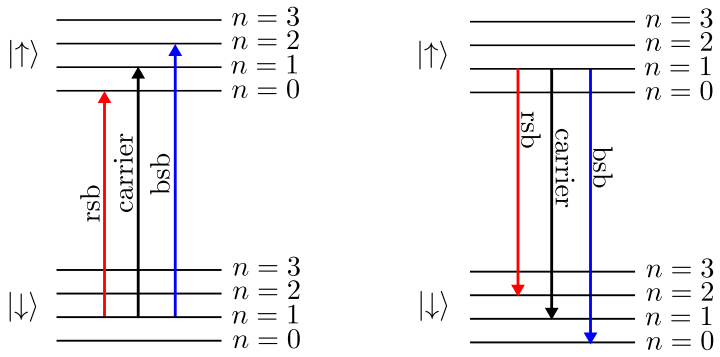

Figure 3.1: Schematic representation of first-order sideband and carrier transitions between the ion's qubit states. Its internal state is represented by the two-level system with the ground state labeled $|\downarrow\rangle$ and an upper state labeled $|\uparrow\rangle$. Each of these states exhibits equidistant motional levels consecutively numbered by n, representing the motional degree of freedom. A red sideband transition (rsb) induces a spin flip and simultaneously reduces/increases the ion's motion by one quantum of motion in case of it being initially in $|\downarrow\rangle/|\uparrow\rangle$, as shown in the left/right picture. A blue sideband transition (bsb) will induce a spin flip and in contrast reduce/increase the ion's motion by one quantum of motion in case of it being initially in $|\uparrow\rangle/|\downarrow\rangle$. The carrier transition does not affect the ion's motion and only changes the spin state for both cases.

implemented by motional sideband transitions by which a quantum of motion is added or substracted while changing the internal state. Adressing only the internal degree of freedom can be implemented by a carrier transition which consists in a spin flip without affecting the motional degree of freedom. These transitions can be controlled by the electromagnetic radiation of a laser beam. Assuming electric dipole transitions, the interaction between an ion and the electric field of the laser beam can be written as

$$H_{\text{int}}(t) = -\mathbf{d}\cdot\mathbf{E} = -\mathbf{d}\cdot E_0\hat{\epsilon}_{\text{L}}\cos(k\tilde{z}-\omega_{\text{L}}t+\phi)\,, \tag{3.1}$$

where $\mathbf{d}$ is the electric dipole operator being proportional to $\sigma^+ + \sigma^-$ with $\sigma^+ \equiv |\uparrow\rangle\langle\downarrow|$ and $\sigma^- \equiv |\downarrow\rangle\langle\uparrow|$. E_0 is the electrical field amplitude, k the k-vector, ω_{L} the frequency and ϕ the phase of the laser beam. The polarization of the laser beam $\hat{\epsilon}_{\text{L}}$ is characterized with respect to the quantization axis of the ion and expressed in terms of left circular ($\hat{\sigma}^-$), right circular ($\hat{\sigma}^+$) and linear ($\hat{\pi}$) polarizations according to $\hat{\epsilon}_{\text{L}} = e_-\hat{\sigma}^- + e_0\hat{\pi} + e_+\hat{\sigma}^+$ with $|e_-|^2+|e_0|^2+|e_+|^2= 1$. The ion position operator $\tilde{z} = z_0(a+a^\dagger)$ can be written in terms of the ground state wavepacket size z_0 and the creation $a^\dagger$ and the annihilation a operator associated with the trap frequency ω_z for the harmonic oscillator of the trapping potential. In the Lamb-Dicke regime, where the extent of the ion's motion is much less than $\lambda/2\pi = 1/k$, within the interaction frame and the rotating wave approximation [43] the Hamiltonian can

be approximated by [63]:

$$H_{\text{int}} \simeq \hbar(\Omega e^{i\phi})\sigma^{+} e^{-i(\omega_{\text{L}}-\omega_0)t}[1 + i\eta(a e^{-i\omega_{\text{z}}t} + a^{\dagger} e^{i\omega_{\text{z}}t})] + \text{h.c.} \tag{3.2}$$

The shortcut h.c. stands for the Hermitian conjugate including the terms proportional to σ^{-}.

$$\Omega \equiv E_0 \langle\uparrow|\mathbf{d}\cdot\hat{\epsilon}_{\text{L}}|\downarrow\rangle/(2\hbar) \tag{3.3}$$

is the single-photon Rabi frequency[1] and $\eta = k \cdot z_0$ the single-beam Lamb-Dicke parameter. From Equation 3.2 it can be seen that for certain choices of the laser frequency ω_{L} the dominating term of the Hamiltonian of interaction yields a first-order sideband or carrier transition:

- **Blue sideband transition**
  for $\omega_{\text{L}} = \omega_0 + \omega_{\text{z}}$: $H_{\text{int}} \simeq i\eta\hbar(\Omega e^{i\phi})\sigma^{+}a^{\dagger} + \text{h.c.}$
  with:
  $|\downarrow\rangle \rightarrow |\uparrow\rangle$ transitions accompanied by $|n\rangle \rightarrow |n+1\rangle$
  $|\uparrow\rangle \rightarrow |\downarrow\rangle$ transitions accompanied by $|n\rangle \rightarrow |n-1\rangle$

- **Red sideband transition**
  for $\omega_{\text{L}} = \omega_0 - \omega_{\text{z}}$: $H_{\text{int}} \simeq i\eta\hbar(\Omega e^{i\phi})\sigma^{+}a + \text{h.c.}$
  with:
  $|\downarrow\rangle \rightarrow |\uparrow\rangle$ transitions accompanied by $|n\rangle \rightarrow |n-1\rangle$
  $|\uparrow\rangle \rightarrow |\downarrow\rangle$ transitions accompanied by $|n\rangle \rightarrow |n+1\rangle$

- **Carrier transition**
  for $\omega_{\text{L}} = \omega_0$: $H_{\text{int}} \simeq \hbar(\Omega e^{i\phi})\sigma^{+} + \text{h.c.}$
  with:
  $|\downarrow\rangle \rightarrow |\uparrow\rangle$ transitions accompanied by $|n\rangle \rightarrow |n\rangle$
  $|\uparrow\rangle \rightarrow |\downarrow\rangle$ transitions accompanied by $|n\rangle \rightarrow |n\rangle$

Whether a sideband transition adds or removes a quantum of motion depends on the initial spin state of the ion, as visualized in Figure 3.1. If the ion is prepared in $|\downarrow\rangle$, the implementation of a single red sideband with frequency $\omega_{\text{L}} = \omega_0 - \omega_{\text{z}}$ will reduce its motion, whereas if it is initialized in $|\uparrow\rangle$, a blue sideband at $\omega_{\text{L}} = \omega_0 + \omega_{\text{z}}$ is required for cooling purposes. Further note that if there is no motional state to couple to at the applied sideband frequency $\omega_{\text{L}} = \omega_0 \pm \omega_{\text{z}}$, the ion's internal and external state will remain unchanged.

[1] Equation 3.3 for the single-photon Rabi frequency follows the definition introduced at the National Institute of Standards and Technology (NIST) in Boulder, CO. Other commonly used definitions (e.g. [64, 65]) deviate by a factor of 2: $\Omega \equiv E_0\langle\uparrow|\mathbf{d}\cdot\hat{\epsilon}_{\text{L}}|\downarrow\rangle/(\hbar)$

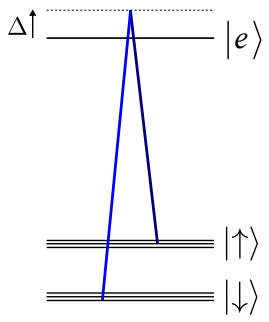

Figure 3.2: Illustration of the two-photon stimulated Raman process. Two Raman beams induce a ground-state sublevel coupling via interaction with a virtual excited state being detuned by Δ from a real excited state $|e\rangle$. If the detuning is large enough to not strongly populate the excited state, the ion can perform transitions between $|\downarrow\rangle$ and $|\uparrow\rangle$ by absorbing light from one beam and emitting it into the other beam when their frequency difference is equal to the ground-state splitting.

3.1.1 Raman transitions

For spin qubits implemented in two hyperfine ground-state levels, the coherent transitions are typically carried out with lasers[2] using two-photon stimulated Raman transitions [63]. The coupling of the qubit states is achieved by applying two phase coherent Raman laser beams which have a frequency difference equal to the ground-state splitting. Each beam is connecting one of the ground-state sublevels to a virtual excited state, which is detuned by Δ from resonance with a real excited state $|e\rangle$ as shown in Figure 3.2.
For sufficiently large detunings, the population of the excited state is negligible and the state can be adiabatically eliminated. The system then behaves as an effective two-level system leading to the desired ground-state sublevel coupling. The ion can perform transitions by absorbing light at ω_L from one beam and emitting at $\omega_\mathrm{L} \pm \omega_\mathrm{qubit}$ into the other beam. As the process is driven by two laser beams, the interaction Hamiltonian in Equation 3.2 must be adjusted accordingly. k, ω_L and ϕ must here for be replaced by the k-vector, frequency and phase difference $\Delta k = |\mathbf{k}_1 - \mathbf{k}_2|$, $\omega_1 - \omega_2$ and $\phi_1 - \phi_2$ between the laser beams. Furthermore the single-photon Rabi frequency must be replaced by the two-photon Rabi frequency[3]

[2] An alternative approach applies microwaves to directly implement the level coupling [59], as realized in the surface-electrode ion trap experiment described in section 5.1. This approach cannot be applied for the high-field (anti-)proton experiment, due to the large qubit splitting on the order of 140 GHz, wherefor the established method using Raman transitions is pursued.

[3] Equation 3.4 again follows the NIST definition. In case the single-photon Rabi frequency has been chosen in the other existing definition, a factor of 2 must be added in the denominator according to: $\Omega_\mathrm{eff} = \dfrac{\Omega_1 \cdot \Omega_2}{2\Delta}$ with Ω_1 and Ω_2 being the single-photon Rabi frequencies given by $\Omega \equiv E_0 \langle\uparrow|\mathbf{d} \cdot \hat{\epsilon}_\mathrm{L}|\downarrow\rangle/(\hbar)$.

[63]:

$$\Omega = \frac{\Omega_1 \cdot \Omega_2}{\Delta} = \frac{E_1 E_2}{4\hbar^2} \frac{\langle\uparrow|\mathbf{d}\cdot\hat{\epsilon}_{\mathrm{L}_2}|e_i\rangle\langle e_i|\mathbf{d}\cdot\hat{\epsilon}_{\mathrm{L}_1}|\downarrow\rangle}{\Delta_i} \tag{3.4}$$

The indices 1 and 2 denote the two laser beams, Ω_1 and Ω_2 their single-photon Rabi frequencies according to Equation 3.3, Δ_i their detuning from the excited state $|e_i\rangle$ of the Raman process. The Lamb-Dicke parameter is now proportional to Δk and given by $\eta \equiv \Delta k \cdot z_0$.
Tuning the frequency difference between the two Raman beams to resonance with either the red or blue sideband or the carrier transition, the system will undergo a coherent evolution according to [63]:

$$|\downarrow\rangle|n\rangle \rightarrow \cos(\Omega_{n,n'}t)|\downarrow\rangle|n\rangle - ie^{i\phi}\sin(\Omega_{n,n'}t)|\uparrow\rangle|n'\rangle \tag{3.5}$$

$$|\uparrow\rangle|n\rangle \rightarrow -ie^{-i\phi}\sin(\Omega_{n,n'}t)|\downarrow\rangle|n\rangle + \cos(\Omega_{n,n'}t)|\uparrow\rangle|n'\rangle \tag{3.6}$$

The sideband Rabi frequencies are given by $\Omega_{n,n'} \equiv \eta\,\Omega\sqrt{n_>}$, with $n_>$ being the upper of n and n', leading to:

- **Blue sideband transition**
  for $|\omega_1 - \omega_2| = \omega_0 + \omega_z$: $n' = n + 1$: $\Omega_{\mathrm{bsb}} \equiv \eta\,\Omega_c\sqrt{n+1}$
- **Red sideband transition**
  for $|\omega_1 - \omega_2| = \omega_0 - \omega_z$: $n' = n - 1$: $\Omega_{\mathrm{rsb}} \equiv \eta\,\Omega_c\sqrt{n}$
- **Carrier transition**
  for $|\omega_1 - \omega_2| = \omega_0$: $n' = n$: $\Omega_c = \Omega_{n,n'}$

Under these conditions the system will perform Rabi oscillations between the qubit states. The probability of finding the ion in the upper or the lower qubit state oscillates with the corresponding Rabi frequency. The time required for implementing a π-pulse[4] is given by [63]:

$$t_\pi = \frac{\pi}{2\Omega} \tag{3.7}$$

If the duration of laser operation is adjusted to this time a single transition will be executed, as required for implementing the sympathetic cooling and spin state

[4]The formula 3.7 follows the NIST definition. Due to the deviating formulas for the single-photon and two-photon Rabi frequency (see footnote 1 and 2), also the formula for the π-time differs by a factor of 2 between the existing definitions. Within the other mentioned definition the π-time is given by: $t_\pi = \frac{\pi}{\Omega}$

transfer scheme. Note that in order to achieve an efficient coupling of spin and motion the two Raman beams must be directed onto the ion from different directions as the coupling is proportional to Δk, given by the linear dependence of the sideband Rabi frequencies on the two-photon Lamb-Dicke parameter $\eta = \Delta k \cdot z_0$. The absorption of a photon from one beam and emission into the other beam causes a momentum change of $\hbar\Delta k$ along the direction of the wavevector difference Δk, which allows coupling to the ion's motion along the direction given by Δk.

3.1.2 Rabi frequency

While the above treatment of the Raman process was simplified to the exemplary case of a single excited state, it needs to be generalized to multiple excited states for calculation of experimentally relevant Rabi oscillations. The Rabi frequency is then given by the sum over all contributing level couplings [63]:

$$\Omega = \frac{E_1 E_2}{4\hbar^2} \sum_i \frac{\langle\uparrow|\mathbf{d}\cdot\hat{\epsilon}_{\mathrm{L}_2}|e_i\rangle\langle e_i|\mathbf{d}\cdot\hat{\epsilon}_{\mathrm{L}_1}|\downarrow\rangle}{\Delta_i} \tag{3.8}$$

The sum over i includes the contribution of all excites states $|e_i\rangle$ with respective detunings Δ_i.
The calculation of the Rabi frequency can be simplified by expressing the two-photon Rabi frequency in terms of a single-photon Rabi frequency of a closed-cycle transition. This further simplifies the comparison with other ion species having a comparable level structure. For a closed-cycle transition the dipole matrix element can be set in relation to an experimentally measured spontaneous emission rate using Fermi's golden rule for an atom coupled to free space. The relation is given by [65]:

$$\mu_{\mathrm{ct}}^2 = \frac{3\gamma\epsilon_0\hbar\lambda^3}{2} \tag{3.9}$$

With μ_{ct} denoting the dipole matrix element of the cycling transition (ct), λ the wavelength, γ the linewidth and ϵ_0 the vacuum permittivity. This relation allows the single-photon Rabi frequency of this transition[5] to be expressed in terms of the saturation intensity [46]:

$$g_{\mathrm{ct}}(I) = \sqrt{\frac{\gamma^2 I}{8 I_{\mathrm{sat}}}} \tag{3.10}$$

With the saturation intensity I_{sat} given by [64]:

$$I_{\mathrm{sat}} = \frac{\gamma\hbar c}{6\lambda^3} = \frac{\gamma^2 c\epsilon_0\hbar^2}{4\mu_{ct}^2} \tag{3.11}$$

[5] A factor 2 in the denominator in Equation 3.10 comes for the NIST definition of the Rabi frequency

Here $I = \frac{c\epsilon_0}{2} E_0^2$ is the laser beam intensity at the position of the ion and λ the wavelength of the laser. The Rabi frequency of the closed-cycle transition therefore, besides some atomic constants, only depends on the laser's intensity and is given by:

$$g_{\mathrm{ct}}(I) = \sqrt{\frac{3\gamma I \lambda^3}{4\hbar c}} = \frac{E_0}{2\hbar}\mu_{ct} \tag{3.12}$$

This relation can then be used to simplify the calculation of any other Rabi frequency according to:

$$\Omega_{\mathrm{eg}} = \frac{E_0}{2\hbar}\langle e|\mathbf{d}\cdot\hat{\epsilon}_{\mathrm{L}}|g\rangle = \frac{E_0}{2\hbar}\mu_{\mathrm{ct}} \cdot \frac{\langle e|\mathbf{d}\cdot\hat{\epsilon}_{\mathrm{L}}|g\rangle}{\mu_{\mathrm{ct}}} = g_{\mathrm{ct}} \cdot \frac{\langle e|\mathbf{d}\cdot\hat{\epsilon}_{\mathrm{L}}|g\rangle}{\mu_{\mathrm{ct}}}\,, \tag{3.13}$$

where e and g stand for the involved excited and ground-state levels. The two-photon Rabi frequency from Equation 3.8 can hence be calculated by:

$$\Omega = g_{\mathrm{ct}}(I_1) g_{\mathrm{ct}}(I_2) \sum_i \frac{\langle\uparrow|\mathbf{d}\cdot\hat{\epsilon}_{\mathrm{L}_2}|e_i\rangle\langle e_i|\mathbf{d}\cdot\hat{\epsilon}_{\mathrm{L}_1}|\downarrow\rangle}{\Delta_i \cdot \mu_{\mathrm{ct}}^2} \tag{3.14}$$

3.1.3 Scattering rate

A fundamental source of decoherence is spontaneous emission induced by the off-resonant laser radiation during the Raman process. The scattering of photons can be minimized by detuning the Raman laser beams from resonance with the optical transitions, but it cannot be eliminated completly. In case an excited state gets populated, it can spontaneously decay back into the ground state. In the presence of multiple gound-state sublevels two kinds of photon scattering occur. For *Raman* scattering the population is transferred to other sublevels than the initial state, always causing a loss of coherence. *Rayleigh* scattering in contrast does not change the ground-state population after the scattering event and therefore not necessarily affects coherence. Decoherence of the qubit superposition state occurs if the scattered photon carries information about the qubit state, leading to dephasing of the superposition. The decohering part due to Rayleigh scattering has been found to be determined by the difference between the elastic scattering *amplitudes* for the two qubit levels [66]. For small splittings between the ground-state qubit levels, the difference of scattering amplitudes for beryllium is small and decoherence due to off-resonant light scattering is dominated by Raman scattering, as experimentally been shown in [67]. For large qubit splittings, decoherence due to Rayleigh scattering cannot be neglected, as the difference of scattering amplitudes can be large.

The rate of photon scattering events, for which an ion initially in $|g_{\mathrm{ini}}\rangle$ after the scattering event ends in $|g_{\mathrm{final}}\rangle$ is given by the Kramers-Heisenberg relation [68, 69, 70]. Excluding the case where $|g_{\mathrm{ini}}\rangle = |g_{\mathrm{final}}\rangle$ and summing over all level

contributions yields the Raman scattering rate Γ_{Raman}. For an ion initially in the spin state $|g_{\text{ini}}\rangle = m_S$, the j-th Raman laser beam with polarization $\hat{\epsilon}_{\text{L}_j}$ causes a rate of:

$$\begin{aligned}\Gamma_{\text{Raman}_j}(m_S) &= \gamma \frac{E_{0_j}^2}{4\hbar^2} \sum_q \left| \sum_i \frac{\langle g_{\text{final}}|\mathbf{d}\cdot\hat{\epsilon}_q|e_i\rangle \cdot \langle e_i|\mathbf{d}\cdot\hat{\epsilon}_{\text{L}_j}|m_S\rangle}{\mu_{\text{ct}}\cdot(\Delta_i - \mathbf{i}\frac{\gamma}{2})} \right|^2, \text{for } g_{\text{final}} \neq m_S \\ &= \gamma\, g_{\text{ct}}^2(I_j) \sum_q \left| \sum_i \frac{\langle g_{\text{final}}|\mathbf{d}\cdot\hat{\epsilon}_q|e_i\rangle \cdot \langle e_i|\mathbf{d}\cdot\hat{\epsilon}_{\text{L}_j}|m_S\rangle}{\mu_{\text{ct}}^2\cdot(\Delta_i - \mathbf{i}\frac{\gamma}{2})} \right|^2, \text{for } g_{\text{final}} \neq m_S\end{aligned} \tag{3.15}$$

The sum over i includes the contribution of all excites states $|e_i\rangle$ with respective detunings Δ_i. q denotes the polarization of the scattered photons with respect to the ion's quantization axis, $\hat{\epsilon}_q$ the respective polarization vector, μ_{ct} the dipole matrix element of a closed-cycle transition according to Equation 3.9 and g_{ct} the Rabi frequency of the cycling transition according to Equation 3.12. The complex damping factor $-\mathbf{i}\frac{\gamma}{2}$ corresponds to the linewidth of the excited states and avoids infinity on resonance.
The case $|g_{\text{ini}}\rangle = |g_{\text{final}}\rangle$ yields the Rayleigh scattering rate for an ion initially being in the spin state $|g_{\text{ini}}\rangle = m_S$. This rate does not provide information about the induced decoherence. The decohering part due to Rayleigh scattering is proportional to the square of the difference of the probability *amplitudes* for elastic scattering of the two qubit levels and given by [66]:

$$\begin{aligned}\Gamma_{\text{el}_j} &= \gamma \frac{E_{0_j}^2}{4\hbar^2} \sum_q \left| \sum_i \frac{\langle\downarrow|\mathbf{d}\cdot\hat{\epsilon}_q|e_i\rangle \cdot \langle e_i|\mathbf{d}\cdot\hat{\epsilon}_{\text{L}_j}|\downarrow\rangle}{\mu_{\text{ct}}\cdot(\Delta_i - \mathbf{i}\frac{\gamma}{2})} - \sum_{i'} \frac{\langle\uparrow|\mathbf{d}\cdot\hat{\epsilon}_q|e_{i'}\rangle \cdot \langle e_{i'}|\mathbf{d}\cdot\hat{\epsilon}_{\text{L}_j}|\uparrow\rangle}{\mu_{\text{ct}}\cdot(\Delta_{i'} - \mathbf{i}\frac{\gamma}{2})} \right|^2 \\ &= \gamma\, g_{\text{ct}}^2(I_j) \sum_q \left| \sum_i \frac{\langle\downarrow|\mathbf{d}\cdot\hat{\epsilon}_q|e_i\rangle \cdot \langle e_i|\mathbf{d}\cdot\hat{\epsilon}_{\text{L}_j}|\downarrow\rangle}{\mu_{\text{ct}^2}\cdot(\Delta_i - \mathbf{i}\frac{\gamma}{2})} - \sum_{i'} \frac{\langle\uparrow|\mathbf{d}\cdot\hat{\epsilon}_q|e_{i'}\rangle \cdot \langle e_{i'}|\mathbf{d}\cdot\hat{\epsilon}_{\text{L}_j}|\uparrow\rangle}{\mu_{\text{ct}^2}\cdot(\Delta_{i'} - \mathbf{i}\frac{\gamma}{2})} \right|^2\end{aligned} \tag{3.16}$$

Of special interest is the probability of off-resonant light scattering occurring during qubit operations. One measure for this is the calculation of the scattering probability occurring during the time required to carry out a π-pulse on the carrier transition [63], given by the product of the total scattering rate times the π-time of the carrier Rabi oscillation:

$$P_{\text{scat}} = \Gamma_{\text{total}} \cdot t_\pi \tag{3.17}$$

In order to account for spontaneous emission induced decoherence, the total decoherence rate is evaluated for the superposition of qubit states, which for the j-th Raman beam is given by:

$$\Gamma_{\text{total}_j} = \frac{1}{2}(\Gamma_{\text{Raman}_j}(\downarrow) + \Gamma_{\text{Raman}_j}(\uparrow) + \Gamma_{\text{el}_j}) \tag{3.18}$$

For qubit operations implemented by two Raman beams the total decoherence rate is given by the sum of the total rates for each Raman beam.

3.1.4 Stark shift

So far Stark shifts induced by off-resonant laser radiation have not been accounted for. The time-varying electric field of the laser leads to a shift of the atomic Zeeman levels. In the limit that $\Delta_i \gg \gamma$ the absolute Stark shift from the j-th beam on the level $|g\rangle$ within the ground-state manifold is given by [63]:

$$\begin{aligned}\delta(g,j) &= \frac{E_{0_j}^2}{4\hbar^2}\sum_i \frac{|\langle g|\mathbf{d}\cdot\hat{\epsilon}_{\mathrm{L}_j}|e_i\rangle|^2}{\Delta_i} \\ &= g_{\mathrm{ct}}^2(I_j)\sum_i \frac{|\langle g|\mathbf{d}\cdot\hat{\epsilon}_{\mathrm{L}_j}|e_i\rangle|^2}{\mu_{\mathrm{ct}}^2\,\Delta_i}\end{aligned} \tag{3.19}$$

The sum over i includes all excited level contributions with respective detunings Δ_i. μ_{ct} denotes the dipole matrix element of a closed-cycle transition according to Equation 3.9 and g_{ct} the Rabi frequency of the cycling transition according to Equation 3.12. Of special interest is the relative shift denoting the effective direction of each ground-state level shift. It can be calculated by subtracting the mean of the absolute Stark shift of all ground-state manifold levels. The relative shift from the j-th beam on the level $|g\rangle$ is given by:

$$\Delta_{\mathrm{mean}}(g,j) = \delta(g,j) - \frac{1}{\chi}\sum_{g=1}^{\chi}\delta(g,j) \tag{3.20}$$

With χ denoting the number of levels within the ground-state manifold. Comparing the relative shifts for two qubit states gives the change of the qubit frequency induced by the off-resonant laser irradiation.

3.2 Qubit control using an optical frequency comb

Raman transitions are typically realized using continuous wave (CW) laser beams. For this either two phase locked CW lasers or a single CW laser modulated by acousto-optic (AOM) or electro-optic modulators (EOM) are used. In contrast pulsed lasers have a sufficiently broad spectrum to directly bridge the qubit splitting without needing a second laser or a high frequency modulator, if their spectral bandwidth is larger than the qubit splitting. This advantage is of special interest for the (anti-)proton g-factor measurement experiment, where the qubit splitting of 140 GHz is significantly larger than for typical trapped-ion experiments. Due to the lack of efficient high frequency AOMs and EOMs and due to the technical

complexity of phase locking two lasers with frequency difference of 140 GHz, the CW laser approach is rather unfavorable. Optical frequency combs for this application offer the unique advantage of providing a broad spectrum with phase coherent, regularly spaced sharp comb modes, which allows a precise connection between the distant qubit frequencies. This feature allows to directly bridge the large splitting in a controllable way. In this section the basic properties of optical frequency combs will be presented and the general concept of their implementation in terms of coherent qubit control will be discussed.

3.2.1 Optical frequency combs

An optical frequency comb by definition describes a spectrum consisting of several laser modes equidistantly spaced in frequency [44, 71] and is commonly generated by mode-locked lasers. In the time domain picture such lasers produce a periodic sequence of ultrashort phase-coherent pulses separated by the round-trip time of the laser cavity T_{rep}, as shown in Figure 3.3. The frequency domain representation is given by the Fourier transformation of the pulse train. The resulting spectrum has a frequency width which is inversely proportional to the temporal width of a single pulse envelope τ_{p} and is centered at the optical frequency of its carrier ω_{c}. The comb line spacing is inversely proportional to the time between the pulses $\frac{1}{T_{\mathrm{rep}}} = f_{\mathrm{rep}} = \frac{\omega_{\mathrm{rep}}}{2\pi}$ and hence given by the repetition rate of the laser generating the pulses f_{rep}. The spectral width of each comb mode is Fourier limited and approximately scales like $\sim \frac{f_{\mathrm{rep}}}{N}$, with N being the number of involved pulses of the corresponding pulse train. In the limit of an infinite pulse train the spectral shape of each mode is given by a delta-function. The optical frequency of the n-th comb tooth can be written as $f_n = n \cdot f_{\mathrm{rep}} + f_{\mathrm{ceo}}$, where n is an integer that indexes the comb line and $f_{\mathrm{ceo}} = \frac{f_{\mathrm{rep}} \Delta\phi_{\mathrm{ceo}}}{2\pi}$ is an offset frequency of the entire comb structure originating from the pulse to pulse shift of the carrier envelope phase $\Delta\phi_{\mathrm{ceo}}$. This phase shift occurs because of differing group and phase velocities (see section 4.3.1) inside the laser cavity. For the application of performing two-photon stimulated Raman transitions this shift is irrelevant [45] and the electric field of an ideal pulse train of N pulses at a fixed point in space can be written as:

$$E(t) = \sum_{n=0}^{N-1} f_{\mathrm{p}}(t - nT_{\mathrm{rep}}) \cdot \mathrm{e}^{i\omega_{\mathrm{c}} t} \tag{3.21}$$

Here $f_{\mathrm{p}}(t)$ denotes the envelope of a single pulse, which is periodically repeated with time period T_{rep} and multiplied with the carrier wave. The corresponding comb spectrum $\tilde{E}(\omega)$ of the pulse train is given by the Fourier transform[6]:

$$\tilde{E}(\omega) = \mathbf{FT}[E(t)] = \frac{1}{2\pi} \int_{-\infty}^{\infty} E(t) \mathrm{e}^{i\omega t} dt \tag{3.22}$$

[6] All calculations are performed within the inverse non-unitary Fourier transformation definition

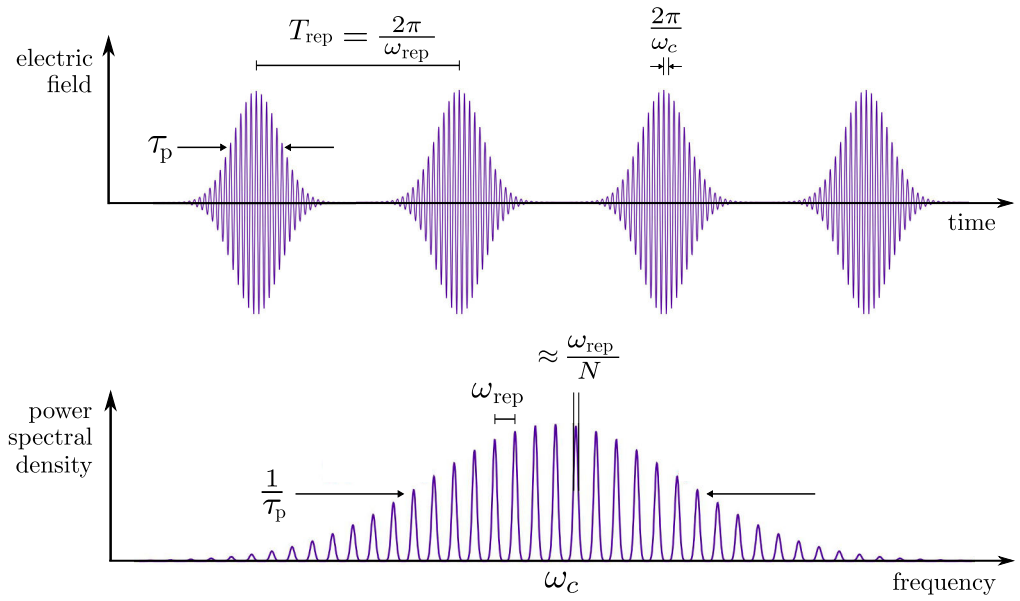

Figure 3.3: Representation of the electric field of a pulse train emitted by a mode-locked laser in the time domain and its corresponding characteristic comb spectrum in the spectral domain. The pulse train is composed of a periodically repeated envelope of a single pulse and a carrier wave with frequency ω_{c}. The comb line spacing in the frequency domain is inversely proportional to the time between the pulses $T_{\mathrm{rep}} = \frac{2\pi}{\omega_{\mathrm{rep}}}$ and given by the repetition rate of the laser ω_{rep}. The spectrum has a bandwidth which is inversely proportional to the pulse duration of a single pulse τ_{p} and is centered at the carrier wave frequency ω_{c}. The width of each comb mode is Fourier limited and scales with $\sim \frac{\omega_{\mathrm{rep}}}{N}$, with N denoting the number of pulses.

It can be calculated by composing the separate Fourier transforms of the periodic envelope function $p(t) = \sum_n f_{\mathrm{p}}(t - nT_{\mathrm{rep}})$ and the carrier wave $c(t) = \mathrm{e}^{i\omega_{\mathrm{c}}t}$ according to the convolution theorem (e.g. [72]):

$$\tilde{E}(\omega) = \mathbf{FT}[E(t)] = \mathbf{FT}[p(t) \cdot h(t)] = \tilde{p}(\omega) * \tilde{c}(\omega) \tag{3.23}$$

With $\tilde{p}(\omega)$ and $\tilde{c}(\omega)$ denoting the Fourier transforms of $p(t)$ and $c(t)$. The periodic envelope function $p(t)$ itself can be seen as a convolution of the single pulse envelope $f_{\mathrm{p}}(t)$ and a periodic series of Dirac delta distributions spaced at intervals of T_{rep}, $d(t) = \sum_n \delta(t - nT_{\mathrm{rep}})$. In the limit of an infinite number of pulses the periodic envelope function can hence be written as:

$$p(t) = f_{\mathrm{p}}(t) * \sum_{n=-\infty}^{\infty} \delta(t - nT_{\mathrm{rep}}) \tag{3.24}$$

The Fourier transform of the periodic envelope function $\tilde{p}(\omega)$ is, according to the convolution theorem, given by the product of the Fourier transforms of the single

functions, corrected by a normalization factor:

$$\tilde{p}(\omega) = \mathbf{FT}[p(t)] = \mathbf{FT}[f_{\mathrm{p}}(t) * d(t)] = 2\pi \cdot \tilde{f}_p(\omega) \cdot \tilde{d}(\omega) \tag{3.25}$$

With $\tilde{f}_{\mathrm{p}}(\omega)$ and $\tilde{d}(\omega)$ denoting the Fourier transforms of $f_{\mathrm{p}}(t)$ and $d(t)$. With the well known Fourier transform of a periodic series of Dirac delta distributions[7] [73] spaced at intervals of $T_{\mathrm{rep}} = \frac{2\pi}{\omega_{\mathrm{rep}}}$,

$$\tilde{d\omega} = \mathbf{FT}[\sum_{n=-\infty}^{\infty} \delta(t - nT_{\mathrm{rep}})] = \frac{1}{2\pi} \cdot \omega_{\mathrm{rep}} \sum_{k=-\infty}^{\infty} \delta(\omega - k\omega_{\mathrm{rep}}) \,, \tag{3.26}$$

the Fourier transform of the periodic envelope function becomes:

$$\tilde{p}(\omega) = \omega_{\mathrm{rep}} \cdot \tilde{f}_{\mathrm{p}}(\omega) \sum_{k=-\infty}^{\infty} \delta(\omega - k\omega_{\mathrm{rep}}) = \omega_{\mathrm{rep}} \sum_{k=-\infty}^{\infty} \tilde{f}_{\mathrm{p}}(k\omega_{\mathrm{rep}}) \cdot \delta(\omega - k\omega_{\mathrm{rep}}) \tag{3.27}$$

It consists of sharp comb lines spaced by ω_{rep} where the electric field of the j-th comb tooth is given by $E_j = \omega_{\mathrm{rep}} \tilde{f}_{\mathrm{p}}(j\omega_{\mathrm{rep}})$. Together with the Fourier transform of the carrier wave,

$$\tilde{c}(\omega) = \mathbf{FT}[c(t)] = \mathbf{FT}[e^{i\omega_{\mathrm{c}} t}] = \delta(\omega + \omega_{\mathrm{c}}), \tag{3.28}$$

the spectrum of the pulse train in Equation 3.21 in the limit of an infinite number of pulses is:

$$\begin{aligned} \tilde{E}^0(\omega) = \lim_{N\to\infty} \tilde{E}(\omega) = \tilde{p}(\omega) * \tilde{c}(\omega) &= \omega_{\mathrm{rep}} \cdot \tilde{f}_{\mathrm{p}}(\omega + \omega_{\mathrm{c}}) \sum_{k=-\infty}^{\infty} \delta(\omega + \omega_{\mathrm{c}} - k\omega_{\mathrm{rep}}) \\ &= \omega_{\mathrm{rep}} \cdot \sum_{k=-\infty}^{\infty} \tilde{f}_{\mathrm{p}}(k\omega_{\mathrm{rep}}) \delta(\omega + \omega_{\mathrm{c}} - k\omega_{\mathrm{rep}}) \end{aligned} \tag{3.29}$$

This equation describes an ideal frequency comb, whose envelope function, given by $\tilde{f}_{\mathrm{p}}(\omega)$, is centered at the carrier frequency ω_{c}. The Dirac Delta distribution is only non-zero if $\omega = k\omega_{\mathrm{rep}} - \omega_{\mathrm{c}}$. Introducing the new variables

$$\omega_k \equiv k\omega_{\mathrm{rep}} - \omega_{\mathrm{c}} \tag{3.30}$$

and

$$E_k \equiv \omega_{\mathrm{rep}} \cdot \tilde{f}_{\mathrm{p}}(\omega_k + \omega_{\mathrm{c}}) = \omega_{\mathrm{rep}} \cdot \tilde{f}_{\mathrm{p}}(k\omega_{\mathrm{rep}}) \tag{3.31}$$

[7] The Fourier transform of a periodic infinite series of Dirac delta distributions is again a periodic series of Dirac delta distributions with inversed periodicity. The scaling factor arises from the Fourier coefficient in the Fourier series representation.

Equation 3.29 can be written as:

$$\tilde{E}^0(\omega) = \sum_{k=-\infty}^{\infty} E_k \, \delta(\omega - \omega_k) \tag{3.32}$$

The inverse Fourier transformation of Equation 3.29 gives the electric field of an infinite pulse train:

$$E^0(t) = \mathbf{F}\mathbf{T}^{-1}[\tilde{E}(\omega)] = \sum_{k=-\infty}^{\infty} \omega_{\mathrm{rep}} \cdot \tilde{f}_{\mathrm{p}}(k\omega_{\mathrm{rep}}) e^{-ik\omega_{\mathrm{rep}}t} e^{i\omega_{\mathrm{c}}t} \tag{3.33}$$

Where Equation 3.33 is simply an infinite pulse train written as a Fourier series. Using the variables ω_k and E_k it becomes:

$$E^0(t) = \sum_{k=-\infty}^{\infty} E_k e^{-i\omega_k t} \tag{3.34}$$

These expressions for an infinite pulse train can be used to describe the implementation of Raman transitions.

3.2.2 Single-beam spin control

Carrier Raman transitions, as described in section 3.1, can be implemented with a single train of pulses. The physical requirement is that the spectrum of the corresponding frequency comb contains teeth which are separated by the ground-state qubit splitting, which for a carrier transition is given by the spin qubit frequency ω_0. As the spacing of the comb teeth is given by the repetition rate of the laser, the carrier resonance condition is given by [45]:

$$\omega_0 = q \cdot \omega_{\mathrm{rep}}, \quad q \in \mathbb{Z} \tag{3.35}$$

Rabi oscillations with a single pulsed laser beam can hence occur if the spin qubit splitting ω_0 is an integer multiple of the repetition rate of the laser ω_{rep}, as illustrated in Figure 3.4. A photon can be absorbed by one comb tooth and emitted into another one in order to drive transitions. Due to the regularity of the comb line spacing several pairs of comb teeth exist, which all contribute to the Raman process.

The Hamiltonian describing the interaction of the ion with the pulse train is given by:

$$H_{\mathrm{int}}(t) = -\mathbf{d} \cdot \mathbf{E}(t) = -\mathbf{d} \cdot \sum_{k=-\infty}^{\infty} E_k \, \hat{\epsilon}_{\mathrm{L}} \, \mathrm{Re}[e^{-i\omega_k t}] \, , \tag{3.36}$$

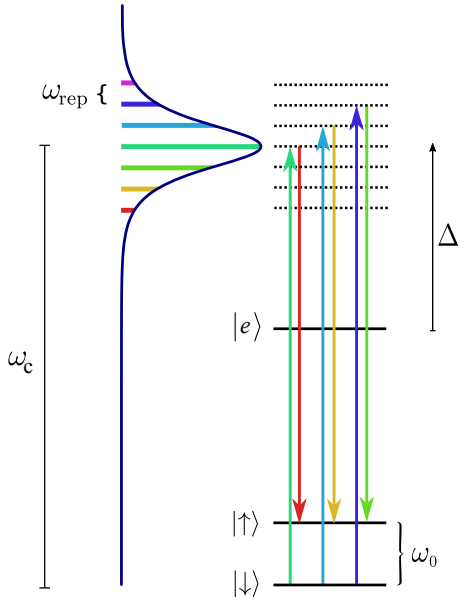

Figure 3.4: Schematical view of the two-photon stimulated Raman process driven by a single beam of an optical frequency comb. Carrier Raman transitions are performed by stimulated absorption from one comb tooth and stimulated emission into another comb tooth, if the spin qubit splitting ω_0 is an integer multiple of the repetition rate ω_{rep} of the laser. The qubit ground-state coupling between $|\downarrow\rangle$ and $|\uparrow\rangle$ is achieved via several virtual excited states being detuned from the real excited state $|e\rangle$.

where Equation 3.34 has been inserted for the electric field of the pulse train. Assuming the optical fields of the pulse train to be detuned far enough from resonance, the time-averaged dynamics can be described by an effective Hamiltonian directly coupling the qubit states [74]. Following the notation from section 3.1 and neglecting the Stark shift, the Hamiltonian terms relevant for carrier transitions for a single pair of comb teeth in the approximation of large detunings is given by [75]:

$$H_{\mathrm{int}}(t) \simeq \frac{\hbar\Omega_m\Omega_n}{\Delta}\sigma^+ e^{i(|\omega_m-\omega_n|-\omega_0)t} + h.c. \tag{3.37}$$

Here the indices m and n denote the comb teeth, from which one couples to the qubit state $|\downarrow\rangle$ and the other to the qubit state $|\uparrow\rangle$. Each comb mode has a frequency given by Equation 3.30 and the single-photon Rabi frequency Ω_m and Ω_n according to Equation 3.3 with an electric field approximated by Equation 3.31. A solution for the performance of carrier transitions can be obtained by considering only the resonant, stationary terms for which the time-dependence in the exponential functions vanish. The requirement for this is $|\omega_m - \omega_n| - \omega_0 = 0$. Inserting the frequencies of the m-th and n-th comb mode, $\omega_m = m\omega_{\mathrm{rep}} - \omega_{\mathrm{c}}$ and $\omega_n = n\omega_{\mathrm{rep}} - \omega_{\mathrm{c}}$, leads to the resonance condition of $|m - n| = \frac{\omega_0}{\omega_{\mathrm{rep}}}$, which is the mathematical description of the physical requirement that the qubit splitting must

be an integer multiple of the repetition rate. The effective Hamiltonian of the entire frequency comb is given by the sum over all comb tooth pairs fulfilling this requirement. The comb can therefore be thought of as an ensemble of CW lasers. In the approximation of large detunings the Rabi frequency is given by [45]:

$$\Omega = \sum_i \frac{\sum_k E_k E_{k-q}}{4\hbar^2} \frac{\langle \uparrow | \mathbf{d} \cdot \hat{\epsilon}_\mathrm{L} | e_i \rangle \langle e_i | \mathbf{d} \cdot \hat{\epsilon}_\mathrm{L} | \downarrow \rangle}{\Delta_{i,k}} \text{ , with } q = \frac{\omega_0}{\omega_\mathrm{rep}} \in \mathbb{Z} \tag{3.38}$$

This Equation can be derived from the formula 3.8 for the two-photon Rabi frequency implemented with two CW beams, by replacing the product of electric field amplitudes by the sum over all comb tooth pairs fulfilling the resonance condition 3.35. In contrast to the CW approach, where one beam drives the ion into the excited state and the other beam drives it back to the other qubit ground state, a single comb tooth cannot be dedicated to either the absorption part or the emission part of the Raman process. Due to the regularity of comb line spacing each comb tooth can participate in both processes, if the resonance condition is fulfilled. The optical frequency comb therefore uses its power twice as efficiently [75].

If the sum over k in Equation 3.38 is replaced by an integral, an analytic expression for the Rabi frequency can be obtained. The Rabi frequency can then be expressed as a product of the time-averaged resonant Rabi frequency of the pulse train Ω_0 times a function $\zeta[f_\mathrm{p}(\omega_0, \Delta\omega_\mathrm{FWHM})]$ depending on the pulse shape of the envelope and the qubit splitting [45]:

$$\Omega \approx \Omega_0 \cdot \zeta[f_\mathrm{p}(\omega_0, \Delta\omega_\mathrm{FWHM})] \tag{3.39}$$

The function ζ is shown in Table 3.1 for different functional forms of the pulse envelope and plotted in Figure 3.5 as a function of the spectral bandwidth. If the spectral bandwidth of the frequency comb is large compared to the qubit splitting, the function ζ converges towards unity for any pulse shape. In this case the Rabi frequency Ω is approximately given by Ω_0. If the spectral bandwidth of the comb is reduced, the net transition rate is supressed, according to the drop of ζ shown in Figure 3.5. This results from the fact that fewer pairs of comb teeth exist that contribute to the Raman process. A general requirement for efficient Rabi oscillations performed by an optical frequency comb is hence given by $\Delta\omega_\mathrm{FWHM} \gg \omega_0$.
The time-averaged resonant "two-photon" Rabi frequency of the pulse train Ω_0 can be expressed in terms of the saturation parameter $s = \bar{I}/I_\mathrm{sat}$ with the average intensity[8] [45]

$$\bar{I} = f_\mathrm{rep} \frac{c\epsilon_0}{2} \int_{-\infty}^{\infty} dt |f(t)|^2 = 2\pi f_\mathrm{rep} \frac{c\epsilon_0}{2} \int_{-\infty}^{\infty} d\omega |\tilde{f}(\omega)|^2 \tag{3.40}$$

[8]The additional factor of 2π in the expression with the integral over $d\omega$ comes from the inverse non-unitary Fourier transformation definition.

pulse form	$\mathbf{f_p(t)}$	$\zeta[f_p(\omega_0)]$
sech	$f_{\text{sech}}(t) = \sqrt{\frac{\pi}{2}}\, E_0\, \text{sech}\left[\frac{\Delta\nu_{\text{FWHM}}\cdot t}{0.1787}\right]$	$\zeta_{\text{sech}}(\omega_0) = \frac{0.179\,\pi\,\omega_0\,\text{Csch}\left[\frac{0.179\,\pi\,\omega_0}{2\,\Delta\nu_{\text{FWHM}}}\right]}{2\,\Delta\nu_{\text{FWHM}}}$
gauss	$f_{\text{gauss}}(t) = \left(\frac{\pi}{2}\right)^{-\frac{1}{4}} E_0\; e^{-\left(\frac{\Delta\nu_{\text{FWHM}}\cdot t}{0.375}\right)^2}$	$\zeta_{\text{gauss}}(\omega_0) = e^{-\left(\frac{0.375\,\omega_0}{2.828\,\Delta\nu_{\text{FWHM}}}\right)^2}$
sinc	$f_{\text{sinc}}(t) = E_0\,\Theta\left[\frac{\Delta\nu_{\text{FWHM}}\cdot t}{0.886}\right]$	$\zeta_{\text{sinc}}(\omega_0) = \frac{2\,\Delta\nu_{\text{FWHM}}\;\text{Sin}\left[\frac{0.886\,\omega_0}{2\,\Delta\nu_{\text{FWHM}}}\right]}{0.886\;\omega_0}$

Table 3.1: Table showing the function ζ for different functional forms of the pulse envelope $f_{\text{p}}(t)$. The functions ζ and the corresponding spectral envelope functions $\tilde{f}(\omega)^2$ are shown in Figure 3.5.

scaled to the saturation intensity I_{sat} of a closed-cycle transition, as given by Equation 3.11. Ω_0 can therefore be calculated in terms of the dipole matrix element of the closed-cycle transition μ_{ct}, given by Equation 3.9, according to [45]:

$$\Omega_0(\bar{I}) = \frac{\gamma^2 \bar{I}}{8\Delta I_{\text{sat}}} = \frac{\frac{2\bar{I}}{c\epsilon_0}}{4\hbar^2}\frac{\mu_{\text{ct}}^2}{\Delta} \tag{3.41}$$

The relation between the time-averaged resonant "two-photon" Rabi frequency of the frequency comb Ω_0 and the CW single-photon Rabi frequency of a closed-cycle transition g_{ct}, as introduced in section 3.1.2, is given by:

$$\frac{g_{\text{ct}}(I=\bar{I})\cdot g_{\text{ct}}(I=\bar{I})}{\Delta} = \Omega_0(\bar{I}) \tag{3.42}$$

Due to the fact that each comb mode contributes to the emission and to the absorption part of the Raman process, the associated CW single-photon Rabi frequencies g_{ct} in Equation 3.42 both are scaled to the full available averaged intensity $\bar{I}$ of the pulse train.

3.2.3 Multiple-beam qubit control

The realization of motional sideband transitions requires the existence of pairs of comb teeth, which are separated by the qubit splitting given by $\omega_{\text{qubit}} = \omega_0 \pm \omega_{\text{z}}$. As the Raman frequency for sideband transitions is proportional to $\eta = \Delta k \cdot z_0$, as discussed in section 3.1.1, it is further required that the comb teeth must originate from separated beams directed onto the ion from different directions. The absorption of a photon from one beam tooth and emission into a tooth from the second beam causes a momentum change of $\hbar\Delta k$ along the direction of the wavevector difference Δk, which allows coupling to the ion's motion. The resonance

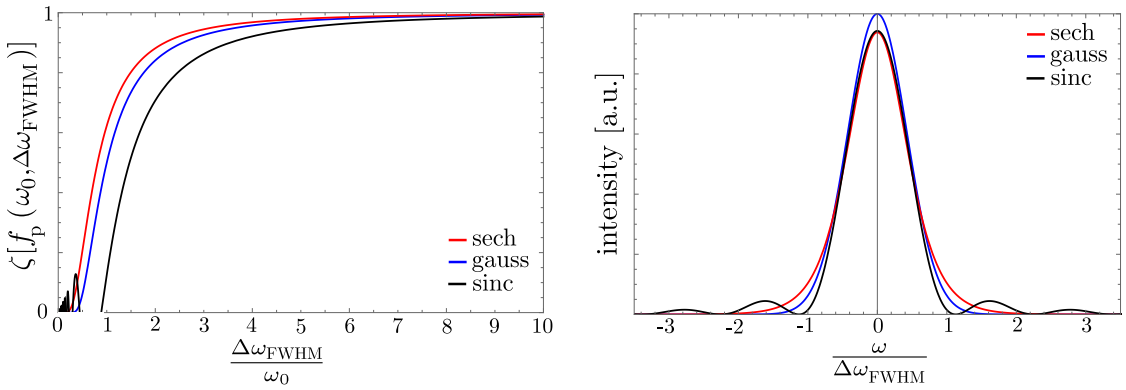

Figure 3.5: Comparison of the function $\zeta[f_p(\omega_0, \Delta\omega_{FWHM})]$ for different functional forms of the pulse envelope, plotted as a function of the ratio between the spectral bandwidth in full width half maximum (FWHM) definition $\Delta\omega_{FWHM}$ and the internal state qubit splitting ω_0. In the left graph, ζ is shown, in red of a sech-shaped, in blue of a gaussian and in black of a sinc-shaped spectrum. All functions are scaled to the same average intensity, as shown on the right. The envelope functions are shown in Table 3.1. For broad spectra with spectral bandwidths being several multiples of the qubit splitting, the function converges towards unity for any pulse shape.

condition is fulfilled by shifting the frequencies of both beams relative to each other, such that teeth from the one beam paired with teeth of the other beam are resonant with the qubit splitting, as illustrated in Figure 3.6. This ensures the participation of both beams. The resonance condition for sideband transitions is given by [45]:

$$j \cdot \omega_{rep} \pm \Delta\omega = \omega_0 \pm \omega_z, \;\; j \in \mathbb{Z} \tag{3.43}$$

With j being an integer, ω_0 the separation of the internal qubit states, ω_z the trap frequency and $\Delta\omega$ the frequency shift between both beams. The optimum frequency shift for performing sideband transitions is on the order of one-third of the laser's repetition rate or multiples of it, $\Delta\omega_{opt} \approx (l+1/3)\,\omega_{rep}, l \in \mathbb{Z}$, and not as in the case of using CW lasers given by the entire qubit splitting. This is a major advantage of this approach, especially relevant for the (anti-)proton g-factor measurement experiment possessing the large qubit splitting on the order of 140 GHz. In order to avoid having the single beams accidently driving carrier transitions, $\Delta\omega$ should not be a harmonic of an integer or half integer of the laser repetition rate ω_{rep} [46]. In the former case, each comb itself directly fulfills the carrier resonance condition of a single beam, given by Equation 3.35, whereas in the latter case both combs fulfill the second harmonic of the carrier resonance condition, which in both cases supresses the sideband signal. In order to ensure coupling only to the sideband transition over a wide range of frequencies, a large repetition rate is beneficial. A detailed discussion on the general limit criterion for resolving motional sidebands

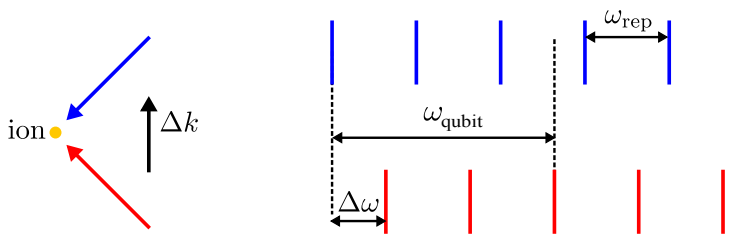

Figure 3.6: Demonstration of the Raman resonance condition fulfilled by comb tooth pairs originating from two separate beams of the pulsed laser, indicated by the blue and red beam. The right picture shows the equally spaced comb teeth of each beam's spectrum in relation to the qubit splitting ω_{qubit}. In order to bridge the qubit splitting the relative frequency shift $\Delta\omega$ must be introduced between the beams, such that a tooth of one beam in combination with a tooth from the second beam are separated by ω_{qubit}. For carrier transitions the qubit splitting is given by $\omega_{\text{qubit}} = \omega_0$. Sideband transitions with motional coupling along the direction of Δk can be performed if $\omega_{\text{qubit}} = \omega_0 \pm \omega_z$.

is performed in [75]. The sideband transition amplitude is found to dominate the carrier transition amplitude if:

$$N = t_{\text{probe}} \cdot f_{\text{rep}} \gg \frac{f_{\text{rep}}}{\eta\omega_z} \tag{3.44}$$

With η being the Lamb-Dicke parameter and N the number of pulses of the pulse train, determined by the product of the experimental probe duration t_{probe} and the repetition rate of the laser. The limitation can therefore be interpreted as a limit criterion concerning the linewidth of a single comb mode. In case of short probe durations, corresponding to a small number of involved pulses, the linewidth of each comb mode is broadened and motional sidebands cannot be resolved in the limit of Equation 3.44.

Whereas the use of two beams is mandatory for the implementation of sideband transitions, carrier transitions can be performed by either using a single beam or by using two beams of the pulsed laser train. Within the two-beam configuration, the frequency shift $\Delta\omega$ between the lasers beams must be set, such that pairs of teeth exist which are separated by the qubit frequency $\omega_{\text{qubit}} = \omega_0$. The general resonance condition for performing two-photon stimulated Raman transitions with two pulsed laser beams is given by:

$$j \cdot \omega_{\text{rep}} \pm \Delta\omega = \omega_{\text{qubit}}, \;\; j \in \mathbb{Z} \tag{3.45}$$

Figure 3.7 schematically demonstrates the Raman process implemented by two beams of a pulsed laser. Each comb represents the spectrum from one beam. Raman transitions are performed by pairs of comb teeth, whereby teeth from one comb are

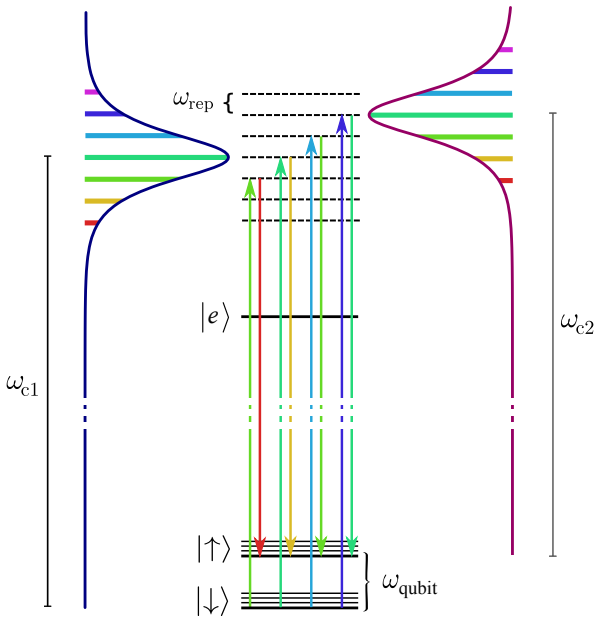

Figure 3.7: Schematical view of the two-photon stimulated Raman process driven by two beams of a pulsed laser. On the left the comb spectrum of beam 1 is shown, with carrier frequency ω_{c_1} and on the right the comb of beam 2 with carrier frequency ω_{c_2}. Raman transitions are performed by pairs of comb teeth originating from the different beams, if the resonance condition from Equation 3.43 is fulfilled. Assuming the ion to be initialized in $|\downarrow\rangle$, in this picture teeth from the first beam's spectrum are always responsible for the absorption part and teeth from the second beam are always responsible for the emission part of the Raman process. The Raman coupling is given by the sum over all contributing pairs of comb teeth, which can be found along the virtual excited states indicated by the dashes lines, detuned from the real excited state $|e\rangle$. Note that the frequency shift between the beams is on the order of $\frac{\omega_{\mathrm{rep}}}{3}$ and not of the qubit splitting ω_{qubit}, which is difficult to see due to the representation of shared virtual states.

always responsible for the absorption part and the teeth from the second comb for the emission part of the process. Due to the regularity of the comb line spacing the resulting Rabi frequency is then again given by the sum over all pairs of teeth, fulfilling the resonance condition 3.45.

The carrier Rabi frequency implemented by two beams can be derived analogous to the case of a single beam. The Hamiltonian describing the interaction of the ion with the two beams of the pulse train is given by:

$$H_{\mathrm{int}}(t) = -\mathbf{d}\cdot[\mathbf{E}_1(t)+\mathbf{E}_2(t)] = -\mathbf{d}\cdot\mathrm{Re}\left[\sum_{k_1=-\infty}^{\infty} E_{k_1}\,\hat{\epsilon}_{\mathrm{L}_1}\,e^{-i\omega_{k_1}t} + \sum_{k_2=-\infty}^{\infty} E_{k_2}\,\hat{\epsilon}_{\mathrm{L}_2}\,e^{-i\omega_{k_2}t}\right] \tag{3.46}$$

Neglecting Stark shifts and assuming large detunings, the effective Hamiltonian terms relevant for carrier transitions for a single pair of comb teeth originating from different beams is given by:

$$H_{\text{int}}(t) \simeq \frac{\hbar\Omega_{1_m}\Omega_{2_n}}{\Delta}\sigma^{+}e^{-i(|\omega_{1m}-\omega_{2n}|-\omega_{\text{qubit}})t} + h.c. \tag{3.47}$$

Here the index m denotes the m-th comb tooth from laser beam 1 and n denotes the n-th comb tooth from laser beam 2. As discussed for the single-beam approach, an approximate solution for the performance of carrier transitions can be obtained by picking out the stationary resonant terms, which requires $|\omega_{1_m} - \omega_{2_n}| - \omega_{\text{qubit}} = 0$, with the frequencies of each beam given by Equation 3.30. In contrast to the single-beam approach both comb tooth frequencies are now referenced to different carrier frequencies due to the applied frequency shift $\Delta\omega$. Inserting the frequencies $\omega_{1_m} = m\omega_{\text{rep}} - \omega_{\text{c}_1}$ and $\omega_{2_n} = n\omega_{\text{rep}} - \omega_{\text{c}_2} = n\omega_{\text{rep}} - \omega_{\text{c}_1} \pm \Delta\omega$ leads to:

$$|m-n| = \frac{\omega_{\text{qubit}} \pm \Delta\omega}{\omega_{\text{rep}}} \tag{3.48}$$

Introducing the parameters

$$q' \equiv \frac{\omega_{\text{qubit}} + \Delta\omega}{\omega_{rep}} \text{ and } q'' \equiv \frac{\omega_{\text{qubit}} - \Delta\omega}{\omega_{rep}}, \tag{3.49}$$

it can be seen that the resonance condition can either be fulfilled by requiring q' or q'' to be an integer. This differentiation corresponds to the fact, that due to the applied frequency shift between the beams, a clear designation is introduced identifying which beam is responsible for the absorption part and which beam for the emission part of the Raman process.
Because the transition is driven by both pulse trains it is further required that the individual pulses must arrive simultaneously at the ion. A derivation of this condition can be obtained by introducing a temporal delay in the expression of the electrical field of a pulse train. The calculations show that when the delay between both beams is zero also either q' or q'' is an integer, implying that the two pulses must arrive the ion simultaneously for efficient Rabi oscillations [75]. Further assuming that the pulse trains are not chirped and all contributions add up in phase, the beat note between the two frequency combs will resonantly drive Raman transitions and the Rabi frequency, for example in the case of q' being an integer, is given by:

$$\Omega = \sum_i \frac{\sum_k E_{k_1} E_{k_2-q'}}{4\hbar^2} \frac{\langle \uparrow | \mathbf{d}\cdot\hat{\epsilon}_{\text{L}_1}|e_i\rangle\langle e_i|\mathbf{d}\cdot\hat{\epsilon}_{\text{L}_2}|\downarrow\rangle}{\Delta_{i,k}}, \text{with } q' = \frac{\omega_{\text{qubit}} + \Delta\omega}{\omega_{\text{rep}}} \in \mathbb{Z} \tag{3.50}$$

The Rabi frequency in case of two offset combs performing the Raman process can hence be expressed similar to the case of a single beam, with the difference

that each tooth from contributing comb mode pairs can be dedicated to either the absorption or the emission part of the Raman process. The beam from which a comb tooth originates is therefore labeled with the index 1 for emission and 2 for absorption. By this also the electric field amplitude of each comb mode in Equation 3.50 is referenced to the power contained in the specific beam. This in consequence means that if the power contained within a single pulse train is divided into two beams, the achievable Raman coupling strength implemented by the two-beam approach is reduced by a factor of two compared to the coupling strength achievable with the single-beam approach. This relation can be pointed out in the limit of $\Delta\omega_{\mathrm{FWHM}} \gg \omega_0$. The Rabi frequency from Equation 3.50 in this case can also be approximated by a "two-photon" time-averaged resonant Rabi frequency of the pulse train Ω_0. Further a "single-photon" time-averaged resonant Rabi frequency g_0 can be introduced, which can be set in relation to the saturation intensity of a closed-cycle transition I_{sat} and the closed-cycle matrix element μ_{ct} according to [46]:

$$g_0(\bar{I}) = \sqrt{\frac{\gamma^2 \bar{I}}{8 I_{\mathrm{sat}}}} = \frac{\sqrt{\frac{2\bar{I}}{c\epsilon_0}}}{2\hbar}\mu_{\mathrm{ct}} \tag{3.51}$$

The relation to the single-photon CW Rabi frequency of the closed-cycle transition g_{ct} is given by:

$$g_0(\bar{I}) = g_{\mathrm{ct}}(I = \bar{I}) \tag{3.52}$$

The resulting time-averaged "two-photon" resonant Rabi frequency Ω_0 of the Raman process implemented by two beams can be expressed as:

$$\Omega_0 = \frac{g_0(\bar{I}_1) \cdot g_0(\bar{I}_2)}{\Delta} \tag{3.53}$$

In contrast to the "two-photon" time-averaged resonant Rabi frequency for the single-beam approach in Equation 3.42, the associated single-photon Rabi frequencies now are scaled to the averaged intensities of the particular beams, denoted as $\bar{I}_1$ and $\bar{I}_2$. In case of dividing the available average intensity of a pulse train $\bar{I}$ into two beams, each beam only has an intensity of $\frac{\bar{I}}{2}$. Whereas for the single-beam approach each associated single-photon Rabi frequency is scaled to the entire average intensity of the pulse train $\bar{I}$, due to the fact that each comb mode can participate to the absorption and to the emission part of the process. The coupling strength is therefore reduced by a factor of two within the two-beam approach. This is in full analogy with the implementation of Raman transitions with two CW beams. Here also the power contained in one beam is available for the absorption part and the power contained in other beam is available for the emission part of the Raman process.

The Rabi frequencies for motional sideband transitions can be obtained based on the Equations derived in section 3.1.1. The sideband Rabi frequencies depend on

the motional state of the ion n and are naturally weaker than the carrier (c) Rabi frequency by a factor given by the Lamb Dicke parameter η. The Rabi frequency for the red sideband (rsb) and blue sideband (bsb) are given by:

$$\Omega_{\mathrm{rsb}} = \eta\Omega_{\mathrm{c}}\sqrt{n} \tag{3.54}$$

$$\Omega_{\mathrm{bsb}} = \eta\Omega_{\mathrm{c}}\sqrt{n+1} \tag{3.55}$$

with the Lamb-Dicke parameter

$$\eta = \Delta k\sqrt{\frac{\hbar}{2m_{\mathrm{ion}}\omega_{\mathrm{z}}}}, \tag{3.56}$$

where m_{ion} denotes the mass of the ion. A direct derivation of the effective Hamiltonian and the sideband Rabi frequencies for the pulsed laser approach can be found in [75].

The calculation of the scattering rates $\Gamma_{\mathrm{Raman}_{\mathrm{ofc}_j}}$, $\Gamma_{\mathrm{el}_{\mathrm{ofc}_j}}$ and the Stark shift $\delta(g)_{\mathrm{ofc}_j}$ induced by the j-th optical pulse train can be derived from the CW equations (Equation 3.15, Equation 3.16, Equation 3.19) by replacing the product of electric field amplitudes by the sum over comb tooth pairs, $E_{0_j}^2 \rightarrow \sum_k E_k^2$. Alternatively the expressions can be approximated by replacing the CW Rabi frequency of the cycling transition by the time-averaged resonant single-photon Rabi frequency, $g_{\mathrm{ct}}(I_j) \rightarrow g_0(\bar{I}_j)$, leading to:

$$\Gamma_{\mathrm{Raman}_{\mathrm{ofc}_j}}(m_s) = \gamma g_0^2(\bar{I}_j)\sum_q \left|\sum_i \frac{\langle g_{\mathrm{final}}|\mathbf{d}\cdot\hat{\epsilon}_q|e_i\rangle\cdot\langle e_i|\mathbf{d}\cdot\hat{\epsilon}_{\mathrm{L}_j}|m_S\rangle}{\mu_{\mathrm{ct}}^2\cdot(\Delta_i - \mathbf{i}\frac{\gamma}{2})}\right|^2, \text{for } g_{\mathrm{final}} \neq m_S \tag{3.57}$$

$$\Gamma_{\mathrm{el}_{\mathrm{ofc}_j}} = \gamma\, g_0^2(\bar{I}_j)\sum_q \left|\sum_i \frac{\langle\downarrow|\mathbf{d}\cdot\hat{\epsilon}_q|e_i\rangle\cdot\langle e_i|\mathbf{d}\cdot\hat{\epsilon}_{\mathrm{L}_j}|\downarrow\rangle}{\mu_{\mathrm{ct}^2}\cdot(\Delta_i - \mathbf{i}\frac{\gamma}{2})} - \sum_{i'}\frac{\langle\uparrow|\mathbf{d}\cdot\hat{\epsilon}_q|e_{i'}\rangle\cdot\langle e_{i'}|\mathbf{d}\cdot\hat{\epsilon}_{\mathrm{L}_j}|\uparrow\rangle}{\mu_{\mathrm{ct}^2}\cdot(\Delta_{i'} - \mathbf{i}\frac{\gamma}{2})}\right|^2 \tag{3.58}$$

$$\delta(g)_{\mathrm{ofc}_j} = g_0^2(\bar{I}_j)\sum_i \frac{|\langle g|\mathbf{d}\cdot\hat{\epsilon}_{\mathrm{L}_j}|e_i\rangle|^2}{\mu_{\mathrm{ct}}^2\cdot\Delta_i} \tag{3.59}$$

The average intensity $\bar{I}_j$ denotes the average intensity available in the j-th pulse train of the Raman process. Within this expression the Rabi frequency is given by:

$$\Omega_{\mathrm{ofc}} = g_0(\bar{I}_1)g_0(\bar{I}_2)\sum_i \frac{\langle\uparrow|\mathbf{d}\cdot\hat{\epsilon}_{\mathrm{L}_1}|e_i\rangle\langle e_i|\mathbf{d}\cdot\hat{\epsilon}_{\mathrm{L}_2}|\downarrow\rangle}{\mu_{\mathrm{ct}}^2\cdot\Delta_i}\cdot\zeta[f_{\mathrm{p}}(\omega_0,\Delta\omega_{\mathrm{FWHM}})] \tag{3.60}$$

The function $\zeta[f_{\mathrm{p}}]$ implements the drop of Raman coupling strength in case the spectral bandwidth $\Delta\omega_{\mathrm{FWHM}}$ does not significantly exceed the qubit splitting ω_0, as discussed in section 3.2.2.

3.3 Beryllium ion qubit control using an optical frequency comb

In this section specific requirements for qubit control of beryllium ions using a pulsed Raman system will be discussed. A specific challenge arises from the atomic level structure of beryllium, which requires a careful control of the spectral comb properties in order to optimize the ratio between the Raman coupling strength and the total scattering rate. Once the requirements for the (anti-)proton g-factor measurement experiment are met, the pulsed Raman system presents a flexible tool allowing for qubit control of $^9Be^+$ ions at any less stringent conditions given at lower magnetic fields. The level structure of $^9Be^+$ and its hyperfine qubits at different experimental conditions will be introduced and corresponding numerical simulations of the relevant atomic processes occurring in the $^9Be^+$ ion as well as resulting requirements discussed.

3.3.1 Beryllium qubit

Quantum logic inspired trapped-ion experiments require ions which exhibit a pair of long-lived energy levels which can be identified as qubit levels. Furthermore simple techniques for cooling the ion and for initializing, detecting and coupling the qubit levels should be available, restricting the list of appropriate ions to ones which are alkali-like, thus having a single unpaired valence electron when being ionized. Beryllium has been chosen for the (anti-)proton g-factor measurement experiment due to its lightest mass along the established qubit ions. It belongs to the alkali earth metals, has the atomic number $Z = 4$ and two valence electrons. Experiments in the group are performed with singly ionized $^9Be^+$ which is the only stable isotope. In the following the electronic level structure and the implementation of qubit levels will be discussed.

Beryllium level structure

The relevant atomic structure of ionized beryllium is shown in Figure 3.8. For a derivation of its atomic description see e.g. [76, 65]. $^9Be^+$ exhibits a singlet ground state in the s-orbital, $^2S_{1/2}$, and two p-levels, $^2P_{1/2}$ and $^2P_{3/2}$, following the spectroscopic notation $^{2S+1}L_J$, where L is given by the subshell letter L=0,1,2,...≡ S,P,D,... . The transition between the ground state and the lower p-level is near $\lambda_{Be} \approx 313\,\text{nm}$, which is, up to the detuning from the excited states Δ which has to be set, the wavelength required for implementing Raman transitions. The fine-structure splitting between the p-levels is $\omega_{fs} = 2\pi \cdot 198\,\text{GHz}$. The fine structure results from the coupling of the spin angular momentum $\mathbf{S}$ and the orbital angular

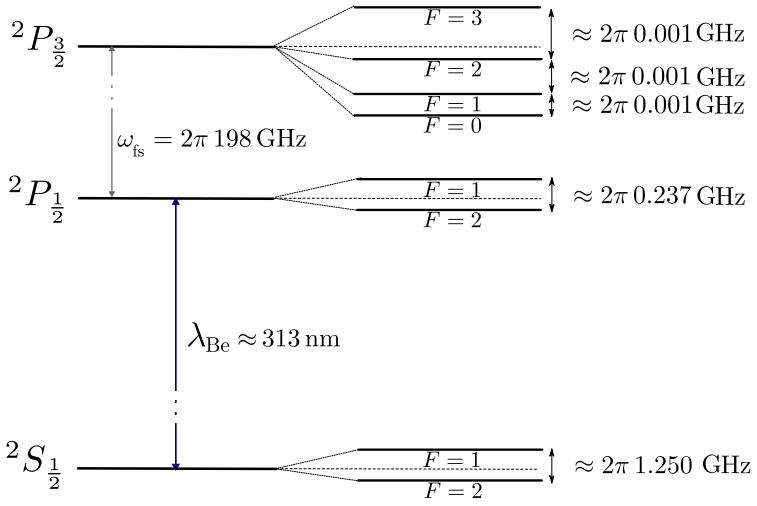

Figure 3.8: Atomic structure of ionized beryllium (not to scale). $^9Be^+$ has a singlet ground state in the s-orbital, $^2S_{1/2}$, and two excited levels in the p-orbital, $^2P_{1/2}$ and $^2P_{3/2}$, with a fine-structure splitting of $\omega_{\mathrm{fs}} = 2\pi \cdot 198\,\mathrm{GHz}$. Each level is split into hyperfine sublevels due to the coupling to the nuclear spin of $I = 3/2$ resulting in corresponding quantum numbers characterized by **F**. The hyperfine ground-state splitting is 1.25 GHz.

momentum **L** to the resulting electron angular momentum **J** by $\mathbf{J} = \mathbf{L} + \mathbf{S}$ leading to the corresponding quantum number J, with $J \in \{|L-S|, ..., L+S\}$. Accordingly with $S = 1/2$ the ground state with $L = 0$ has a single level with $J = 1/2$, whereas the excited state with $L = 1$ exhibits two levels with $J = 1/2$ and $J = 3/2$. These fine-structure levels are further split into hyperfine sublevels due to the coupling of the nuclear angular momentum **I** to the electron angular momentum **J** resulting in the atomic angular momentum **F** by $\mathbf{F} = \mathbf{J} + \mathbf{I}$ leading to the corresponding quantum number F, with $F \in \{|J - I|, ..., J + I\}$. With a nuclear spin of $I = 3/2$ the ground state and the first excited p-level are split into two sublevels with $F = 1$ and $F = 2$, with an energy splitting of 1.25 GHz and 237 MHz, whereas the second excited p-level is split into four sublevels with $F = 0$, $F = 1$, $F = 2$ and $F = 3$ with splittings around 1 MHz [77, 78]. Each of these levels has $2F + 1$ sublevels which are degenerate at zero magnetic field. The degeneracy gets broken when applying a magnetic field, where the description and energy of the levels depend on the strength of the magnetic field.

Hyperfine qubits

Beryllium ion qubit levels are chosen within the electronic $^2S_{1/2}$ ground-state manifold while applying a magnetic field resolving the sublevels. The Hamiltonian describing the interaction of the external magnetic field **B** with the hyperfine

structure is given by

$$H = hA\mathbf{I}\cdot\mathbf{J} - \boldsymbol{\mu}\cdot\mathbf{B}\,, \tag{3.61}$$

with h being the Planck constant, A a hyperfine constant and $\boldsymbol{\mu}$ the magnetic dipole operator. The interaction with the magnetic field is described by $-\boldsymbol{\mu}\cdot\mathbf{B}$ and depends on the strength of the applied magnetic field. In the weak-field regime, known as Zeeman regime, the interaction of $\mathbf{I}\cdot\mathbf{J}$ dominates over the effect of the external magnetic field, and I, J, F, m_F are good quantum numbers, with m_F denoting the projection of F onto the quantization axis. The separation of the energy levels for a magnetic field in z-direction is described by

$$\Delta E_{\mathrm{B}} = \mu_{\mathrm{B}}\, g_F\, m_F\, B_{\mathrm{z}}\,, \tag{3.62}$$

with the Bohr magneton μ_{B} and the Landé g-factor g_F. For the strong-field regime, known as Paschen-Back regime, the interaction with the magnetic field dominates the coupling of $\mathbf{I}\cdot\mathbf{J}$ and J, I, m_J, m_I are good quantum numbers, with m_I and m_J denoting the projection of I and J onto the quantization axis. The separation of the energy levels is given by

$$\Delta E_{\mathrm{B}} = (\mu_{\mathrm{B}}\, g_J\, m_J\, + \mu_{\mathrm{K}}\, g_I\, m_I\,)\, B_{\mathrm{z}}\,, \tag{3.63}$$

with g_I, g_J denoting the Landé g-factors and μ_{K} the nuclear magneton. In the intermediate regime neither $|F, m_F\rangle$ nor $|m_I, m_J\rangle$ are good quantum numbers. The energy levels are obtained by diagonalizing the combined Hamiltonian. An analytical expression is given by the Breit-Rabi formula:

$$\Delta E_{\mathrm{B}} = -\frac{\Delta E_{\mathrm{HFS}}}{2(2I+1)} + m g_I \mu_{\mathrm{B}} B \pm \frac{\Delta E_{\mathrm{HFS}}}{2} \begin{cases} 1 \pm x & m = \pm(I+1/2) \\ \\ \sqrt{1 + \frac{4m}{2I+1}x + x^2} & \text{otherwise} \end{cases} \tag{3.64}$$

where $m = m_I \pm m_J = m_I \pm 1/2$ and x is defined by

$$x = \frac{(g_J - g_I)\mu_{\mathrm{B}}}{\Delta E_{\mathrm{HFS}}} \cdot B \tag{3.65}$$

and ΔE_{HFS} is given by

$$\Delta E_{\mathrm{HFS}} = A \cdot \left(I + \frac{1}{2}\right). \tag{3.66}$$

The $\pm$ in Equation 3.64 preceding the last term refers to $F = I \pm 1/2$.

Figure 3.9 shows the energy levels of the $^2\mathrm{S}_{1/2}$ ground-state manifold of beryllium as a function of an externally applied magnetic field for the low-field and intermediate regime, determined with the Breit-Rabi formula (Equation 3.64),

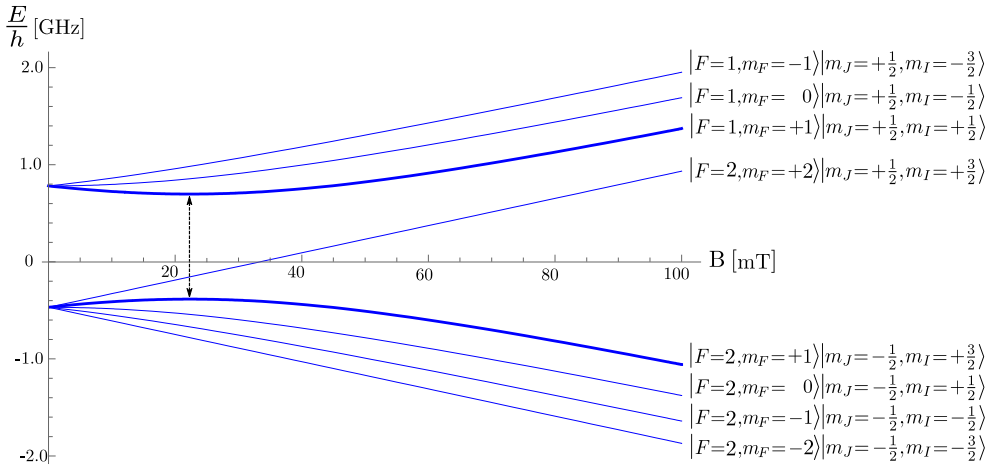

Figure 3.9: Energy levels of the hyperfine ground-state manifold of $^9Be^+$ as a function of an externally applied magnetic field in the low-field and intermediate regime, determined by the Breit-Rabi formula 3.64. Experiments, as described in chapter 5, work at a magnetic field of 22.3 mT where the transition between $|F = 2, m_F = 1\rangle$ and $|F = 1, m_F = 1\rangle$ is first-order field independent.

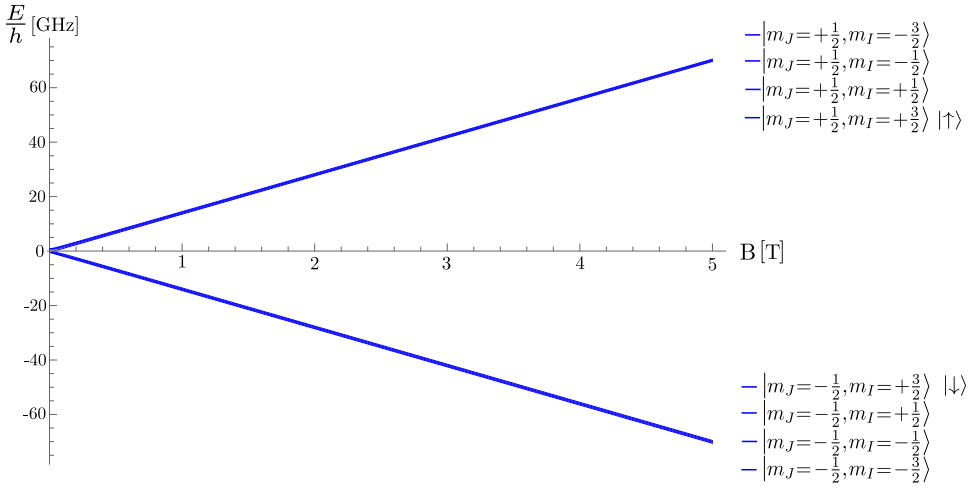

Figure 3.10: Energy levels of the hyperfine ground-state manifold of $^9Be^+$ as a function of an externally applied magnetic field in the high field regime. At a magnetic field of 5 T, as applied within the (anti-)proton g-factor measurement experiment, two energy level bundles exist being characterized by $m_J = +1/2$ and $m_J = -1/2$, with four sublevels each according to $m_I \in (-3/2, -1/2, +1/2, +3/2)$ being separated by ≈ 300 MHz. Experiments will be carried out in the $m_I = +3/2$ subsystem.

where the states are labeled with both, $|F, m_F\rangle$ and $|m_I, m_J\rangle$. In this regime experiments are typically performed at a magnetic field, at which a magnetic field-insensitive transition exists. In this case the slopes of the qubit energy levels, given by the derivative of the Breit-Rabi formula with respect to the magnetic field strength, are identical. Such transitions have the huge advantage of being first-order insensitive to magnetic field fluctuations leading to long lived qubit states. Experiments, as described in chapter 5, were carried out at a magnetic field of 22.3 mT at which the transition between $|F = 2, m_F = 1\rangle$ and $|F = 1, m_F = 1\rangle$ is first-order field independent. Further field-independent transitions exist at B = 11.9446 mT, B = 11.9642 mT and B = 0.0254 mT as discussed in [79, 80].
For a magnetic field of 5 T, as to be applied in the (anti-)proton g-factor measurement experiment, the energy levels are described in the Paschen-Back regime. The energy levels of the $^2S_{1/2}$ ground-state manifold as a function of the magnetic field for the high-field regime are plotted in Figure 3.10. Two energy level bundles exist, being characterized by $m_J = +\frac{1}{2}$ and $m_J = -\frac{1}{2}$, with four sublevels each according to $m_I \in (-3/2, -1/2, +1/2, +3/2)$ being separated by ≈ 300 MHz. Qubit levels and all laser transitions should be chosen within the same m_I subsystem, in order to achieve high coupling efficiencies. A change of m_I is accompanied by a nuclear spin flip, for which the probability is suppressed by several orders of magnitude. Because of the existence of closed-cycle transitions, being typically used for implementing the Doppler cooling and state detection beam, either the $m_I = +\frac{3}{2}$ or $m_I = -\frac{3}{2}$ subsystem are available for choice. For the (anti-)proton g-factor measurement experiment the subsystem $m_I = +\frac{3}{2}$ is chosen, because the excited state of the closed-cycle transition is most separated from neighboring sublevels. The level structure of the subsystem at an externally applied magnetic field of 5 T is shown in Figure 3.11. The qubit states within the ground-state manifold are $|\downarrow\rangle = |m_J = -\frac{1}{2}, m_I = +\frac{3}{2}\rangle$ and $|\uparrow\rangle = |m_J = +\frac{1}{2}, m_I = +\frac{3}{2}\rangle$ with an internal state splitting of $\omega_0 = 2\pi \cdot 139.1850$ GHz. The closed-cycle transition couples the $|\uparrow\rangle = |m_J = +\frac{1}{2}, m_I = +\frac{3}{2}\rangle$ state to the excited $^2P_{3/2}, |m_J = +\frac{3}{2}, m_I = +\frac{3}{2}\rangle$ level.

3.3.2 Calculation of dipole matrix elements

The calculation of Rabi frequencies, scattering rates and Stark shifts for the implementation of the two-photon stimulated Raman process requires the determination of the electric dipole couplings between the qubit ground states and relevant excited states. In this thesis the relevant matrix elements are scaled to the matrix element of the closed-cycle transition between the $^2S_{1/2}, |m_J = +\frac{1}{2}, m_I = +\frac{3}{2}\rangle$ and the $^2P_{3/2}, |m_J = +\frac{3}{2}, m_I = +\frac{3}{2}\rangle$ levels:

$$\mu_{\mathrm{ct}}^2 = |\langle {}^2S_{1/2}, m_J = +\frac{1}{2}, m_I = +\frac{3}{2}|\mathbf{d} \cdot \hat{\sigma}^+|{}^2P_{3/2}, m_J = +\frac{3}{2}, m_I = +\frac{3}{2}\rangle|^2 \quad (3.67)$$

With $\mathbf{d} \cdot \hat{\sigma}^+$ denoting the right circular component of the electric dipole operator. For this transition the relation to an experimentally measured spontaneous emission

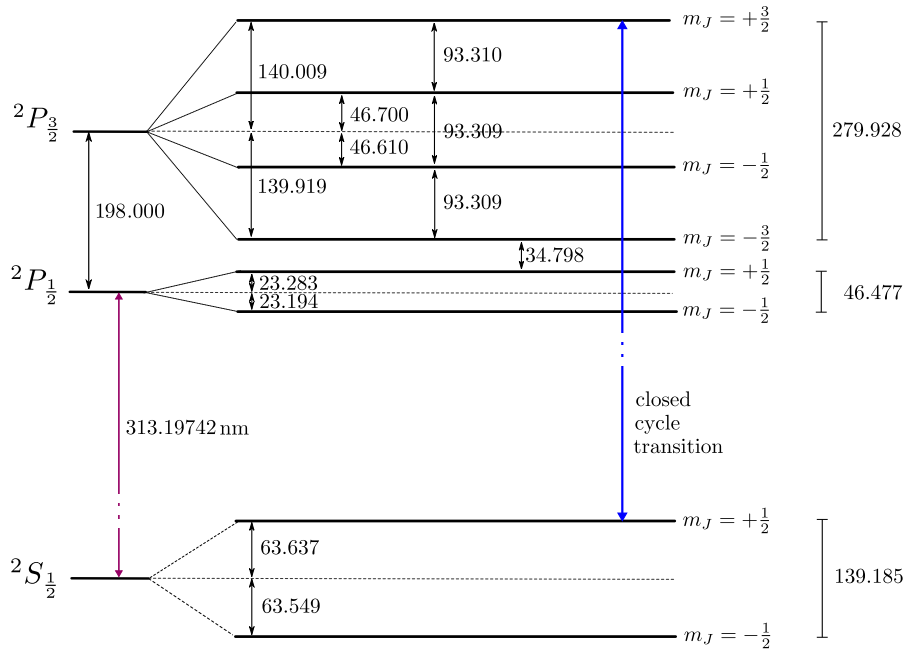

Figure 3.11: Beryllium level splittings in GHz within the $m_I = +3/2$ subsystem at an externally applied magnetic field of 5 T (not to scale). The internal qubit states $|\downarrow\rangle = |m_J = -1/2, m_I = +3/2\rangle$ and $|\uparrow\rangle = |m_J = +1/2, m_I = +3/2\rangle$ are separated by $\omega_0 = 2\pi \cdot 139.1850\,\text{GHz}$. A closed-cycle transition exists between the $|\uparrow\rangle = |m_J = +1/2, m_I = +3/2\rangle$ and the $^2P_{3/2}, |m_J = +3/2, m_I = +3/2\rangle$ levels. The excited state of this transition is separated by a frequency of $2\pi \cdot 93.3095\,\text{GHz}$ from the next subsystem level, which allows to optimally suppress accidental state transfer during cooling and detection.

rate, given by Equation 3.9, holds. Based on this, all Rabi frequencies, scattering rates and Stark shifts are calculated in terms of the intensity dependent resonant Rabi frequency of this closed-cycle transition.

The relevant dipole matrix elements can be evaluated by applying the Clebsch-Gordan algebra. According to the Wigner-Eckart theorem the dipole matrix elements can be expressed as products of an angular momentum coupling coefficient $A_{J'm'_J,J,m_J}$ (or $A_{F'm'_F,F,m_F}$) and a radial part $R_{n'l',nl}$. The angular part shows the relative weights of different contributions and results from recoupling all Clebsch-Gordan coefficients occurring during basis transformation while expanding the corresponding Eigenfunctions [64]. The radial part $R_{n'l',nl}$, also known as reduced matrix element $\langle n'l'\|\mathbf{d}\|nl\rangle$, is independent from the projection of any angular momentum quantum number on the quantization axis. Since all relevant matrix elements for beryllium couple between a ground-state level in the s-orbital and an excited state in the p-orbital, the reduced matrix elements $R_{n'l',nl}$ are identical for the closed-cycle transition and any transition between $|e\rangle$ and $|g\rangle$ contributing to the Raman process. The ratio of a matrix element scaled to the matrix element

of the closed-cycle transition is therefore determined by the ratio of the angular momentum coupling coefficients.
For low magnetic fields, where F and m_F are good quantum numbers, the angular momentum coupling coefficient for the Zeeman regime is given by [64]:

$$A_{F'm'_F,F,m_F} = (-1)^{1+L'+S+J+J'+1-m'_F}\sqrt{(2J+1)(2J'+1)(2F+1)(F'+1)} \cdot \begin{Bmatrix} L' & J' & S \\ J & L & 1 \end{Bmatrix} \begin{Bmatrix} J' & F' & 1 \\ F & J & 1 \end{Bmatrix} \begin{pmatrix} F & 1 & F' \\ m_F & q & -m'_F \end{pmatrix} \tag{3.68}$$

For high magnetic fields, in the Paschen-Back regime, with m_J, m_I being good quantum numbers the angular momentum coupling coefficient ist given by [64]:

$$A_{J'm'_J,J,m_J} = (-1)^{L'+S-m'_J}\sqrt{(2J+1)(2J'+1)} \begin{Bmatrix} L' & J' & S \\ J & L & 1 \end{Bmatrix} \begin{pmatrix} J & 1 & J' \\ m_J & q & -m'_J \end{pmatrix} \tag{3.69}$$

With the curly brackets denoting Wigner 6j and the round brackets Wigner 3j symbols. The quantum numbers with prime correspond to the involved excited state, without prime to the involved ground state quantum numbers. q indicates the polarization of the light with $q = 0$ for linear and $q = \pm 1$ for right- and left-circular polarized light. In the intermediate regime a numerical diagonalization at the given magnetic field is required in order to obtain the corresponding basis coefficients of the Eigenstates. A detailed derivation can be found in [81].

Approximation of excited state contributions

The existence of several excited states possibly leads to quantum interferences between different Raman contributions. Within a simple approximation the relative weights of different excited state contributions can be obtained. In the limit of large detunings and neglecting the differing detunings from the hyperfine level splittings as well as the different detunings of participating comb modes, the relevant energy levels of beryllium for this simplified pre-calculation are shown in Figure 3.12. Following the notation in [63, 82] the Raman beam coupling to the $|\downarrow\rangle$ level is designated as blue Raman (b) and the beam coupling to $|\uparrow\rangle$ as red Raman (r) beam, with respective frequencies ω_b and ω_r. The corresponding laser polarizations are expressed with respect to the quantization axis of the ion according to $E_j\hat{\epsilon}_j = j_-\hat{\sigma}^- + j_0\hat{\pi} + j_+\hat{\sigma^+}$ with $|j_-|^2 + |j_0|^2 + |j_+|^2 = 1$ and $j =$ r,b. In terms of qubit control implemented by optical frequency combs, the two contributions r and b can be seen as exemplary comb lines being responsible for the absorption part and the emisson part of the process. For the two-beam approach they originate from different beams, whereas for single-beam spin control they can originate from the same beam. The detuning Δ has its origin at the line center of the $^2P_{1/2}$ level and positively increases for larger energies. Within the simple pre-approximation

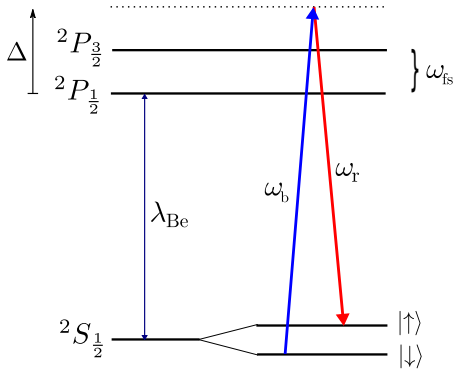

Figure 3.12: Schematical view of notations relevant for the numerical simulations of the two-photon stimulated Raman process in beryllium. The detuning Δ has its origin at the line center of the $^2P_{1/2}$ level and increases for larger energies. Within the simple pre-approximations, the detuning from the $^2P_{3/2}$ level is expressed in terms of the p-level fine-structure splitting ω_{fs}. For accurate simulations the detuning is precisley calculated with respect to the line center of the $^2P_{1/2}$ level. The Raman beam coupling to the $|\downarrow\rangle$ level is designated as blue Raman (b) and the beam coupling to $|\uparrow\rangle$ as red Raman (r) beam, with respective frequencies ω_{b} and ω_{r}.

the detuning to the $^2P_{3/2}$ is expressed in terms of the p-level fine-structure splitting ω_{fs}.
Using the appropriate Clebsch-Gordan coefficients, given by the angular coupling coefficient in Equation 3.69, the terms $\langle\downarrow,\uparrow|\mathbf{d}\cdot E_j\hat{\epsilon_j}|e_i\rangle$ can be evaluated. The Rabi frequency of the qubit transition $|\downarrow\rangle = |m_J = -\frac{1}{2}, m_I = +\frac{3}{2}\rangle \leftrightarrow |\uparrow\rangle = |m_J = +\frac{1}{2}, m_I = +\frac{3}{2}\rangle$ following Equation 3.60 is found to be:

$$\Omega = -\frac{\sqrt{2}}{3} g_b g_r (b_0 r_- + b_+ r_0) \frac{\omega_{\mathrm{fs}}}{\Delta(\Delta - \omega_{\mathrm{fs}})} \tag{3.70}$$

With g_{b} and g_{r} denoting the single-photon Rabi frequencies of the closed-cycle transition and b_0, r_0 being the linearly polarized and b_+,r_- the right and left circular polarized components of the blue and red Raman beam. This simple approximation gives a first intuitive insight to the different polarization contributions occurring when summing over all hyperfine levels. It can be seen that the maximum Rabi frequency for the qubit transition can be obtained by two different combinations of laser beam polarizations. The optimum Raman coupling can be achieved if the polarization of the Raman beam coupling to $|\downarrow\rangle$ refers to atomic σ^+ transitions and the polarization of the Raman beam coupling to $|\uparrow\rangle$ refers to atomic π transitions. Alternatively, within this simple approximation, a similar coupling can be achieved by combining π transitions for coupling to $|\downarrow\rangle$ with σ^- transitions for coupling to $|\uparrow\rangle$.

Accurate detunings and dipole matrix elements

Neglecting the different detunings within the hyperfine structure at an applied magnetic field of 5 T is not a valid approximation. For an accurate calculation the exact detunings of each level contributions must be taken into account. Table 3.2 summarizes the relevant matrix elements for the $m_I = +3/2$ subsystem and denotes each detuning referenced to the transition betwen the $^2S_{1/2}$ and $^2P_{1/2}$ line centers, given by the wavelength $\lambda_{\mathrm{Be}} = 313.19742\,\mathrm{nm}$ [83]. Figure 3.13 illustrates all relevant coupling transitions between the ground-state manifold and the excited p-levels of $^9\mathrm{Be}^+$ at an applied magnetic field of 5 T. The possible Raman coupling contributions for the denoted qubit states are pointed out. Comparing the corresponding matrix elements they can be proved to result in similar electric dipole couplings. Due to the large energy splittings and differing detunings between the possible contribution paths, the combination of atomic σ^+ transitions for coupling to $|\downarrow\rangle$ and atomic π transitions for coupling to $|\uparrow\rangle$ leads to slightly stronger Raman couplings.

ground state	excited state	matrix element	detuning	polarization
$\|\downarrow\rangle\ {}^2S_{\frac{1}{2}}\ \|m_J{=}-\frac{1}{2}\rangle$	${}^2P_{\frac{1}{2}}\ \|m_J{=}-\frac{1}{2}\rangle$	+0.57734	+ 46.355	π
$\|\downarrow\rangle\ {}^2S_{\frac{1}{2}}\ \|m_J{=}-\frac{1}{2}\rangle$	${}^2P_{\frac{1}{2}}\ \|m_J{=}+\frac{1}{2}\rangle$	+0.81649	+ 92.832	σ^+
$\|\downarrow\rangle\ {}^2S_{\frac{1}{2}}\ \|m_J{=}-\frac{1}{2}\rangle$	${}^2P_{\frac{3}{2}}\ \|m_J{=}-\frac{3}{2}\rangle$	−0.99999	+127.630	σ^-
$\|\downarrow\rangle\ {}^2S_{\frac{1}{2}}\ \|m_J{=}-\frac{1}{2}\rangle$	${}^2P_{\frac{3}{2}}\ \|m_J{=}-\frac{1}{2}\rangle$	−0.81649	+220.939	π
$\|\downarrow\rangle\ {}^2S_{\frac{1}{2}}\ \|m_J{=}-\frac{1}{2}\rangle$	${}^2P_{\frac{3}{2}}\ \|m_J{=}+\frac{1}{2}\rangle$	−0.57735	+314.248	σ^+
$\|\uparrow\rangle\ {}^2S_{\frac{1}{2}}\ \|m_J{=}+\frac{1}{2}\rangle$	${}^2P_{\frac{1}{2}}\ \|m_J{=}-\frac{1}{2}\rangle$	−0.81650	− 92.830	σ^-
$\|\uparrow\rangle\ {}^2S_{\frac{1}{2}}\ \|m_J{=}+\frac{1}{2}\rangle$	${}^2P_{\frac{1}{2}}\ \|m_J{=}+\frac{1}{2}\rangle$	−0.57735	− 46.354	π
$\|\uparrow\rangle\ {}^2S_{\frac{1}{2}}\ \|m_J{=}+\frac{1}{2}\rangle$	${}^2P_{\frac{3}{2}}\ \|m_J{=}-\frac{1}{2}\rangle$	−0.57735	+ 81.734	σ^-
$\|\uparrow\rangle\ {}^2S_{\frac{1}{2}}\ \|m_J{=}+\frac{1}{2}\rangle$	${}^2P_{\frac{3}{2}}\ \|m_J{=}+\frac{1}{2}\rangle$	−0.81650	+175.063	π
$\|\uparrow\rangle\ {}^2S_{\frac{1}{2}}\ \|m_J{=}+\frac{1}{2}\rangle$	${}^2P_{\frac{3}{2}}\ \|m_J{=}+\frac{3}{2}\rangle$	+1.00000	+268.372	σ^+

Table 3.2: Table of relevant Raman coupling contributions for the $m_I = +3/2$ subsystem at 5 T showing the involved states, the corresponding transition matrix elements, detunings and polarizations. The matrix elements are scaled to the closed-cycle transition between the $^2S_{1/2}$, $m_J = +1/2$ and the $^2P_{3/2}$, $m_J = +3/2$ levels und the detunings are specified in GHz and referenced to the transition between the $^2S_{1/2}$ and $^2P_{1/2}$ line center.

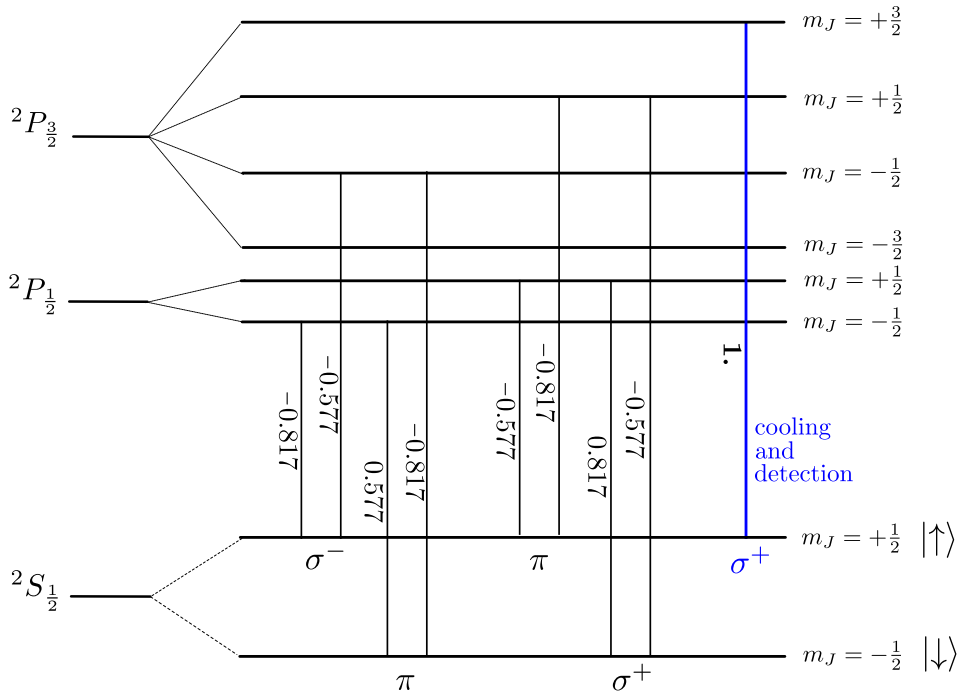

Figure 3.13: Illustration of possible transitions between the ground-state manifold and the excited p-levels of $^9Be^+$ at an applied magnetic field of 5 T for the $m_I = +3/2$ subsystem. In this subsystem a closed-cycle transition exists between the $^2S_{1/2}$, $m_J = +1/2$ and the $^2P_{3/2}$, $m_J = +3/2$ levels. All illustrated matrix elements are scaled to this transition and are summarized in Table 3.2 with respective detunings referenced to the transition between the $^2S_{1/2}$ and $^2P_{1/2}$ line center. Efficient coupling of the denoted qubit states can be obtained with either a π polarization coupling to $|\downarrow\rangle$ and σ^- to $|\uparrow\rangle$ or with σ^+ polarization coupling to $|\downarrow\rangle$ and π polarization to $|\uparrow\rangle$.

3.3.3 Numerical simulations

In this section numerical simulations of the relevant atomic processes occurring in beryllium ions during two-photon stimulated Raman transitions using an optical frequency comb will be presented. The atomic level structure of $^9Be^+$ requires special care concerning the spectral properties of the pulse envelope in order to maximize the Raman coupling strength while supressing decoherence induced by off-resonant light scattering. Operating within the optimized region of parameters is mandatory in order to achieve appropriate Raman coupling strengths. Once fulfilling the requirements for the (anti-)proton g-factor measurement experiment, the Raman laser represents a flexible tool for qubit control of beryllium ions at any less stringent experimental conditions given at lower magnetic fields. A qualitative and quantitative discussion of simulation results will be presented.

Qualitative discussion of parameters

The aim when implementing Raman transitions is to maximize the Rabi frequency while controlling decoherence induced by off-resonant light scattering during qubit operations. As derived in section 3.2 the Rabi frequency for the use of an optical frequency comb (ofc) is proportional to:

$$\Omega_{\mathrm{ofc}} \propto \frac{\sum_k E_k E_{k-q}}{\Delta} \propto \frac{\bar{I} \cdot \zeta[f_{\mathrm{p}}(\omega_0, \Delta\omega_{\mathrm{FWHM}})]}{\Delta} \tag{3.71}$$

High Rabi frequencies, corresponding to fast π-times $t_\pi \propto 1/\Omega_{\mathrm{ofc}}$, can hence be achieved for spectral bandwidths being significantly broader than the qubit splitting resulting in $\zeta[f_{\mathrm{p}}(\omega_0, \Delta\omega_{\mathrm{FWHM}})] \cong 1$ and for small detunings from the excited states. In general it is advantageous to implement qubit operations as fast as possible for being unsusceptible to experimental fluctuations. For the implementation of qubit operations using an optical frequency comb, a lower limit concerning the probe duration results from the condition for resolving motional sidebands given in Equation 3.44. For an expected axial trap frequency on the order of 4 MHz for the (anti-)proton g-factor experiment, the probe duration for implementing sideband transitions should exceed $t_{\mathrm{probe}} \gg 2\,\mu s$. A fundamental upper limit cannot be defined. We aim for carrier transition π-times on the order of tens of μs, but slower operation need not limit the experiment.
Decoherence induced by off-resonant light scattering in contrast can be highly detrimental. A challenging benchmark is to keep the scattering probability below 10^{-4}, which allows to enter the regime of fault-tolerant qubit operations [84]. As derived in section 3.2 the total scattering rate in the limit of large detunings is proportional to:

$$\Gamma_{\mathrm{ofc}} \propto \frac{\sum_k E_k^2}{\Delta^2} \propto \frac{\bar{I}}{\Delta^2} \tag{3.72}$$

Since the scattering rate increases quadratically with smaller detunings a compromise of parameter settings must be found optimizing the ratio between Raman coupling and scattering rate.

Specific challenge of beryllium qubit control

For atomic level structures exhibiting two excited fine structure p-levels an established compromise within the CW laser approach is to choose a detuning between the excited state manifolds. At this position there is a local maximum of the Rabi frequency, due to a strong coupling to both excited states, combined with a local minimum of the scattering rate. In case of a large fine structure splitting between the excited p-levels, this benefit can also be used for the implementation using a pulsed Raman laser. The pioneers of qubit control using an optical frequency comb, D. Hayes and C. Monroe, have taken advantage of this. Entanglement of atomic qubits using an optical frequency comb has for the first time and so far

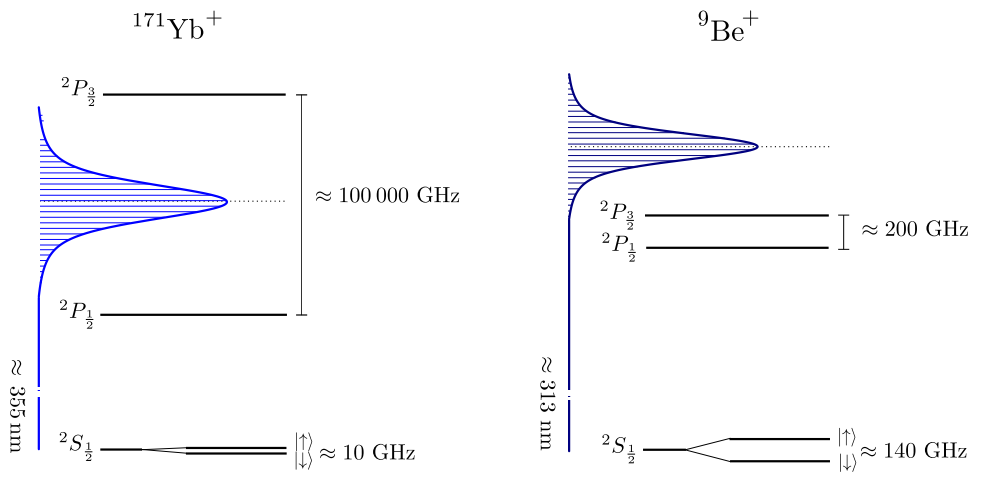

Figure 3.14: Comparison of the atomic structure of $^{171}Yb^+$ and $^9Be^+$ relevant for the implementation of Raman transitions using an optical frequency comb. $^{171}Yb^+$, as used by the pioneers of this technique [45], exhibits one ground state in the s-orbital and two excited states in the p-orbital, similar to $^9Be^+$. The fine-structure splitting between the p-levels of ytterbium is 500-times larger than for beryllium, which allows to choose a Raman detuning between these states. This is advantageous for obtaining an optimized ratio between the Raman coupling strength and the scattering rate. In contrast, due to the small fine-structure splitting of $^9Be^+$, a detuning outside the p-level manifold must be chosen, which requires a careful control of the spectral comb properties to operate in the optimum region maximizing the Raman coupling while keeping the scattering rate acceptably low.

only been demonstrated within the hyperfine ground-state manifold of $^{171}Yb^+$ [45]. The level structure of ytterbium offers several advantages for implementation of pulsed laser qubit control. A comparison with the level structure of $^9Be^+$ is shown in Figure 3.14. $^{171}Yb^+$ also exhibits a single ground state in the s-orbital, where the qubit levels are chosen within the hyperfine manifold while applying a magnetic field resolving the sublevels. The qubit level splitting during experiments has been on the order of 10 GHz [45]. Furthermore two excited states in the p-orbital exist. The fine-structure splitting between them is 100 THz, which is extremely large. This is of huge advantage for the implementation of qubit control using an optical frequency comb, as it allows operating at the optimum position between the p-levels, while providing a large detuning. The large detuning not only reduces scattering, it also ensures the spectral bandwidth to be easily made much broader than the qubit splitting, which is essential for efficient Raman coupling. Also the spectral properties of the frequency comb are irrelevant due to the large detunings. A further advantage of ytterbium is that commercial high power lasers are available at the ideal frequency between the p-levels near 355 nm.

In comparison, the implementation of qubit control using an optical frequency comb for beryllium is more challenging due to the combination of the large qubit splitting and a small excited state fine-structure splitting. The fine-structure splitting of the excited states of only $\omega_{\mathrm{fs}} = 2\pi \cdot 198\,\mathrm{GHz}$ requires the Raman detuning to be chosen outside the p-level fine-structure manifold in order to not resonantly excite the p-levels with the outer-lying frequency components of the spectrum. A detuning outside the p-level manifold in general allows for small scattering rates during the Raman process when choosing large detunings, but it also limits the maximum achievable coupling strength, as the contribution from one of the excited-state manifolds is reduced. In addition the application of the pulsed-laser approach demands a further tradeoff concerning the optimal spectral bandwidth. On the one hand efficient Raman coupling requires the spectral bandwidth to be much broader than the qubit splitting, whereas on the other hand a broader spectrum also requires a larger detuning in order to control the scattering rate. In consequence due to the larger detuning, the Raman coupling strength drops, despite the broader spectrum. This behaviour requires an accurate optimization of the laser's spectral properties to enable efficient qubit operations. As the required wavelength near 313 nm, in contrast to the required wavelength of 355 nm for ytterbium, is not commercially available with high power, it is important to operate within the optimum region in order to achieve appropriate Rabi frequencies.

Quantitative simulations

Numerical simulations of the Raman process implemented by an optical frequency comb have been carried out according to Equation 3.60 for the Rabi frequency[9] and according to Equations 3.57 and 3.58 for the calculation of the scattering rates. The product of the time-averaged resonant single-photon Rabi frequencies in both equations has been calculated by:

$$\begin{aligned} g_0(\bar{I}_1) \cdot g_0(\bar{I}_2) &= \sum_k g_0(E_{1,k}) g_0(E_{2,k-q}) \\ &= \sum_k g_0[\omega_{\mathrm{rep}} \tilde{f}_{\mathrm{p}_1}(k\omega_{\mathrm{rep}})] \cdot g_0[\omega_{\mathrm{rep}} \tilde{f}_{\mathrm{p}_2}((k-q)\omega_{\mathrm{rep}})] \\ &\approx \frac{1}{\omega_{\mathrm{rep}}} \int g_0[\omega_{\mathrm{rep}} \tilde{f}_{\mathrm{p}_1}(\omega)] \cdot g_0[\omega_{\mathrm{rep}} \tilde{f}_{\mathrm{p}_2}(\omega - \omega_0)] d\omega \end{aligned} \tag{3.73}$$

[9] For the single-beam approach the full average intensity of the pulse train is available for both single-photon Rabi frequencies. For the two-beam approach the average intensities denote the power contained in each beam separately.

and

$$\begin{aligned} g_0^2(\bar{I}) &= \sum_k g_0^2(E_k) \\ &= \sum_k g_0^2[\omega_{\mathrm{rep}} \tilde{f}_{\mathrm{p}}(k\omega_{\mathrm{rep}})] \\ &\approx \frac{1}{\omega_{\mathrm{rep}}} \int g_0^2[\omega_{\mathrm{rep}} \tilde{f}_{\mathrm{p}}(\omega)] d\omega \ . \end{aligned} \tag{3.74}$$

The electric field amplitudes for the spectral envelope functions are each obtained from the average intensity according to Equation 3.40. For spectral bandwidths being not significantly larger than the qubit splitting, the function $\zeta[f_{\mathrm{p}}(\omega_0, \Delta\omega_{\mathrm{FWHM}})]$ in Equation 3.60 accounts for the drop of the Raman coupling strength based on deviating electric field amplitudes according to $E_0(\sum_k E_k E_{k-q}) = E_0(\bar{I}) \cdot \sqrt{\zeta[f_{\mathrm{p}}(\omega_0, \Delta\omega_{\mathrm{FWHM}})]}$. The detuning of each comb tooth is considered within the detuning in the aforementioned equations. For accurate calculations the sum over each discrete comb mode is carried out, which accounts for resonances of any comb tooth with any level of the excited-state manifold. Replacing the sum by a frequency integral yields to a valid approximation if single resonances are not of interest and if the spectral bandwidth exceeds the comb tooth spacing.
Within the numerical simulations a hyperbolic secant (sech) function has been assumed as standard pulse shape, representing a typical envelope form of pulsed lasers:

$$f_{\mathrm{sech}}(t) = \sqrt{\frac{\pi}{2}} E_0 \mathrm{sech}\left(\frac{\Delta\nu_{\mathrm{FWHM}} \cdot t}{0.1787}\right) \tag{3.75}$$

The corresponding spectrum is given by the (non-unitary) Fourier transform, yielding:

$$\tilde{f}_{\mathrm{sech}}(\omega) = \sqrt{\frac{\pi}{2}} E_0 \frac{0.1787}{2\Delta\nu_{\mathrm{FWHM}}} \mathrm{sech}\left[\frac{0.1787\pi \cdot \omega}{2\Delta\nu_{\mathrm{FWHM}}}\right] \tag{3.76}$$

Further it has been assumed that the pulses are not chirped and are time-bandwidth limitied. For the assumed pulse envelope the FWHM pulse duration τ_{FWHM} is connected to the FWHM spectral bandwidth $\Delta\nu_{\mathrm{FWHM}}$ by the time bandwidth product $TBP = \tau_{\mathrm{FWHM}} \cdot \Delta\nu_{\mathrm{FWHM}} = 0.315$. The average intensity according to Equation 3.40 is given by:

$$\bar{I}_{\mathrm{sech}} = \frac{c\epsilon_0}{2} E_0^2 \cdot \frac{0.1787\pi}{\Delta\nu_{\mathrm{FWHM}}} f_{\mathrm{rep}} \tag{3.77}$$

For the relation to the average laser power a gaussian pulse profile is assumed according to $\bar{I} = \frac{2P_{\mathrm{av}}}{\pi w_0^2}$ with w_0 being the beam radius (in $1/e^2$ definition) and P_{av} the average power given by $P_{\mathrm{av}} = E_{\mathrm{p}} \cdot f_{\mathrm{rep}}$ with the laser pulse energy E_{p} and the laser repetition rate f_{rep}. Within the following calculations a laser repetition rate near 100 MHz and a beam radius of $w_0 = 15\,\mu$m are assumed. Further assumed are

Raman beam laser polarizations corresponding to atomic σ^+-polarisation coupling to $|\downarrow\rangle$ and atomic π-polarization coupling to $|\uparrow\rangle$. Dependencies of the Raman detuning are exemplarily shown for positive detunings being blue detuned from the excited p-level manifold and referenced to the line center of the $^2P_{1/2}$-level. For comparisons of simulation results of different pulse envelopes, functional forms as listed in Table 3.1 have been applied, scaled to the same average intensity.

Importance of spectral properties

For a Raman detuning outside of the p-level manifold the spectral properties of the pulsed laser are of extreme importance, because they determine the minimum detuning Δ_{min} which is required to control the total scattering rate. This detuning strongly influences and limits the maximum achievable Rabi frequency:

$$\Gamma_{\mathrm{total}} \longrightarrow \Delta_{\mathrm{min}} \left(\tilde{f}_p(\Delta\omega_{\mathrm{FWHM}}) \right) \longrightarrow \Omega_{\mathrm{max}} \tag{3.78}$$

Figure 3.15 schematically demonstrates the dependence of the required detuning on the spectral envelope, assuming the scattering rate to be kept below a certain threshold. The detuning is referenced to the carrier frequency of the envelope. For a given pulse envelope function the required detuning therefore increases with increasing spectral bandwidth. Furthermore the absolute value of the required detuning strongly depends on the pulse shape. Due to the characteristic sidelobes of a sinc-shaped spectrum, the required detuning for example is much larger than the one required for an ideal sech-shaped spectrum of identical bandwidth. The effect on the maximum achievable corresponding Raman coupling strength has been calculated for both pulse shapes. The results are shown in Figure 3.16.
In order to obtain the optimum combination of spectral bandwidth and detuning, the required power for achieving a carrier π-time of $t_\pi = 5\,\mu$s and a scattering probability of $(\Gamma_{\mathrm{total1}} + \Gamma_{\mathrm{total2}}) \cdot 5\,\mu\mathrm{s} = 10^{-4}$ for different combinations of detunings and bandwidths has been calculated. The required power is plotted against the spectral bandwidth of the pulses and further the corresponding minimum required detuning for each bandwidth is shown. It can be seen that the minimum required power, in order to achieve the desired Rabi frequency, occurs for a spectral comb width being slightly broader than the qubit splitting near 140 GHz. For lower bandwidths the required power increases, which can be explained by the fact that less contributing comb pairs exist. For larger spectral bandwidths the achievable Rabi frequency also drops because of the increasing required detuning, as shown in the corresponding plot. This general behaviour is the same for both exemplarily shown pulse shapes. A clear optimal bandwidth at a narrow width exists, which results from a compromise between the number of contributing comb tooth pairs for the Raman process and the smallest possible detuning which still allows to control the scattering rate. The values of required power and required detuning however differ strongly. The required power within optimum conditions for the sinc-shaped

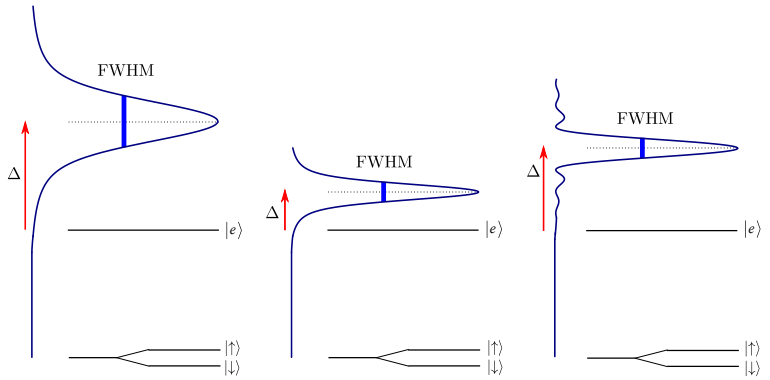

Figure 3.15: Schematical illustration of the minimum required detuning in order to keep the scattering rate below a certain threshold, depending on different spectral envelopes. For a given spectral shape the required detuning increases the broader the spectrum is. The absolute value of the required detuning further depends on the pulse shape. If frequency components exist located close to resonance with the excited state, a larger detuning is required.

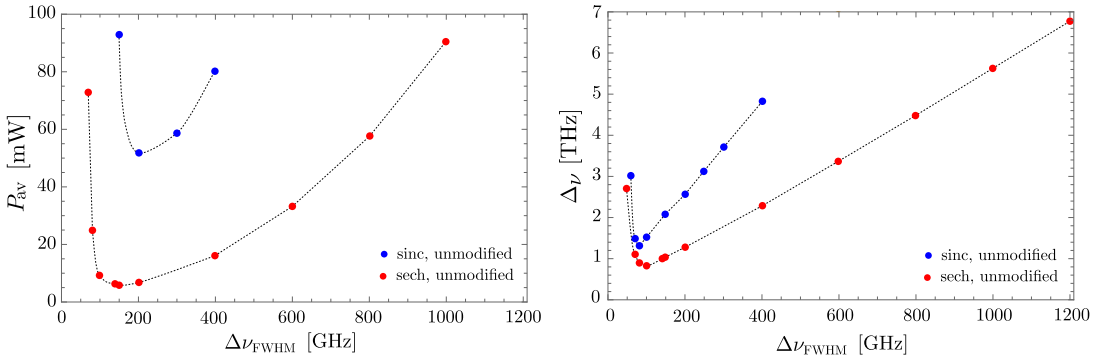

Figure 3.16: Numerical simulation results comparing the influence of different pulse shapes on the achievable Raman coupling strength for an applied magnetic field of 5 T. In the left graph the average power P_{av} is shown, required in order to achieve a spin flip within $t_\pi = 5\,\mu$s and while ensuring the scattering probability to be $(\Gamma_{\mathrm{total1}}+\Gamma_{\mathrm{total2}})\cdot 5\,\mu\mathrm{s} = 10^{-4}$, as a function of the spectral bandwidth $\Delta\nu_{\mathrm{FWHM}}$. On the right side the corresponding required detunings Δ_ν are shown. In red the data points for a sech-shaped spectrum are plotted and in blue for a sinc-shaped spectrum. The dotted lines represent guides to the eye.

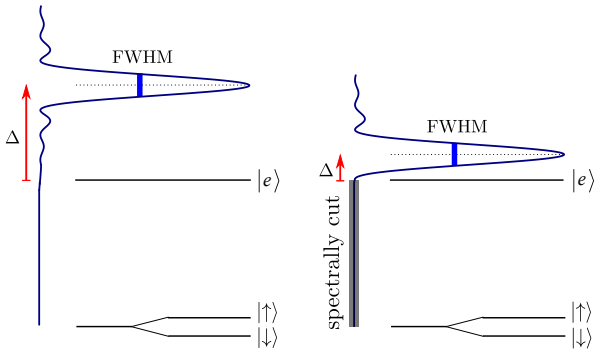

Figure 3.17: Schematical illustration comparing the minimum required detuning in order to keep the scattering rate below a certain threshold for an unmodified sinc-shaped spectrum (left) and for the identical spectrum where the frequency components close to resonance to the excited state are blocked (right).

spectrum is about 8-9 times higher than for the sech-shaped spectrum. This is due to the much larger required detuning, being $\approx 1\,\mathrm{THz}$ larger within optimum conditions than the required detuning for the sech-shaped pulses within optimum conditions, as shown in Figure 3.16.
These calculations show that the optimum bandwidth, under the constraint of controlling the scattering rate, is very small, being only slightly broader than the qubit splitting. Further they show the major importance and influence of the spectral envelope. Any frequency components contained in a spectrum located close to resonance strongly limit the achievable Raman coupling strength due to the larger required detuning. As such spectral sidelobes and imperfections often occur during nonlinear processes which are required to achieve the UV wavelength of 313 nm, the spectral shape of the pulse envelope must be controlled in order to achieve appropriate Rabi frequencies.

Advantage of spectral pulse shaping

Due to the strong limiting effect of the detuning on the maximum achievable Rabi frequency, spectral pulse shaping efforts have a large impact on improving results. For this it is convenient to spectrally block unwanted frequency components of the spectrum located close to the excited states during the Raman process. The absence of those frequency components allows for a much smaller detuning, as schematically demonstrated in Figure 3.17. The improvements on the achievable Raman coupling strength have been calculated, similar to the previously discussed calculations. In Figure 3.18 the results of the unmodified sinc-shaped spectrum under conditions as before are compared to the case where the frequency components of all characteristic sidelobes are blocked, as illustrated in Figure 3.20.
The required detuning in order to control the scattering rate for the cut spectrum is

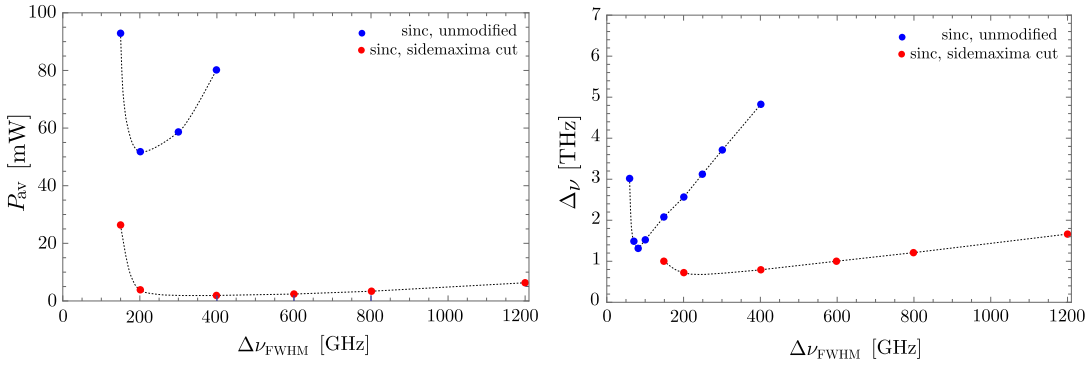

Figure 3.18: Numerical simulation results comparing the influence of spectral pulse shaping on the achievable Raman coupling strength for an applied magnetic field of 5 T. In the left graph the average power P_{av} is shown, required in order to achieve a spin flip within $t_\pi = 5\,\mu$s and while ensuring the scattering probability to be $(\Gamma_{total1}+\Gamma_{total2})\cdot 5\,\mu s = 10^{-4}$, depending on the spectral bandwidth $\Delta\nu_{FWHM}$. On the right side the corresponding required detunings Δ_ν are shown. In blue the data for an unmodified sinc-shaped spectrum are plotted and in red the data for the identical spectrum, where all sidelobes close to resonance to the excited states are blocked, as schematically illustrated in Figure 3.17 and visualized in Figure 3.20. The dotted lines are guides to the eye.

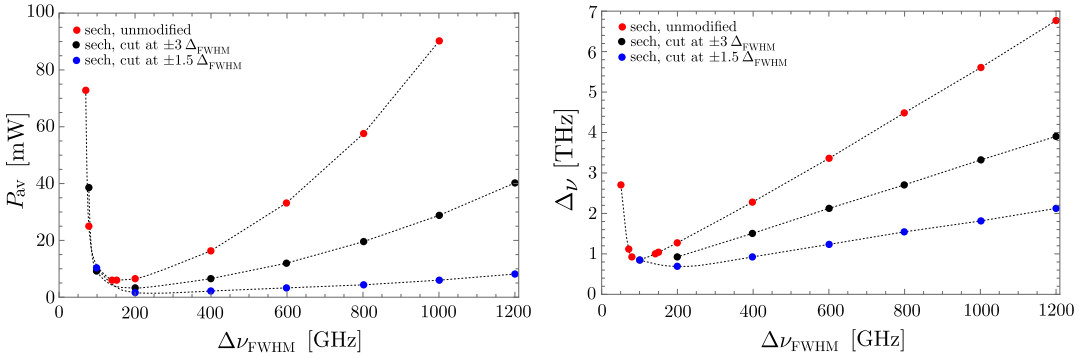

Figure 3.19: Numerical simulation results comparing the influence of different amounts of spectral blocking of frequency components on the achievable Raman coupling strength for an applied magnetic field of 5 T. In the left graph the average power P_{av} is shown, required in order to achieve a spin flip within $t_\pi = 5\,\mu$s and while ensuring the scattering probability to be $(\Gamma_{total1} + \Gamma_{total2}) \cdot 5\,\mu s = 10^{-4}$, depending on the spectral bandwidth $\Delta\nu_{FWHM}$. On the right side the corresponding required detunings Δ_ν are shown. In red the data for an unmodified sech-shaped spectrum are plotted. In black the data for the identical spectrum being blocked at a spectral cutoff position of $\pm 3\,\Delta_{FWHM}$ are shown and in blue the data for the spectrum being blocked at a spectral cutoff position of $\pm 1.5\,\Delta_{FWHM}$. The dotted lines represent guides to the eye.

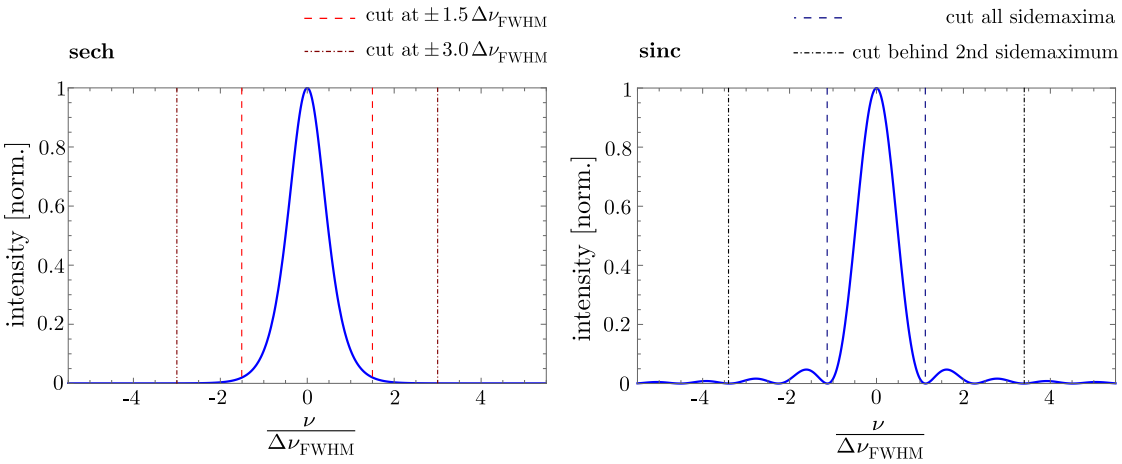

Figure 3.20: Visualization of the spectral cutoff positions as assumed for the numerical simulations. On the left the corresponding positions are shown for a sech-shaped and on the right for a sinc shaped spectrum. The respective power loss has been neglected.

much smaller and does not significantly exceed with larger bandwidths within the plotted spectral region. As consequence the required power to achieve the desired Rabi frequency is strongly reduced and also shows a very insensitive dependence on the spectral bandwidth. This further allows operating with broader spectra, which within the shown spectral range in general can be achieved with higher efficiency. As such sharp spectral cutting edges are not realistic to achieve in an actual implementation, Figure 3.19 further shows simulation results obtained for different cutoff positions of a sech-shaped spectrum. The corresponding blocking positions are visualized in Figure 3.20. The slopes of the increase of required detuning with increasing spectral bandwidth clearly depend on the spectral cutoff position, which directly affects the achievable Raman coupling strength.
The presented simulations show the strong influence of the spectral pulse shaping on improving results. In order to achieve strong Raman couplings spectral pulse shaping is mandatory. The smaller the required detuning for a given spectrum is, the stronger the possible Raman coupling strength becomes. The optimal spectral bandwidth and the value of achievable Raman coupling depend on the position and hence on the resolution of the cutting edge while controlling the spectrum and on the spectral envelope shape.

Simulation data - required laser parameters

In order to estimate the Raman coupling strength which can be expected for the (anti-)proton g-factor experiment at an applied magnetic field of 5 T, a sech-shaped spectrum cut at $1.5\Delta_{\mathrm{FWHM}}$ is assumed as an exemplary case for a well performed spectral pulse shaping. For comparison, a sinc-shaped spectrum cut

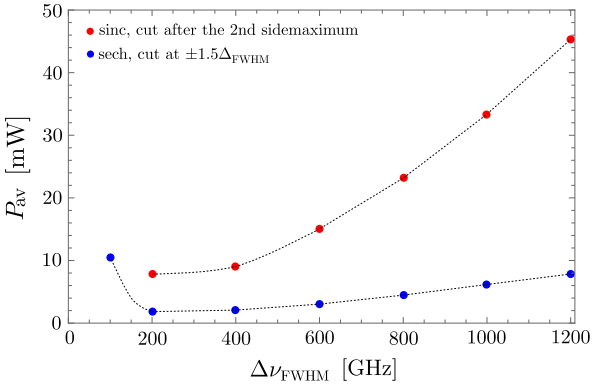

Figure 3.21: Numerical simulation results of beryllium ion qubit control at 5 T demonstrating achievable Raman couplings when implementing spectral pulse shaping. Shown is the required power in order to achieve a spin flip in $t_\pi = 5\,\mu$s as a function of the spectral bandwidth. For each data point the minimal required detuning to achieve a total scattering probability of $(\Gamma_{\text{total1}} + \Gamma_{\text{total2}}) \cdot 5\,\mu\text{s} = 10^{-4}$ is assumed. The blue data points correspond to a sech-shaped spectrum with frequency components blocked at a spectral cutoff position of $\pm\,1.5\,\Delta_{\text{FWHM}}$. The red data points correspond to a sinc-shaped spectrum with frequency components blocked after the second side-maxima. The cutoff positions are visualized in Figure 3.20. The dotted lines are guides to the eye.

behind its second side maximum is assumed in order to obtain an estimation for the exemplary case of a non-perfectly implemented pulse shaping. Both cutoff positions are visualized in Figure 3.20 and simulations results are shown in Figure 3.21.

As discussed before, the optimal spectral bandwidth and the absolute achievable Raman coupling strength strongly depend on the position of the cutting edge when blocking outer-lying frequency components and on the spectral envelope. Without implementing any spectral control, the required detunings for spectral bandwidths being significantly broader than the qubit splitting are too high to achieve appropriate Raman couplings, whereas the achievable π-times with implemention of spectral pulse shaping show promising values. Assuming a well implemented spectral modification, only a few mW per Raman beam are required in order to achieve spin flips in the aimed range of tens of microseconds. In this case no significant loss of coupling strength occurs for spectral bandwidths in the range between $\approx 200\,$GHz and $\approx 1000\,$GHz. In contrast, for less perfect frequency blocking and for low available laser powers, operating with a narrow spectrum, with an optimal bandwidth near 300 GHz, becomes important in order to achieve the desired range of Raman coupling strengths. The simulations therefore show that for achieving efficient beryllium ion qubit control it is mandatory to combine efforts towards the generation of narrow-bandwidth UV pulses with a technique to control the outer-lying frequency components.

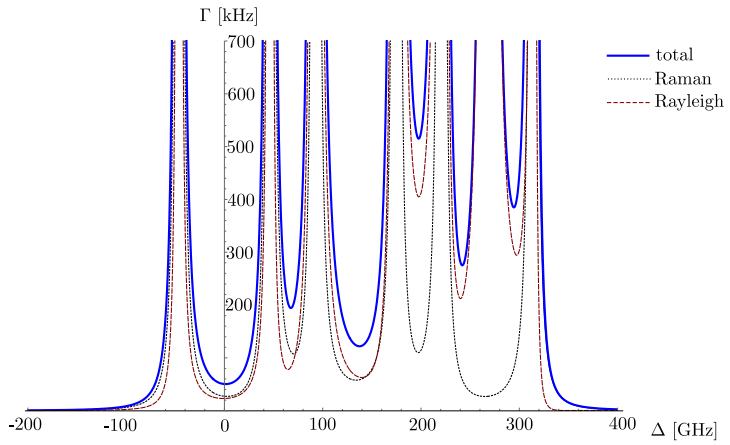

Figure 3.22: Simulation results of the total scattering rate for the superposition of qubit states at an applied magnetic field of 5 T, calculated for CW beams with 5.0 mW of laser power. Shown is the total scattering rate in blue as a function of the detuning referenced to the $^2P_{1/2}$ line center, being composed of Raman scattering in black (dotted) and Rayleigh scattering in red (dashed).

The dependence of the achievable Raman coupling and π-times on varying laser parameters can be estimated from the shown results. The dependence on the average power can be approximated to be linear. A deviation of the available laser power by a certain factor will reduce the π-time by this factor. A deviation of the assumed focal waist size can be approximated similarly with inverse quadratical behaviour. Further a deviation of the pulse duration caused by temporal broadening reduces the intensity at the ion, which effectively can be approximated by a respective reduction of average power, while keeping the spectral bandwidth constant.
Whereas the data shown here have been calculated for the exemplary case of positive detunings, the dependencies for negative detunings in general show the same behaviour. For the chosen combination of Raman beam laser polarizations, with atomic σ^+-polarisation coupling to $|\downarrow\rangle$ and atomic π-polarization coupling to $|\uparrow\rangle$, negative detunings however allow for slightly higher Raman couplings, due to a small asymmetry of the scattering rate with respect to the maxima of the corresponding Rabi frequency. The total scattering rate, composed of Raman scattering and Rayleigh scattering, for the superposition of the qubits states is shown in Figure 3.22. The data are calculated for CW beams which results in a similar behavior of the curve as for pulsed laser beams. The maxima of the corresponding Rabi frequency are located at +20 GHz for coupling to the $^2P_{1/2}$ level and at +240 GHz for coupling to the $^2P_{3/2}$ level. Relative to these maxima, negative detunings allow for slightly smaller values when tolerating a specific scattering rate and hence allow for slightly stronger Raman couplings. The difference in required power for optimal

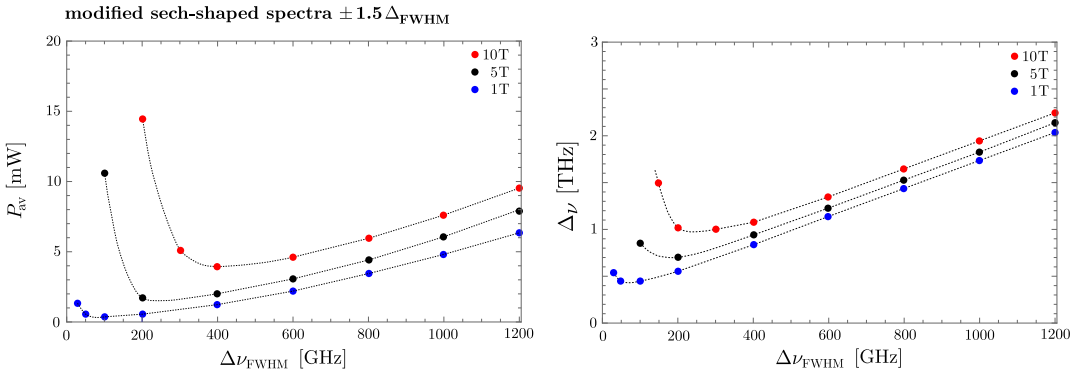

Figure 3.23: Numerical simulation results demonstrating achievable Raman couplings for different applied magnetic fields in the Paschen-Back regime for sech-shaped spectra with frequency components being blocked at a spectral cutoff position of $\pm\,1.5\,\Delta_{\mathrm{FWHM}}$, as shown in Figure 3.20. In the left graph the average power P_{av} is shown, required in order to achieve a spin flip within $t_\pi = 5\,\mu$s and while ensuring the scattering probability to be $(\Gamma_{\mathrm{total1}} + \Gamma_{\mathrm{total2}}) \cdot 5\,\mu\mathrm{s} = 10^{-4}$, depending on the spectral bandwidth $\Delta\nu_{\mathrm{FWHM}}$. On the right side the corresponding required detunings Δ_ν are shown. The black data points correspond to an applied magnetic field of 5 T as to be set in the (anti-)proton experiment, the blue data points correspond to an applied magnetic field of 1 T and the red data points to an applied magnetic field of 10 T. The dotted lines represent guides to the eye.

positive and for optimal negative detuning is below 10%, wherefor in case of an asymmetric intensity distribution, the orientation of the detuning should instead be chosen based on the specific given pulse envelope of the UV beam. Differing amounts of power loss when spectrally blocking outer-lying frequency components will most likely be more important than the effect of the sign of the detuning.

Simulation data - flexible quantum control

Once fulfilling the requirements for qubit control at an applied magnetic field of 5 T, the identical laser parameter settings allow for qubit control of beryllium ions at lower magnetic fields with equal or higher efficiency. Also for higher magnetic fields only a small drop of coupling strength occurs when operating with appropriate spectral properties. Figure 3.23 shows a comparison of different magnetic fields from 1 T to 10 T in the high-field Paschen-Back regime for a sech-shaped pulse being cut at a spectral position of $\pm\,1.5\,\Delta_{\mathrm{FWHM}}$. The lower the magnetic field strength is, the smaller the required detunings are in order to control the scattering rate and in consequence the lower the required power is in order to achieve a specific π-time. Depending on the applied spectral bandwidth, Raman couplings for higher magnetic fields than 5 T are only slightly reduced, if operating with a spectral bandwidth being larger than the corresponding qubit splitting.
If the interplay of scattering rate and Raman couplings are comparable, the identical

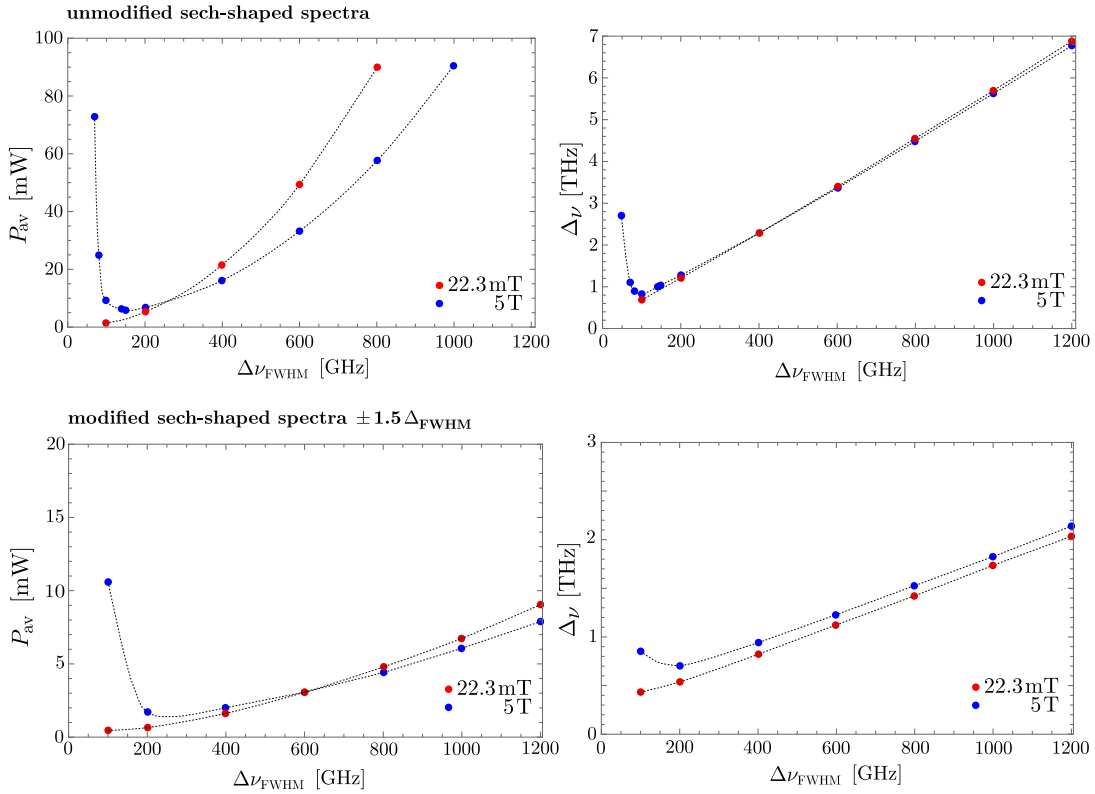

Figure 3.24: Numerical simulation results demonstrating achievable Raman couplings for different qubit transitions at different magnetic field regimes for unmodified sech-shaped spectra (top) and for sech-shaped spectra with frequency components blocked at a spectral cutoff position of $\pm\,1.5\,\Delta_{\mathrm{FWHM}}$ (bottom), as visualized in Figure 3.20. In the left graphs the average power P_{av} is shown, required in order to achieve a spin flip within $t_\pi = 5\,\mu$s and while ensuring the scattering probability to be $(\Gamma_{\mathrm{total1}} + \Gamma_{\mathrm{total2}}) \cdot 5\,\mu\mathrm{s} = 10^{-4}$, as a function of the spectral bandwidth $\Delta\nu_{\mathrm{FWHM}}$. On the right side the corresponding required detunings Δ_ν are shown. The blue data points correspond to an applied magnetic field of 5 T as to be set in the (anti-)proton experiment. The red data points correspond to the field-independent qubit transition $|\downarrow\rangle = |F = 2, m_F = 1\rangle \leftrightarrow |\uparrow\rangle = |F = 1, m_F = 1\rangle$ at an applied magnetic field of 22.3 mT, as discussed in Figure 3.9. The dotted lines represent guides to the eye.

laser parameter settings further allow for qubit control of other qubit transitions also in different magnetic field regimes without significant change of efficiency, if spectral control is implemented. Figure 3.24 herefor shows a comparison of simulation results for the discussed qubit transition at an applied magnetic field of 5 T to simulation results for the first-order field-independent qubit transition $|\downarrow\rangle = |F = 2, m_F = 1\rangle \leftrightarrow |\uparrow\rangle = |F = 1, m_F = 1\rangle$ at an applied magnetic field of 22.3 mT, as discussed in Figure 3.9. Results are compared for unmodified sech-

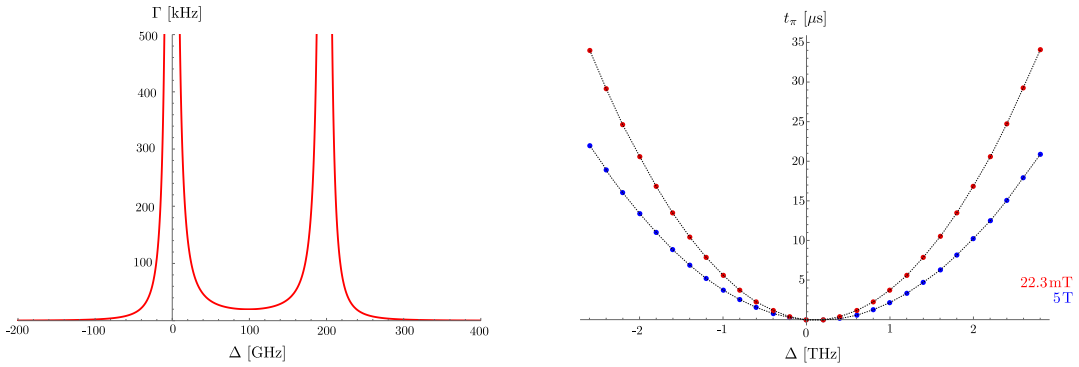

Figure 3.25: Left: Simulation results of the total scattering rate for the superposition of qubit states of the field-independent qubit transition $|\downarrow\rangle = |F = 2, m_F = 1\rangle \leftrightarrow |\uparrow\rangle = |F = 1, m_F = 1\rangle$ at an applied magnetic field of 22.3 mT, calculated for CW beams with 5.0 mW of laser power. Right: Comparison of the dependence of the π-time on the detuning referenced to the $^2P_{1/2}$ line center, calculated for CW beams with 5.0 mW of power for the high field qubit transition at 5 T (blue data points) and the field-independent qubit transition at 22.3 mT (red data points). The dotted lines represent guides to the eye.

shaped pulses as well as for ones being blocked at $\pm 1.5\,\Delta_{\mathrm{FWHM}}$. It can be seen that the minimum required detuning for the low-field qubit is similar to the high-field one for unmodified spectra, whereas it is smaller in case of spectral modification. This is due to a lower scattering rate of the low-field qubit, as shown in Figure 3.25, calculated for CW beams, resulting in a similar behavior of the curve as for pulsed laser beams. The smaller required detuning in general allows for stronger Raman couplings. Nevertheless the low-field qubit also exhibits a lower Raman coupling strength for relevant values of the detuning, as shown in Figure 3.25. In consequence the slope of increasing power with increasing spectral bandwidth in Figure 3.24 is steeper for the low-field qubit. Without spectral control the achievable Raman coupling therefore is significantly reduced for spectral bandwidths exceeding 300 GHz, whereas with spectral pulse shaping, the required power is on the same order of magnitude for both applied magnetic fields in the shown range of spectral bandwidths. The simulation data hence show that in case of implementing spectral modification, the optical frequency comb is a flexible tool allowing for qubit control in multiple magnetic field regimes and for different qubit transitions.

Chapter 4

Raman laser system

In this chapter the development of a narrow-bandwidth ultraviolet (UV) frequency comb providing sufficient power and spectral properties for coherent qubit control of beryllium ions (at 5 T) will be discussed. The system is based on a customized femtosecond optical frequency comb operating near 626 nm, carried out using well established erbium- and ytterbium-fiber technology. The output is then frequency up-converted to the UV in order to generate the desired wavelength near 313 nm. To selectively generate narrow-bandwidth pulses, a nonlinear spectral compression technique is implemented during the second-harmonic generation process into the UV. The method uses the second-order nonlinear process in presence of large temporal walkoff to efficiently transfer the energy of the broadband fundamental femtosecond pulses into narrowband second-harmonic ones. The spatio-temporal coupling, induced by simultaneous spatial walkoff, further allows a simple subsequent spectral pulse shaping in order to selectively screen out the outer-lying parts of the generated UV spectrum. In this chapter the pulsed laser system providing a wavelength near 626 nm, the generation of narrow-bandwidth UV pulses and the following spectral pulse shaping will be separately presented and discussed.

4.1 System overview and requirements

Figure 4.1 shows an overview of the key parts of the Raman system. It is based on an erbium-fiber master oscillator providing a wavelength near 1550 nm. Part of the light is shifted to 1050 nm and is then recombined with the unmodified light in a sum-frequency generation (SFG) unit, leading to an output wavelength near 626 nm. The compression of the spectral bandwidth is controlled during the following second-harmonic generation (SHG), producing the desired UV signal near 313 nm. Subsequently the modification of the spectral pulse shape is carried out.

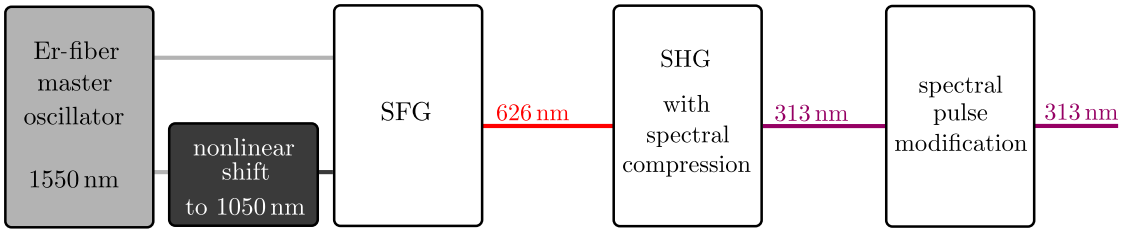

Figure 4.1: Schematical overview of the key parts of the pulsed Raman laser system. Based on a custom-built optical frequency comb generating pulses near 626 nm two further key operations are implemented. The UV-generation with simultaneous control of the spectral bandwidth is implemented during the second-harmonic generation process and followed by the subsequent spectral pulse shaping.

System requirements

The pulsed Raman system is designed to be a versatile tool for qubit control of trapped $^9Be^+$ ions under various experimental conditions. To keep the maximum degree of flexibility, adjustability of the wavelength, the spectral properties and the repetition rate are guaranteed. The required wavelength of the system is determined by the intended detuning during the Raman process. To ensure supressing decoherence induced by off-resonant light scattering for any spectrum, detunings of up to several THz should be accessible. The corresponding wavelength range should hence cover UV wavelenghts of $313\,\text{nm} +/- 0.5\,\text{nm}$. The optimum spectral bandwidth strongly depends on the pulse shape and the resolution of the cutoff when blocking outer-lying spectral components, being close to the atomic resonance. To ensure operating near the optimum range for any experimental condition, the bandwidth should be selectively reducible to values between $\approx 1\,\text{THz}$ and $\approx 300\,\text{GHz}$. In the optimal case the corresponding pulse durations are time-bandwidth limited, leading to temporal durations in the (sub)ps regime. The repetition rate of the laser is chosen to be around 100 MHz. This value arises from the compromise between obtaining high peak intensities and hence high conversion efficiencies during the nonlinear processes and providing a large comb line spacing, corresponding to a large spectral range supporting the realization of motional sideband transitions, as discussed in section 3.2.3. A tunability of the repetition rate is further required in order to not adversely affect motional sideband transitions by accidently fulfilling the carrier resonance condition or harmonics of it. For appropriate Rabi frequencies the average power at the position of the ion should exceed a few mW per beam. Further a high degree of stability of all laser parameters is required, whereas the carrier envelope offset frequency in contrast is irrelevant. An overview of the system requirements is shown in Table 4.1.

parameter	requirement	explanation
λ ; $\Delta\lambda$	$\approx$313 nm ; $\approx$0.5 nm	realize and adjust different Raman detunings of up to 5 THz
f_{rep} ; Δf_{rep}	$\gtrsim$ 100 MHz ; $\gtrsim$ 0.2 MHz	provide and adjust spectral range resolving motional sideband transitions
$\Delta\nu_{\mathrm{FWHM}}$	selective compression down to $\approx$ 300 GHz	optimize ratio of Raman coupling strength and scattering rate
spectral envelope	blocking of outer-lying frequency components	reduce required detuning to maximize Raman coupling strength
P_{av}	$\gtrsim$ few mW at ion	achieve π-times in the order of tens of μs
f_{ceo}	not relevant	comb mode separation relevant, not a common shift

Table 4.1: Overview of the Raman laser system requirements for $^9Be^+$ ion qubit control using an optical frequency comb

4.2 Erbium-fiber based customized frequency comb

In Figure 4.2 an overview of the customized pulsed laser system[1] providing an output wavelength near 626 nm is shown. It is based on an erbium-doped mode-locked fiber laser providing a wavelength near 1550 nm. The length of the fiber ring laser resonator determines the repetition rate of the system according to $f_{\mathrm{rep}} = c/L_{\mathrm{cav}}$ and is set to generate a value near 100 MHz. A piezo-electric actuator and a stepper motor allow to change the resonator length by up to $\pm$ 5 mm leading to a tuning range of the repetition rate of $\approx \pm 0.2$ MHz. The output signal is divided into two paths, from which one part is coupled into a highly nonlinear fiber, where the signal near 1050 nm is generated based on spectral broadening [85]. The frequency-shifted and the unmodified pulses near 1550 nm are then independently amplified according to the chirped pulse amplification scheme, in which the pulses are stretched, amplified and then recompressed in order to lower peak intensities and avoid damages of the gain medium during amplification. To ensure identical optical path lengths in all optical fiber paths, the pulse stretching modules are thermally stabilized. The power in each arm is boosted to levels near 1 W using high-power amplifiers. A high-power erbium-doped fiber amplifier is used for the 1550 nm light and a high-power ytterbium-doped fiber amplifier for the 1050 nm signal. The complete path inside the amplifiers is based on polarization maintaining fibers, ensuring linear polarized output signals. The compressors enable the compensation of second- and third-order group delay dispersion (see section 4.3.1). The design is based on high efficiency transmission gratings and prisms. For the erbium-based path, pulses with temporal durations around 400 fs and spectral widths around

[1] fabricated by Menlo Systems GmbH

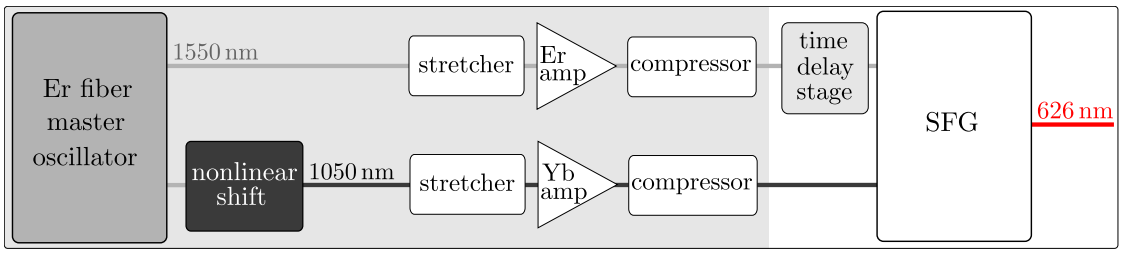

Figure 4.2: Schematical view of the erbium-fiber based custom-built laser system. The system is based on a single master oscillator operating near 1550 nm. Part of the light is shifted to 1050 nm and recombined with the unmodified pulses in a sum-frequency generation process, generating pulses near 626 nm. To enhance the output power level, the infrared pulses are separately amplified according to the chirped pulse amplification scheme and synchronized in time.

12 nm are achieved, while the frequency-shifted arm at 1050 nm generates pulses with durations around 100 fs and spectral widths around 27 nm. The compressed free space output signals at 1050 nm and 1550 nm are then overlapped using a dichroic mirror and focused into a nonlinear crystal for sum-frequency generation leading to the output signal near 626 nm. The periodically poled lithium niobate (PPLN) crystal is located inside a heated oven. By tuning the temperature, the output wavelength can be set in a range between 623 nm and 628 nm. To ensure an efficient conversion process, both fundamental signals are synchronized in time and in space. For adjustment of the temporal overlap a time delay stage is implemented. Any relative change of the optical beam path lengths affects the SFG process and hence the output signal at 626 nm. To support stable operation, the temperature of the baseplate is stabilized by water-cooling to 25 °C.
The average output power at 626 nm is up to $P_{\mathrm{av}} \approx 450\,\mathrm{mW}$, corresponding to a pulse energy of $E_{\mathrm{p}} = P_{\mathrm{av}}/f_{\mathrm{rep}} \approx 4.5\,\mathrm{nJ}$. A simple approximation of the pulse duration is obtained by measuring the power generated during SFG as a function of the delay stage position, controlling the temporal overlap between the fundamental signals at 1050 nm and 1550 nm. The results are shown in Figure 4.3. The delay stage consists of two orthogonally aligned prisms mounted on a linear translation stage. A linear translation of the stage corresponds to a change of the optical beam path length Δl_{opt} by a factor of two with respect to its movement. Assuming the simple relation $\tau_{\mathrm{p}} \approx \Delta l_{\mathrm{opt}}/c$, the measured data yield an estimated full width half maximum pulse duration in the range of $\approx 420\,\mathrm{fs}$. Sample spectra for different temperatures of the PPLN crystal are shown in Figure 4.4. The peak wavelength is shifted for the different temperatures, whereas the spectrum is nearly unaffected. Its shape exhibits substantial, asymmetric sidelobes and the spectral bandwidth is $\Delta\lambda \approx 1\,\mathrm{nm}$.

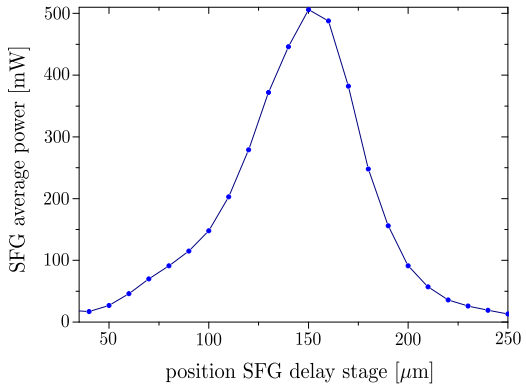

Figure 4.3: Average laser power at 626 nm generated during the sum-frequency generation as a function of the absolute delay stage position, controlling the temporal overlap between the fundamental signals at 1050 nm and 1550 nm. The solid line is a guide to the eye.

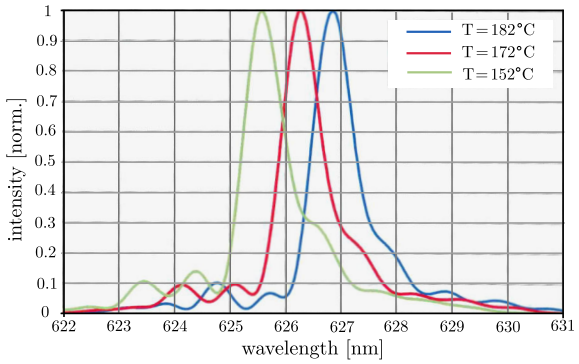

Figure 4.4: Sample spectra at 626 nm for different crystal temperatures of the PPLN crystal. The peak wavelength is shifted, whereas the spectral shape is approximately unaffected. The spectral bandwidth is $\Delta\lambda \approx 1\,\mathrm{nm}$.

4.3 UV generation and spectral compression

In this section the generation of narrow-bandwidth UV pulses will be discussed. The implementation is carried out by nonlinear effects simultaneously occurring inside a nonlinear bismuth triborate (BiBO) crystal. For the generation of the UV light, phase-matching conditions for frequency doubling of the output signal near 626 nm of the previously described laser system are fulfilled by critical phase matching. By choosing crystals of different lengths in combination with different focusing strengths, the spectral bandwidth of the generated UV pulses is simultaneously selectively compressed during the conversion process. The effect is based on controlling the temporal broadening of the generated pulses, occurring due to the group velocity mismatch (GVM) between the fundamental and the second-harmonic

signal, being directly accompanied by a spectral compression. Efficient energy transfer from the broadband fundamental pulses into narrowband second-harmonic ones is achieved by simultaneously occurring intrapulse sum-frequency generation (SFG) within the frequency comb structure. This compression technique has first been demonstrated in [86] for the generation of narrow-bandwidth pulses in the visible spectral region. Here the technique has been extended into the UV region. In addition, the influence of substantial spatial walkoff and resulting spatio-temporal effects has been investigated for the first time. In this chapter basics of nonlinear and ultrashort optics will be reviewed, details on the spectral compression technique presented and simulations as well as experimental results of a systematic survey discussed.

4.3.1 Basics of nonlinear and ultrafast optics

In this section relevant basics of ultrashort laser pulses and pulse propagation in nonlinear media will be introduced, required to understand the spatio-temporal coupling effects, inducing the spectral compression presented in 4.3.2. In addition, relevant basics on nonlinear frequency conversion with pulsed lasers are summarized. Derivations and further details of pulsed and nonlinear optics can e.g. be found in [87] and [88].

Pulse propagation in dispersive media

Ultrashort laser pulses are mathematically described either in the time domain or in the frequency domain. Both descriptions are equivalent and coupled via Fourier transformation. In the time domain the propagation of an electromagnetic wave at a fixed position in space is in general described by the time-dependent electric field $E(t)$, which is composed of a time-dependent envelope $E_0(t)$ and a carrier wave with carrier frequency ω_0 and temporal phase $\phi(t)$. The complex representation is given by

$$E(t) = E_0(t)e^{i(\omega_0 t+\phi(t))} + c.c.\,, \tag{4.1}$$

whereas the electric field $E(t)$ is always real and c.c. denotes the complex conjungate. The spectral profile is given by

$$\tilde{E}(\omega) = \tilde{E}_0(\omega-\omega_0)e^{-i(\phi(\omega-\omega_0))} + c.c.\,, \tag{4.2}$$

with $\phi(\omega-\omega_0)$ being the spectral phase. The spectral phase is of special relevance for describing nonlinear dispersion effects, as they occur for example during propagation through nonlinear crystals. For an analytic description a Taylor expansion of the spectral phase $\phi(\omega)$ for a fixed position z_0 is performed:

$$\phi(\omega) = \phi_0 + \phi_1\frac{\omega-\omega_0}{1!} + \phi_2\frac{(\omega-\omega_0)^2}{2!} + ... \tag{4.3}$$

The zero-order phase ϕ_0 is the absolute phase between the envelope and the oscillating carrier wave. The linear phase $\phi_1 = \frac{d\phi}{d\omega}|_{\omega=\omega_0}$ is called group delay, GD, and corresponds to a delay in time without affecting the pulse shape. The second-order term $\phi_2 = \frac{d^2\phi}{d\omega^2}|_{\omega=\omega_0}$ is called group delay dispersion, GDD, and describes the second-order dispersion, which in general causes a pulse modification during propagation through a nonlinear medium.
The nonlinear interaction of ultrashort laser pulses with the medium they are propagating through causes a phase distortion, where the spectral phase of the output light is given by the sum of the initial spectral phase and the spectral phase due to the medium. The additional spectral phase term due to the medium (m) is given by

$$\phi_{\mathrm{m}}(\omega) = k(\omega)L, \tag{4.4}$$

with $k(\omega)$ denoting the frequency-dependent wavevector and L the lenght of the nonlinear medium. Dispersion effects are typically described by the frequency-dependent wavevector

$$k(\omega) = \frac{\omega\, n(\omega)}{c}\,, \tag{4.5}$$

where $n(\omega)$ is the frequency-dependent index of refraction. The Taylor expansion of the phase due to the medium $\phi_{\mathrm{m}}(\omega)$, equivalent to Equation 4.3, therefore becomes:

$$k(\omega)L = k(\omega_0)L + k'(\omega_0)(\omega-\omega_0)L + \frac{1}{2}k''(\omega_0)(\omega-\omega_0)^2L + ... \tag{4.6}$$

The zero-order term corresponds to ϕ_0 and is related to the phase velocity v_{ph} by $k(\omega_0) = \dfrac{\omega_0}{v_{\mathrm{ph}}(\omega_0)}$. The phase velocity is the velocity of the carrier wave and given by the velocity with which the phase fronts propagate in a medium:

$$v_{\mathrm{ph}} = \frac{c}{n(\omega)} \tag{4.7}$$

The first-order term corresponds to ϕ_1 and is related to the group velocity by $k'(\omega_0) = \dfrac{1}{v_{\mathrm{gr}}(\omega_0)}$. The group velocity v_{gr} is the velocity with which the wave packet envelope propagates in a medium. It is given by:

$$v_{\mathrm{gr}} = \frac{d\omega}{dk} = \frac{1}{\dfrac{n(\omega)}{c} + \dfrac{\omega}{c}\dfrac{dn(\omega)}{d\omega}} = \frac{v_{\mathrm{ph}}}{1 + \dfrac{\omega}{n(\omega)}\dfrac{dn(\omega)}{d\omega}} \tag{4.8}$$

As the refractive index $n(\omega)$ depends on the frequency ω, the phase and group velocities in general differ inside a medium. For normal dispersion, where n increases with ω, the phase velocity is larger than the group velocity.
The second-order term in Equation 4.6 corresponds to ϕ_2, where $k''(\omega) = \dfrac{d(\frac{1}{v_{\mathrm{gr}}})}{d\omega}$ is

called group velocity dispersion, GVD. It describes the phenomenon that the group velocity in a medium depends on the optical frequency and is typically expressed in terms of the wavelength by $k''(\omega) = \frac{\lambda_0^3}{2\pi c^2}\frac{d^2n}{d\lambda^2}$. Due to the broad spectral bandwidth of pulsed lasers, this term is responsable for dispersive temporal distortion of the envelope during propagation in nonlinear media. The effect is accompanied by a linear frequency variation called chirp. A positive chirp corresponds to normal dispersion (GVD > 0) where the red components contained in a spectrum travel faster than blue components, leading to a temporal broadening of the pulse. To generate a negative chirp, as required for compensating the pulse broadening, the use of prism or grating pairs or special customized mirrors is necessary.
Also higher-order dispersion effects occur, which are not relevant for this work.

Time-bandwidth product

Due to the Fourier connection between the time and frequency domain, the spectral bandwidth and the pulse duration are inversely proportional. This yields the general relation that the shorter the pulse duration, the broader the spectrum and vice versa. The product of the time-domain width Δt and the frequency-domain width $\Delta\nu$ is given by the time-bandwidth product

$$TBP \equiv \Delta t \cdot \Delta\nu\,, \tag{4.9}$$

where the value depends on the specific pulse shape. In the full width half maximum definition, the TBP for a squared hyperbolic secant (sech) pulse shape is for example ≈ 0.315 and for a gaussian-shaped pulse ≈ 0.441. A pulse which exhibits a pulse duration at its lower limit according to the characteristic TBP of its spectrum is called fourier-transform-limited. In this case it possesses a frequency-independent spectral phase and therefore does not contain a chirp. Introducing a spectral compression is always accompanied by a temporal broadening, with the minimal pulse duration given by the corresponding TBP. In contrast, a temporal pulse broadening caused by the influence of second-order nonlinear dispersion is not accompanied by a spectral compression.

Nonlinear frequency conversion with pulsed lasers

Nonlinear frequency conversion describes the process where two photons of an electromagnetic wave propagating through a suitable nonlinear medium can mix together and generate a coherent output photon at higher harmonics, sum frequencies and difference frequencies of the fundamental ones. The effect arises from the nonlinear response of the medium to the electric field E of an intense optical wave. The electric field excites dipole moments of the material to oscillate, which

induces a polarization. For low fields the induced polarization depends linearly on E. For high excitation intensities, it nonlinearly depends on E and the dipoles can oscillate with a nonlinear response and radiate energy at higher frequencies than the original one. This phenomenon is in good approximation described by a Taylor series expansion of the induced dielectric polarization density P in terms of the electric field E,

$$P = \epsilon_0[\chi^{(1)}E + \chi^{(2)}E^2 + \chi^{(3)}E^3 + ...]\,, \tag{4.10}$$

where ϵ_0 is the vacuum permittivity and $\chi^{(k)}$ the optical susceptibility of k-th order. The polarization density and the electrical field are considered as scalars for simplicity. In this work second-order processes are relevant, where the induced polarization depends quadratically on the field strength and the magnitude of the nonlinear response of the crystal is described by $\chi^{(2)}$. $\chi^{(2)}$ is a third-order tensor, where the entries correspond to several possible orientations of the crystal axes and the polarization of the propagating light. For a known nonlinear medium and for a given working direction and polarization, all entries are known and the scalar, effective susceptibility χ_{eff} indicates the second-order conversion properties of the material. Often the nonlinear properties are instead expressed in terms of the effective nonlinear coefficient d_{eff}, which originates from a tensor of second order being derived from $\chi^{(2)}$ due to symmetry considerations.

Assuming an electric field to be composed of two monochromatic sources with frequencies ω_1 and ω_2 it can be written as $E(t) = E_1 e^{i\omega_1 t} + E_2 e^{i\omega_2 t} + c.c.$, where *c.c.* stands for the complex conjungate. The second-order polarization term of Equation 4.10 is then given by:

$$P^{(2)} = \epsilon_0\chi^{(2)}[E_1^2 e^{i2\omega_1 t} + E_2^2 e^{i2\omega_2 t} + 2E_1E_2e^{i(\omega_1+\omega_2)t} + 2E_1E_2e^{i(\omega_1-\omega_2)t} + c.c.] + \text{OR} \tag{4.11}$$

The oscillatory components in the first two terms in particular contain a new frequency at the double of the fundamental frequencies. The generation of these frequencies is known as second-harmonic generation, SHG. The third term refers to a sum-frequency generation, SFG, leading to a new frequency given by the sum of the driving ones. The difference frequency in the forth term describes the process of difference frequency generation, DFG, respectively. OR stand for optical rectification presenting non-oscillatory terms. All processes can be generated, whereas they in general do not occur simultaneously due to material property and phase-matching aspects.

Phase matching

For efficient generation of any second-order frequency conversion process, phase matching between the fundamental frequency (FF) beams and the generated signal (SIG) beam must be achieved. Only for perfect phase matching, given by $k_{\text{SIG}} = k_{\text{FF}}$,

all generated signal contributions, from all oscillating dipoles at different positions within the nonlinear crystal, coherently add up. In lowest order, this requires that the generated signal field and the fundamental fields have the same phase velocity inside the medium, $v_{\mathrm{ph,FF}} = v_{\mathrm{ph,SIG}}$. According to Equation 4.7 this is equivalent to them having the same refractive indices $n_{\mathrm{FF}} = n_{\mathrm{SIG}}$. For materials exhibiting normal dispersion, where n increases with the frequency, this condition cannot be satisfied.

Critical phase matching

The most common way to achieve phase matching is to use birefringent crystals. Such crystals exhibit two different indices of refraction, typically denoted as the ordinary refraction index n_{o} and extraordinary refractive index n_{e}, depending on the polarization and propagation direction of the beam. The direction of the ordinary beam, denoted by the unity vector $\vec{n}_{\mathrm{o}}$, is defined by the dielectric polarization with refractive index n_{o} being invariant on the orientation of the direction of the wavevector $\vec{k}$ within a principle plane of the crystal. The refractive index of the extraordinary beam in contrast depends on the propagation direction. Its dielectric polarization, specifying the direction of the extraordinary beam given by the unity vector $\vec{n}_{\mathrm{e}}$, is orthogonal to $\vec{k}$ and to $\vec{n}_{\mathrm{o}}$. The corresponding extraordinary refractive index n_{e} is given by the coordinate on the index ellipsoid [88, 89]. Due to the sensitive angle tunability of the extraordinary index of refraction this technique is called angle or critical phase matching.
Based on this behaviour various situations can be implemented allowing to match the refractive indices of the FF beams and the signal beam, depending on the specific birefringent crystal. In uniaxial crystals, one main crystal axis can be identified providing the optical anisotropy, called optic axis. Such crystals can be either positive or negative uniaxial. For positive crystals, with $n_{\mathrm{e}}(\omega) > n_{\mathrm{o}}(\omega)$, type I phase matching can be achieved by implementing $n_{\mathrm{e}}(\omega_{\mathrm{FF}}) = n_{\mathrm{o}}(\omega_{\mathrm{SIG}})$. For negative crystals, with $n_{\mathrm{o}}(\omega) > n_{\mathrm{e}}(\omega)$, polarizations and crystal orientation must be chosen to fulfill $n_{\mathrm{o}}(\omega_{\mathrm{FF}}) = n_{\mathrm{e}}(\omega_{\mathrm{SIG}})$. The type of the conversion process is specified depending on the polarization of the fundamental beams. In type I, as relevant for this work, the two fundamental mixing photons have the same polarization, whereas in type II they are orthogonally polarized.
Biaxial crystals, as applied in this work, in constrast to uniaxial crystals have three different refractive indices in all main crystal directions and no single crystal axis can be identified providing the optical anisotropy. The assignment of ordinary and extraordinary directions in the crystal is hence in general not useful. Nevertheless, if phase matching is achieved with a propagation direction being within one of the main crystal planes, two refractive indices can be identified analogous to the case of uniaxial crystals. In this working plane the crystal can be described to behave as a positive or a negative crystal. The angle fulfilling the respective phase-matching

condition is typically denoted as Θ and encloses the beam propagation direction given by the wavevector $\vec{k}$ and the main crystal direction providing the optical anisotropy for the specific working plane.

Temporal walkoff and spectral acceptance range

A perfect phase matching with mismatch of $\Delta k = 0$ can only be achieved for a single frequency. The spectral acceptance range, in which phase matching can be realized, is limited due to chromatic dispersion. In first order, this limitation is based on different group velocities between the fundamental beam and the generated signal beam, which is called group velocity mismatch, GVM, and for SHG is given by:

$$GVM = \frac{1}{v_{\mathrm{gr}_{\mathrm{FF}}}} - \frac{1}{v_{\mathrm{gr}_{\mathrm{SH}}}} \tag{4.12}$$

As result, the involved frequency components, which initially are overlapping in time, lose their temporal overlap after some propagation distance. This effect is called temporal walkoff and in general limits the effective interaction length and hence conversion efficiencies. Therefore typically crystal lengths are chosen, which ensure temporal overlap over the entire length. An estimation for this is to ensure that the temporal separation δt due to the GVM stays smaller than the pulse duration τ_{p}, according to $\delta t \ll \tau_{\mathrm{p}}$. The limit concerning the crystal length arising due to the temporal walkoff described in the time-domain, is directly related to the limited acceptance range, which denotes the limitations in the frequency domain description. A simple approximation of the spectral acceptance range is hence given by the Fourier transform of δt.
A more accurate derivation of the spectral acceptance range, including also higher dispersion orders, can be obtained from the wavevector mismatch Δk of the nonlinear process. The intensity of the generated signal can be shown to be proportional to the phase mismatch factor $\mathrm{sinc}^2(\Delta k \cdot L/2)$, where L denotes the crystal length [88]. Tolerating a drop of intensity of 50 % yields the following condition for the wavevector difference:

$$\frac{|\Delta k| \cdot L}{2} \leq 0.886\,\pi \tag{4.13}$$

With $0.886\,\pi$ denoting the full width half maximum of the phasemismatch factor. The corresponding spectral acceptance range is obtained by calculating the wavevector mismatch Δk and resolving the spectral bandwidth.

Spatial walkoff

A further limitation concerning the useful interaction length in birefringent crystals is given by the fact that the propagation direction of the intensity distribution, given by the Poynting vector, of the extraordinary beam can differ from the direction of its wavevector, denoting the normal of the wavefronts. This phenomenon is

related to the angle dependence of the extraordinary refractive index and does therefore not occur for the ordinary beam. For this beam the energy transport is always along the beam axis being defined by its wavevector. As result the energy flux of the fundamental beam and the generated beam will spatially drift away from each other during propagation through the crystal. The angle between the directions of energy transport of the beams is given by $\rho = -\frac{1}{n_\mathrm{e}}\frac{\partial n_\mathrm{e}}{\partial \theta}$, where n_e is the extraordinary refractive index and θ the phase-matching angle, being enclosed by the direction of the wavevectors $\vec{k}$ and the optic axis of the crystal [90]. This effect is called spatial walkoff and related to an angular acceptance range. The effective interaction length depends on the beam size and decreases with smaller the beam extensions. As a result the conversion efficiency drops and the spatial beam profile may be broadened and the beam quality reduced.

Quasi phase matching

Spatial walkoff can be avoided by using non-critical phase-matching techniques, which do not depend on angle tuning in birefringent crystals. A so-called quasi phase matching can be achieved with periodically poled crystals. Such crystals face the problem of wavevector mismatch by periodically introducing a phase jump of π between the polarizations of the fundamental and the generated signal, with a period being matched to the coherence length $l_\mathrm{c} = \frac{\pi}{\Delta k}$. Whereas for non-periodically poled crystals the constructive add-up of the generated signal converts into a destructive one after a propagation length of l_c, the implemented phase jump in periodically poled crystals resets the phase mismatch between the fundamental field and the generated field to zero after each time traveling the distance of the coherence length. The implementation of the phase jump is realized by converting the orientation of the crystal, such that the sign of the nonlinear coeefficient d_eff is alternating between positive and negative between each poling period. By this also the direction of spatial walkoff is inverted, whereby spatial overlap between the fundamental and the generated signal can be obtained over long distances. The results which can be achieved with this technique do not conform to the case of perfect phase matching, wherefore it is called quasi phase matching, but it allows the signal of the generated light to grow monotonically over the entire length of the crystal. For the generation of wavelengths near 313 nm the required poling period is $\approx 1\,\mu$m. Crystals with such small period are commercially not available. Alternatively operating with higher-order periods is possible, for example for UV generation when using five times the typical poling period. Since the achievable conversion efficiency is reduced respectively, the technique of quasi phase matching is not profitable for UV generation in the spectral region of interest.

4.3.2 Spectral compression process

Optical frequency combs based on the well established fiber technology typically provide broadband femtosecond pulses. As several applications exist which require narrow-bandwidth pulses, such as many time-resolved spectroscopy experiments [91, 92], a broad variety of spectral compression methods have been investigated in the past [93, 94, 95]. Whereas simply increasing the pulse duration, by generating a temporal delay between different frequency components, is not accompanied by spectral compression, a straightforward method to obtain a narrow spectrum is to apply linear operations, as for example a narrow-bandpass filter [96] or a slit in the Fourier plane of a zero-dispersion $4f$ pulse shaper [97]. Linear techniques are however very inefficient, as the loss of energy is approximately proportional to the amount of spectral narrowing. Non-linear techniques instead allow to transfer a large amount of the energy of broadband pulses into narrowband ones. The technique applied in this work follows the method which has been demonstrated by M. Marangoni and G. Cerullo [86] for a generated wavelength range of 720 nm to 890 nm. The simple method uses the SHG process in presence of large group velocity mismatch to generate narrowband SH pulses derived from broadband FF ones. Efficient results have been obtained with long periodically poled crystals. For implementing the technique to our research an extension of the wavelength range into the UV has been realized for specific laser parameters. One challenge arises from the fact that for frequency doubling into the UV, practical solutions to directly avoid spatial walkoff are lacking. Because of this, the influence of spatial walkoff onto the spectral narrowing process had to be taken into account for the first time, substantially influencing the process due to spatio-temporal coupling dynamics.

Spectral compression without spatial walkoff

The spectral compression technique during the second-harmonic generation, without appearance of spatial walkoff, can be easily understood in the time-domain picture. The spectral compression directly results from the temporal broadening of the generated signal, occurring due to the temporal walkoff between the fundamental pulse (FF) and the second-harmonic pulse (SH) inside the nonlinear crystal. When the fundamental pulse enters the crystal it will generate a SH pulse, if phase-matching conditions for SHG are fulfilled. At this moment the FF and SH pulses overlap in time. When the FF pulse has traveled through the crystal and exits the end facet, the initially generated SH pulse lags behind in time due to its smaller group velocity about

$$\delta t \approx |GVM| \cdot L\,, \tag{4.14}$$

with the crystal length L and the group velocity mismatch GVM. As the FF pulse continuously generates a SH wave while traveling through the crystal, this

temporal separation corresponds to the temporal width of the resulting SH signal, as depicted in Figure 4.5:

$$\delta t \approx \Delta t_{\mathrm{SH}} \tag{4.15}$$

The Fourier transform of this broad temporal pulse directly yields the narrow spectrum. The spectral compression is hence directly linked to the amount of temporal broadening of the generated SH signal.
Without the appearance of spatial walkoff the resulting SH temporal pulse profile is approximated to be rectangularly shaped due to the one dimensional temporal broadening as illustrated in Figure 4.5. The resulting width of the corresponding spectrum is therefore given by [98, 86]:

$$\Delta\nu_{\mathrm{SH}} \approx \frac{0.886}{|GVM| \cdot L} \tag{4.16}$$

The spectral bandwidth of the generated SH pulse hence depends on the GVM and the crystal length L. The longer the crystal and the higher the GVM, the narrower the output spectrum. The approximation of a rectangular temporal profile also determines the SH spectral shape, which in this case is given by a sinc-shaped spectrum.

The spectral width, given by Equation 4.16, approximately also specifies the spectral acceptance range of the SHG process. It corresponds to a wavevector mismatch of $\Delta k_{\mathrm{SHG}} = 2k(\omega_{\mathrm{FF}}) - k(\omega_{\mathrm{SH}}) = |GVM| \cdot \Delta\omega$, which can be derived by applying a Taylor series expansion of each wavevector and letting the wavevector of the FF vary by $\Delta\omega/2$ and hence the one of the SH vary by $\Delta\omega$ [86]:

$$k_{\mathrm{FF}}(\omega) = k(\omega_{\mathrm{FF}}) + k'(\omega_{\mathrm{FF}})\frac{\Delta\omega}{2} \tag{4.17}$$

$$k_{\mathrm{SH}}(\omega) = k(\omega_{\mathrm{SH}}) + k'(\omega_{\mathrm{SH}})\Delta\omega \tag{4.18}$$

Inserting the resulting wavevector mismatch Δk_{SHG}, with $|GVM| = |k'(\omega_{\mathrm{FF}}) - k'(\omega_{\mathrm{SH}})|$, into Equation 4.13 and resolving the spectral width, the SHG phase matching bandwidth can be derived:

$$\Delta\nu_{\mathrm{SHG}} \approx \frac{0.886}{|GVM| \cdot L} \tag{4.19}$$

This width denotes the spectral components for which critical phase matching can be simultaneously achieved. As a consequence of this limited acceptance range, frequency doubling of broad spectra is typically performed using short crystals featuring a low GVM. Here, on purpose, long crystals with large GVM are chosen, such that the acceptance range, and hence the resulting SH output bandwidth, equals the desired narrow SH bandwidth.

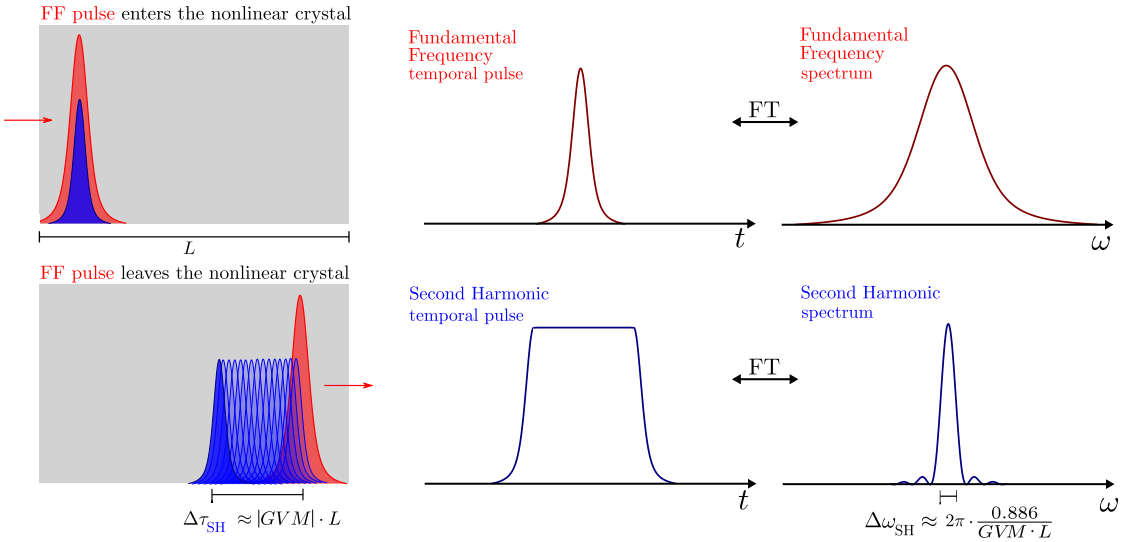

Figure 4.5: Schematical illustration of the spectral compression process during second-harmonic generation without spatial walkoff. If phase-matching conditions are fulfilled, the fundamental frequency pulse (FF), shown in red, continuously generates a second-harmonic wave (SH), shown in blue, while travelling through the nonlinear crystal. Due to the smaller group velocity, the second-harmonic signal lags behind in time about $\delta t = GVM \cdot L$ at the moment when the fundamental pulse exits the nonlinear crystal. This temporal separation corresponds to the temporal broadening of the generated SH signal, $\Delta\tau_{\mathrm{SH}}$, which is directly accompanied by a spectral compression, as shown on the right.

In terms of the SHG process therefore only a small fraction of the FF pulse is used and converted into the SH one for the generation of narrow spectra. Based on this, a very low conversion efficiency would be expected. However, to the first order also phase matching for intrapulse sum-frequency generation is fulfilled, generating the same frequencies as resulting from the frequency doubling, as depicted in Figure 4.6. The second-harmonic frequency, $\omega_{\mathrm{SH}} = 2\omega_{\mathrm{pm}}$, with pm denoting the phasematched fundamental center frequency, is for the SHG process generated by:

$$\omega_{\mathrm{pm}} + \omega_{\mathrm{pm}} = 2\omega_{\mathrm{pm}} \tag{4.20}$$

With the fundamental frequency $\omega_{\mathrm{FF}} = \omega_{\mathrm{pm}}$. The corresponding phase-matching condition

$$k(\omega_{\mathrm{pm}}) + k(\omega_{\mathrm{pm}}) = k(2\omega_{\mathrm{pm}}) \tag{4.21}$$

is assumed to be fulfilled. The intrapulse SFG process generates the same frequency $\omega_{\mathrm{iSF}} = 2\omega_{\mathrm{pm}} = \omega_{\mathrm{SH}}$ by mixing spectral components of the FF spectrum which are symmetric around the phase-matching frequency ω_{pm} about $\pm\Delta\omega$:

$$(\omega_{\mathrm{pm}} + \Delta\omega) + (\omega_{\mathrm{pm}} - \Delta\omega) = 2\omega_{\mathrm{pm}} \tag{4.22}$$

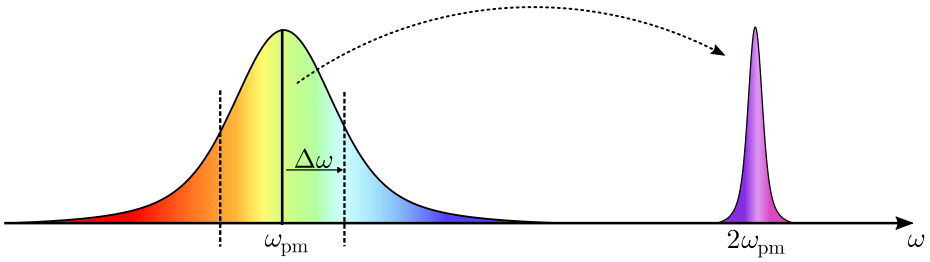

Figure 4.6: Schematical representation of the energy transfer of broadband fundamental pulses into narrowband, frequency-doubled pulses in presence of SHG and intrapulse SFG. The SH frequency $\omega_{\mathrm{SH}} = 2\,\omega_{\mathrm{pm}}$ with pm denoting the phasematched fundamental center frequency is generated by $\omega_{\mathrm{pm}} + \omega_{\mathrm{pm}} = 2\,\omega_{\mathrm{pm}}$ for the SHG and by $(\omega_{\mathrm{pm}} + \Delta\omega) + (\omega_{\mathrm{pm}} - \Delta\omega) = 2\,\omega_{\mathrm{pm}}$ for the intrapulse SFG.

The SFG phase-matching condition

$$k(\omega_{\mathrm{pm}} + \Delta\omega) + k(\omega_{\mathrm{pm}} - \Delta\omega) = k(2\omega_{\mathrm{pm}}) \tag{4.23}$$

is approximately simultaneously fulfilled.
The corresponding phase-matching acceptance bandwidth can be derived from the wavevector mismatch of the process. Applying the following Taylor series expansions of the corresponding mixing wavevectors with frequencies $\omega_1 = \omega_{\mathrm{pm}} + \Delta\omega$ and $\omega_2 = \omega_{\mathrm{pm}} - \Delta\omega$,

$$k(\omega_1) = k(\omega_{\mathrm{FF}}) + k'_{\mathrm{FF}}\Delta\omega + \frac{1}{2}k''_{\mathrm{FF}}\Delta\omega^2 + ... \tag{4.24}$$

$$k(\omega_2) = k(\omega_{\mathrm{FF}}) - k'_{\mathrm{FF}}\Delta\omega + \frac{1}{2}k''_{\mathrm{FF}}\Delta\omega^2 + ...\,, \tag{4.25}$$

the wavevector mismatch Δk_{SFG} is found to be [86]

$$\Delta k_{\mathrm{SFG}} = k(\omega_1) + k(\omega_2) - k(\omega_{\mathrm{SH}}) \approx k''_{\mathrm{FF}}\Delta\omega^2\,, \tag{4.26}$$

with k''_{FF} denoting the group velocity dispersion of the fundamental frequency. From this the spectral acceptance range for the intrapulse SFG process can be derived according to Equation 4.13:

$$\Delta\nu_{\mathrm{SFG}} \approx \sqrt{\frac{0.886}{2\pi L k''_{\mathrm{FF}}}} \tag{4.27}$$

This acceptance range of intrapulse SFG is typically broader than the acceptance range of the simultaneously occurring SHG process, wherefore this spectral compression technique allows to effciently convert broadband FF pulses into frequency

doubled narrowband pulses. The width of the resulting SH pulses is determined by the acceptance range of the SHG process, which approximately equals the corresponding bandwidth of the resulting SH spectrum.
This spectral compression method has been successfully demonstrated for the generation of narrow-bandwidth pulses in the visible region [86]. Efficient results have been achieved with long periodically poled crystals, which are effectively free of spatial walkoff and therefore guarantee an overlap of the SH and the FF pulses over the entire crystal length. As discussed in section 4.3.1 for the generation of UV light near 313 nm no practical solutions exist to directly avoid spatial walkoff. The spatial walkoff and the resulting spatio-temporal coupling effects strongly influence the compression process and have to be taken into account in order to selectively and effciently generate narrow-bandwidth UV pulses.

Spectral compression with spatial walkoff

In the presence of spatial walkoff, the FF and the SH pulses not only lose overlap due to the temporal walkoff between them because of their different group velocities, they are further separated in space due to their different propagation directions based on spatial walkoff. This strongly affects the resulting SH pulse profile during the SHG and hence also the spectral compression process. In general less temporal broadening and therefore less spectral compression can be achieved for the same crystal length, compared to the case without spatial walkoff. Furthermore the resulting SH temporal shape gets distorted and cannot be approximated by a rectangular pulse shape anymore. Due to the different propagation directions, combined with the different group velocities, the resulting SH profile experiences a pulse front tilt [99], as shown in Figure 4.7.
The generation of the temporal SH profile including the influence of spatial walkoff can be understood in the time-domain picture, analogous to the simple picture presented in Figure 4.5. When the FF pulse enters the crystal it will generate a SH pulse, if phase-matching conditions for SHG are fulfilled. At this moment the FF and SH pulses overlap in time and in space. When the FF pulse has traveled through the crystal along its direction of propagation and exits the crystal end facet, the initially generated SH pulse lags behind in time due to its smaller group velocity. Due to the different propagation direction compared to the FF, the initially generated SH pulse is not only located at a different position along the direction of propagation, it is also located at a different transverse position inside the nonlinear crystal. As the FF pulse continuously generates SH waves while traveling through the crystal, the combination of temporal and spatial walkoff causes a tilted pulse front of the generated SH signal when leaving the nonlinear crystal.

The precise temporal profile not only depends on the walkoff angle ρ, the GVM and the propagation distance of the FF inside the nonlinear crystal. Furthermore

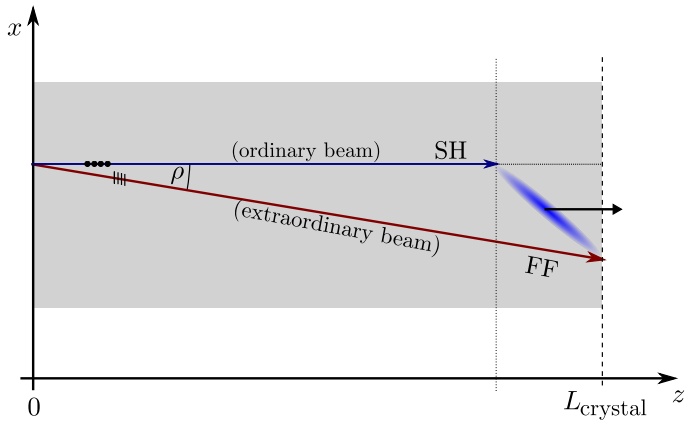

Figure 4.7: Schematical illustration of the generation of the pulse front tilt of the second harmonic (SH) signal, caused by simultaneous spatial and temporal walkoff during the SHG. The initial FF propagation direction and hence the direction of both wavevectors of the FF and SH inside the crystal is denoted as z-direction. The perpendicular orientation of the nonlinear crystal, in which the direction of the spatial walkoff takes place, is denoted as the x-direction. The fundamental beam direction is shown in red and experiences a spatial walkoff about the angle ρ compared to the propagation direction of the SH beam, shown in blue. The combination of different propagation directions and different group velocities between the FF and the generated SH signal leads to a tilted pulse front of the SH signal when leaving the nonlinear crystal, indicated by the blue ellipse.

the focusing strength is of great importance, influencing the temporal profile by affecting the effective interaction length between the FF and SH signal. Whereas in the case without spatial walkoff the interaction length is independent of the focusing strength, leading to the same spectral results for any focusing conditions, the interaction length is in general reduced by the effect of spatial walkoff. The limitation of the interaction length becomes the stronger, the tighter the focusing is. For weak focusing, corresponding to large beam sizes, the interaction length is larger, whereas in the limit of very large beam sizes an interaction over the entire crystal length can possibly be achieved, approximately leading to similar results as in the case without spatial walkoff.
A comparison of the resulting SH temporal pulse fronts for the two cases of tight focusing and weak focusing are exemplarily shown in Figure 4.8. It can be seen that the resulting SH pulse profiles differ in space and in time for the compared focusing strengths. In consequence also their spectra given by the corresponding 2D Fourier transformation will differ and hence the amount of spectral compression. This focusing dependency, induced by the additional spatial walkoff, cannot be neglected and is a substantial difference compared to previous work presented in [86] and has been investigated for the first time in the framework of a prestudy as presented in the next section.

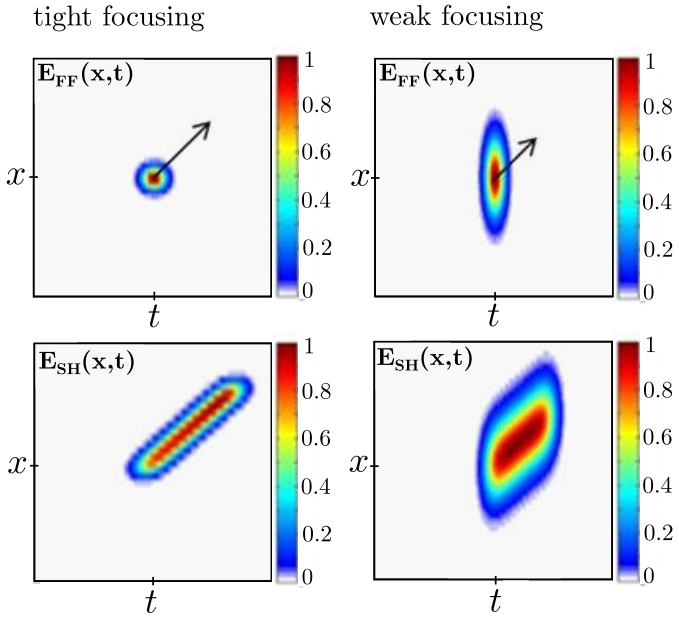

Figure 4.8: Schematical demonstration of the influence of the focusing strength of the FF pulse during SHG on the pulse front of the generated SH signal. The upper two pictures represent the electric field of the fundamental frequency (FF) pulse in a space-time (x, t) diagram, $E_{\mathrm{FF}}(x, t)$, when entering the nonlinear crystal. The arrows indicate the direction of propagation and its length the propagation distance according to the length of the nonlinear crystal. The FF beam is assumed to experience the spatial walkoff, wherefore the arrow is tilted against the time axis t. The left picture presents the case of tight focusing, indicated by a small extension of the FF field along the space axis x. The right picture shows the case of weak focusing respectively. Below the corresponding generated electric fields of the second-harmonic (SH) pulse profiles are shown, $E_{\mathrm{SH}}(x, t)$, as they have built up at the time when the FF pulse exits the nonlinear crystals. The differing SH profiles in space and in time are accompanied by different spectra and hence different amounts of spectral compression.

4.3.3 Simulations and experimental results

In order to be able to efficiently and selectively generate narrow-bandwidth UV pulses near 313 nm despite the substantial, so far unexplored influence of spatial walkoff, a systematic study has been carried out. Based on simulation results, spectral compression induced in nonlinear BiBO crystals of different shape and with different lengths have been investigated for varying focusing conditions. In this section the crystal choice, simulations and experimental results of the systematic study will be discussed.

	BiBO	**BBO**
crystal type	biaxial in YZ plane: positive eeo	uniaxial negative ooe
refractive index	$n = 1.888$	$n = 1.667$
spatial walkoff angle	$\rho = 73.12\,\mathrm{mrad}$	$\rho = 80.63\,\mathrm{mrad}$
effective nonlinear coefficient	$d_{\mathrm{eff}} = 3.36\,\mathrm{pm/V}$	$d_{\mathrm{eff}} = 1.91\,\mathrm{pm/V}$
group velocity mismatch	$GVM = 984\,\mathrm{fs/mm}$	$GVM = 367\,\mathrm{fs/mm}$

Table 4.2: Table summarizing the relevant properties of BiBO in comparison to BBO for the SHG from 626 nm to 313 nm, extracted from [100]. Of superior importance for the implementation of efficient spectral compression is the large effective nonlinear coefficient and the large amount of GVM.

Crystal choice

In order to achieve high conversion efficiencies during UV generation, a nonlinear crystal with appropriate transparency range and a high effective nonlinear coefficient d_{eff} must be chosen. Furthermore a small spatial walkoff angle ρ in general allows for better beam profiles and a longer effective interaction length for a given crystal length. These restrictions already strongly limit the amount of possible materials. Due to their deep UV transparency range and high optical damage threshold lithium triborate LiB3O5, LBO, and beta barium borate β-BaB3O4, BBO, are established materials of choice. LBO has the advantage of offering a small spatial walkoff angle, of $\rho = 17.82\,\mathrm{mrad}$ [100], but suffers from a low nonlinear coefficient, $d_{\mathrm{eff}} = 0.51\,\mathrm{pm/V}$ [100], wherefore BBO with its higher nonlinear coefficient is popularly used for existing experiments requiring wavelengths near 313 nm despite its larger walkoff angle. Here instead the relatively new nonlinear crystal BiBO [101, 102, 103] is used due to multiple reasons. Its relevant properties for SHG from 626 nm to 313 nm are shown and compared to BBO's properties in Table 4.2. BiBO is a biaxial crystal allowing for versatile phase-matching characteristics. The most advantageous configuration for SHG from 626 nm to 313 nm is along the YZ principle plane. In this working plane its nonlinear coefficient of $d_{\mathrm{eff}} = 3.36\,\mathrm{pm/V}$ is nearly twice as high as for BBO. A further important advantage is its high GVM which is required in order to achieve a strong spectral compression. Its value is 2.7-times higher than the GVM of BBO. This allows to achieve a certain amount of spectral compression with a shorter crystal length, by which also problems

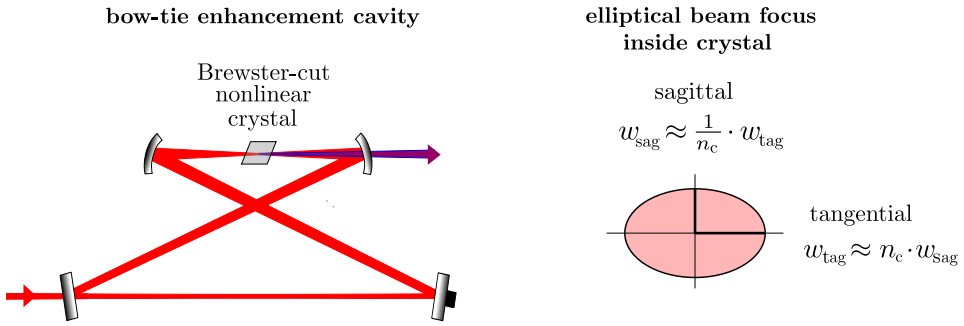

Figure 4.9: Cartoon picture of a typical configuration of a bow-tie enhancement cavity. The circulating light passes two plane and two curved mirrors. The two curved mirrors generate a focus inbetween, where the crystal is placed in order to enhance conversion efficiencies. The tilted impact of the beam on the curved mirrors generates an astigmatism, which can be compensated by the tilted surfaces of the Brewster-cut crystal. For the optimized distance between curved mirrors and crystal side facets, the focal position in the sagittal and tangential plane are located at the same position, whereas the focus has an elliptical shape with ellipicity given by $e = \frac{w_{\mathrm{tag}}}{w_{\mathrm{sag}}} = \tan(\theta_{\mathrm{B}}) \approx n_{\mathrm{c}}$ as shown in Figure 4.10. The major axis lies along the tangential plane.

induced by spatial walkoff are reduced, as the spatial walkoff angle ρ is on the same order of magnitude for both crystals. Also the damage thresholds are reported to be comparably high for both crystals [102, 104]. Another benefit is BiBO's inertness to moisture which simplifies the treatment, especially beneficial for the systematic survey with several crystals. BBO in comparison shows a hygroscopic behaviour which requires special care. BiBO and BBO also differ in their crystal structure. Within the YZ principle plane the biaxial BiBO crystal behaves as a positive uniaxial crystal. Therefore the fundamental beam is the extraordinary beam when conditions for critical phase matching are fulfilled. For this beam the direction of energy flux differs from the direction of the wavevector. BBO in comparison is a negative uniaxial crystal, where the generated SH signal experiences the spatial walkoff and the fundamantal beam behaves ordinary. For a rectangularly shaped crystal this difference is mostly irrelevant, as it only slightly affects the orientation of the pulse front tilt of the generated signal. But the difference becomes of importance in context of different crystal cuts as they are for example used in enhancement cavities for astigmatism compensation.
Enhancement cavities are optical resonators which are used to enhance the optical power of the circulating light [105, 106]. By placing the nonlinear crystal inside the cavitiy, conversion efficiencies can hence be boosted. A typical configuration is a bow-tie shape, where the cavity consits of two plane and two curved mirrors as shown in Figure 4.9. The two curved mirrors generate a focus in between them where the crystal is placed. The tilted incidence of the beam on the curved mirrors

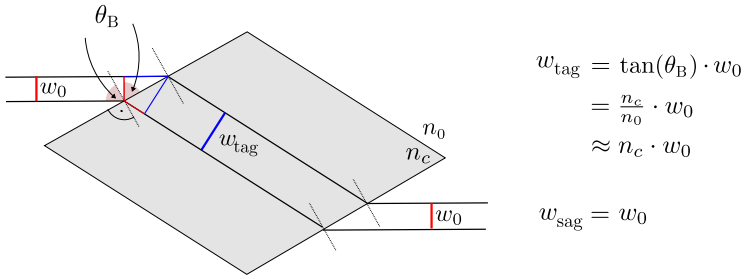

Figure 4.10: Schematic of the formation of the ellipticity of a beam passing through a Brewster-cut crystal. Along the tangential plane (tag), the incident collimated beam of size w_0 experiences an optical beam path difference, which causes an enlargement of the beam size by a factor of $w_{\text{tag}} = \tan(\theta_B) \cdot w_0 \approx n_c \cdot w_0$ inside the crystal. In the sagittal plane (sag) no beam path difference occurs and the waist size is unchanged.

introduces astigmatism. This results in differing focal distances in the vertical and horizontal plane. One can either keep the angle of incidence as small as possible to minimize this effect or compensate the astigmatism by using Brewster-cut crystals. Such crystals have a tilted surface of entrance and exit relative to the incident beam, as shown in Figure 4.10. The angle of the crystal cut is chosen such that the reflective losses of the circulating light are zero, given at the Brewster angle $\theta_B = \arctan(n_c/n_0)$, with n_c denoting the refractive index of the crystal and n_0 the one of the surrounding medium. This tilted surface also introduces an astigmatism, through which the beam experiences different geometric paths in the vertical and horizontal plane. This effect can be used to compensate for the astigmatism introduced by the tilted incidence on the curved mirrors. By matching the distances between the crystal and the curved mirrors, the position of the focus in both planes can be brought to be located at the same point. This is relevant in terms of stability considerations and advantageous for conversion efficiencies. Nevertheless the focal width in the horizontal and vertical plane differ, leading to an elliptical focus. A simple geometric consideration can be used to derive this ellipticity, as illustrated in Figure 4.10. Assuming a collimated beam being incident under Brewster's angle onto the crystal surface, its direction of propagation will be changed according to Snellius's law. In the plane in which the tilted angle of incidence occurs, typically denoted as the tangential plane, the beam width is enlarged by a factor of $\tan(\theta_B)$ due to the occurring optical path difference within the extension of the beam. Under the approximation that the medium surrounding the crystal has a refractive index of $n_0 \approx 1$ this factor is given by the refractive index of the crystal n_c. In the orthogonal plane, typically denoted as the sagittal plane, no change occurs, as no optical path difference exists within the beam extension. This discrepancy between the two planes causes the elliptical focus, with the ellipticity approximately given by $e \approx n_c$.

Of special interest is the orientation of the elliptic focus relativ to the direction of spatial walkoff. For Brewster-cut crystals the major axis of the elliptic focus can either lie within the plane of spatial walkoff or perpendicular to it, depending on whether the FF or the SH beam experiences the spatial walkoff. This can be shown by applying Maxwell's equations. The direction of spatial walkoff, given by the direction of the Poynting vector $\vec{S}$, must lie within the plane spanned by the electric field vector $\vec{E}$ and the wavevector $\vec{k}$ [89]. The spatial walkoff direction is therefore always found to be along the direction given by the polarization of the extraordinary beam. For Brewster-cut crystals the Brewster angle is chosen such that the p-polarization[2] of the fundamental frequency is zero. This defines the orientation of the polarizations of both, the FF and the SH, fields relative to the crystal geometry. Depending on which beam exhibits the extraordinary behaviour, the spatial walkoff therefore lies within the sagittal or within the tangential plane. For negative uniaxial crystals, such as BBO, the spatial walkoff lies along the minor axis of the elliptic focus, for positive uniaxial crystals, such as BiBO, it lies along the major axis of the elliptic focus. As a certain beam size in the direction of the spatial walkoff is required to maintain an effective interaction between the FF and SH and to reach a certain amount of spectral compression, it is strongly advantageous that the direction of spatial walkoff is orientated along the major axis of the elliptical focus. The tighter focus along the minor axis then enhances the intensity by a factor of n_c for a given waist along the walkoff direction. In comparison, for negative crystals for the same given waist along the walkoff direction, the intensity is reduced by a factor of n_c due to the enlarged waist in the perpendicular direction. Thus, BiBO has a further great advantage compared to BBO when using Brewster-cut crystals. As the use of an enhancement cavity might be an important tool for improving conversion efficiencies, both, Brewster and rectangularly cut crystals, have been investigated within the pre-study.

Simulation model

For analysis of the spectral compression process under influence of spatial walkoff, a model is required including all possible second-order interaction processes as well as phase matching, diffraction and walkoff for the involved pulses. Furthermore spatio-temporal pulse dynamics must be taken into account. For this a suitable (2+1)-dimensional simulation model developed by T. Lang [107] was applied. It has been established for obtaining a deeper understanding of complex spatial and temporal dynamics occurring during non-collinear ultra-broadband interaction in optical parametric amplification processes and gives access to full information of the intensity and phase of the involved pulses in space and time at every position

[2]The p-polarization exhibits an electric field being polarized parallel to the plane of incidence. In context of the Brewster-cut geometry this polarization lies within the tangential plane of the crystal.

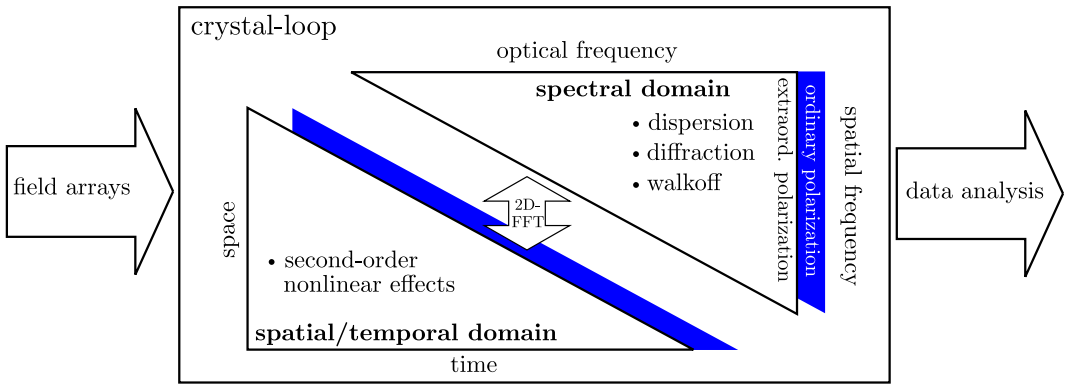

Figure 4.11: Schematical illustration of the principle of the calculation loop of the applied split-step simulation model following [108]. For numerical calculation, the crystal is divided in small steps dz and propagation and nonlinear interaction are successively calculated for each dz, based on given starting conditions. Second-order nonlinear effects are calculated in the spatial/temporal domain. Subsequently, dispersion, diffraction and walkoff are calculated in the spectral domain. For the next propagation step, second-order nonlinear effects of the new spectral fields are calculated again in the spatial/temporal domain. The alternating calculations are applied to the instantaneous ordinary and extraordinary fields, until the entire crystal length L is covered. Both Fourier domains are connected by the two-dimensional Fourier transformation.

in the crystal. Unlike other typical approaches, this model handles the nonlinear interaction with only two coupled differential equations for the two orthogonally polarized ordinary $E_{\mathrm{o}}(x,t)$ and extraordinary $E_{\mathrm{e}}(x,t)$ electric fields within a birefringent crystal. Due to phase-matching considerations the model can therefore be restricted to one spatial transverse dimension including the direction of spatial walkoff without substaintial loss of accuracy[3]. This transverse direction is denoted as the x-direction and is orthogonal to the main direction of propagation along the z-axis. The angle between the z-direction and the optic axis of the crystal is chosen to fulfill phase-matching conditions, characterized by the angle θ.

For numerical calculations of the pulse evolution during the nonlinear conversion process, the crystal is divided in small steps dz and propagation and nonlinear interaction are successively calculated for each dz. The second-order nonlinear interaction, including temporal and spatial effects, is modelled in the temporal/spatial domain, with temporal axis t and the relevant spatial axis x. The pulse propagation, including dispersion, diffraction and walkoff for each propagation step dz, is subsequently calculated in the spectral domain, with optical frequency f_{t} and spatial frequency f_{x} revealed by the two-dimensional Fourier transformation of the complex

[3]The negligence of propagation and diffraction along the orthogonal transverse direction yields a good approximation if the crystal length is shorter than the Rayleigh length of the laser focus.

electric fields $\mathbf{FT}[E_{\mathrm{o/e}}(x,t)] = E_{\mathrm{o/e}}(f_{\mathrm{x}}, f_{\mathrm{t}})$. Based on given starting conditions this loop with alternating calculations in the different Fourier domains for each dz, always applied to the current optical fields, is repeated until the entire length of the crystal is covered. Based on this split-step Fourier algorithm, the model gives direct access to the full spectral/temporal and spatial/angular information in amplitude and phase at each point of the nonlinear propagation through the crystal. The principle of the calculation loop is depicted in Figure 4.11. The corresponding mathematical operations for pulse propagation and nonlinear interaction will be described in the following.

The electric field orientation of a pulse at a certain z-position inside the birefringent crystal can be expressed as a superposition of the ordinary and extraordinary fields $E_{\mathrm{o/e}} = \vec{e}_{n_{\mathrm{o/e}}} A e^{ikz}$, with the unity vectors $\vec{e}_{n_{\mathrm{o/e}}}$ pointing in the direction of the ordinary and extraordinary dielectric polarizations, with A being their complex field amplitude, and e^{ikz} their accumulated phase during propagation along z. By using a solution of the paraxial wave equation [109], the propagation of this wave in space and time along the z-direction can be described by a superposition of a series of plane waves, each with spatial frequency f_{x} and optical frequency $f_{\mathrm{t}} = c/\lambda$. The propagation can therefore be handled by adding the accumulated phase $e^{ik_{\mathrm{z}}z}$ to each plane wave [110]. The z-component of the wavevector contains their particular spatial frequency f_{x} and optical frequency f_{t} components. Under the assumption of negligible diffraction and propagation in the y-direction ($k_{\mathrm{y}} = 0$), the z-component of the wavevector is given by:

$$k_{\mathrm{z}}(f_{\mathrm{t}}, f_{\mathrm{x}}) \approx \sqrt{\left(\frac{2\pi f_{\mathrm{t}} n_{\mathrm{o/e}}(f_{\mathrm{t}}, f_{\mathrm{x}})}{c}\right)^2 - (2\pi f_{\mathrm{x}})^2} \tag{4.28}$$

The linear evolution for each propagation step dz within the numerical calculation loop can therefore be performed by applying two propagation equations for E_{o} and E_{e} [107]:

$$E_{\mathrm{o/e}}(f_{\mathrm{t}}, f_{\mathrm{x}}, z + dz) = E_{\mathrm{o/e}}(f_{\mathrm{t}}, f_{\mathrm{x}}, z) \cdot e^{(\mathrm{i}k_{\mathrm{z}}dz)} \tag{4.29}$$

With k_{z} given by Equation 4.28 and with the refractive indices $n_{\mathrm{o}}(f_{\mathrm{t}})$ and $n_{\mathrm{e}}(f_{\mathrm{t}}, f_{\mathrm{x}})$ given by the Sellmeier formalism and the index ellipsoid of the crystal [89].
As especially the extraordinary refractive index not only depends on optical frequency f_{t}, but further on the direction of propagation, expressed by f_{x}, an iterative algortithm is used for calculation of $n_{\mathrm{e}}(f_{\mathrm{t}}, f_{\mathrm{x}})$. The connection between the spatial frequency f_{x} and its propagation direction relative to the main propagation direction is depicted in Figure 4.12. This deviation is expressed by the angle α, which describes a change of $\Delta\theta$ to the main phase-matching angle θ, which is enclosed by the z-axis and the optical axis of the crystal:

$$\alpha_{\mathrm{e}}(f_{\mathrm{t}}, f_{\mathrm{x}}, n_{\mathrm{e}}) = \arcsin\left(\frac{k_{\mathrm{x}}}{k_{\mathrm{t}}}\right) = \arcsin\left(\frac{f_{\mathrm{x}}}{f_{\mathrm{t}}} \frac{c}{n_{\mathrm{e}}(f_{\mathrm{t}}, \alpha_{\mathrm{e}} + \theta)}\right) \tag{4.30}$$

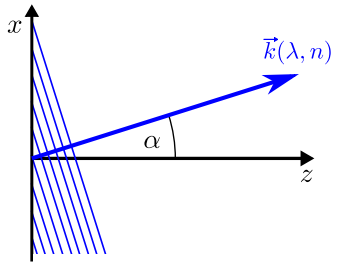

Figure 4.12: Illustration of the connection between spatial frequency, derived from the x-component of $\vec{k}(\lambda, n)$, and the propagation angle α towards the main propagation direction z.

Because of the interdependence between $\alpha_\mathrm{e}(f_\mathrm{t}, f_\mathrm{x}, n_\mathrm{e})$ and $n_\mathrm{e}(f_\mathrm{t}, \alpha_\mathrm{e}+\theta)$ the iterative algorithm is used to calculate the extraordinary refractive index. Based on this calculation, the phase term in Equation 4.29 automatically implements dispersion, diffraction and walkoff in the spectral domain.

The nonlinear interaction between and inside each field, for each dz within the calculation loop, is modeled in the time/space domain by two differential equations for the two fields $E_\mathrm{o}(x,t)$ and $E_\mathrm{e}(x,t)$ [107]:

$$\begin{aligned}
\frac{\partial E_\mathrm{o}(t,x)}{\partial z} &= -\mathrm{i}\,\kappa_\mathrm{o}\,(\overbrace{\underbrace{2E_\mathrm{e}E_\mathrm{o}^*}_{\mathrm{oo-e}}+\underbrace{E_\mathrm{e}E_\mathrm{e}}_{\mathrm{ee-o}}}^{\text{Type I}}+\overbrace{\underbrace{2E_\mathrm{e}E_\mathrm{e}^*}_{\mathrm{eo-e}}+\underbrace{2E_\mathrm{o}E_\mathrm{e}^*}_{\mathrm{eo-o}}+\underbrace{2E_\mathrm{e}E_\mathrm{o}}_{\mathrm{eo-o}}}^{\text{Type II}}) \\
\frac{\partial E_\mathrm{e}(t,x)}{\partial z} &= -\mathrm{i}\,\kappa_\mathrm{e}\,(\underbrace{E_\mathrm{o}E_\mathrm{o}}_{\mathrm{oo-e}}+\underbrace{2E_\mathrm{o}E_\mathrm{e}^*}_{\mathrm{ee-o}}+\underbrace{2E_\mathrm{e}E_\mathrm{o}^*}_{\mathrm{eo-e}}+\underbrace{2E_\mathrm{e}E_\mathrm{o}}_{\mathrm{eo-e}}+\underbrace{2E_\mathrm{o}E_\mathrm{o}^*}_{\mathrm{eo-o}}),
\end{aligned} \tag{4.31}$$

The different terms correspond to different types of conversion processes as denoted. Within the performed simulations only ee-o, type I processes are considered, where both fundamental beams exhibit extraordinary (e) behaviour and the signal beam is the ordinary (o) beam. Since the nonlinear interaction parameter $\kappa_\mathrm{o/e} = \pi f_\mathrm{t} d_\mathrm{eff}/(n_\mathrm{o/e}(f_\mathrm{t}, f_\mathrm{x})c)$, representing the strength of the nonlinear interaction, depends on the optical frequency f_t and the direction-dependent refractive index $n_\mathrm{e}(f_\mathrm{t}, f_\mathrm{x})$, the factor is implemented in the spectral domain before continuing with the calculation loop, where the next propagation step is then applied by Equation 4.29 to the new spectral fields. Due to the generalization of the three involved pulses of the nonlinear conversion process, typically denoted as pump, signal and idler, to only one ordinary and one extraordinary field, mixing products, temporal, spatial and parasitic effects are automatically taken into account [107].

Simulation results

As depicted in Figure 4.11, the numerical calculation loop requires certain starting conditions concerning the field arrays $E_{o/e}(f_x, f_t)$ and the crystal properties. Here, initially dispersion free, time-bandwidth limited pulses with gaussian intensity profile are assumed propagating along the z-direction, which encloses a phase-matching angle[4] of $\theta = 50.23°$ in the YZ plane for BiBO. The field arrays are characterized by their wavelength λ, pulse duration τ_p, pulse energy E_p and focal radius w_0, related by $I_{max} = 2E_p/(\pi w_0^2 \sum I(t)dt)$. Concerning the crystal properties, all dispersion characteristics of BiBO are taken into account, its transmission $T(f_t)$ as well as the nonlinear interaction strength d_{eff}. Furthermore only the length of the crystal must be set.
Concerning the data analysis of the simulation results, the properties of the generated second-harmonic field are of special interest. As the simulation model directly yields full spectral/temporal and spatial/angular information, the resulting SH field after propagating the distance of the crystal length can be directly presented in both applied Fourier domains (x, t) and (f_x, f_t). Each representation visualizes different characteristics of the generated field. In the space/time domain resulting pulse profiles can be seen, showing spatio-temporal effects of the process. An illustrative way of interpreting the data in the spectral Fourier domain, given by (f_x, f_t), can be obtained by plotting the generated field against λ and α, derived by applying Equation 4.30. Furthermore this representation allows to intuitively extract the normalized spectrum, directly visualizing the spectral shape and the spectral bandwidth of the generated pulses.

In order to obtain a qualitative understanding of the so far uninvestigated influence of spatial walkoff on the spectral compression process, simulations for BiBO crystals have been performed comparing the cases of weak and tight focusing in absence and presence of spatial walkoff. The spatial walkoff can therefore be simply included or excluded in the calculations. Exemplary results of the generated second-harmonic pulses are shown in Figure 4.13. For each case the results of the generated SH pulses are represented in the (x, t), the (f_x, f_t) and the (λ, α) domain. Furthermore the corresponding normalized spectra are shown.
As discussed in section 4.3.2, the resulting SH profile is temporally broadened due to the GVM between the FF and SH pulses. In absence of spatial walkoff the resulting SH profile is approximately given by a rectangular shape independent of the focusing strength. The broad extension along the t-axis transforms into a narrow width along the optical frequency axis f_t in the corresponding spectral Fourier domain, and hence leads to a narrow spectrum. Different focusing strengths transfer

[4]Note that different conventions exist concerning the orientation of the phase-matching angle. The convention referenced in [100] for example differs by $\pi - \theta$. The value applied for the simulations is obtained by Sellmeier coefficients following [111].

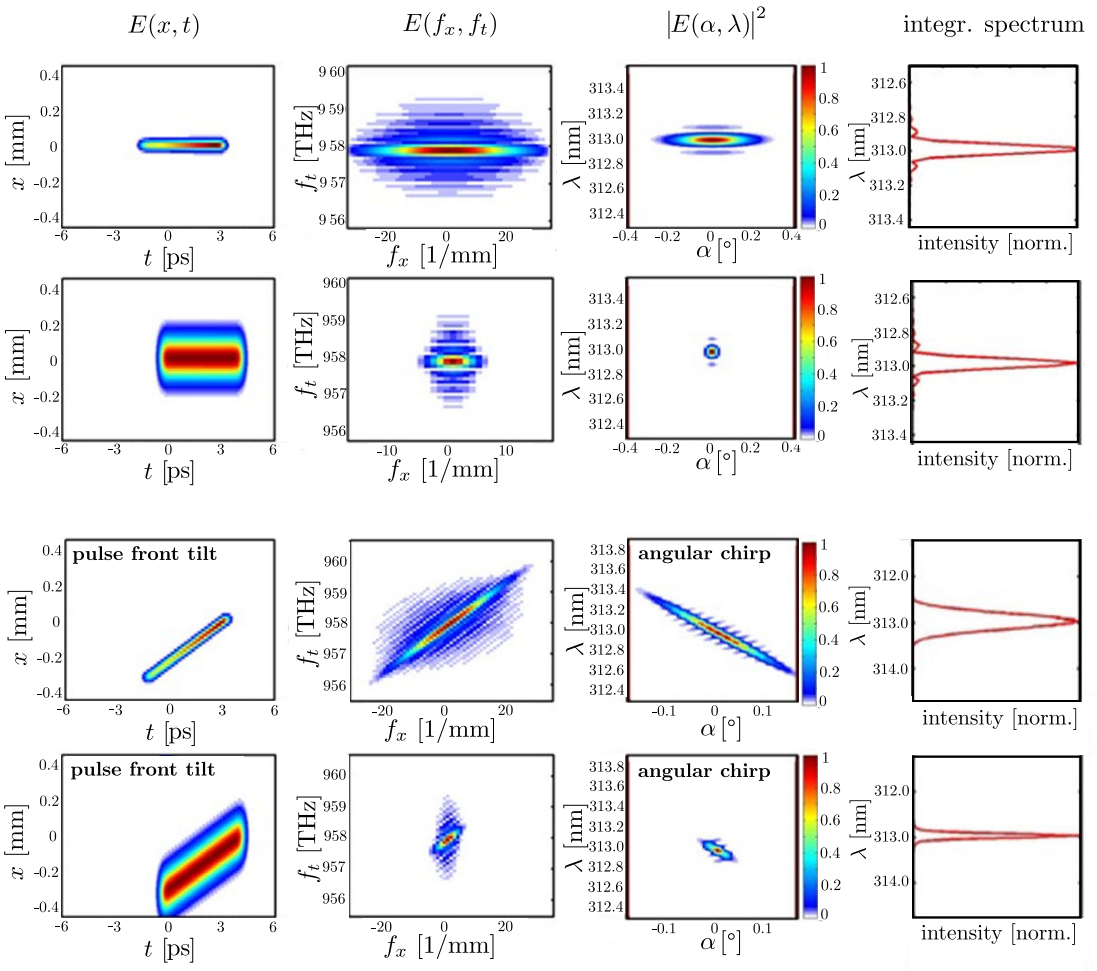

Figure 4.13: Qualitative simulation results, showing the generated SH fields in different representations, obtained by the split-step simulation model for different process assumptions. The upper two rows of plots exclude the influence of spatial walkoff, whereas the lower two rows include the effect of spatial walkoff. The upper row each corresponds to the case of tight focusing of the FF beam, indicated by a small SH field extension along the x-axis and a broad extension along the f_x-axis. The lower row each corresponds to weak focusing of the FF pulses with inversed field extension behavior. For each condition, the generated electric fields of the SH pulse are represented, from left to right, in the (x,t) Fourier domain, $E(x,t)$, in the (f_x,f_t) Fourier domain, $E(f_x,f_t)$, and in the (λ,α) representation, $|E(\alpha,\lambda)|^2$, obtained by Equation 4.30. Further each corresponding normalized spectrum is shown on the right. The simulations show that the spatial walkoff causes a pulse front tilt in the (x,t)-domain, which is accompanied by an angularly dispersed output of the generated SH pulses, as to be seen in the (f_x,f_t) Fourier domain and in the (λ,α) representations. Furthermore the amount of spectral compression in presence of spatial walkoff depends on the focusing strength and compared to the case without spatial walkoff, is reduced for tighter focusing.

into different extensions of the spatial frequencies f_x in the spectral domain. As given by Equation 4.30, different spatial frequencies belong to different propagation directions, denoted by the angle α. This distribution of angles can be interpreted as an angular spread equivalent to the divergence angle within a focused gaussian beam. For tight focusing the total angular spread of the beam in the far field is large, while for weak focusing only small divergence angles occur. As the frequency components are equally spread with respect to α, the focusing strength does not affect the spectral results. The spectral shape and the spectral bandwidth of the generated SH signals are hence independent of the focusing strength.
In comparison the results for the case with spatial walkoff strongly depend on the focusing strength. Furthermore each representation gives rise to specific characteristics of the generated SH fields. Regarding the fields in the space/time domain, it can be seen that the generated SH pulses experience a pulse front tilt, occurring due to spatio-temporal couplings, as discussed in section 4.3.2. The direction of the pulse front tilt is maintained during transformation into the spectral domain (f_x, f_t). The different spread of spatial frequencies f_x in the spectral Fourier domain and accordingly the different spread of angles α, can again be interpreted in analogy with the different divergence angles within differently focused gaussian beams. In contrast to the case without spatial walkoff, different spectral components now correspond to different propagation directions, denoted by the angle α. This behaviour is known as an angular chirp [112] and is an important qualitative result of the simulations. The angular chirp causes the spectral components to spatially separate after some propagation, which requires special care for applications. Furthermore the pulse front tilt, caused by spatio-temporal couplings, directly affects the spectral shape of the resulting SH spectrum. As the temporal profile strongly differs froms a rectangular shape, also the spectrum deviates from a sinc profile. As a further important qualitative result the simulations show that the resulting SH spectral bandwidth depends on the focusing strength. The differing spread of wavelengths $\Delta\lambda$, equivalent to the different spread of optical frequencies Δf_t, for the focusing conditions compared, are related to varying temporal broadenings in the time domain. This can be explained by different effective interaction lengths depending on the focusing strength. For tight focusing the effective interaction length and hence the amount of spectral compression is most strongly reduced. This reduction of achievable spectral compression, compared to the case without spatial walkoff, is the larger, the smaller the beam sizes of the involved pulses are.

In conlusion, the quantitative analysis shows that the spatial walkoff causes a pulse front tilt due to spatio-temporal couplings, which is accompanied by an angularly dispersed output of the generated SH pulses, where different frequency components exit the crystal in different directions. Furthermore, the spectral compression strongly depends on the focusing conditions and is, compared to the case without spatial walkoff, the stronger reduced the tighter the focusing is.

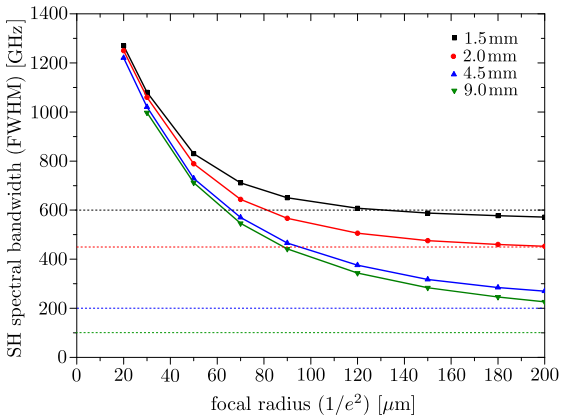

Figure 4.14: Quantitative simulation results concerning the spectral compression, showing the resulting SH spectral bandwidth depending on the focal radius along the walkoff direction for different crystal lengths. The points represent the simulation data, whereas the solid lines are guides to the eye. Assumed are time-bandwidth limited fundamental pulses with a spectral bandwidth of $\Delta\lambda = 1.5\,\text{nm}$, corresponding to $\Delta\nu = 1150\,\text{GHz}$. Only for very large foci the results converge towards the bandwidths which would be expected in absence of spatial walkoff according to Equation 4.16, illustrated by the dotted lines. For tighter focusing the resulting SH bandwidths increases.

For quantitative analysis, simulations have been performed investigating the resulting SH spectral bandwidth as a function of the focal waist size along the direction of spatial walkoff for BiBO crystals of different lengths. Exemplary results for time-bandwidth limited fundamental pulses at 626 nm with spectral bandwidth of 1.5 nm are shown in figure 4.14 for four different crystals lengths. Further shown are the corresponding bandwidths, which would be expected in the case without spatial walkoff according to Equation 4.16. It can be seen that only for very large waist sizes, the calculated resulting SH bandwidth approximately converges to this value. As previously discussed this is related to the large effective interaction length which can despite spatial walkoff be ensured for very large beam sizes. For tighter focusing the amount of achievable spectral compression accordingly decreases, the stronger the tighter the focusing is. The resulting SH FWHM bandwidths therefore increase for smaller beam radii and converge to a certain value, depending on the initially assumed bandwidth of the fundamental pulses, for every crystal length.
Quantitative simulation results concerning the pulse duration of the generated second-harmonic signal as a function of the focal waist size along the direction of spatial walkoff for BiBO crystals of different lengths are shown in Figure 4.15. Assumed are fundamental pulses at 626 nm with pulse durations of 400 fs. The resulting pulse durations are obtained by evaluating the intensity distribution in the time-space domain. The resulting temporal width of the second-harmonic signal is the broader, the longer the crystal and the weaker the focusing is.

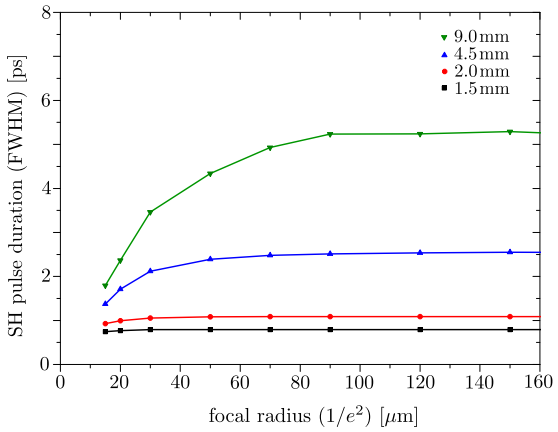

Figure 4.15: Quantitative simulation results for the pulse duration of the resulting SH signal as a function of the focusing strength of the fundamental pulses for different crystal lengths. Assumed is an initial fundamental frequency pulse duration of 400 fs. The resulting SH pulse durations are calculated from the generated intensity distribution in the space-time diagram. The points correspond to simulation data, whereas the lines are guides to the eye.

Experimental pre-study

Based on the quantitative and qualitative simulation results, a systematic survey was performed, especially investigating the resulting spectral SH bandwidths and conversion efficiencies during single-pass frequency doubling in BiBO crystals, for different crystal lengths, crystal cuts and focusing strengths. Other than in the case without spatial walkoff, focusing cannot be chosen to maximize the conversion efficiency, as the focal size along the direction of spatial walkoff determines the amount of spectral compression. Since, according to the quantitative simulation results, different combinations of crystal lengths and focusing strengths are expected to lead to identical resulting SH bandwidths, the systematic survey is carried out to yield optimal conditions, allowing to selectively generate specific desired spectral bandwidths with highest conversion efficiencies and with the best compromise concerning the beam profile, spectral shape and chirp characteristics.
Based on the quantitative simulation results, crystals with lengths between 1.5 mm and 6.0 mm are investigated. As it can be seen in Figure 4.14, crystals longer than 4.5 mm do not significantly further reduce resulting spectral bandwidths, whereas they in general are expected to increase problems due to spatial walkoff. In addition the pulse durations are expected to increase as shown in figure 4.15, reducing the achievable beam intensity. Shorter crystals do not bring sufficient spectral compression and conversion efficiencies for reaching specific bandwidths are expected to be below efficiencies being realizable with longer crystals, achieving the same SH bandwidth in combination with a tighter focusing.

Concerning the crystal cuts, rectangularly cut and Brewster-cut crystals have been investigated within the pre-study, because the use of an enhancement cavity might become an important add-on tool in order to boost conversion efficiencies when setting up the (anti-)proton experiment. During the test experiments nevertheless only single-pass frequency conversion experiments were performed, because the focusing strength within a future enhancement cavity is given by design and cannot be varied.
The geometry of the Brewster-cut crystals requires special attention for the associated simulations. One aspect occurs due to astigmatism. Whereas inside an enhancement cavity the astigmatism introduced by the tilted side facets of the Brewster cut crystal is used to compensate the astigmatism introduced by the tilted beam incidence onto the curved mirros, it in single-pass configuration causes the focal positions and the focal waist sizes to differ in the tangential and sagittal plane. Concerning the configuration which maximizes the SHG conversion efficiency during the experimental alignment, some approximations must therefore be made. For a circular beam without astigmatism it is typically assumed that the highest conversion efficiency is obtained for the focus being located in the middle of the crystal with respect to the crystal length [113, 114]. Taking astigmatism into account, only either the tangential waist or the sagittal waist can satisfy this assumption. As the sagittal waist is tighter by a factor of approximately n_c, this waist has been assumed to have a stronger influence on maximizing the conversion efficiency, and thus to lie closer to the crystal center.
Brewster-cut crystals further exhibit higher Fresnel losses than rectangularly cut crystals. The reflection losses for the generated SH signal with near 30% are approximately three times as high as for rectangular cut crystals, due to the tilted impact of the SH beam on the crystal end facet when leaving the crystal. A special coating could prevent these losses, but for this pre-study, the focus has been put on the qualitative understanding and qualitative optimization of the spectral compression process.

Experimental setup

The concept of the experimental setup used to investigate spectral compression induced during single-pass SHG in BiBO crystals of different lengths and different cuts is shown in Figure 4.16. Broadband FF pulses near 626 nm are focused into single BiBO crystals under varying conditions. Behind the crystal, a coated mirror, highly reflective for 626 nm and highly transmittive for 313 nm, is used to separate the fundamental light from the generated light near 313 nm. The UV output beam is then recollimated and focused into a Czerny–Turner spectrometer for analysis of the generated spectrum. The spectrometer design has a slit in the entrance plane, placed within the effective focus of a curved mirror, which collimates the incident light onto a grating. The horizontally dispersed and diffracted light is then collected

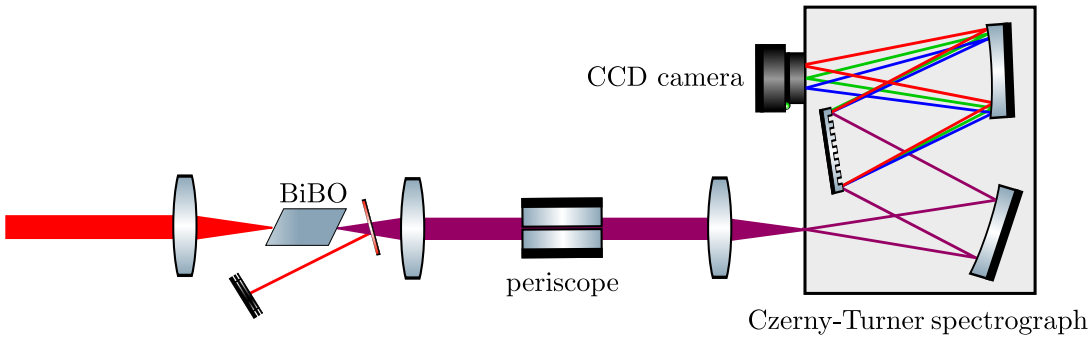

Figure 4.16: Setup applied to investigate the spectral compression induced during single-pass SHG in BiBO crystals. Broadband fundamental pulses near 626 nm are focused into BiBO crystals under varying conditions. A coated mirror behind the crystal separates the fundamental light from the generated light near 313 nm. A periscope is applied to rotate the plane of spatial chirp into the vertical, before the collimated UV beam is focused into a Czerny-Turner spectrometer for spectral analysis.

by another curved mirror, which refocuses each spectral component horizontally separated onto a CCD camera. The horizontal plane therefore contains the spectral information of the incident pulses, whereas the vertical plane can additionally give information about the height distribution of the spectral components, if the optics contained within the spectrometer setup compensate for aberration and astigmatism effects. The angular chirp of the generated UV pulses requires special care concerning the relative orientation with respect to the diffraction plane of the grating. In order to obtain correctly mapped frequency separation along the horizontal plane, the angular chirp must be orientated along the vertical direction when entering the spectrometer. For this, the orientation of the initially horizontally angular dispersed light coming out of the crystal end facet was rotated by 90° using a periscope.
The input pulses near 626 nm in Figure 4.16 were obtained from different sources within the pre-study. Part of the experiments have been carried out at the Politecnico di Milano in cooperation with G. Cerullo, M. Marangoni and C. Manzoni, while the customized frequency comb described in section 4.2 was still under development. As part of the facility “Laserlab Europe”, a laser system was available offering suitable spectral properties at 626 nm, which allowed to obtain a first experimental understanding of the spectral compression process including spatial walkoff. The equivalent experiments have then been performed at a later date with the actual Raman laser system. Both systems are based on an erbium-fiber master oscillator, where part of the light is shifted to 1050 nm and then recombined with the unshifted light at 1550 nm in a SFG unit yielding a wavelength near

626 nm. The system in Milano had a repetition rate of 100 kHz, pulse durations of approximately 100 fs and a spectral bandwidth of 10 nm. In order to match the spectral properties of the pulses near 626 nm, linear spectral filters have been applied, reducing the spectral bandwidth to either 2.4 nm or 1.5 nm, according to the expected bandwidth region of the Raman laser system. Thus, an evenly shaped gaussian-like spectrum was obtained, which is the main qualitative difference to the experiments performed with the Raman laser system, providing substantial sidelobes of asymmetric intensity. Also the available diagnostic tools were different, depending on the laboratory where the experiments were performed. At Politecnico di Milano a 1D spectrometer[5] was used, which did not provide information about the height distribution of different spectral components. In order to increase the resolution, the UV spectrum was investigated in the third diffraction order of the grating. This in general increases the spatial spread of spectral components at the position of the camera by a factor of three, which effectively enhances the resolution of the data. A correction factor, depending on the specific geomery of the spectrograph, must be considered if the angle of incidence onto the grating changes for the observations in different diffraction orders. For analysis of the spectral compression induced by the Raman laser system, a 2D imaging spectrometer[6] was applied, providing sufficiently high resolution of 0.03 nm for directly analyzing the UV spectra in first diffraction order. The combination with the 2D pixel array of an imaging EMCCD camera[7] further allowed to extract information about the vertical distribution of the contained frequency components, which has been of special interest due to the expected angular chirp of the generated UV pulses.

Experimental results - spectral shape

For a gaussian-shaped fundamental input spectrum the generated SH spectrum during spectral compression is expected to remain gaussian-like according to the simulations. This behaviour could be confirmed with the laser system applied in Milano, as exemplarily shown in Figure 4.17. As a linear filter has been applied to narrow the FF spectrum to the desired width, its shape can be described as approximately gaussian. Therefore the generated UV spectra nicely prove the expected behaviour concerning the resulting spectral shape.
For comparison, the spectra obtained with the Raman laser system are shown. The spectral shape of the fundamental pulses near 626 nm strongly deviates from a gaussian shape and contains substaintial sidelobes of asymmetric intensity. This dominant shape is transferred to the generated second-harmonic spectra, as shown for an exemplary generated UV spectrum.

[5] Princeton Instruments, Acton SP2150, f=150 mm, grating 1200 l/mm
[6] Andor, Shamrock 500i, f=500 mm, 2400 l/mm
[7] Andor iXon3 885, 1004 x 1002 pixel, pixel size 8 μm x 8 μm

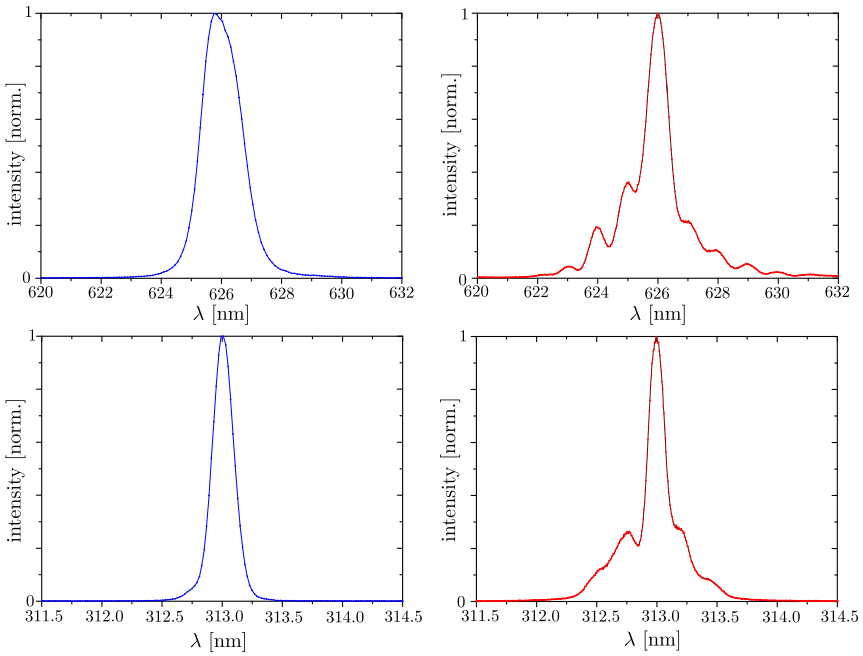

Figure 4.17: Sample spectra obtained during the spectral compression process with the laser system in Milano (blue/left) and with the Raman laser system (red/right). The upper pictures each show the fundamental spectrum near 626 nm and the lower pictures each a corresponding second-harmonic spectrum. Due to the application of a linear spectral filter, the spectral shapes obtained in Milano are nearly gaussian-like, whereas the generated spectra obtained with the Raman laser system exhibit substantial sidelobes of asymmetric intensity.

Experimental results - spectral bandwidth

Concerning the spectral compression, a dependency on the crystal length and the focal size along the direction of spatial walkoff is expected, according to the simulation results shown in Figure 4.14. Experimental results of the generated SH FWHM spectral bandwidth for exemplary crystal lengths of 2.0 mm and 4.5 mm measured with the Milano system as well as with the Raman laser system in comparison are shown in Figure 4.18. The relevant difference between the measurements is the intitial bandwidth of the fundamental pulses near 626 nm. The shown results, obtained by the Milano system, were performed with an initial FF bandwidth of 1.5 nm, while the initial bandwidth of the pulses generated by the Raman laser system was measured to be 0.9 nm. It can be seen that the amount of spectral compression which can be achieved in the limit of tight focusing clearly depends on this value. Whereas for the laser system used in Milano the resulting SH spectra were very insensitive to the adjustment of the critical phase-matching angle, special care had to be taken for the alignment using the Raman laser system. Due to the

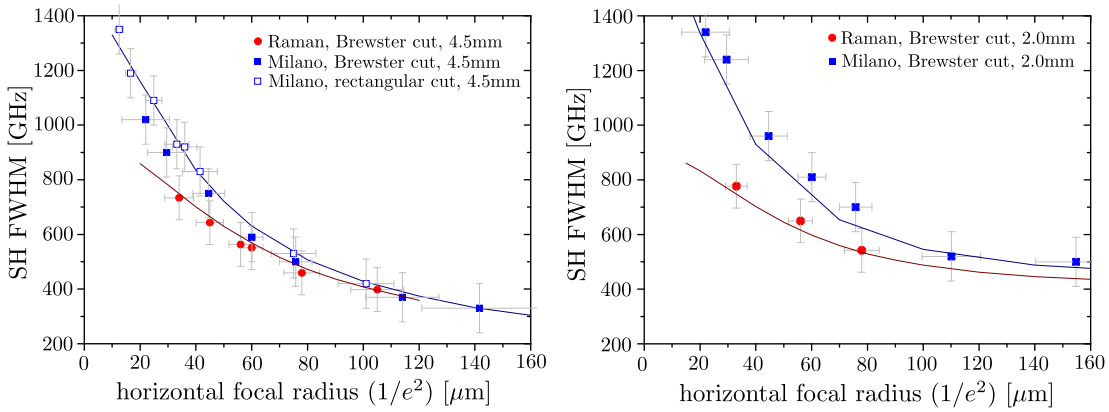

Figure 4.18: Experimental results of the spectral compression process showing the resulting SH bandwidth as a function of the focal waist size along the direction of spatial walkoff, denoted as the horizontal direction. On the left results are shown obtained with 4.5 mm long BiBO crystals and on the right results obtained with 2.0 mm long BiBO crystals. In each plot simulation data (solid lines) and experimental results are compared for the laser system in Milano with an initial fundamental pulse bandwidth of 1.5 nm (blue) and for the Raman laser system with an initial fundamental pulse bandwidth of 0.9 nm (red).

uneven spectral shape, the exact shape and hence the spectral bandwidth of the generated UV pulses strongly depend on the critical phase-matching angle. A slight change strongly affected the resulting spectrum, while no significant change in the conversion efficiency could be measured. The results shown here are obtained by carefully aligning to maximum peak count on the spectrometer, while still ensuring highest possible conversion efficiency. With the restriction of this procedure, the results show a good agreement with the simulations in both cases. Furthermore it could be proven that the crystal cut does not influence the spectral results and the amount of spectral compression only depends on the waist size along the direction of spatial walkoff.

Experimental results - conversion efficiencies

For relaxed focusing strengths, conversion efficiencies are assumed to scale with the intensity of the fundamental pulses as well as with the temporal and spatial overlap between the fundamental and generated signal pulses. For a given pulse shape and pulse energy this yields a strong expected dependence on the focal waist size, with special attention to the focal size along the direction of spatial walkoff, denoted as the horizontal direction. In Figure 4.19 measured conversion efficiencies obtained with the Raman laser system at an average power of 400 mW are plotted for 4.5 mm long crystals. Shown are results obtained by rectangularly cut crystals in comparison to results obtained by Brewster-cut crystals of the same length, scaled

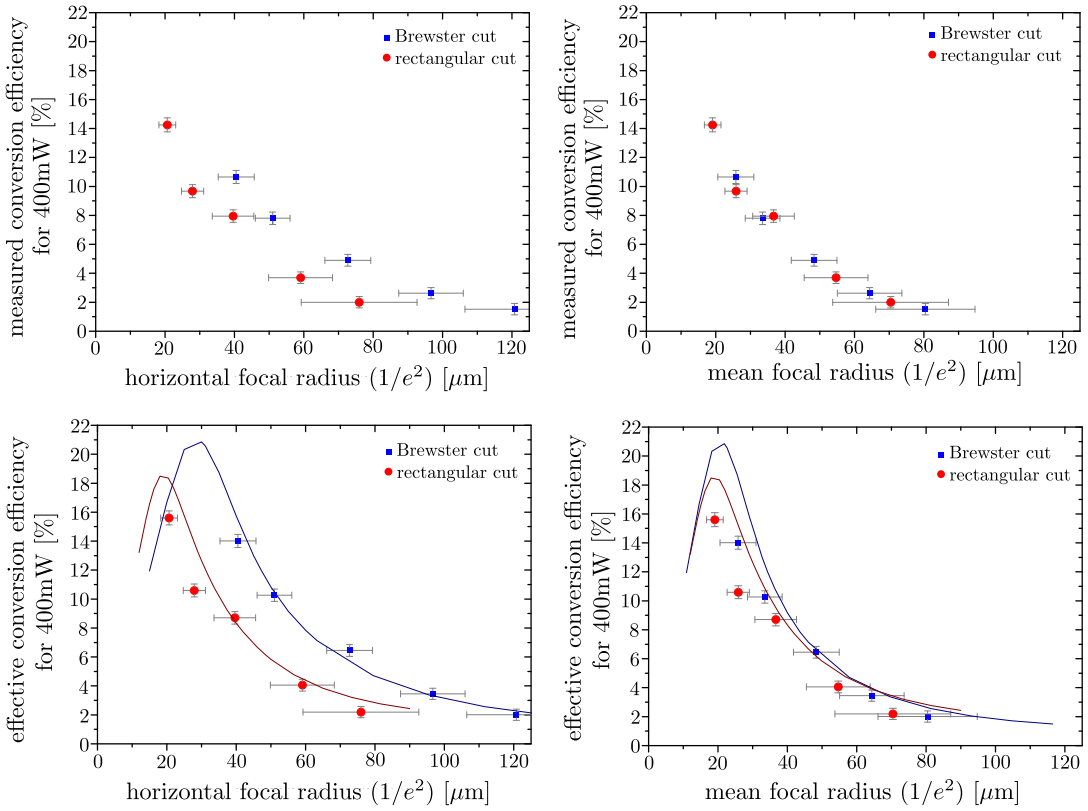

Figure 4.19: Experimental SHG results obtained with the pulsed Raman laser system, showing the conversion efficiency as a function of the horizontal radial focus (left) and as a function of the mean radial focus (right) for an average input power of 400 mW. The top graphs show measured conversion efficiencies, the bottom ones a comparison of simulation data to the Fresnel loss corrected measured efficiencies. Plotted are data obtained with 4.5 mm long BiBO crystals, in blue for a Brewster cut and in red for a rectangular cut. For the corresponding simulation data (solid lines) transform-limited gaussian input pulses with a FWHM pulse duration of 400 fs were assumed. The nonlinear interaction was calculated with the simulation model, extended to three spatial dimensions in order to account for the elliptical focusing conditions in Brewster-cut crystals. Deviations from the measured data might originate from an deviating pulse duration or from to the strongly deviating spectral shape. The uncertainty range of the calculated waist sizes results from a non-perfect beam collimation and in case of Brewster-cut crystals from additional astigmatism.

separately to the horizontal focal and to the mean focal radius. According to the drop of intensity within the focus of the fundamental frequency beam, conversion efficiencies decrease with increasing focal beam size. Scaled to the horizontal focal size, Brewster-cut crystals in comparison clearly yield higher conversion efficiencies

than rectangularly cut crystals of the same length, due to the elliptical focus with larger extension along the direction of spatial walkoff. As it has been experimentally proven that the resulting SH bandwidth only depends on the waist size along this direction, the tighter focus in the orthogonal direction increases the intensity and hence conversion efficiencies for achieving specific bandwidths. Also when scaling the conversion efficiencies to the mean radial focus, and hence to equal intensities, Brewster-cut crystals are expected to be advantageous for tight focusing, as evident from the corresponding simulations. In order to account for elliptical focusing the simulation model has been extended to three spatial dimensions. As Brewster-cut crystals ensure a stronger overlap between the fundamental and generated signal pulses, conversion efficiencies are higher than for corresponding circular focusing conditions, as present in case of rectangularly cut crystals. Within the uncertainty range of the measured data this difference could not significantly be resolved. In contrast, the difference between the crystal cuts has been clearly proven when scaling efficiencies to the horizontal radius, for which the achieved Fresnel loss-corrected data show a good agreement with corresponding simulations. Deviations might result from the spectral shape of the fundamental pulses, which strongly differs from the assumed gaussian profile.
The attempt of introducing focusing conditions with even stronger ellipticity than given by the Brewster cut geometry to further increase conversion efficiencies for generating a specific bandwidth, did not yield significant improvements, whereas beam profiles got strongly distorted.
Furthermore, the comparison of Brewster-cut crystals of different length has proven shorter crystals to result in lower conversion efficiencies. With the longest investigated Brewster-cut crystal of 6.0 mm length, slightly higher conversion efficiencies could be observed, while a loss in beam quality occurred, most likely caused due to a larger beam separation caused by the spatial walkoff. Based on these results, for generating spectra with spectral bandwidths in the region of interest, Brewster-cut crystals with 4.5 mm length yield a convincing compromise of spectral compression, conversion efficiency and beam profile.

Experimental results - observation of the spatial chirp

During the experiments which have been carried out with the Raman laser system, the available diagnostic tools further allowed to investigate the vertical distribution of the contained frequency components. As the orientation of the spatial chirp has been orientated into the vertical before entering the spectrometer, this feature allows to qualitatively observe the spatial chirp, which was predicted by the simulations. Different spectral components contained within the spectrum were found to be positioned at different heigths on the 2D pixel array of the applied CCD camera, forming a vertically tilted ellipse with respect to the wavelength axis.

Conclusion pre-study

In conclusion, a convincing agreement of simulations and experimental results has been achieved concerning the properties of the generated SH pulses. Based on the results of the pre-study, efficient and selective generation of UV pulses with a predictable bandwidth within the pursued spectral range between 300 GHz and 1000 GHz is possible. The uneven spectral shape of the pulses near 626 nm of the customized laser system however requires special treatment concerning the precise control of the resulting UV spectrum. As the formation of an externally implemented elliptical focusing did not conveniently improve results, the use of Brewster-cut crystals lead to highest conversion efficiencies for generation of the desired spectral bandwidths. Within the investigated Brewster-cut crystals the length of 4.5 mm lead to the best compromise between the spectral compression, conversion efficiency and beam profile. Furthermore the predicted spatial chirp has been proven, which allows a simple and efficient spectral pulse shaping as discussed in section 4.4.

4.4 Spectral pulse shaping

As last key part of the Raman laser system the spectral shape of the UV pulses is controlled. The spectrum of the customized frequency comb at 626 nm and hence all generated UV spectra contain substantial sidelobes, as shown in the previous section. In order to suppress spontaneous scattering and allow for appropriate Rabi frequencies, blocking of the outer-lying frequency components close to resonance with the excited states during the Raman process is essential, as discussed in section 3.3.3.
Adressing certain frequency components contained in a spectrum of a pulsed laser beam usually requires special effort in spatially resolving them. A typically used, established setup for pulse shaping is the so-called $4f$-configuration [115, 116]. It consists of two gratings and two lenses. The collimated beam is sent on the first grating by which the contained frequency components are angularly dispersed. The first lens, located at a distance equal to its focal length f, focuses the components to small diffraction limited spots at its back focal plane. The lens therefore converts the angular dispersion of the grating into a spatial separation along one direction, called Fourier plane. In this plane the separated frequency components can be modified. The second similar combination of lens and grating then recombines all frequency components into a collimated beam without introducing dispersion. Such a setup is quite inefficient for UV beams since it requires passing UV gratings twice, which typically have high losses when providing a strong dispersion.
Here instead, a simple, innovative, space-saving and nearly lossless shaping scheme is implemented, based on the spatial chirp generated by spatio-temporal coupling

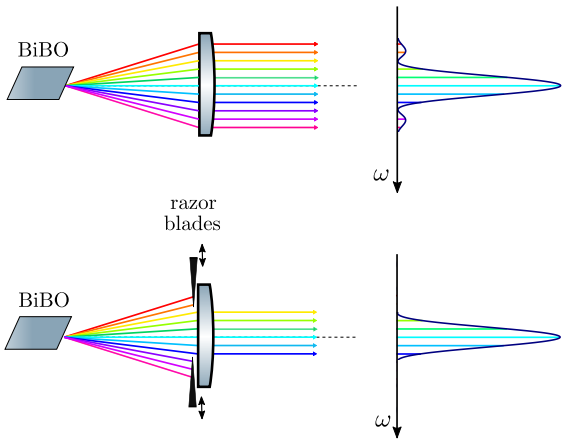

Figure 4.20: Schematical illustration of the applied pulse shaping technique. Razor blades located behind the nonlinear crystal address the outer-lying frequency components of the spectrum, enabled by the angularly dispersed output signal.

effects inside the nonlinear frequency doubling crystal. As discussed in the previous section, the combination of substantial temporal and spatial walkoff inside the nonlinear crystal causes an angularly dispersed UV signal. The red and blue components exit the end facet of the crystal under different angles α, as to be seen in the simulation data shown in Figure 4.13. This feature allows to simply use razor blades located behind the crystal in order to directly and selectively block the outer-lying parts of the generated UV spectrum, as schematically demonstrated in Figure 4.20. Exemplary modified UV spectra, for which the sides of the spectrum have been cut with this technique are presented in Figure 4.21. Shown is a normalized UV spectrum, for which each side of the spectrum has successively and independently been blocked. The spectrum corresponding to the closest positions of the razor blades, for which no drop of the intensity of the main peak occurred provides much steeper slopes on the side of the spectrum compared to the unmodified spectrum. This improvement is of superior importance for reaching the desired Rabi frequencies during the Raman process, as it allows to set a significantly smaller detuning without suffering from the scattering rate. This strongly improves the achievable Raman coupling strength, as discussed in section 3.3.3. For this reason, the successful implementation of this nearly lossless spectral modification technique is a great feature of the Raman laser system.
In combination with the previously discussed spectral compression technique, allowing for selective and efficient control of the spectral bandwidth as well as the tunability of the repetition rate and the wavelength, all requirements for efficient $^9Be^+$ ion qubit control are fulfilled.

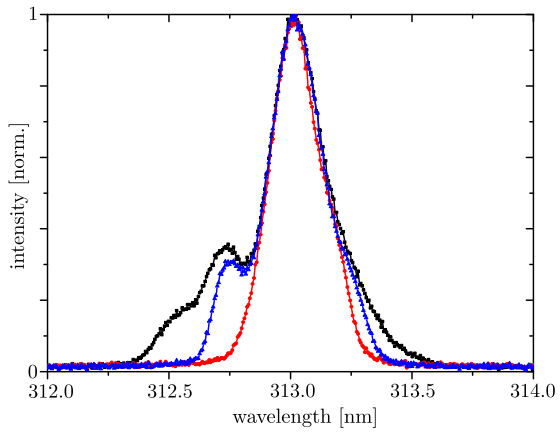

Figure 4.21: Measurement data of an exemplary modified UV spectrum, for which the sides of the spectrum have independently been cut with razor blades located behind the SHG crystal as depicted in Figure 4.20. The black spectrum corresponds to the unmodified spectrum, the blue one to an intermediate position of the razor blades and the red spectrum refers to the closest positions of the razor blades for which no drop of the intensity of the main peak occurred.

Chapter 5

Demonstration of $^9Be^+$ ion qubit control

For verifying the successful operation of qubit control using the developed pulsed Raman system, a trapped-ion experiment is required, which allows loading, cooling, state preparation and detection of beryllium ions. Since the high magnetic field (anti-)proton g-factor measurement experiment is currently still under progress, the Raman system has been tested at a different ion experiment in the group, allowing for the demonstration of beryllium qubit control. The trap, the setup and the experimental conditions will be briefly described in the first part of this chapter. The second and third part discuss the experimental implementation and demonstration of quantum control using the pulsed Raman system with the focus on single-beam spin control in section 5.2 and the focus on spin-motion coupling using two separated beams of the pulsed Raman laser system in section 5.3.

5.1 Surface-electrode ion trap experiment

The key element of the experiment at which the pulsed Raman laser has been tested, is a segmented surface-electrode trap, where different electrodes arranged in a planar geometry provide a confining trap potential, by which ions are captured above the surface. Instead of using a laser-based technique, the control of the quantum states of the ions is implemented by a single microwave meander-shaped structure integrated into the trap. This microwave conductor produces the required field configuration by design and is optimized for a qubit transition of $^9Be^+$ near 1 GHz at an externally applied magnetic field of 22.3 mT. Spin-motion coupling is achieved by using a gradient in the near-field of the dedicated conductors being near-resonant with the ion's spin flip frequency [58, 59]. The combination of this integrated microwave near-field method with the surface-electrode trap geometry

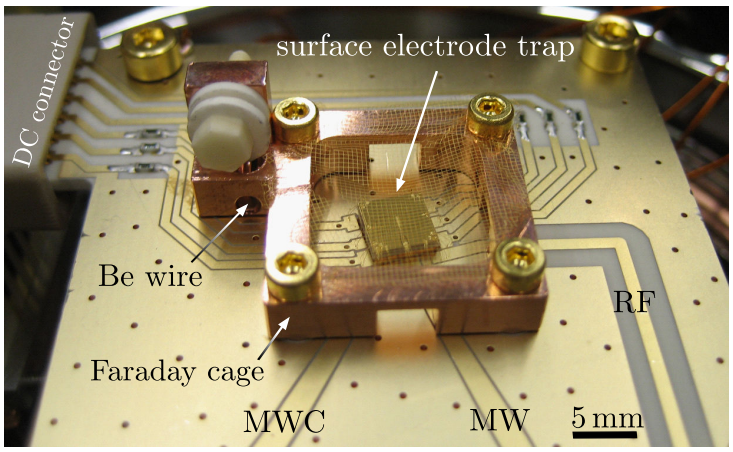

Figure 5.1: Photographic image of the segmented surface electrode trap mounted on a filterboard providing the voltage supply. The chip is located inside a Faraday cage shielding stray electric fields. As a source for neutral atoms a beryllium wire is fixed to the cage. Gaps in the mounting and the cage provide laser access to the wire and free access from the wire to the trap center.

allows a scalable approach to quantum information processing and simulation with trapped ions [117, 8, 118, 119].

5.1.1 Trap setup

The experimental apparatus is located at the Physikalisch Technische Bundesanstalt (PTB) in Braunschweig. Preliminary work on the design and installation has been carried out by M. Wahnschaffe and M. Kohnen and is described in [120]. Here a brief overview of the relevant setup will be given.
As shown in Figure 5.1 the key part, the micro segmented surface trap, is mounted onto a filterboard providing the voltage supply for the electrodes in order to create the desired fields. Axial confinement of the ions is achieved by the electrostatic fields generated by six direct current (DC) electrodes, while radial confinement is provided by the radio-frequency (RF) potential of a single segmented electrode. These fields allow to trap the ions 45 μm above the surface. The microwave (MW) electrode generates a fixed magnetic near-field above the surface, designed to control the ion's internal and motional degree of freedom. Its geometry is optimized for control of a field-independent hyperfine qubit transition, shown in Figure 5.4. Currents applied to a further, so-called microwave carrier electrode (MWC), allow transfer pulses in the hyperfine ground-state manifold of beryllium. The 5 mm x 5 mm large chip on the filterboard is surrounded by a Faraday cage in order to block stray electric fields. A gold mesh covering the cage further shields electric fields. As a source for neutral atoms a beryllium wire is fixed in an extended mounting of the shielding cage. Gaps in the cage at trap center height ensure laser access to

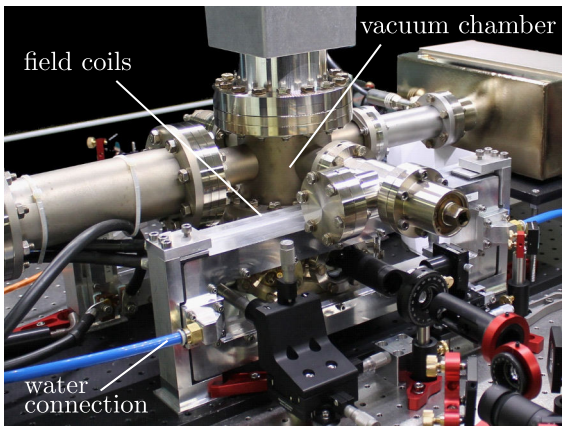

Figure 5.2: Photographic image of the overall setup with the vacuum chamber and the water-cooled magnetic field coils.

the beryllium wire. A further opening is pointing towards the trap center, also necessary for loading of beryllium ions, as described in section 5.1.3.
The entire filterboard is embedded in an ultra-high vacuum chamber to reduce background collisions and increase lifetimes. Outside the vacuum enclosure directly water cooled magnetic field coils generate the magnetic field of 22.3 mT at the position of the ion, which defines the quantization axis. Optical Viewports in the vacuum chamber allow optical laser access to the trap center along and perpendicular to the magnetic field direction. The orientation of the trap axes, defined by the axial and radial direction, is rotated about these directions. The magnetic field direction and the direction of the radial modes enclose an angle of 12 ° as depicted in Figure 5.3. This ensures all normal modes of the ion to have some overlap with a single laser cooling beam.
Below the vacuum chamber an imaging system is attached for state detection. The state-dependent fluorescence light of the ions is directed either onto a CCD camera[1] for alignment purposes or onto a photomultiplier module[2] for quantitative data analysis. Detected photons are counted by an experimental control unit. This unit is based on field programmable gate arrays (FPGA) and was developed at the National Institute of Standars and Technology (NIST) in Boulder, CO. Reconfigurable digital logic devices, able to generate arbitrary logic functions, control the communication between the computer and the hardware components, as described in detail in [121, 122]. The same system also generates the DC voltages as well as the frequencies and phases of the microwaves. Furthermore it controls the operation of acousto-optic modulators (AOM), required to control the laser interaction.

[1]Electron Multiplying Charge-Coupled Device Camera, iXonEM+ from Andor Technology Ltd., Belfast, UK
[2]H8259-01 from Hamamatsu Photonics K.K, Japan

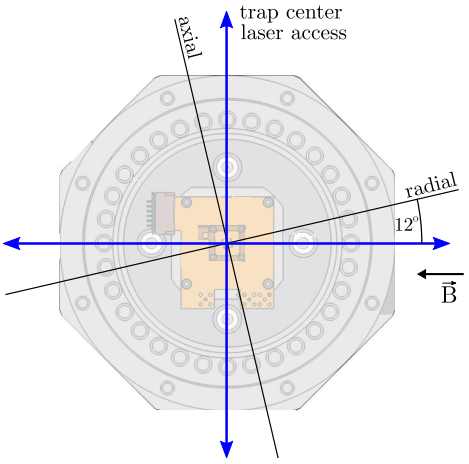

Figure 5.3: Schematical illustration of the orientation of the radial and axial trap axes with respect to the magnetic field direction and the available laser access directions.

5.1.2 Beryllium qubit

Experiments with the surface-electrode ion trap are performed in the electronic ground-state hyperfine manifold of $^9Be^+$ at an externally applied magnetic field of 22.3 mT. The relevant atomic structure is shown in Figure 5.4. The hyperfine manifold of the $^2S_{1/2}$ ground state consists of eight sublevels, labeled in the $|F, m_F\rangle$ notation. The transition frequencies all lie in the MW regime, allowing for direct microwave adressing. Qubit operations performed by the designed MW meander-shaped structure are implemented on the first-order field-independent transition between $|\downarrow\rangle = |2,1\rangle$ and $|\uparrow\rangle = |1,1\rangle$ with a frequency splitting of $\omega_0 = 2\pi \cdot 1082.55\,\text{MHz}$. Due to the first-order insensitivity to magnetic field fluctuations this transition provides long coherence times. While in this system the coherence time has not been characterized yet, similar setups have seen coherence times of up to one minute [79]. Between the $^2S_{1/2}$, $|2,2\rangle$ ground-state level and the $^2P_{3/2}$, $|3,3\rangle$ excited-state level a closed-cycle transition near 313 nm exists, which is used for state preparation, cooling and detection as described in the next section. Unlike the levels of the ground-state manifold, the states of the excited $^2P_{3/2}$ level at an applied magnetic field of 22.3 mT are correctly described by the quantum numbers m_I and m_J. The excited state of the closed-cycle transition will in the following therefore be denoted by $^2P_{3/2}$, $|m_I = +3/2, m_J = +3/2\rangle$.

5.1.3 Loading and cooling

The loading scheme applied to this experiment is based on the simultaneous generation of a neutral beryllium atom cloud and the ionization of single atoms. The neutral atoms are generated by irradiating a beryllium wire with a pulsed laser as

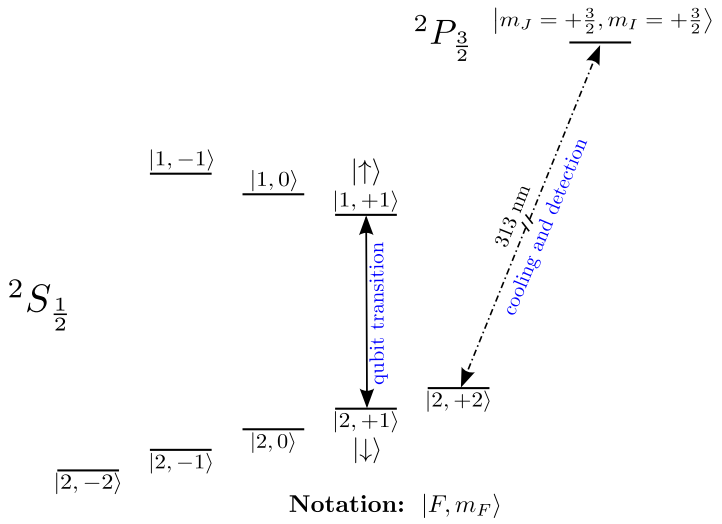

Figure 5.4: Illustration of the $^2S_{1/2}$ ground-state hyperfine manifold of $^9Be^+$ labeled in the $|F, m_F\rangle$ notation. Qubit operations controlled by the MW meander-shaped structure are performed on the field-independent transition between $|\downarrow\rangle = |2,1\rangle$ and $|\uparrow\rangle = |1,1\rangle$ with a frequency splitting of 1082.55 GHz. For laser cooling and detection the closed-cycle transition between the $^2S_{1/2}$, $|2,2\rangle$ ground state and the $^2P_{3/2}$, $|m_I = +3/2, m_J = +3/2\rangle$ excited state near 313 nm is addressed.

shown in Figure 5.5. This ablation laser has a wavelength of 1064 nm and its pulse energy density is set to reliably remove beryllium atoms with a single shot. A hole in the Faraday cage guides the removed atom flux towards the trap center. At the same time an ionization laser is pointed over the trap center as shown in Figure 5.5. Its wavelength of 235 nm allows the ionization of single beryllium atoms by a two-photon process. A first absorbed photon excites an atom from the ground state into an excited state, while a second absorbed photon then enables the ionization of the atom. Since the ionization takes place above the trap center, the atoms are trapped by the applied oscillating and static electric trapping fields as soon as they are ionized. Depending on the laser power, a single ion or several ions can be loaded in a chain above the chip surface within a few seconds with this technique.
In order to prevent the ions from escaping the trapping potential and to increase their lifetimes cooling is necessary. The reduction of the ion's kinetic energy is achieved by the interaction with a Doppler cooling laser, which is focused onto the ions as shown in Figure 5.5. The wavelength is near 313 nm and red detuned from the closed-cycle transition $^2S_{1/2}$, $|F = 2, m_F = 2\rangle \leftrightarrow {}^2P_{3/2}$, $|m_I = +3/2, m_J = +3/2\rangle$, shown in Figure 5.4. The cooling technique (e. g. [37]) is based on a velocity-dependent absorption process, being accompanied by an effective momentum kick in the direction of the wavevector of the laser. By choosing different detunings, ions with different velocities moving towards the laser beam can be addressed and their

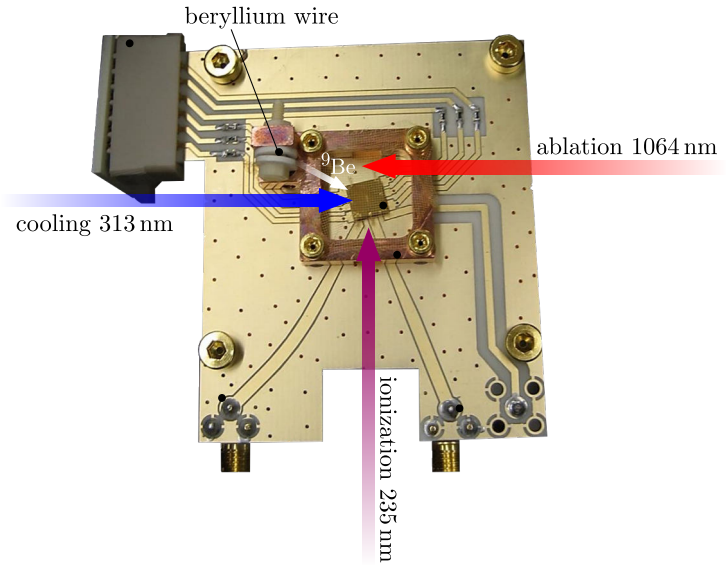

Figure 5.5: Sketch of the laser beam paths required for the loading and cooling sequence. The ablation laser generates a neutral beryllium atom flux being guided towards the trap center, where the ionization laser enables the ionization via a two-photon absorption process. As soon as ionized, the atoms are trapped above the trap center and cooled by interaction with the Doppler cooling beam.

oscillations be damped. During the loading process a larger detuning is chosen in order to cool hotter ions. In a next step a near-resonant Doppler beam is applied to further cool slower ions. It is essential that every motional mode has some overlap with the laser beam direction, which is ensured by the angle between the trap axes and the laser direction, as shown in Figure 5.3. The cooling achieved by this technique is sufficient for the experiments performed with the pulsed Raman laser.

All lasers required for loading and cooling are described in detail in [120]. The wavelength of 235 nm of the photoionization laser is provided by a frequency quadrupled 940 nm diode laser, as described in [123]. The laser system near 313 nm is based on the scheme presented in [124, 123]. Sum-frequency generation of two near-infrared CW lasers, at 1050 nm and 1550 nm, generates light at 626 nm which is then frequency-doubled by a second-harmonic generation process to generate the desired wavelength near 313 nm. In order to generate the near-resonant and far-detuned Doppler cooling frequencies, the UV beam is divided into two parts. The frequency of each beam path is shifted using an AOM, being separately controlled by the experiment control unit. Subsequently the beams are recombined and coupled into a UV fiber ([125, 126]) for mode cleaning and beam pointing stability. Behind the fiber, the polarization is set and the overlapping beams are focused into the chamber, as shown in Figure 5.7.

5.1.4 State initialization and detection

After loading and Doppler cooling the trapped ions are initialized in the $|2,2\rangle$ state of the $^2S_{1/2}$ ground-state manifold of beryllium depicted in Figure 5.4. From this state the ion can be prepared into any state of interest relevant for the experiment, by applying a suitable sequence of microwave carrier pulses resonant with the corresponding hyperfine transitions. The oscillating magnetic field of the microwaves can drive magnetic dipole transitions. This coupling results in Rabi flopping between the two states. By applying the microwave radiation for a time corresponding to a π-pulse, the population can be transferred. More details on this can be found in [120].
Once an experimental sequence including the interaction with the pulsed Raman laser is finished, the population of the prepared state is determined by transferring its population back to the initial $|2,2\rangle$ state of the ground-state manifold. A laser beam resonant with the closed-cycle transition $^2S_{1/2}$, $|F=2,m_F=2\rangle \leftrightarrow {}^2P_{3/2}$, $|m_I=+3/2,m_J=+3/2\rangle$ induces a state-dependent fluorencence signal, which is detected on a photomultiplier module and used for data analysis. If the $|2,2\rangle$ state in the ground-state manifold is populated, the detection laser is resonant and the ion will cycle between the ground and excited state and scatter photons. If the state is not populated, the laser is far off-resonant and no scattered photons appear. The state of the ion is therefore indicated by the presence or absence of scattered light.
The detection laser beam is generated by adjusting the frequency of the near-resonant Doppler cooling beam to resonance with the cycling transition.

5.2 Single-beam spin control

In this section the demonstration of spin control using the pulsed Raman system will be presented. A single train of laser pulses fulfilling the Raman resonance condition will therefor drive Raman transitions between two sublevels of the ground-state manifold of $^9Be^+$. The experimental implementation under given boundary conditions of the existing experiment, measurements and results will be discussed.

5.2.1 Qubit choice

In order to perform stimulated Raman transitions between two ground-state sublevels of $^9Be^+$, a qubit must be chosen, for which the resonance condition can be fulfilled by a single beam of the pulsed Raman laser. Furthermore the accessible free laser ports of the existing setup must allow the realization of required polarizations for reaching appropriate Rabi frequencies on the chosen qubit transition.

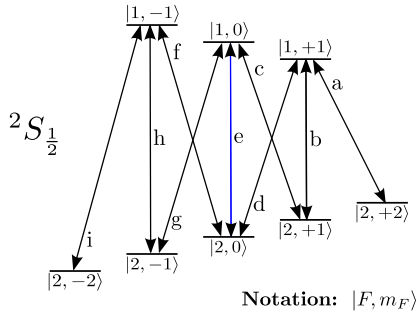

f_a =	853.644 MHz	$f_{\mathrm{rep},a}$ =	94.849 MHz
f_b =	1082.547 MHz	$f_{\mathrm{rep},b}$ =	98.414 MHz
f_c =	1239.921 MHz	$f_{\mathrm{rep},c}$ =	103.349 MHz
f_d =	1240.188 MHz	$f_{\mathrm{rep},d}$ =	103.340 MHz
f_e =	1397.562 MHz	$f_{\mathrm{rep},e}$ =	99.826 MHz
f_f =	1525.457 MHz	$f_{\mathrm{rep},f}$ =	101.697 MHz
f_g =	1525.724 MHz	$f_{\mathrm{rep},g}$ =	101.715 MHz
f_h =	1653.618 MHz	$f_{\mathrm{rep},h}$ =	97.272 MHz
f_{i} =	1764.456 MHz	$f_{\mathrm{rep,i}}$ =	98.026 MHz

Figure 5.6: Overview of all transitions frequencies between the hyperfine levels of the $^2S_{1/2}$ ground-state manifold of $^9Be^+$ at an applied magnetic field of 22.3 mT. Single-beam spin control with the pulsed Raman laser can be achieved on transition e with $|\downarrow\rangle = |F = 2, m_F = 0\rangle$ and $|\uparrow\rangle = |F = 1, m_F = 0\rangle$. The Raman resonance condition is fullfilled by $\nu_0 = 1397.562\,\mathrm{MHz} = q \cdot f_{\mathrm{rep}} = 14 \cdot 99.826\,\mathrm{MHz}$.

Resonance condition

As described in section 3.2.2, Rabi oscillations with a single pulsed laser beam can occur if the qubit splitting is an integer multiple of the repetition rate of the laser:

$$\omega_0 = q \cdot \omega_{\mathrm{rep}} \quad , q \in \mathbb{Z} \tag{5.1}$$

The frequency comb then contains teeth which are separated by the qubit splitting. A photon can be absorbed by one comb tooth and emitted into another one, in order to drive Raman transitions. The Rabi frequency will then be given by the sum over the pairs of comb teeth contributing to the process. Fulfilling this resonance condition is the most stringent requirement for demonstrating spin control. Due to the limited tuning range of the laser's repetition rate, $f_{\mathrm{rep,min}} = 99.82\,\mathrm{MHz}$ and $f_{\mathrm{rep,max}} = 100.21\,\mathrm{MHz}$, only one transition in the ground-state manifold of beryllium at an applied magnetic field of 22.3 mT exists, for which the resonance condition can be fulfilled with a single train of pulses. This transition occurs between $|2,0\rangle$ and $|1,0\rangle$, as shown in Figure 5.6. The frequency splitting of $\nu_0 = 1397.562\,\mathrm{MHz}$ can be achieved with a repetition rate of $f_{\mathrm{rep}} = 99.826\,\mathrm{MHz}$ multiplied by $q = 14$.

Magnetic field sensitivity

The $|2,0\rangle \leftrightarrow |1,0\rangle$ qubit transition is magnetic field dependent. Its magnetic field sensitivity is given by the derivative of the energy levels, described by the Breit-Rabi formula in Equation 3.64, with respect to the magnetic field. While both states of the field-independent transition $|2,1\rangle \leftrightarrow |1,1\rangle$ exhibit the same slope at the applied magnetic field of 22.3 mT, on this transition the slope of each qubit level has a different sign, as to be seen in Figure 3.9 discussed in section 3.3.1. The

resulting magnetic field sensitivity of the transition is given by 1.253 MHz/gauss. As consequence small fluctuations in the magnetic field change the qubit splitting. In order to keep these fluctuations as small as possible, a current servo loop, controlling the generation of the magnetic field, has been built. Further the temperature of the water which is cooling the magnetic field coils has been stabilized to $\pm 0.01°$C. For this the existing water reservoir has been enlarged and an accurate temperature sensor has been implemented.

Polarization and beam geometry

In order to identify the optimal polarization of the Raman beam maximizing the Raman coupling strength, the sum over all excited state Raman contributions must be calculated. Coupling of the $|2,0\rangle$ and $|1,0\rangle$ qubit states to excited states of the p-orbital can in general be obtained by any atomic polarization. The relevant matrix elements, scaled to the matrix element of the closed-cycle transition $^2S_{1/2}$, $|F = 2, m_F = 2\rangle \leftrightarrow {}^2P_{3/2}$, $|m_I = +3/2, m_J = +3/2\rangle$, their detunings and corresponding polarizations are summarized in Table 5.1. As discussed in section 3.3.2, the existence of several excited states can lead to destructive quantum interferences between different Raman contributions. A simple approximation can be obtained by neglecting the accurate detunings of the p-levels and applying the appropriate Clebsch-Gordan coefficients, given by the angular coupling coefficient in Equation 3.68. Following the notations shown in Figure 3.12 the Rabi frequency according to Equation 3.60 of the qubit transition $|2,0\rangle \leftrightarrow |1,0\rangle$ is found to be:

$$\Omega_{\mathrm{ofc}} = \frac{1}{3} g_0^2 (e_-^2 - e_+^2) \frac{\omega_{\mathrm{fs}}}{\Delta(\Delta - \omega_{\mathrm{fs}})} \tag{5.2}$$

With g_0 being the time-averaged, resonant single-photon Rabi frequency of the closed-cycle transition, ω_{fs} the fine-structure splitting between $^2P_{1/2}$ and $^2P_{3/2}$, and e_- and e_+ the left and right circular polarized components of the Raman beam. The optimal polarization for achieving the maximum Raman coupling is hence given by either a pure σ^+ or a pure σ^- polarization. In contrast, the contributions for a superposition of σ^+ and σ^- destructively interfere. As consequence the Rabi frequency is reduced by three orders of magnitude compared to the Rabi frequency which could be achieved under the same assumptions with a pure atomic σ polarization. Also the sum over the contributions of π transitions is nearly zero, as the different contributions have nearly the same value, but different signs. For demonstrating Rabi oscillations on the $|2,0\rangle \leftrightarrow |1,0\rangle$ qubit transition it is therefore strongly desirable to induce pure atomic σ couplings. This can be achieved with a circularly polarized laser beam whose direction is parallel to the quantization axis of the ion, given by the magnetic field direction.

ground state	excited state	matrix element	detuning	polarization
$\|\downarrow\rangle$	$^2P_{\frac{1}{2}}\,\|m_J{=}-\frac{1}{2}, m_I{=}-\frac{3}{2}\rangle$	−0.41245	+ 0.379	σ^-
$\|\downarrow\rangle$	$^2P_{\frac{1}{2}}\,\|m_J{=}-\frac{1}{2}, m_I{=}+\frac{3}{2}\rangle$	+0.32207	+ 0.414	π
$\|\downarrow\rangle$	$^2P_{\frac{1}{2}}\,\|m_J{=}-\frac{1}{2}, m_I{=}+\frac{3}{2}\rangle$	+0.38071	+ 0.460	σ^+
$\|\downarrow\rangle$	$^2P_{\frac{1}{2}}\,\|m_J{=}+\frac{1}{2}, m_I{=}+\frac{3}{2}\rangle$	+0.58092	+ 0.684	σ^+
$\|\downarrow\rangle$	$^2P_{\frac{1}{2}}\,\|m_J{=}+\frac{1}{2}, m_I{=}-\frac{3}{2}\rangle$	−0.47917	+ 0.730	π
$\|\downarrow\rangle$	$^2P_{\frac{1}{2}}\,\|m_J{=}+\frac{1}{2}, m_I{=}-\frac{3}{2}\rangle$	+0.11892	+ 0.765	σ^-
$\|\downarrow\rangle$	$^2P_{\frac{3}{2}}\,\|m_J{=}-\frac{3}{2}, m_I{=}+\frac{3}{2}\rangle$	+0.84989	+197.918	σ^-
$\|\downarrow\rangle$	$^2P_{\frac{3}{2}}\,\|m_J{=}-\frac{1}{2}, m_I{=}+\frac{3}{2}\rangle$	−0.69331	+198.334	π
$\|\downarrow\rangle$	$^2P_{\frac{3}{2}}\,\|m_J{=}-\frac{1}{2}, m_I{=}-\frac{3}{2}\rangle$	+0.30565	+198.334	σ^-
$\|\downarrow\rangle$	$^2P_{\frac{3}{2}}\,\|m_J{=}+\frac{1}{2}, m_I{=}-\frac{3}{2}\rangle$	−0.43126	+198.750	π
$\|\downarrow\rangle$	$^2P_{\frac{3}{2}}\,\|m_J{=}+\frac{1}{2}, m_I{=}+\frac{3}{2}\rangle$	−0.48981	+198.751	σ^+
$\|\downarrow\rangle$	$^2P_{\frac{3}{2}}\,\|m_J{=}+\frac{3}{2}, m_I{=}-\frac{3}{2}\rangle$	−0.52696	+198.166	σ^+
$\|\uparrow\rangle$	$^2P_{\frac{1}{2}}\,\|m_J{=}-\frac{1}{2}, m_I{=}-\frac{3}{2}\rangle$	−0.66737	− 1.018	σ^-
$\|\uparrow\rangle$	$^2P_{\frac{1}{2}}\,\|m_J{=}-\frac{1}{2}, m_I{=}+\frac{3}{2}\rangle$	−0.47917	− 0.983	π
$\|\uparrow\rangle$	$^2P_{\frac{1}{2}}\,\|m_J{=}-\frac{1}{2}, m_I{=}+\frac{3}{2}\rangle$	−0.23529	− 0.937	σ^+
$\|\uparrow\rangle$	$^2P_{\frac{1}{2}}\,\|m_J{=}+\frac{1}{2}, m_I{=}+\frac{3}{2}\rangle$	−0.35903	− 0.713	σ^+
$\|\uparrow\rangle$	$^2P_{\frac{1}{2}}\,\|m_J{=}+\frac{1}{2}, m_I{=}-\frac{3}{2}\rangle$	−0.32207	− 0.668	π
$\|\uparrow\rangle$	$^2P_{\frac{1}{2}}\,\|m_J{=}+\frac{1}{2}, m_I{=}-\frac{3}{2}\rangle$	+0.19242	− 0.633	σ^-
$\|\uparrow\rangle$	$^2P_{\frac{3}{2}}\,\|m_J{=}-\frac{3}{2}, m_I{=}+\frac{3}{2}\rangle$	−0.52695	+196.520	σ^-
$\|\uparrow\rangle$	$^2P_{\frac{3}{2}}\,\|m_J{=}-\frac{1}{2}, m_I{=}+\frac{3}{2}\rangle$	+0.43126	+196.937	π
$\|\uparrow\rangle$	$^2P_{\frac{3}{2}}\,\|m_J{=}-\frac{1}{2}, m_I{=}-\frac{3}{2}\rangle$	+0.48981	+196.937	σ^-
$\|\uparrow\rangle$	$^2P_{\frac{3}{2}}\,\|m_J{=}+\frac{1}{2}, m_I{=}-\frac{3}{2}\rangle$	−0.69331	+197.353	π
$\|\uparrow\rangle$	$^2P_{\frac{3}{2}}\,\|m_J{=}+\frac{1}{2}, m_I{=}+\frac{3}{2}\rangle$	+0.30566	+197.353	σ^+
$\|\uparrow\rangle$	$^2P_{\frac{3}{2}}\,\|m_J{=}+\frac{3}{2}, m_I{=}-\frac{3}{2}\rangle$	−0.84989	+197.769	σ^+

Table 5.1: Table of relevant Raman coupling contributions between the ground state qubit levels, $|\downarrow\rangle = |F = 2, m_F = 0\rangle = |m_J = -1/2, m_I = +1/2\rangle$ and $|\uparrow\rangle = |F = 1, m_F = 0\rangle = |m_J = +1/2, m_I = +1/2\rangle$, and levels of the excited p-states at an applied magnetic field of 22.3 mT. Shown are the corresponding transition matrix elements being $\geq 10^{-2}$ scaled to the matrix element of the closed-cycle transition between the $^2S_{1/2}$, $|2, 2\rangle$ and the $^2P_{3/2}$, $|m_I = +3/2, m_J = +3/2\rangle$ level as well as the respective detunings in GHz referenced to the transition between the $^2S_{1/2}$ and $^2P_{1/2}$ line centers and the corresponding atomic polarizations.

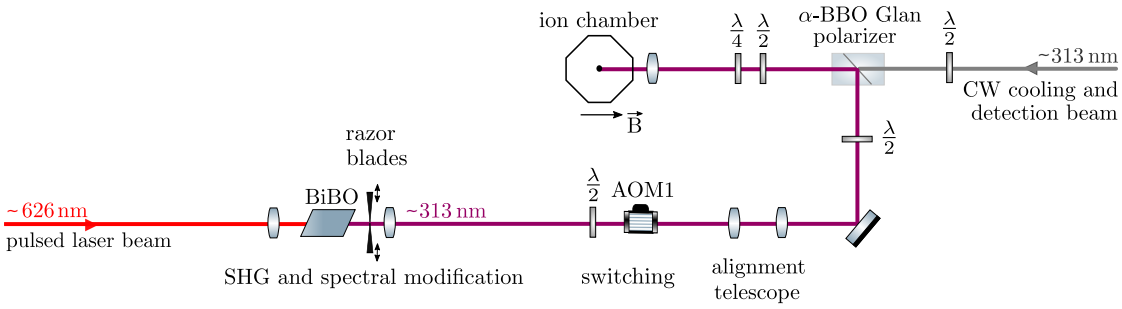

Figure 5.7: Overview of the experimental setup for single-beam spin control. The spectrally modified pulsed UV Raman beam is delivered free space from one opticle table to the optical table where the ion experiment is located. Here the beam passes a single-pass AOM setup for switching and a two-lens telescope for alignment purposes. The Raman pulse train is then overlapped with the CW cooling and detection beam by entering the side facet of an α-BBO Glan polarizer and focused onto the ion in counterpropagating direction with respect to the magnetic field. The polarizations are set to σ^+ for the CW and to σ^- for the pulsed beam.

5.2.2 Experimental setup

An overview of the entire experimental setup is shown in Figure 5.7. The key parts of the Raman system are placed on a separate optical table. The generated and spectrally modified pulsed UV beam is then sent to the table, where the ion experiment is located. Here the overlap with the cooling and detection beam, an alignment telescope and an AOM for switching is implemented. In order to reduce beam pointing instabilities, induced by separate vibrations on either one of the tables, both optical tables have been unfloated.

Raman system

The Raman laser system, as described in detail in chapter 4, allows for adjustment of the wavelength and the spectrum required for optimizing the performance of Rabi oscillations between the $|2,0\rangle \leftrightarrow |1,0\rangle$ qubit states at the applied magnetic field of 22.3 mT. Based on simulation results presented in section 3.3.3, the optimal Raman detuning and spectral properties have been estimated.
The exact output wavelength is tuned by changing the temperature of the SFG process generating light near 626 nm. Due to the subsequent frequency doubling this sets the UV wavelength and hence the detuning from the excited states during the Raman process.
For second-harmonic generation a single-pass process in a 4.5 mm long Brewster-cut BiBO crystal is applied. Here a focusing strength was chosen which results in a compromise between a high SHG conversion efficiency and appropriate spectral

properties. Due to the possibility of accurately blocking unwanted frequency components, a broader spectrum with higher available average power has generally been preferred. The subsequent spectral shaping is realized with a razor blade mounted closely behind the BiBO crystal as discussed in section 4.4.

Switching

In order to control the experimental probe duration of the Raman laser, an AOM in single-pass configuration is implemented. The switching is operated by the experiment control unit. To ensure precise timing it is locked to an external 10 MHz reference provided by the PTB. The frequency and orientation of the AOM are not of importance, since the Rabi oscillations are driven by pairs of comb teeth of the comb spectrum. An absolute shift of the entire comb structure due to the AOM does not affect the spacing between the comb teeth and is therefore not relevant. Due to availability a 110 MHz AOM[3] has been applied, implemented as down-shift and enabling efficiencies on the order of 65 %.

Beam alignment

In order to not affect the existing setup, the alignment of the pulsed Raman laser beam has been carried out by a two lens telescope, located before the α-BBO Glan polarizer combining the pulsed Raman beam with the CW cooling and detection beam. Besides generating a collimated beam with desired beam size, it has been designed such that a translation of the telescope's first lens results in a translation of the beam at the position of the ion. The amount of the translation is given by the ratio of the focal length of the second lens of the telescope and the focal length of the lens before the vacuum chamber, $f_{\mathrm{ion_{CW}}} = 150\,\mathrm{mm}$. In order to obtain a sensitive movement the focal length of the second lens of the telescope should hence be chosen as large as possible.

Beam overlap

The overlap of the beams is implemented by sending the pulsed laser beam through the side facet of an α-BBO Glan polarizer, which is applied in order to clean the polarization of the cooling and detection beam. The polarization of the pulsed Raman laser beam needs to be orthogonally linear compared to the p-polarization of the through going CW beam. By this up to 60 % of the light could be overlapped with the cooling and detection beam. The following $\lambda/2$ and $\lambda/4$ waveplates are set to generate σ^+ light for the cooling and detection beam, in order to drive transitions on the closed-cycle transition between the $^2S_{1/2}$, $|F = 2, m_F = 2\rangle$ and $^2P_{3/2}$, $|m_I = +3/2, m_J = +3/2\rangle$ level. The orthogonal, linear s-polarization

[3] Gooch and Housego, I-M110-2C10BB-3-GH27

of the pulsed Raman beam is therefore converted into circularly polarized light, corresponding to atomic σ^- transitions.

5.2.3 Measurements

In order to measure Rabi oscillations the Raman beam is aligned onto the ion and the resonance condition needs to be matched. A pre-alignment is carried out by shortening the duration of level depletion induced by near-resonant components of the spectrum. A more accurate alignment is subsequently performed by maximizing the dephasing induced by the laser during a spin-echo based Ramsey experiment. As an additional preparation step the accurate qubit frequency splitting under experimental conditions is determined. Imperfect experimental conditions lead to an offset of the frequency compared to the theoretical expected frequency according to the Breit-Rabi formula. This frequency difference can be measured in advance by using microwaves. A rough measurement is performed by scanning the resonance, whereas a more precise resolution is achieved with a Ramsey experiment. Furthermore the off-resonant laser field of the Raman beam induces a Stark shift of the qubit levels, which has to be considered. The amount can be calculated by the phase shift, measured with the spin-echo based Ramsey experiment used for the beam alignment. Based on these measurements the repetition rate of the laser is set. A scanning of the Raman resonance condition is subsequently implemented by scanning over the detuning of an off-resonant MW field being simultaneously applied with the laser irradiation. The parameter settings obtained by this procedure allow the realization of Rabi oscillations, where the Raman resonance condition is fulfilled by the simultaneous presence of the Raman laser beam and the MW tuning field.

Typical experimental sequence

For a typical experimental sequence a single beryllium ion is trapped and initialized in the $|2,2\rangle$ state as described in 5.1.4. In order to perform Rabi oscillations and other preparation measurements on the $|2,0\rangle \leftrightarrow |1,0\rangle$ qubit transition, the ion is prepared in the $|2,0\rangle$ state by applying a sequence of two resonant MW pulses as shown in Figure 5.8. The first one transfers the population to the $|1,1\rangle$ and the second one to the $|2,0\rangle$ level. Following the application of the Raman laser beam, the population of $|2,0\rangle$ is transferred back to $|2,2\rangle$ for detection, as described in section 5.1.4. To avoid coexistent off-resonant transitions from the $|2,1\rangle$ state into the $^2P_{3/2}$ manifold during detection, the population from this state is shelved to either the $|1,1\rangle$ state or the $|1,0\rangle$ state before applying the detection beam.

State depletion

Since the qubit transition is field sensitive and the transition frequency is not stable over time, the beam is aligned by using a process which does not depend

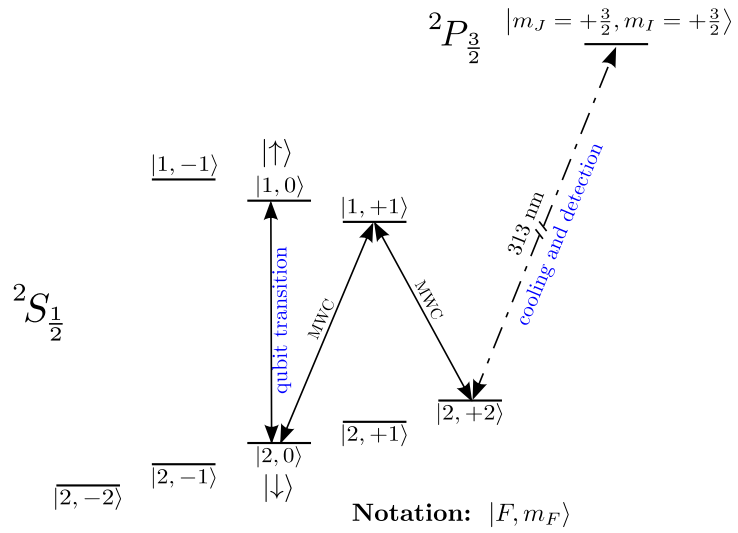

Figure 5.8: Hyperfine level structure and transitions of $^9Be^+$ relevant for the demonstration of single beam induced carrier Raman transitions on the $|\downarrow\rangle = |2,0\rangle \leftrightarrow |\uparrow\rangle = |1,0\rangle$ qubit. After loading and cooling, the ion is initialized in the $|2,2\rangle$ state. A sequence of two resonant microwave carrier (MWC) pulses transfers the population into the $|2,0\rangle$ state. Subsequent to probing the ion with the Raman laser, the population of the $|2,0\rangle$ state is transferred back to the initial $|2,2\rangle$ state and detected by collecting the fluorescence signal induced by the detection beam, being resonant with the closed-cycle transition between $S_{1/2}$, $|F = 2, m_F = 2\rangle \leftrightarrow P_{3/2}$, $|m_I = +3/2, m_J = +3/2\rangle$.

on the frequency resonance condition. A simple pre-alignment has been carried out by measuring the level depletion induced by near-resonant components of the spectrum. For this the UV spectrum was completely uncut in order to contain as many frequency components as possible close to resonance with the excited states. The ion can be prepared in any state of the ground-state manifold from which coupling to an excited state occurs at the applied laser polarization. Here the $|2,0\rangle$ qubit state was chosen. Illuminating the ion with the laser beam partially populates the excited states, which then decay into multiple levels of the ground-state manifold. By this the population of the prepared state decreases. By minimizing the time in which the level population decreases, the beam can be aligned onto the ion. After this pre-alignment the near-resonant components of the spectrum are blocked by translating the razor blade behind the SHG crystal, until no depletion occurs over a timescale of interest.

Ramsey experiments

As a further preparation step a Ramsey experiment is performed. This allows a more precise alignment of the Raman beam onto the ion and also the measurement of the Stark shift induced by the off-resonant laser beam. The amount of Stark

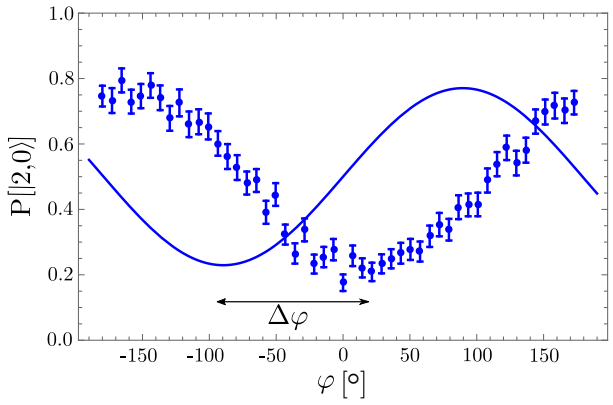

Figure 5.9: Ramsey phase scan used for the alignment of the Raman beam and for the calculation of the Stark shift. The solid line represents the level population of the $|2,0\rangle$ state depending on the phase of the second applied $\frac{\pi}{2}$-pulse without influence of the Raman laser beam. The data points correspond to the phase change induced by irradiation of the Raman laser beam. The phase shift $\Delta\varphi$ between both curves has been maximized in order to align the Raman beam.

shift is required for setting the correct repetition rate of the laser, fulfilling the Raman resonance condition. It furthermore allows an estimation of the electric field of the laser at the position of the ion. From this the expected Rabi frequency and the expected π-time for Rabi oscillations can be calculated.
The measurement is based on a comparison of phase accumulation in a superposition state of the qubit levels. The phase accumulated during a specific time without laser irradiation is compared to the accumulated phase collected during the same amount of time including the effect of the off-resonant laser light. Due to the energy level shifts caused by the laser, the rate of phase accumulation is changed. The dephasing therefore in conclusion allows the calculation of the Stark shift induced by the Raman laser. The basic sequence of such an experiment is as follows: The ion is prepared in the $|2,0\rangle$ state of the qubit. A $\frac{\pi}{2}$-pulse, resonant with the $|1,0\rangle$ qubit level, sets the ion into the superposition state. The off-resonant laser beam is then applied for a certain time t_1. Subsequently the accumulated phase is measured by applying a second $\frac{\pi}{2}$-pulse and detecting the population of the $|2,0\rangle$ state. By scanning over the phase of the second $\frac{\pi}{2}$-pulse and comparing the measurement with laser irradiation to an identical measurement without the influence of the laser, the dephasing $\Delta\varphi$ due to the laser can be calculated, as exemplarily shown in Figure 5.9. The corresponding change of transition frequency is given by:

$$\Delta f = \frac{\Delta\varphi}{2\pi \cdot t_1} \tag{5.3}$$

The sign of the transition frequency shift can be calculated separately as described in section 3.1.4. The calculation of the equivalent Stark shift of the qubit transition

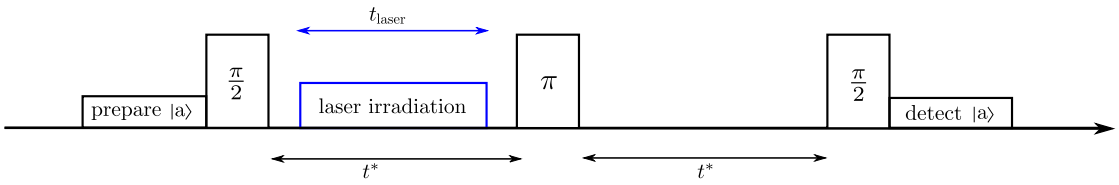

Figure 5.10: Illustration of a Ramsey sequence applied for beam alignment and Stark shift estimation, including a single spin-echo π-pulse. The ion is prepared in state $|a\rangle$ of the transition between $|a\rangle$ and $|b\rangle$. A first $\frac{\pi}{2}$-pulse resonant with the transition to $|b\rangle$ sets the ion into a superposition state. Within the first time period of t^*, the laser is applied for a duration of $t_l \leq t^*$, whereas in the second time period of equal duration t^*, dephasing of the unperturbed atomic transition is collected. The spin-echo π-pulse inbetween cancels out dephasing caused by the influence of magnetic field fluctuations and other sources. The total accumulated phase is measured by applying a second $\frac{\pi}{2}$-pulse and subsequently detecting the population of $|a\rangle$.

allows an estimation of the electric field of the laser at the position of the ion. With this effective field the expected Rabi frequency can be calculated.

In order to reduce the influence of magnetic field fluctuations, spin-echo pulses are applied during each Ramsey sequence. The implementation of a single spin echo is depicted in Figure 5.10. The time between the $\frac{\pi}{2}$-pulses is separated into two parts of same length t^*, whereas in between a resonant spin-echo π-pulse is applied. During the first period of t^* the laser is employed for a time $\mathrm{t_l} \leq t^*$, whereas during the second period of t^* dephasing of the unperturbed atomic transition is collected. Because of the π-pulse applied in between, dephasing due to other sources, such as the drifts in the bias field, can be canceled out. By implementing several spin-echo sequences, the total amount of time during which the laser is illuminating the ion can be increased, without being limited due to the low coherence time of the field-dependent qubit. The longer duration of laser interaction leads to a larger phase shift, which allows a more accurate alignment of the beam.

Carrier transition resonance scan

Due to the magnetic field sensitivity of the qubit transition, its frequency and hence the repetition rate required to fulfill the resonance conditions varies over time. Since the repetition rate of the Raman laser cannot be changed on a fast timescale and any adjustment requires realignment of the laser beam onto the ion, an alternative approach to tune the resonance has been implemented. An off-resonant MW field was applied simultaneously with the Raman laser interaction. The oscillating magnetic field induces an AC Zeeman shift of the qubit levels, depending on the

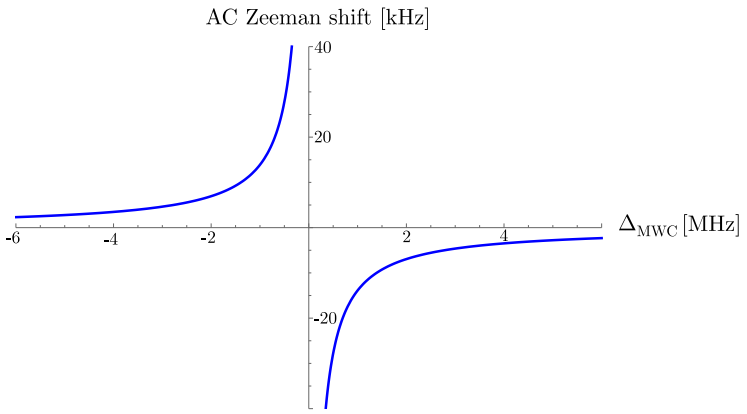

Figure 5.11: Calculated AC Zeeman shift for the $|2,0\rangle \leftrightarrow |1,0\rangle$ qubit transition, depending on the detuning frequency of the off-resonant MW tuning field, for $t_{\varphi\pi} = 3\,\mu$s.

applied detuning [127, 59]. By scanning over the detuning within a reasonable range, a resonance scan of the Raman carrier condition is implemented.
The dependence of the AC Zeeman shift on the MW detuning can be experimentally obtained by performing a Ramsey experiment as described before. Instead of applying the Raman laser for a duration t_{l} and determining the Stark shift induced by the laser, here the MW-field is implemented for a duration t_{MW} and the AC Zeeman shift is obtained. By scanning over t_{MW}, the time required to implement a phase shift of $\Delta\varphi = \pi$ was determined, denoted as $t_{\varphi\pi}$, for each applied MW detuning. According to the relation given by Equation 5.3, the corresponding transition frequency shift is given by:

$$ACZS = \frac{\pi}{2\pi \cdot t_{\varphi\pi}} \tag{5.4}$$

The resulting calculated dependence of the AC Zeeman shift (ACZS) on the applied detuning of the MW field Δ_{MWC} is shown in Figure 5.11.
To not accidentally drive transitions with the applied MW field, the detuning should not be chosen too close to resonance. The appropriate tuning range of the ACZS for the applied power level of the MW field during the experiments was approximated between the absolute values of 2 kHz and 38 kHz. To make use of the largest possible scanning range, the value corresponding to half of the maximum ACZS tuning range, denoted as $\Delta\nu_{\mathrm{ACZS}}$, is taken into account when setting the repetition rate of the laser:

$$f_{\mathrm{rep}} = (\nu_{\text{Breit-Rabi}} + \Delta\nu_{\mathrm{BR,offset}} + \Delta\nu_{\text{Stark shift}} + \Delta\nu_{\mathrm{ACZS}})/14 \tag{5.5}$$

Here $\nu_{\mathrm{BreitRabi}}$ is the theoretical expected level splitting according to the Breit-Rabi formula in Equation 3.64, $\Delta\nu_{\mathrm{BR,offset}}$ denotes the frequency deviation due to imperfect experimental conditions and $\Delta\nu_{\mathrm{Starkshift}}$ is the Stark shift caused by the

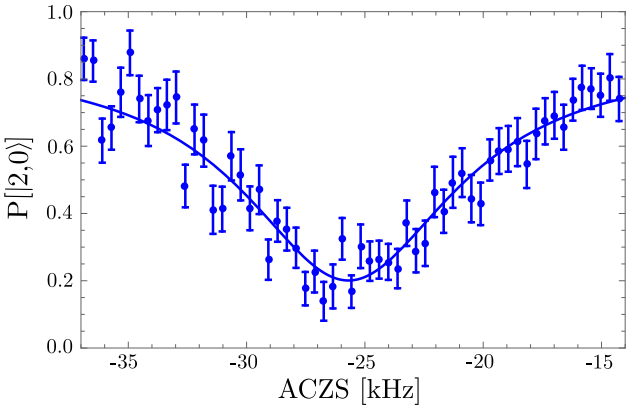

Figure 5.12: Resonance scan for a carrier Raman transition on the $|2,0\rangle \leftrightarrow |1,0\rangle$ qubit. Shown is the population of the $|2,0\rangle$ state as a function of the AC Zeeman shift caused by the additionally applied off-resonant MW field. The solid line shows a fit of the data. At a frequency near -26 kHz, the simultaneous presence of the MW tuning field and the Raman laser beam fulfills the carrier resonance condition and the population of the $|2,0\rangle$ state drops.

Raman laser. For the resonance scan the Raman laser and the detuned MW field are applied for a duration equal to the expected π-time of the Rabi oscillations, estimated by the previously performed Ramsey experiment. By scanning over the detuning of the MW field within the discussed range and detecting the population of the prepared $|2,0\rangle$ state, the resonance for the carrier Raman condition was obtained, as exemplarily shown in Figure 5.12. On resonance the simultaneous presence of the MW tuning field and the Raman laser beam fulfills the carrier Raman condition and the population of the prepared state drops.

Rabi oscillations

To drive Rabi oscillations the AC Zeeman shift is set to the value derived from the previous resonance scan. The simultaneous presence of the corresponding MW tuning field and the Raman laser beam then fulfills the carrier Raman resonance condition and causes the population to oscillate between the two qubit states. The resulting Rabi oscillations are demonstrated in Figure 5.13. Shown is the population of the $|2,0\rangle$ qubit state depending on the laser probe duration. The π-time of the data is $t_\pi = 29.04\,\mu\text{s} \pm 0.07\,\mu\text{s}$. It has been optimized by continuously uncutting the spectrum in order to include as many near-resonant frequency components as possible, as long as no drop of contrast could be measured. The decoherence time has not been influenced by this and is approximated to $233\,\mu\text{s} \pm 23\,\mu\text{s}$. The repetition rate of the laser was measured to be $f_{\text{rep}} = 99.845515\,\text{MHz}$, fulfilling the resonance condition with $q = 14$ and a qubit splitting of $\nu_{\text{qubit}} = 1397.837210\,\text{MHz}$.

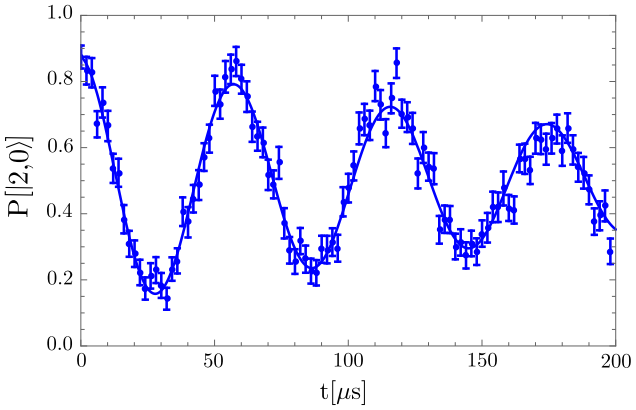

Figure 5.13: Carrier Rabi oscillations on the $|2,0\rangle \leftrightarrow |1,0\rangle$ qubit transition induced by a single train of the pulsed Raman laser. Shown is the population of the $|2,0\rangle$ state depending on the laser probe duration. The fit (solid line) corresponds to a π-time of $t_\pi = 29.04\,\mu\text{s} \pm 0.07\,\mu\text{s}$.

5.2.4 Discussion

The realization of Rabi oscillations driven by a single beam of the pulsed Raman laser system, demonstrates the successful control of the ion's internal degree of freedom. The data illustrate the first coherent spin control using a single train of the optical frequency comb. In this section, the Rabi frequency will be compared to simulations and sources of decoherence as well as improvement strategies will be discussed.

Comparison with simulations

The Rabi frequency depends linearly on the average laser power and the inverse of the focal beam size. Furthermore the detuning, the spectral bandwidth and the pulse duration influence the rate of Rabi oscillations. In order to compare the measurements with simulations these parameters have been extracted from the experimental setup.
The average power of the beam has been measured before the beam overlap with the cooling and detection beam is carried out. The measured value of 14.5 mW at this position is reduced due to losses induced at the following two mirrors, the α-BBO Glan polarizer, two waveplates, one lens and the vacuum window, such that the power at the position of the ion is estimated to be 8.0 mW. The losses are expected to be dominated by the α-BBO Glan polarizer showing a maximal achievable efficiency of 60%. Since the optimized alignment onto the ion might not coincide with perfect incoupling into the polarizer, an uncertainty range of $\pm$ 0.5 mW is estimated for the simulations.
In order to estimate the focal size of the Raman beam at the position of the ion, a

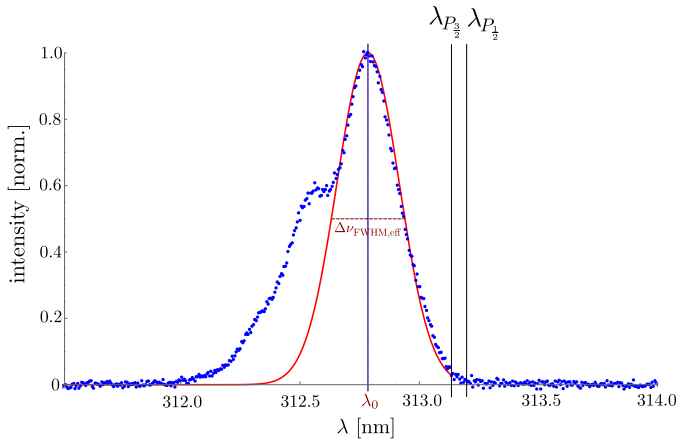

Figure 5.14: UV spectrum of the Raman laser as present during the measurements of the carrier Rabi oscillations on the $|2,0\rangle \leftrightarrow |1,0\rangle$ qubit transition, shown in figure 5.13. The peak wavelength of $\lambda_0 = 312.785\,\mathrm{nm}$ corresponds to a Raman detuning of $\Delta = 1.260\,\mathrm{THz}$ from the line center of the $^2P_{1/2}$ level. The main peak of the spectrum is fitted by a gaussian function (solid line) which corresponds to an effective spectral FWHM bandwidth of $\Delta\nu_{\mathrm{FWHM}} = 940\,\mathrm{GHz}$. Within the gaussian fit of the main peak 73.5 % of the measured average power is contained.

flip mirror was placed at a free position before the Raman beam is overlapped with the cooling and detecting beam. At the distance corresponding to the distance at which the focal lens is positioned, the beam size and divergence angle were measured using a beam cam[4]. By adjusting the beam height to graze across the chip surface, the extension of the beam in the horizontal direction could further be visualized on the CCD camera attached to the imaging system. This allows an additional estimation of the true beam extension at the position of the ion by comparing its size to the segmented trap structure. The focal size along this direction can in general be set as tight as possible for the applied focusing lens, but is for the pulsed Raman laser beam limited by the size of the side window of the α-BBO Glan polarizer. The focusing strength in the vertical is further geometrically limited by the trap design, allowing for a minimum focal radius of approximately $15\,\mu\mathrm{m} - 20\,\mu\mathrm{m}$. In order to obtain a tight focus, the beam profile was set to provide an ellipticity of $\mathrm{e} \approx 0.5$, with a mean focal radius of $20\,\mu\mathrm{m} \pm 5\,\mu\mathrm{m}$. The large uncertainty range is assumed because the extension of the beam visualized on the trap structure appeared to be larger than theoretically expected and due to a non-perfect beam collimation.
The spectral properties of the beam can be extracted from the measured spectrum, which is shown in Figure 5.14. The spectral bandwidth of the main peak at $\lambda_0 = 312.785\,\mathrm{nm}$ is fitted by a gaussian function with an effective bandwidth of $\Delta\lambda_{\mathrm{FWHM}} = 0.31\,\mathrm{nm}$, corresponding to a spectral bandwidth of $\Delta\nu_{\mathrm{FWHM}} = 940\,\mathrm{GHz}$.

[4]DAT-BladeCam-XHR-UV

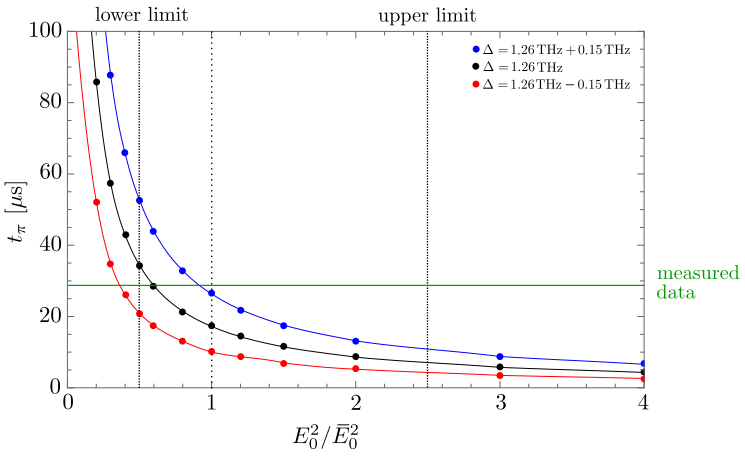

Figure 5.15: Numerical simulations comparing the measured data (green line) of the single-beam carrier Rabi flopping with simulations. Shown is the calculated π-time for three different detunings depending on the squared electric field amplitude E_0^2 scaled to the mean values resulting from the approximated average power, focal radius and pulse duration, $E_0^2/\bar{E}_0^2$. Assumed is a gaussian envelope function as shown in Figure 5.14 with an average power of $P_{\mathrm{av}} = 8.0\,\mathrm{mW} \pm 0.5\,\mathrm{mW}$, a focal radius of $w_0 = 20\ \mu\mathrm{m} \pm 5\,\mu\mathrm{m}$ and a pulse duration of $\tau_{\mathrm{FWHM}} = 2.0\,\mathrm{ps} \pm 0.5\,\mathrm{ps}$. The influence of the pulse duration in terms of temporal broadening compared to the time-bandwidth limited pulse duration is taken into account, by keeping the spectral width of $\Delta\nu_{\mathrm{FWHM}} = 940\,\mathrm{GHz}$ constant and reducing the intensity respectively. The resulting lower limit according to the assumed uncertainty range yields $E_0^2/\bar{E}_0^2 \approx 0.5$ and an upper limit of $E_0^2/\bar{E}_0^2 \approx 2.5$. The black data points correspond to the measured detuning of $\Delta = 1.26\,\mathrm{THz}$. The red data points correspond to a detuning of $\Delta = 1.26\,\mathrm{THz} - 0.15\,\mathrm{THz}$ and the blue data points to a detuning of $\Delta = 1.26\,\mathrm{THz} + 0.15\,\mathrm{THz}$. The solid lines represent guides to the eye.

The Raman detuning is determined by the distance between the peak of the spectrum and the line center of the $^2P_{1/2}$ level at 313.1974 nm [83]. This detuning is calculated to be $\Delta = 1.26\,\mathrm{THz}$.
For the direct measurement of the pulse duration no diagnostic tools were available. Assuming time bandwidth limited pulses a lower limit can be estimated from the measured spectrum. For the fitted gaussian pulse this lower limit is near 0.5 ps. According to the simulations presented in Figure 4.15, pulse durations near 2.5 ps are expected for the applied crystal length and focusing strength. Based on an estimation performed with the two-beam approach presented in section 5.3, a minimum pulse duration of 1.6 ps is assumed leading to an expected pulse duration of $\tau_{\mathrm{FWHM}} = 2.0\,\mathrm{ps} \pm 0.5\,\mathrm{ps}$ for the simulations.

Figure 5.15 shows the calculated π-time for different detunings according to the assumed uncertainty range, depending on the squared electric field amplitude E_0^2 scaled to the squared electric field amplitude given by the approximated average

laser power, focal width and pulse duration, $E_0^2/\bar{E}_0^2$. A gaussian-shaped spectrum has been applied, providing the effective bandwidth of the main peak of the measured spectrum as shown in Figure 5.14. The power contained in the far detuned spectral components has been neglected. The measured π-time lies within the assumed uncertainty range of the parameters influencing the squared electric field amplitude for the measured detuning of 1.26 THz. Assuming an uncertainty of 0.05 nm corresponding to 150 GHz for the absolute frequencies determined with the spectrometer, the simulation data for the lower boundary concerning the detuning slightly disagrees with the measured data, whereas for the upper boundary concerning the detuning an excellent agreement is shown. Not taken into account in the simulations are possible deviations of the measured spectral bandwidth and the chirp of the pulses. Based on the agreement between experiment and simulation, the chirp seems not to significantly influence the quantum control of beryllium ions for the single-beam approach. This might be supported by the low value of $q = 14$ fulfilling the resonance condition. Compared to the entire width of the spectrum, with almost 10 000 contributing comb teeth within the FWHM and about 22 000 contributing comb modes in total, the spacing between the pairs of teeth contributing to the Rabi frequency is quite narrow, which therefore possibly eliminates the influence of the chirp.

Sources of decoherence

The amplitude of the Rabi oscillations measured with the frequency comb decreases on an unexpectedly short timescale. A dominant source of decoherence during Raman transitions is typically given by scattering induced by the off-resonant laser irradiation. The scattering is mainly caused by the near-resonant frequency components of the spectrum. This effect has been applied for the pre-alignment of the Raman beam. By the subsequent blocking of the near-resonant spectral components, the Raman scattering should have been eliminated on the chosen timescale, which by far exceeds the measured decoherence time. Since furthermore no change of the decoherence could be obtained by varying the amount of blocked near-resonant spectral components between different measurements of Rabi flopping, the limiting effect during the Raman process is expected to have a different source than the off-resonant laser irradiation. Simulations further conform this assumption. The calculated probability of scattering during the corresponding π-time is between $0.71 \cdot 10^{-4}$ and $3.34 \cdot 10^{-4}$ for the assumed values within the discussed uncertainty range.
For comparison, Rabi flopping with the MWC electrode has been performed, under conditions providing a comparable sensitivity to decoherence as expected for the pulsed Raman laser. For this the MWC drive has been attenuated in order to result in a similar π-time near 30μs. Thus the MWC drive is expected to exhibit a comparable susceptibility to frequency fluctuations as the pulsed Raman laser.

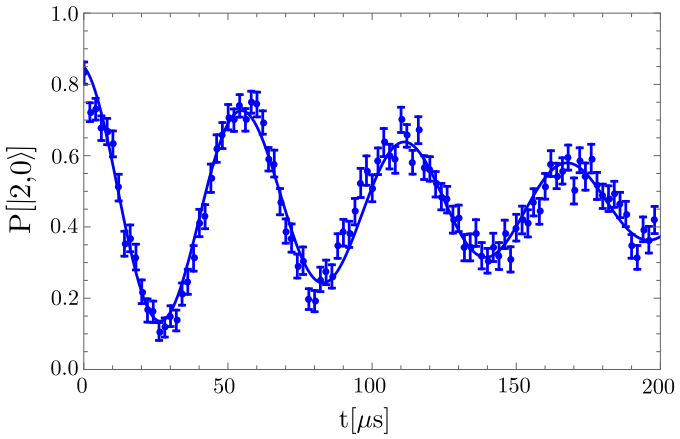

Figure 5.16: Measurement data of carrier Rabi flopping on the $|2,0\rangle \leftrightarrow |1,0\rangle$ qubit transition induced by a slow MWC pulse for decoherence demonstration purposes. Shown is the population of the prepared $|2,0\rangle$ state depending on the probe duration of the attenuated MWC pulse. The solid line shows a fit of the data. The attenuation has been set to result in a comparable π-time to the one obtained by the Raman laser induced carrier Rabi flopping shown in Figure 5.13, being near $30\,\mu$s. On these time scales the decoherence time for the use of microwaves is found to be limited by the same amount as observed during measurements with the Raman laser. The Raman laser beam can hence be excluded as the main source of the observed strong decoherence.

The measured qubit evolution under these conditions is shown in Figure 5.16. The data prove the MWC drive to suffer from a similar amount of decoherence. The Raman laser can therefore be excluded as main source causing the strong observed decoherence.
Decoherence of the qubit states can also be caused by fluctuations in the local magnetic field. A possible reason could be changes in the geometry of the coils induced by fluctuations of the cooling water temperature flowing around them. To test the dependency of the qubit splitting on the water temperature, a systematic test series has been performed. The qubit splitting has been measured for different temperatures of the cooling water, as shown in Figure 5.17. The measurements lead to a dependency of $-48.4\,\mathrm{kHz/°C}$ for the $|2,0\rangle \leftrightarrow |1,0\rangle$ qubit transition. Compared to the observed temperature fluctuations of $\pm 0.01\,°\mathrm{C}$, this can also be excluded as main source of decoherence.
Summarizing, the actual dominating source of decoherence could not be identified. The limiting effect could nevertheless be caused by fluctuations in the local magnetic field having a different origin than the cooling water temperature, as for example noise on the currents to the coils or other ambient field fluctuations, such as from near-by transformers in power supplies. Nevertheless, within the severe experimental constraints, these results successfully demonstrate control over the internal states of the $^9Be^+$ ion using the pulsed Raman laser system.

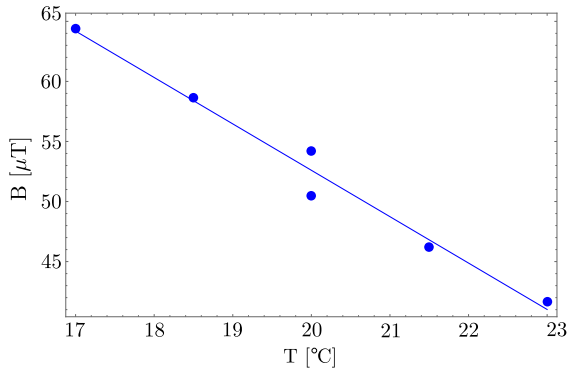

Figure 5.17: Experimental data of the magnetic field dependence on the water temperature cooling the magnetic field coils measured on the $|2,2\rangle \leftrightarrow |1,1\rangle$ qubit transition. The data fit (solid line) yields to a frequency change of -48.4 kHz/°C for the investigated $|2,0\rangle \leftrightarrow |1,0\rangle$ qubit transition, wherefor the observed temperature fluctuations of $\pm 0.01\,°C$ can be excluded as main source of decoherence.

Improvement strategies

Improvements could in general be pursued in terms of reaching higher Rabi frequencies and longer coherence times. A reduction of the magnetic field sensitivity for the existing experimental setup reducing decoherence could be achieved by operating with a different magnetic field strength. This modifies the qubit splitting itself as well as the magnetic field sensitivity of each state. This approach has not been pursued, since only a factor of two could be gained for choosing appropriate settings still allowing qubit control with a single pulse train of the Raman laser and further because a change of magnetic field requires readjustment of several components of the existing experiment.
Strong improvements can instead in general be expected for enhancing the Rabi frequency, by which also the sensitivity to field instabilities would be reduced. Here a systematic survey of the optimal detuning and the optimal spectral distribution of comb modes gives room for strong improvements. Since a change of wavelength is slow and requires a realignment of the beam, no systematic optimization has been performed so far. Also an increase of intensity at the position of the ion would lead to stronger Raman couplings. Here an independent beam line, allowing for tighter focusing, a shorter optical path length and less power losses due to additionally required optical components would enhance the intensity. By additionally applying a special crystal coating, the UV Fresnel losses of 31 % for Brewster-cut crystals could also be strongly reduced. Further, once optimal parameters concerning the spectral bandwidth have been found, the UV power could possibly be increased by applying an enhancement cavity during SHG [105, 106], as widely established for CW lasers [123, 128] and also for pulsed lasers [129] in order to enhance the generated UV power.

5.3 Multiple-beam qubit control

This section deals with the demonstration of qubit control implemented by two separated beams of the Raman laser. By introducing a relative frequency shift between both beams, carrier and sideband transitions are driven by beat notes between both combs. The absorption from a photon from one beam tooth and emission into a tooth originating from the other beam causes a momentum change, allowing to couple to the ion's motion. The implementation of spin control and spin-motion coupling under given boundary conditions of the existing experiment, measurements and results will be discussed.

5.3.1 Qubit choice

In contrast to the single-beam approach, discussed in the previous section, the two-beam configuration in general allows qubit control of any beryllium ground-state sublevel transition. The Raman resonance condition is fulfilled by a relative frequency shift between both beams, being controlled by two AOMs. Still, the geometry of free optical ports limits the polarizations being realizable and sets the direction of possible motional coupling.

Resonance condition

Raman transitions can be driven by an optical frequency comb if pairs of comb teeth exist, which are separated by the qubit frequency. For the single-beam approach these teeth were provided from one frequency comb. For the two-beam approach the resonance condition is fulfilled by shifting the beam's frequencies relative to each other, such that teeth from the one beam paired with teeth from the other beam are resonant with the qubit splitting, as discussed in section 3.2.3. The resonance condition is given by:

$$j \cdot f_{\mathrm{rep}} \pm \Delta_{\mathrm{AOM}} = \nu_{\mathrm{qubit}} \quad , j \in \mathbb{Z} \tag{5.6}$$

With j being an integer, f_{rep} the repetition rate of the laser and ν_{qubit} the qubit splitting. Δ_{AOM} is the relative frequency shift between both combs, fulfilling the resonance condition. As it can be arbitrarily set by sending each beam through an AOM, any transition of the ground-state manifold of beryllium can be chosen as the qubit. Due to the immense advantage of the first-order field-independent transition in terms of coherence times, it is convenient to choose the $|2,1\rangle \leftrightarrow |1,1\rangle$ transition. The qubit is illustrated in Figure 5.4, its frequency is $\nu_0 = 1082.547\,\mathrm{MHz}$.

Beam geometry and polarization

In order to maximize the achievable Raman coupling strength, the polarization of both beams needs to be optimized for the field-independent qubit transition.

ground state	excited state	matrix element	detuning	polarization
$\|\downarrow\rangle$	$^2P_{\frac{1}{2}}\,\|m_J{=}-\frac{1}{2}, m_I{=}+\frac{1}{2}\rangle$	−0.52589	+ 0.257	σ^-
$\|\downarrow\rangle$	$^2P_{\frac{1}{2}}\,\|m_J{=}-\frac{1}{2}, m_I{=}+\frac{3}{2}\rangle$	+0.11768	+ 0.303	π
$\|\downarrow\rangle$	$^2P_{\frac{1}{2}}\,\|m_J{=}+\frac{1}{2}, m_I{=}+\frac{3}{2}\rangle$	+0.57735	+ 0.400	σ^+
$\|\downarrow\rangle$	$^2P_{\frac{1}{2}}\,\|m_J{=}+\frac{1}{2}, m_I{=}+\frac{1}{2}\rangle$	−0.56523	+ 0.527	π
$\|\downarrow\rangle$	$^2P_{\frac{1}{2}}\,\|m_J{=}+\frac{1}{2}, m_I{=}-\frac{1}{2}\rangle$	+0.23828	+ 0.572	σ^-
$\|\downarrow\rangle$	$^2P_{\frac{3}{2}}\,\|m_J{=}-\frac{3}{2}, m_I{=}+\frac{3}{2}\rangle$	−0.70623	+197.759	σ^-
$\|\downarrow\rangle$	$^2P_{\frac{3}{2}}\,\|m_J{=}-\frac{1}{2}, m_I{=}+\frac{3}{2}\rangle$	+0.57591	+198.176	π
$\|\downarrow\rangle$	$^2P_{\frac{3}{2}}\,\|m_J{=}-\frac{1}{2}, m_I{=}+\frac{1}{2}\rangle$	−0.40977	+198.177	σ^-
$\|\downarrow\rangle$	$^2P_{\frac{3}{2}}\,\|m_J{=}+\frac{1}{2}, m_I{=}+\frac{1}{2}\rangle$	−0.57879	+198.593	π
$\|\downarrow\rangle$	$^2P_{\frac{3}{2}}\,\|m_J{=}+\frac{1}{2}, m_I{=}+\frac{3}{2}\rangle$	−0.40672	+198.594	σ^+
$\|\downarrow\rangle$	$^2P_{\frac{3}{2}}\,\|m_J{=}+\frac{3}{2}, m_I{=}+\frac{1}{2}\rangle$	+0.70799	+199.010	σ^+
$\|\uparrow\rangle$	$^2P_{\frac{1}{2}}\,\|m_J{=}-\frac{1}{2}, m_I{=}+\frac{1}{2}\rangle$	+0.52589	− 0.826	σ^-
$\|\uparrow\rangle$	$^2P_{\frac{1}{2}}\,\|m_J{=}-\frac{1}{2}, m_I{=}+\frac{3}{2}\rangle$	+0.56523	− 0.780	π
$\|\uparrow\rangle$	$^2P_{\frac{1}{2}}\,\|m_J{=}+\frac{1}{2}, m_I{=}+\frac{3}{2}\rangle$	+0.57735	− 0.682	σ^+
$\|\uparrow\rangle$	$^2P_{\frac{1}{2}}\,\|m_J{=}+\frac{1}{2}, m_I{=}+\frac{1}{2}\rangle$	+0.11768	− 0.556	π
$\|\uparrow\rangle$	$^2P_{\frac{1}{2}}\,\|m_J{=}+\frac{1}{2}, m_I{=}-\frac{1}{2}\rangle$	−0.23828	− 0.510	σ^-
$\|\uparrow\rangle$	$^2P_{\frac{3}{2}}\,\|m_J{=}-\frac{3}{2}, m_I{=}+\frac{3}{2}\rangle$	−0.70799	+196.677	σ^-
$\|\uparrow\rangle$	$^2P_{\frac{3}{2}}\,\|m_J{=}-\frac{1}{2}, m_I{=}+\frac{3}{2}\rangle$	+0.57879	+197.094	π
$\|\uparrow\rangle$	$^2P_{\frac{3}{2}}\,\|m_J{=}-\frac{1}{2}, m_I{=}+\frac{1}{2}\rangle$	+0.40672	+197.094	σ^-
$\|\uparrow\rangle$	$^2P_{\frac{3}{2}}\,\|m_J{=}+\frac{1}{2}, m_I{=}+\frac{1}{2}\rangle$	+0.57591	+197.511	π
$\|\uparrow\rangle$	$^2P_{\frac{3}{2}}\,\|m_J{=}+\frac{1}{2}, m_I{=}+\frac{3}{2}\rangle$	−0.40978	+197.511	σ^+
$\|\uparrow\rangle$	$^2P_{\frac{3}{2}}\,\|m_J{=}+\frac{3}{2}, m_I{=}+\frac{1}{2}\rangle$	−0.70622	+197.927	σ^+

Table 5.2: Table of relevant Raman coupling contributions between the field-independent qubit levels, $|\downarrow\rangle = |F = 2, m_F = 1\rangle = |m_J = -1/2, m_I = +3/2\rangle$ and $|\uparrow\rangle = |F = 1, m_F = 1\rangle = |m_J = +1/2, m_I = +3/2\rangle$, and levels of the excited p-states at an applied magnetic field of 22.3 mT. Shown are the corresponding transition matrix elements being $\geq 10^{-2}$ scaled to the matrix element of the closed-cycle transition between the $^2S_{1/2}$, $|F = 2, m_F = 2\rangle$ and the $^2P_{3/2}$, $|m_I = +3/2, m_J = +3/2\rangle$ level as well as the respective detunings in GHz referenced to the transition between the $^2S_{1/2}$ and $^2P_{1/2}$ line centers and the corresponding atomic polarizations.

Besides the optical trap access used for the single-beam approach, as discussed in section 5.2.2, the experimental setup offers one additional free laser port. The direction is orthogonal to the previously implemented beam and to the magnetic field direction, as shown in Figure 5.18. The polarization of the Raman beam being overlapped with the cooling and detection beam cannot be changed. The beam is circularly polarized, corresponding to atomic σ^- transitions. In order to identify the optimal polarization of the second Raman beam, the sum over all possible Raman couplings must be evaluated. As discussed before, a simple approximation can be obtained by neglecting the precise detunings from the p-levels and applying the Clebsch-Gordan algebra. Following the notations shown in Figure 3.12 the Rabi frequency according to Equation 3.60 for the qubit transition $|2,1\rangle \leftrightarrow |1,1\rangle$ is found to be:

$$\Omega_{\mathrm{ofc}} = \frac{1}{2\sqrt{3}} g_{\mathrm{b}} g_{\mathrm{r}} (b_- r_- - b_+ r_+) \frac{\omega_{\mathrm{fs}}}{\Delta(\Delta - \omega_{\mathrm{fs}})} \tag{5.7}$$

With g_{r} and g_{b} being the time-averaged single-photon Rabi frequencies of the closed-cycle transition of the designated red and blue beam, ω_{fs} the fine-structure splitting between $^2P_{1/2}$ and $^2P_{3/2}$, and b_-,r_- and b_+,r_+ the left and right circularly polarized components of the red and blue Raman beam respectively. As the polarization of the first Raman beam is fixed to induce σ^- transitions, the optimal polarization of the second Raman beam also corresponds to an atomic σ^- polarization.
Since the beam geometry of the second free port, being orthogonal to the magnetic field direction and therefore to the quantization axis of the ion, does not allow for pure σ transitions, the laser's polarization of the second Raman beam is set to result in a superposition of σ^+/σ^-, achieved with a linear laser polarization, as shown in Figure 5.18. Thus only 50% of the second Raman beam's power effectively contributes to the Raman process. An overview of all relevant matrix elements, scaled to the matrix elements of the closed-cycle transition $^2S_{1/2}$, $|F = 2, m_F = 2\rangle \leftrightarrow {}^2P_{3/2}, |m_I = +3/2, m_J = +3/2\rangle$, their detunings and corresponding polarizations is shown in Table 5.2.

Motional coupling

As derived in section 3.1 the Raman coupling strength for motional sideband transitions in the Lamb-Dicke regime is proportional to the Lamb-Dicke parameter η:

$$\Omega_{\mathrm{sb}} = \eta \cdot \Omega_{\mathrm{c}} \cdot \sqrt{n_>} \tag{5.8}$$

With the motional state being $n_> = (n+1)$ for blue and $n_> = n$ for red sideband transitions, with Ω_{c} denoting the carrier Rabi frequency and with the Lamb-Dicke parameter η given by:

$$\eta = \Delta k \cdot \sqrt{\frac{\hbar}{2\, m_{\mathrm{ion}}\, \omega_{\mathrm{z}}}} \tag{5.9}$$

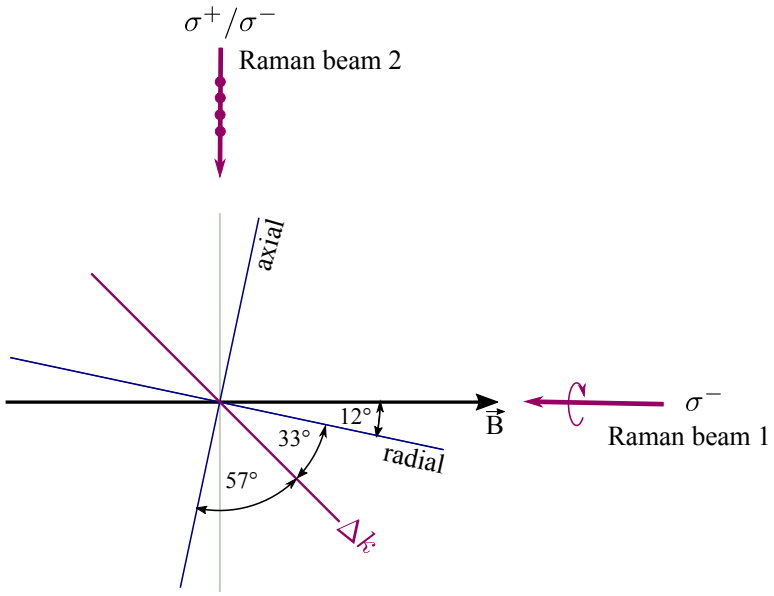

Figure 5.18: Illustration of the orientation of the wavevector difference Δk between both Raman beams relative to the direction of the radial and axial trap axes. The angles enclosed are 33° for the radial and 57° for the axial mode direction. The Raman beam 1 being counterpropagating to the direction of the magnetic field is circularly polarized, inducing atomic σ^- transitions. The Raman beam 2 propagating from an orthogonal direction to the magnetic field direction is linearly polarized, inducing a superposition of σ^+/σ^- atomic transitions.

Coupling to the ion's motion hence requires the interaction of two Raman beams being directed onto the ion under different angles. The absorption of a photon from one beam and emission into the other one causes a momentum change of $\hbar\Delta$k along the direction of wavevector difference Δk between both beams. Thus, motional states of the ion can be addressed if their mode oscillations have an overlap with the direction given by Δk. For a given beam geometry, determining the value of Δk, the achievable Raman sideband coupling is the stronger, the larger the overlap between the motional mode direction and the direction of Δk is and the smaller the motional trap frequency ω_z is.
The orientation of the radial and axial mode directions relative to the direction of the wavevector difference is shown in Figure 5.18. The angle enclosed is 57° for the axial and 33° for the radial mode. In addition the radial mode is tilted in the vertical direction by $\approx 20\,°$, which leads to the following projections onto the mode directions:

$$\text{radial}_{\Delta k}/\Delta k = \text{Cos}(33°)\text{Cos}(20°) \approx 0.788 \tag{5.10}$$

$$\text{axial}_{\Delta k}/\Delta k = \text{Cos}(57°) \approx 0.545 \tag{5.11}$$

The trap frequency of the axial mode oscillation is on the order of 1 MHz, the radial mode oscillations exhibit frequencies near 10 MHz. The resulting Lamb-Dicke parameter for the axial mode is hence a factor of $\sqrt{10} \approx 3.163$ larger than for the radial mode. For the discussed geometry of orthogonal beams the values are:

$$\eta_{\text{radial}} = \eta(10\,\text{MHz}) \approx \sqrt{2}\frac{2\pi}{\lambda_{\text{Be}}} \cdot \sqrt{\frac{\hbar}{2\,m_{\text{Be}}\,(2\pi\,10\,\text{MHz})}} \approx 0.213 \tag{5.12}$$

$$\eta_{\text{axial}} = \eta(1\,\text{MHz}) = \sqrt{10} \cdot \eta_{\text{radial}} \approx \sqrt{2}\frac{2\pi}{\lambda_{\text{Be}}} \cdot \sqrt{\frac{\hbar}{2\,m_{\text{Be}}(2\pi\,1\,\text{MHz})}} \approx 0.673 \tag{5.13}$$

With λ_{Be} being approximated by 313 nm for both Raman beams and m_{Be} being the mass of a single beryllium ion.
The resulting achievable Rabi sideband frequency of the axial mode is more than twice as large as for the radial mode and therefore chosen for implementation:

$$\Omega_{\text{sb,radial}} = \text{radial}_{\Delta k}/\Delta k \cdot \eta(10\,\text{MHz}) \cdot \Omega_{\text{c}} \cdot \sqrt{n_>} \approx 0.168 \cdot \Omega_{\text{c}} \cdot \sqrt{n_>} \tag{5.14}$$

$$\Omega_{\text{sb,axial}} = \text{axial}_{\Delta k}/\Delta k \cdot \eta(1\,\text{MHz}) \cdot \Omega_{\text{c}} \cdot \sqrt{n_>} \approx 0.366 \cdot \Omega_{\text{c}} \cdot \sqrt{n_>} \tag{5.15}$$

5.3.2 Experimental setup

An overview of the experimental setup for the two-beam approach is shown in Figure 5.19. The key parts of the Raman system, as described in section 5.2.2, are placed on a separate optical table. The pulsed UV beam is sent free space to the experiment table and separated in two arms using an α-BBO Glan polarizer. The through-going beam, in the following denoted as Raman beam 1, is overlapped with the CW cooling and detection beam by entering the side facet of another α-BBO Glan polarizer, as described for the single-beam approach. Further, a two lens telescope is applied for alignment purposes and AOM1[5] is implemented in single-pass geometry for switching and frequency adjustment. The second beam, in the following denoted as Raman beam 2, is focused onto the ion from an orthogonal direction. It passes AOM2[6] in single-pass geometry for switching and frequency adjustment and further a time delay stage, in order to match the optical beam path lengths of both Raman arms.
Whereas the AOM within the single-beam approach has only been applied for switching, both AOMs now are additionally used to fulfill the Raman resonance condition. The frequency of AOM1, set near 112.9696 MHz, has been implemented as down shift, whereas the frequency of AOM2, 270.6590 MHz, is set as an up shift, leading to a net relative frequency shift near $\Delta_{\text{AOM}} = 383.6286\,\text{MHz}$. In combination with a set repetition rate of 99.8455 MHz and a value j=7, only small

[5]Gooch and Housego, 110 MHz, I-M110-2C10BB-3-GH27
[6]Intraaction, 270 MHz, ASM-2702AF5

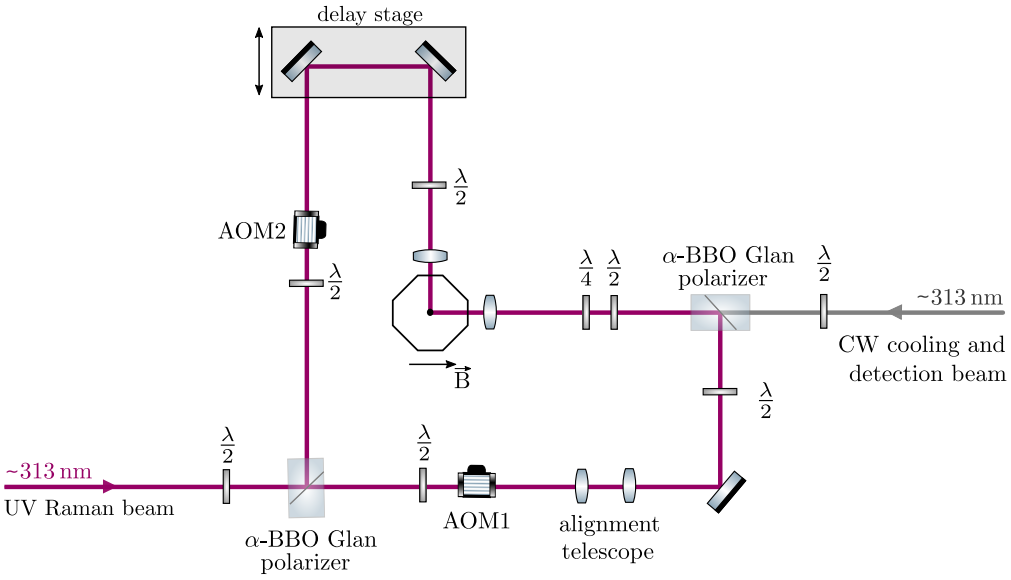

Figure 5.19: Experimental setup for multiple-beam qubit control, implemented by two beams of the pulsed Raman laser. The UV beam is aligned free space from one optical table to the optical table where the ion experiment is located on. Here it is separated into two beam paths using an α-BBO Glan polarizer. The through-going beam is overlapped with the CW cooling and detection beam by entering the side facet of a further α-BBO Glan polarizer. Before a two lens telescope is set up for alignment purposes and AOM1 is passed for switching and frequency adjustment. The second Raman beam is focused onto the ion from an orthogonal direction. It passes AOM2 for switching and frequency adjustment as well as a time delay stage in order to match the optical beam path lengths of both Raman arms.

deviations on AOM1 are applied, in order to fulfill the resonance condition for either carrier or sideband transitions:

$$7 \cdot f_{\text{rep}} + [270.6590\,\text{MHz} - (-112.9696\,\text{MHz} \mp \nu_{\text{axial}})] = \nu_{0,\text{BreitRabi}} \pm \nu_{\text{axial}} \quad (5.16)$$

5.3.3 Measurements

As preparation the two beams are separately aligned onto the ion and temporal overlap between both arms is ensured. Matching the optical path lengths is implemented by scanning the position of the optical delay stage, while ensuring the resonance condition for carrier Raman transitions to be fulfilled. Once temporal overlap is guaranteed, carrier Rabi oscillations are observed. Prior to driving sideband transitions, an accurate determination of the axial trap frequency is carried out and a resonance scan is implemented by scanning over the frequency of AOM1.

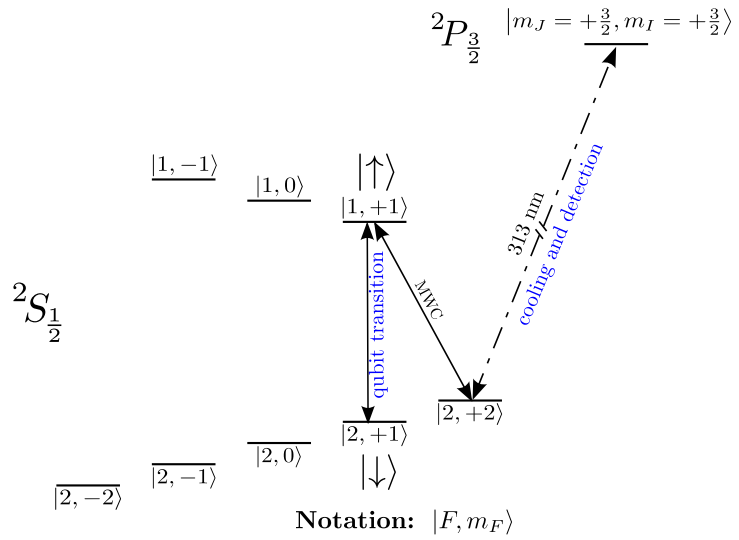

Figure 5.20: Hyperfine level structure and transitions of $^9Be^+$ relevant for the multiple-beam qubit control of the field-independent qubit transition $|\downarrow\rangle = |2,1\rangle \leftrightarrow |\uparrow\rangle = |1,1\rangle$, implemented by two beams of the pulsed Raman laser. After loading and cooling the ion is initialized in the $|2,2\rangle$ state. A resonant microwave carrier pulse (MWC) transfers the population into the $|1,1\rangle$ state. Subsequent to probing the ion with the Raman beams, the population of the $|1,1\rangle$ state is transferred back to the initial $|2,2\rangle$ state and detected by collecting the fluorescence signal induced by the detection beam, being resonant with the closed-cycle transition between $^2S_{1/2}$, $|F = 2, m_F = 2\rangle \leftrightarrow {}^2P_{3/2}$, $|m_I = +3/2, m_J = +3/2\rangle$.

Typical experimental sequence

For a typical experimental sequence a single beryllium ion is loaded and initialized in the $|2,2\rangle$ state, as described in section 5.1.4. In order to perform Raman transitions on the field-independent transition $|2,1\rangle \leftrightarrow |1,1\rangle$ the ion is prepared in the $|1,1\rangle$ state by applying a single resonant MWC pulse, as shown in Figure 5.20. Following the interaction with the pulsed laser the population of the prepared $|1,1\rangle$ state is transferred back to the $|2,2\rangle$ state for detection. In order to avoid coexistent off-resonant transitions from the $|2,1\rangle$ level, this population is shelved to either the $|1,1\rangle$ or $|1,0\rangle$ state, before applying the detection beam.

Beam alignment

As preparation for the measurements both beams are independently aligned on the ion. The procedure for Raman beam 1 is the same as for the single-beam approach. The alignment is performed by first maximizing level depletion induced by near-resonant spectral components, followed by maximizing the Stark shift during a spin-echo based Ramsey experiment.
Due to polarization dependent cancellation effects, the amount of Stark shift being

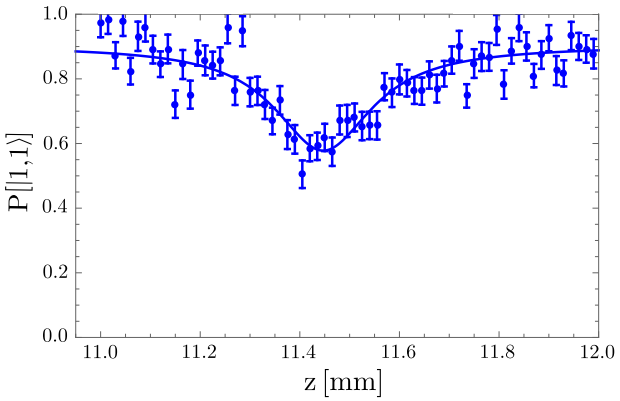

Figure 5.21: Resonance scan for a carrier Raman transition on the $|2,1\rangle \leftrightarrow |1,1\rangle$ field-independent qubit, driven by two beams of the pulsed Raman laser. Shown is the population of the $|1,1\rangle$ state as a function of the position of the delay stage. The solid line shows a fit of the data. At the position denoted by 11.42 mm the simultaneous presence of both Raman beams at the ion fulfills the carrier resonance condition and the population of the prepared $|1,1\rangle$ state drops.

achievable with the second Raman beam is reduced by more than two orders of magnitude for any adjustable polarization. This beam is therefore only aligned by shortening the duration of level depletion induced by near-resonant components of the spectrum, as described in detail in section 5.2.3.

Temporal overlap - carrier transition resonance scan

In order to ensure temporal overlap between both pulsed Raman beams at the position of the ion, both optical path lengths need to be matched to a few hundred micrometers, approximately given by $c \cdot \tau_p$, with τ_p being the temporal pulse duration. For this purpose a temporal delay stage is implemented in the second Raman beam, as shown in Figure 5.19. The stage consists of two orthogonally aligned mirrors mounted on a motorized, linear translation stage[7]. The mirrors are accurately adjusted such that the input beam onto the first mirror is reflected back parallel to itself when passing the second mirror. A linear translation of the delay stage along the direction of the input and output beam therefore does not affect the subsequent beam alignment onto the ion, but changes the optical beam path length by of factor two with respect to its movement. In order to find the required position of the delay stage, ensuring temporal overlap, a resonance scan for carrier Raman transitions is performed, while scanning the delay stage position along the translation axis. For this the frequencies of the AOMs are set to fulfill the carrier Raman resonance condition and the probe duration of both Raman beams is set

[7]Combination of manual translation stage, Newport M-462-X-M, with motorized actuator, Thorlabs Z825B and DC servo motor controller, Thorlabs KDC101

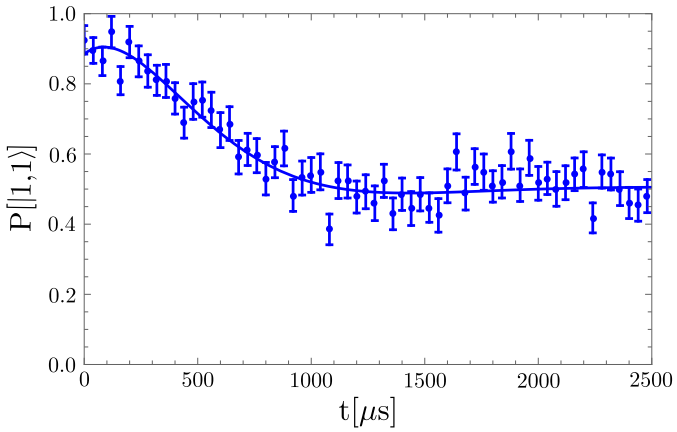

Figure 5.22: Carrier Rabi oscillations on the $|2,1\rangle \leftrightarrow |1,1\rangle$ field-independent qubit transition induced by two orthogonal beams of the pulsed Raman laser. Shown is the population of the prepared $|1,1\rangle$ state as a function of the laser probe duration. The data fit (solid line) corresponds to a π-time of 1.26 ms.

to the expected π-time. To speed up the scanning process, an automized routine has been implemented, successively performing the experimental sequence, while continuously and slowly moving the delay stage. The velocity of movement has been adjusted in order to ensure the expected resonance dip to be resolved. Figure 5.21 shows an exemplary resonance scan, where the population of the $|1,1\rangle$ state was measured as a function of the absolute position of the delay stage. At the position denoted by 11.42 mm the simultaneous presence of both Raman beams at the ion fulfills the carrier resonance condition and the population of the $|1,1\rangle$ state drops.

Carrier Rabi oscillations

Setting the position of the delay stage to the position obtained during the resonance scan directly allows the performance of carrier Rabi oscillations. The resonance condition, $\nu_0 = j \cdot f_{\text{rep}} + \Delta_{\text{AOM}}$, was fulfilled by setting the frequency of AOM1 to 112.9696 MHz, leading to a net relative frequency shift of $\Delta_{\text{AOM}} = 270.6590\,\text{MHz} - (-112.9696\,\text{MHz}) = 383.6286\,\text{MHz}$. Together with the repetition rate of $f_{\text{rep}} = 99.8455\,\text{MHz}$ and $j = 7$ this yields the expected qubit frequency of $\nu_0 = 1082.5471\,\text{MHz}$, obtained by the Breit-Rabi formula in Equation 3.64. The measured Rabi oscillations are presented in Figure 5.22. Shown is the population of the $|1,1\rangle$ state as a function of the laser probe duration. The oscillation shows an apparent decoherence, the π-time is approximated to be 1.26 ms.

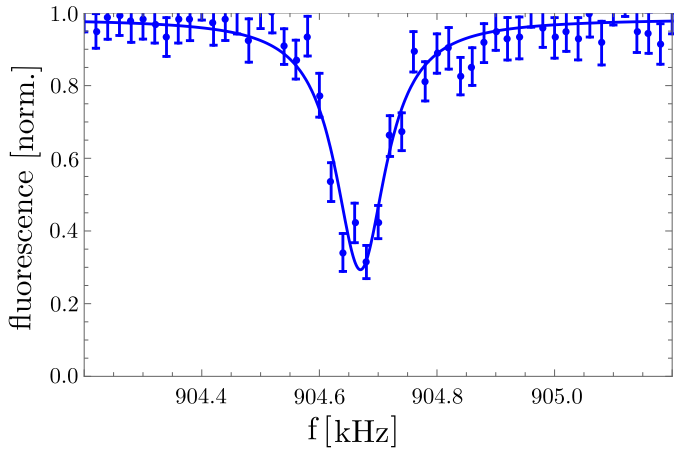

Figure 5.23: Secular frequency measurement (axial direction) performed by resonantly driving the ion's motion using an oscillatory field. The solid line shows a fit of the data. On resonance a loss of the count rate occurs due to Doppler shifts, induced by motional excitation.

Sideband transition resonance scan

In order to address motional sideband transitions, the offset frequency between the two combs Δ_{AOM} needs to be detuned from the carrier resonance condition by the trap frequency. The instantaneous axial trap frequency was measured, as exemplarily shown in Figure 5.23. By applying an oscillatory electric field near the expected secular frequency, the ion's motion can be driven resonantly, resulting in a loss of the count rate on resonance due to Doppler shifts. Based on this measurement the frequency of AOM1 is set to fulfill the sideband resonance condition $\nu_{\mathrm{qubit}} \pm \nu_{\mathrm{trap}} = j \cdot f_{\mathrm{rep}} + \Delta_{\mathrm{AOM}}$. Due to fast fluctuations of the axial trap frequency a resonance scan is subsequently performed, scanning over the frequency applied to AOM1 within the range of a few kHz. The resonance dip for a red motional sideband transition on the axial mode is presented in Figure 5.24. Shown is the population of the $|1,1\rangle$ state as a function of the frequency applied to AOM1 for a laser probe duration of 3 ms. On resonance the frequencies match the condition for red sideband transitions and the population of the $|1,1\rangle$ state drops. The transition frequency for the measured axial trap frequency of $\nu_{\mathrm{trap}} = 0.892\,\mathrm{MHz}$ was given by $\nu_{\mathrm{qubit}} = \nu_0 - \nu_{\mathrm{trap}} = 1081.6551\,\mathrm{MHz}$. It has been obtained with the adjusted repetition rate of $f_{\mathrm{rep}} = 99.8455\,\mathrm{MHz}$, $j = 7$ and relative frequency shift of $\Delta_{\mathrm{AOM}} = (270.6590\,\mathrm{MHz} - (-112.0776\,\mathrm{MHz})) = 382.7366\,\mathrm{MHz}$.

Sideband Rabi oscillations

Based on the identified resonance position, Rabi flopping on the sideband transition can be attempted. The frequency of AOM1 is herfore set to the value derived from the previous scan. The simultaneous presence of both beams at the ion, fulfilling

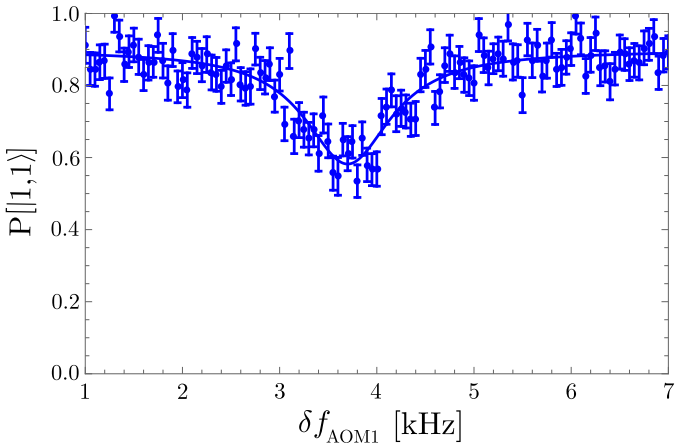

Figure 5.24: Resonance scan for a red sideband Raman transition on the $|2,1\rangle \leftrightarrow |1,1\rangle$ field-independent qubit, driven by two orthogonal beams of the pulsed Raman laser. Shown is the population of the $|1,1\rangle$ state as a function of the frequency applied to AOM1. The data fit (solid line) yields a resonance frequency of $\delta f = 3.7\,\mathrm{kHz}$, at which the simultaneous presence of both Raman beams at the ion fulfills the red sideband resonance condition and the population of the $|1,1\rangle$ state drops.

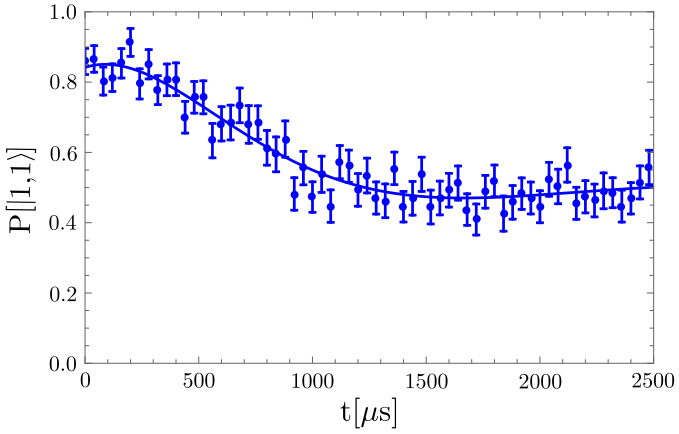

Figure 5.25: Red sideband Rabi oscillations on the $|2,1\rangle \leftrightarrow |1,1\rangle$ field-independent qubit transition induced by two orthogonal beams of the pulsed Raman laser. Shown is the population of the $|1,1\rangle$ state as a function of the laser probe duration. The data fit (solid line) corresponds to a π-time of 1.55 ms

the resonance condition for red sideband Raman transitions on the axial mode, causes the ion to oscillate between the qubit states, as exemplarily presented in Figure 5.25. Shown is the population of the $|1,1\rangle$ state as a function of the laser probe duration. The oscillation shows an apparent decoherence, the π-time is fitted to 1.55 ms.

5.3.4 Discussion

These measurements demonstrate the first ever shown spin-motion coupling of a single beryllium ion using a pulsed Raman system. The data successfully prove the concept introduced in chapter 3. In this section a comparison with simulations will be presented and improvement strategies discussed.

Comparison with simulations

Comparing the experimental results with simulations requires the extraction of several parameters from the experiment as discussed in section 5.2.4. The spectrum which has been applied is shown in Figure 5.26. The main peak has been fitted by a gaussian function. The effective spectral bandwidth is given by $\Delta\nu_{\mathrm{FWHM}} = 840\,\mathrm{GHz}$ and the detuning to the $^2P_{1/2}$ line center by $\Delta = 1.68\,\mathrm{THz}$. While the mean focusing strength of both beams is comparable to the one applied during the single-beam experiments and assumed as $w_0 = 20\,\mu\mathrm{m} \pm 5\,\mu\mathrm{m}$, the power level during these experiments has been much lower. The upper limit of power contribution per beam is estimated to be 0.8 mW. For the simulations an uncertainty range of $\pm$ 0.2 mW is assumed, based on estimated losses occurring in the beam path behind the point of power measurement. The estimated power is the optimum value, which each beam could contribute in case of perfect overlap of all contributing comb mode pairs. This implies that the teeth of both beams which together bridge the qubit splitting arrive simultaneously at the position of the ion. The duration of the effective temporal overlap can be extracted by evaluating the resonance scan of temporal overlap in dependency of the delay stage position, shown in Figure 5.21. A linear translation of the stage corresponds to a change of the optical beam path length l_{optical} by a factor of two with respect to its movement. Assuming the simple relation $\Delta l_{\mathrm{optical}}/c \approx \tau_{\mathrm{overlap}}$, the time of effective overlap τ_{overlap} can be calculated. For a FWHM of the resonance dip of 240 μm, corresponding to an optical path of 480 μm, the duration of constructive temporal overlap is $\tau_{\mathrm{overlap}} \approx 1.6\,\mathrm{ps}$. This value gives a lower limit for the pulse duration. The correct pulse duration might be longer, as the chirp might prevent the generation of a signal in case the relevant pairs of comb teeth are not at the position of the ion at the same time. Based on simulation results shown in Figure 4.15, a temporal duration of $\tau_{\mathrm{FWHM}} = 2.0\,\mathrm{ps} \pm 0.5\,\mathrm{ps}$ is assumed as for the single-beam approach.

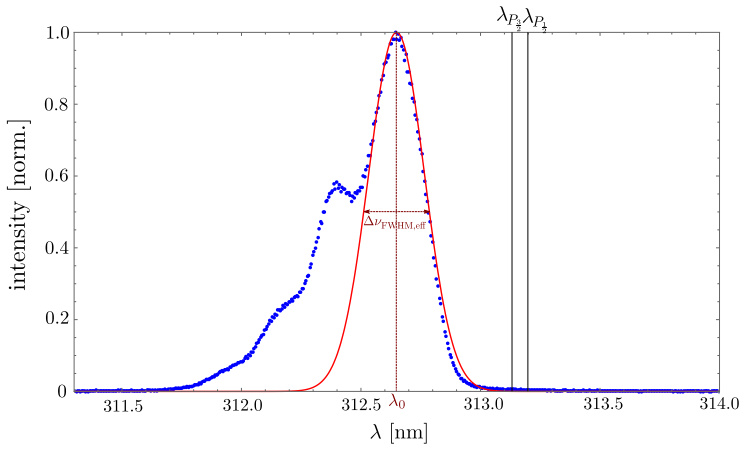

Figure 5.26: UV spectrum of the Raman laser as present during the measurements of the carrier Rabi oscillations on the $|2,1\rangle \leftrightarrow |1,1\rangle$ qubit transition, shown in figure 5.13. The peak wavelength of $\lambda_0 = 312.649\,\mathrm{nm}$ corresponds to a Raman detuning of $\Delta = 1.68\,\mathrm{THz}$ from the line center of the $^2P_{1/2}$ level. The main peak of the spectrum is fitted by a gaussian function (solid line) which corresponds to an effective spectral FWHM bandwidth of $\Delta\nu_{\mathrm{FWHM}} = 840\,\mathrm{GHz}$.

Figure 5.27 shows the calculated π-time for different detunings according to the assumed uncertainty range, depending on the squared electric field amplitude E_0^2 scaled to the squared electric field amplitude given by the approximated average laser power, focal width and pulse duration, $E_0^2/\bar{E}_0^2$. A gaussian-shaped spectrum has been applied, providing the effective bandwidth of the main peak of $\Delta\nu_{\mathrm{FWHM}} = 840\,\mathrm{GHz}$. The power contained in the far detuned spectral components has been neglected. For the mean values of the assumed uncertainty range of the parameters influencing the squared electric field amplitude, the measured π-time exceeds the corresponding simulation data by a factor of 2.2 . Within the estimated uncertainty range, the measurement agrees with the simulation results for the detuning of $\Delta = 1.68\,\mathrm{THz} + 0.15\,\mathrm{THz}$. Not taken into account in the simulations are a possible deviation of the spectral bandwidth and the chirp of the pulses. While the chirp for the single-beam approach has been discussed to be nearly negligible, it now can hinder the availability of all possible pairs of comb teeth, due to the fact that both beams are directed onto the ion from different directions. As the chirp involves that the spectral components of each beam cannot be focused to the ion simultaneously, the setting of the temporal overlap might only optimize a certain fraction of the spectra of both beams to overlap. As a result only a fraction of the power contained in each beam would then contribute to the process.

The Rabi frequency for the sideband oscillations can be derived from the carrier Rabi frequency and is further determined by the Lamb-Dicke parameter and the motional state of the ion. For the applied beam geometry and for a red motional

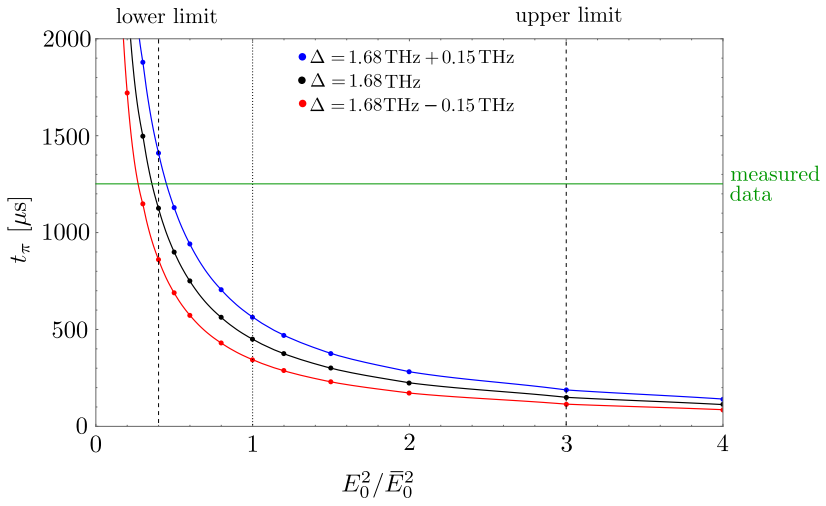

Figure 5.27: Numerical simulations comparing the measured data (green line) of the two beam carrier Rabi oscillations with simulations. Shown is the calculated π-time for three different detunings depending on the squared electric field amplitude E_0^2 scaled to the mean values of the approximated average power, pulse duration and focal radius, $E_0^2/\bar{E}_0^2$. Assumed is a gaussian envelope function with an average power of $P_{\mathrm{av}} = 0.8\,\mathrm{mW} \pm 0.2\,\mathrm{mW}$, a focal radius of $w_0 = 20\ \mu\mathrm{m} \pm 5\,\mu\mathrm{m}$ and a pulse duration of $\tau_{\mathrm{FWHM}} = 2.0\,\mathrm{ps} \pm 0.5\,\mathrm{ps}$. The influence of the pulse duration in terms of temporal broadening compared to the time-bandwidth limited pulse duration is taken into account, by keeping the spectral width of $\Delta\nu_{\mathrm{FWHM}} = 840\,\mathrm{GHz}$ constant and reducing the intensity respectively. The resulting lower limit of the uncertainty range yields $E_0^2/\bar{E}_0^2 \approx 0.4$ and an upper limit of $E_0^2/\bar{E}_0^2 \approx 3.0$. The black data points correspond to the measured detuning of $\Delta = 1.68\,\mathrm{THz}$. The red data points correspond to a detuning of $\Delta = 1.68\,\mathrm{THz}$ - $0.15\,\mathrm{THz}$ and the blue data points to a detuning of $\Delta = 1.68\,\mathrm{THz} + 0.15\,\mathrm{THz}$, according to the assumed uncertainty range. The solid lines represent guides to the eye.

sideband transition the sideband Rabi frequency is given by $\Omega_{\mathrm{sb}} = 0.366 \cdot \Omega_{\mathrm{c}} \cdot \sqrt{n}$, as discussed in section 5.3.1. Comparing the measured π-times for the carrier and sideband Rabi oscillations yields a motional state corresponding to $\bar{n} \approx 5$, which is roughly consistent with Doppler cooling at the given Doppler cooling beam geometry. Since the actual motional state is unknown, no simulations are performed. The sideband oscillations are nevertheless affected by the influence of the chirp in the same way as discussed for the carrier oscillations.

Besides the long π-times, the experimental measurements of Rabi oscillations exhibit a very strong decoherence. For the given beam geometry, the decoherence is expected to be caused by the ion's thermal state of motion and results from the averaging of individual experiments each with a different Rabi rate.
Simulations for the probability of scattering during the corresponding π-time yield values between $0.59 \cdot 10^{-5}$ and $1.77 \cdot 10^{-5}$ for the assumed uncertainty ranges.

Off-resonant light scattering caused by the Raman beams is therefore, as for the single-beam approach, excluded as a major source of decoherence.
Besides the error sources discussed within the single-beam approach, the low power level at each beam makes the process strongly susceptible to drifts of the axial trap frequency and beam pointing instabilities at the ion. Any relative change of the refractive index between the beams, induced for example by temperature drifts or air currents, leads to a change of the optical beam path length and hence to pointing instabilities at the ion, as discussed in detail in [130]. Furthermore strong mechanical vibrations, which have been observed, can hinder the optical beam overlap at the position of the ion.

Improvement strategies

Improvement strategies should focus on enhancing the Rabi frequency to move beyond the proof-of-principal stage realized so far.
As discussed for the single-beam approach, a systematic survey investigating the optimal spectral properties and the optimal detunings gives room for strong improvements. According to the simulations concerning the calculated scattering probability within the two-beam experiments, it is expected that a significantly smaller detuning can be chosen without suffering from off-resonant light scattering. Due to the strong influence of the detuning on the achievable Raman coupling strength, it is most likely to achieve similar or marginally higher π-times as for the demonstrated single-beam approach, for which a smaller detuning has been set. Additionally readjusting and further maximizing the available power will most likely provide π-times on the order of tens of microseconds or below, as desired for the (anti-)proton Penning trap experiment. A further increase of available power might be achieved by applying an enhancement cavity for the SHG process and applying a special crystal coating, reducing the UV Fresnel losses of 31 % for Brewster-cut crystals.
Aside from increasing the power, a stronger signal could possibly be achieved by optimizing the constructive overlap of relevant spectral components of the Raman beams. Since the Raman transitions are performed by the combination of teeth originating from different beams, it is essential for them to arrive the ion simultanously. Assuming that the presence of the chirp reduces the amount of total available teeth pairs, one could either try to manipulate the chirp itself in order to optimize the overlap or one could adjust the spectral properties in order to reduce the influence of the chirp.
Assuming only a small fraction of the spectrum to effectively contribute to the signal due to effects induced by the chirp, it might be more advantegous to generate a very narrow spectrum. Since near-resonant components induce a stronger Raman signal, a lower overall power, but located in a narrow near-resonant peak, could possibly optimize the signal, since not only a fraction but the entire spectrum would

contribute to the process.
A further way to improve the constructive overlap might be given by rotating the orientation of the spatial chirp. During the experiments the orientation has been set to be horizontal. In this configuration an imperfect beam alignment could affect and possibly enhance the chirp by accidently introducing different optical beam path lengths for the red and blue components. In consequence the difference between the arrival times of different spectral components within the beams could be extended and hence the achievable Raman signal reduced. Further it is important to ensure the frequency components temporally arriving the ion first to be synchronized for both beams in order to maximize the number of contributing comb tooth pairs. In both aspects, a rotation into the vertical might lead to an improvement when assuming a horizontal beam alignment. Nevertheless the temporal aspect, of not being able to focus all spectral components simultaneously onto the ion, is not solved by the rotation of the spatial chirp.
Systematic compensation or in general manipulation the chirp alternatively requires a setup which allows to precisely control and modify the optical path lengths of different components of the spectrum. This might also compensate temporal pulse broadening and therfore enhance the intensity at the position of the ion. The manipulation of the chirp nevertheless would be accompanied by additional losses and might therefore not bring an overall improvement. Since the optimization of the power, the detuning and spectral components is expected to provide the desired values of coupling strengths, additional efforts in terms of chirp modification are not mandatory.
A reduction of sensitivity to beam pointing instabilities might further be performed by tubing the entire beam path. In [130] this has been demonstrated to strongly affect and improve results. An independent beam setup, possibly with shorter optical path lengths and fewer required optical components would simplify the realization of a completely enclosed beam path and the optimization in terms of supressing error sources.
In conclusion, the measurements for spin-motion coupling are evaluated to be improvable towards achieving target values concerning the Rabi frequency when optimizing the available power, the detuning and the spectral distribution. Due to comparable coupling strengths as for the chosen qubit at an externally applied magnetic field of 5 T, the pulsed laser approach is expected to fulfill all requirements for $^9Be^+$ ion qubit control within the planned high-precision Penning trap experiment.

Chapter 6

Conclusion and Outlook

Within the framework of this thesis the first $^9Be^+$ ion qubit control using an optical frequency comb has been realized. The qubit operations providing spin-motion coupling are important steps required for ground-state cooling of beryllium and for implementing sympathetic cooling and quantum logic inspired spin-state detection of single (anti-)protons in Penning traps. The work presented in this thesis covers numerical simulations concerning the requirements and the application range of coherent $^9Be^+$ ion control, the development of an appropriate Raman system, which in addition provided novel insight into and application of occurring spatio-temporal coupling dynamics in nonlinear BiBO crystals as well as the experimental implementation and demonstration of coherent laser control in a surface-electrode radio-frequency trap. In this chapter the scientific achievements will be summarized and reviewed in the context of our future high-precision Penning trap experiment and beyond.

The implementation of $^9Be^+$ ion qubit control has been carried out using two-photon stimulated Raman transitions. The ground-state sublevel coupling was obtained by a coherent sum of comb mode pairs, each with a frequency difference equal to the qubit splitting. For spin control the comb teeth of each pair can be provided by a single beam, while for coupling to the ion's motional degree of freedom the comb teeth of each pair must originate from separated beams being directed onto the ion from different directions and synchronized in time. The Raman resonance condition in this case was fullfilled by a relative shift between the beam's frequencies implemented by AOMs. Other than for the CW-laser approach, the required shift is only in the range of one-third of the laser's repetition rate near 100 MHz and does not need to cover the entire qubit splitting. This is one convincing aspect of the pulsed-laser approach which might in future prove useful for the general implementation of sideband cooling in Penning traps, where atomic

ions with hyperfine qubit transitions exhibit large Zeeman splittings due to the high applied magnetic fields.

In order to examine specific requirements for $^9Be^+$ ion qubit control in the environment of an externally applied magnetic field of 5 T, numerical simulations of the relevant atomic processes have been performed. A particular challenge arises from beryllium's small excited state fine-structure splitting near 200 GHz, which requires a Raman detuning to be chosen outside the p-level manifold in order to not resonantly excite the p-levels. Due to conflicting demands for achieving high Raman coupling strengths and simultaneously guaranteeing reasonably low scattering rates, the optimal combination of the Raman detuning and spectral properties of the pulses has been evaluated. The simulations presented in this thesis have shown that the optimal spectral bandwidth is very narrow with a value being only slightly bigger than beryllium's qubit splitting near 140 GHz. For broader spectra a strong loss of Raman coupling occurs because the required detuning for keeping the scattering rate below a certain threshold significantly increases. A significant improvement of this decrease of coupling strength has been found to be achieved by blocking the spectral components close to resonance during the Raman process. The absence of these outer-lying frequency components allows for much smaller detunings, which has a strong impact on maximizing the achievable Rabi frequency. For implementing qubit control for beryllium ions, it was shown to be mandatory to combine efforts towards the generation of narrow-bandwidth UV pulses with a technique to control the outer-lying frequency components in order to obtain appropriate Raman coupling strengths. Simulations showed that for a sharp cut during spectral pulse modification, broader spectra with bandwidths of up to 1 THz can be applied without significant loss of coupling strength, while for a non-perfect, smeared frequency distribution during pulse shaping operating with narrower spectra is more profitable, showing an optimum bandwidth near 300 GHz for the estimated lower limit of pulse shaping resolution. Once operating in the range of these spectral properties, the optical frequency comb was shown to provide enormous flexibility allowing for qubit control at nearly any experimentally relevant conditions in the high-field Paschen-Back as well as in the low-field Zeeman regime. Raman coupling strengths enabling π-times in the range of tens of microseconds were evaluated to be achievable when providing an average laser power in the range of a few milliwatts.

For the realization of the pulsed-laser approach, a narrow-bandwidth ultraviolet frequency comb has been developed. The system is based on a custom-built femtosecond frequency comb operating near 626 nm. It has been designed to provide a tunability ± 0.2 MHz of the repetition rate near 100 MHz, which allows to adjust the range in which motional sideband transitions are well resolved and a tunability of the wavelength, allowing for different Raman detunings of up to nearly 5 THz. The mandatory control of spectral properties was realized by the combination of a

nonlinear spectral compression technique, implemented during the SHG into the UV near 313 nm, and a subsequent blocking of outer-lying frequency components. The wavelength range of this compression technique has been extended into the UV for the first time, where the unavoidable effect of spatial walkoff strongly affects the properties of the generated UV pulses. A model accounting for the spatio-temporal coupling dynamics in second-order nonlinear BiBO crystals has been applied for theoretical investigation. By choosing crystals of different lengths and different focusing conditions, a selective and efficient spectral compression to target values between 300 GHz and 1000 GHz has been achieved, with excellent agreement between simulations and experimental results. The spatio-temporal coupling was further shown to result in angularly chirped output pulses, which allowed the use of razor blades located closely behind the nonlinear BiBO crystal in order to address and block the unwanted outer-lying frequency components. This novel and simple combination of techniques might find use in other applications requiring pulses with similar spectral properties, as for example the cooling of molecules or time-resolved spectroscopy experiments.

Since the (anti-)proton g-factor measurement experiment is currently still under development, the demonstration of spin control and spin-motional coupling has been carried out using an operating planar surface-electrode beryllium ion trap at an externally applied magnetic field of 22.3 mT. Simulations have shown that resulting Raman coupling strengths for both experimental conditions are comparable, despite the vastly different qubit splittings. The experiments performed in this thesis therefore provide a meaningful evidence for the planned high-precision Penning trap experiment with a magnetic field of 5 T. The first ever shown single-beam spin control of beryllium ions has been demonstrated on the field-dependent $|F = 2, m_F = 0\rangle \leftrightarrow |F = 1, m_F = 0\rangle$ transition. The measured π-time of the Rabi oscillations near 30 μs was shown to coincide with corresponding simulations within the uncertainty range under given experimental conditions. The first spin-motion coupling of beryllium ions applied by two orthogonal beams of the developed pulsed Raman laser were performed on the field-insensitive $|F = 2, m_F = 1\rangle \leftrightarrow |F = 1, m_F = 1\rangle$ transition. The achieved π-times of sideband Rabi oscillations were measured to be 1.55 ms. The π-time of the corresponding carrier Rabi oscillations with 1.26 ms were shown to be within the uncertainty range of expected values according to the simulation data. A general deviation from the mean expected value is assumed to be caused by effects associated with the chirp of the UV pulses, which have not been accounted for in the simulations. It is expected that a significantly smaller detuning can be chosen for the experiments providing spin-motion coupling without suffering from off-resonant light scattering. Due to the strong influence of the detuning on the achievable Raman coupling strength, it is most likely to achieve similar or marginally higher π-times as for the demonstrated single-beam approach, for which a smaller detuning

has been set. Additionally readjusting and further maximizing the available power will most likely provide π-times on the order of tens of microseconds or below, as desired for the (anti-)proton Penning trap experiment. Special attention during the implementation in the high-field regime might nevertheless be necessary with regards to the chirp. Due to the larger separation between comb mode pairs contributing to the Raman coupling, the influence of the chirp on reducing the achievable coupling strength might be enhanced, wherefore a systematic optimization of the spectral distribution is recommended.

In conclusion the pulsed-laser approach is expected to fulfill all requirements for $^9Be^+$ ion qubit control within the planned high-precision Penning trap experiment. The achieved results therefore provide strong evidence towards the possibility of realizing ground-state sideband cooling of beryllium ions in Penning traps. The work will support the implementation of sympathetic cooling and spin state transfer of single (anti-)protons and therefore the quantum logic inspired measurement of a single (anti-)proton's g-factor. The pulsed-laser approach might further be applied in the context of other precision experiments and become an important tool for the implementation of quantum logic operations in Penning traps.

Bibliography

[1] H. Dehmelt, Science **247**, 539–545 (1990).

[2] Wolfgang Paul, Reviews of Modern Physics **62**, 531–542 (1990).

[3] David J. Wineland, Reviews of Modern Physics **85**, 1103–1114 (2013).

[4] H.-J. Kluge *et al.*, Physica Scripta **2003**, 167 (2003).

[5] T. Rosenband *et al.*, Science **319**, 1808 –1812 (2008).

[6] M. Block, Hyperfine Interact (2017).

[7] A. Mooser *et al.*, Nature **509**, 596–599 (2014).

[8] D. J. Wineland and D. Leibfried, Laser Physics Letters **8**, 175 (2011).

[9] C. Monroe, Nature **416**, 238–246 (2002).

[10] J. I. Cirac and P. Zoller, Physical Review Letters **74**, 4091 (1995).

[11] Lowell S. Brown and Gerald Gabrielse, Reviews of Modern Physics **58**, 233–311 (1986).

[12] R. C. Thompson *et al.*, Journal of Physics B: Atomic, Molecular and Optical Physics (2009).

[13] K. Blaum, Y. N. Novikov and G. Werth, Contemporary Physics pages 149–175 (2010).

[14] Klaus Blaum, Physics Reports **425**, 1–78 (2006).

[15] J. Wess, Hyperfine Interactions **44**, 1–7 (1989).

[16] C. S. Wu *et al.*, Physical Review **105**, 1413 (1957).

[17] J. H. Christenson *et al.*, Physical Review Letters **13**, 138–140 (1964).

[18] J. P. Lees *et al.*, Physical Review Letters **109**, 211801 (2012).

[19] Ralf Lehnert, Symmetry **8**, 114 (2016).

[20] A. H. G. Peter, Proceedings of Science (2012).

[21] P. J. E. Peebles and B. Ratra, Rev. Mod. Phys. **75** (2003).

[22] R. H. Cyburt, B. D. Fields and K. A. Olive, Physics Letters B pages 227–234 (2003).

[23] V.A. Kostelecký, Ralf Lehnert and J.P. Malcolm, Phys. Rev. **D68** (2003).

[24] Robert Bluhm, V. Alan Kostelecký and Neil Russell, Physical Review Letters **79**, 1432–1435 (1997).

[25] Robert Bluhm, V. Alan Kostelecký and Neil Russell, Physical Review D **57**, 3932–3943 (1998).

[26] D. Hanneke, S. Fogwell and G. Gabrielse, Physical Review Letters **100**, 120801 (2008).

[27] Robert S. Van Dyck, Paul B. Schwinberg and Hans G. Dehmelt, Physical Review Letters **59**, 26–29 (1987).

[28] H. Dehmelt *et al.*, Physical Review Letters **83** (1999).

[29] S. Ulmer *et al.*, Nature **524**, 196–199 (2015).

[30] G. Gabrielse *et al.*, Physical Review Letters **82**, 3198–3201 (1999).

[31] A. Mooser *et al.*, Physics Letters B **723**, 78–81 (2013).

[32] C. Smorra *et al.*, Physics Letters B **769**, 1–6 (2017).

[33] C. Smorra *et al.*, The European Physical Journal Special Topics **224**, 1–54 (2015).

[34] J. DiSciacca and G. Gabrielse, Physical Review Letters **108**, 153001 (2012).

[35] ATRAP Collaboration *et al.*, Physical Review Letters **110**, 130801 (2013).

[36] H. Nagahama *et al.*, Nature Communications **8**, 14084 (2017).

[37] Jürgen Eschner *et al.*, Journal of the Optical Society of America B **20**, 1003–1015 (2003).

[38] F. Diedrich *et al.*, Physical Review Letters **62**, 403 (1989).

[39] P. O. Schmidt *et al.*, Science **309**, 749–752 (2005).

[40] C. W. Chou *et al.*, Physical Review Letters **104**, 070802 (2010).

[41] J. F. Goodwin *et al.*, Physical Review Letters **116**, 143002 (2016).

[42] D. J. Heinzen and D. J. Wineland, Physical Review A **42**, 2977 (1990).

[43] D. J. Wineland *et al.*, J. Res. NIST **103**, 259 (1998).

[44] Th. Udem, R. Holzwarth and Th. Hänsch, The European Physical Journal - Special Topics **172**, 69–79 (2009).

[45] D. Hayes *et al.*, Physical Review Letters **104**, 140501 (2010).

[46] J. Mizrahi *et al.*, (2013).

[47] G. Gabrielse, Physical Review Letters **102**, 172501 (2009).

[48] H. Dehmelt and P. Ekström, Bull. Am. Phys. Soc. **18**, 727 (1973).

[49] H. Häffner *et al.*, The European Physical Journal D - Atomic, Molecular, Optical and Plasma Physics **22**, 163–182 (2003).

[50] A. Mooser *et al.*, Physical Review Letters **110**, 140405 (2013).

[51] C. Monroe *et al.*, Physical Review Letters **75**, 4714–4717 (1995).

[52] Daniel M. Segal and Christof Wunderlich, arXiv:1409.6927 [physics, physics:quant-ph] pages 43–81 (2014), arXiv: 1409.6927.

[53] Alban Kellerbauer and Jochen Walz, New Journal of Physics **8**, 45 (2006).

[54] Juan Manuel Cornejo and Daniel Rodríguez, Advances in High Energy Physics **2012** (2012).

[55] N Daniilidis *et al.*, Journal of Physics B: Atomic, Molecular and Optical Physics **42**, 154012 (2009).

[56] M. Niemann, Ph.D. thesis (2018).

[57] D. Leibfried *et al.*, Reviews of Modern Physics **75**, 281 (2003).

[58] C. Ospelkaus *et al.*, Nature **476**, 181–184 (2011).

[59] C. Ospelkaus *et al.*, Physical Review Letters **101**, 090502 (2008).

[60] Florian Mintert and Christof Wunderlich, Physical Review Letters **87**, 257904 (2001).

[61] K. R. Brown *et al.*, Nature **471**, 196–199 (2011).

[62] M. Harlander *et al.*, Nature **471**, 200–203 (2011).

[63] D. J Wineland *et al.*, Philosophical Transactions of the Royal Society of London. Series A: Mathematical, Physical and Engineering Sciences **361**, 1349–1361 (2003).

[64] William D. Phillips and Harold J. Metcalf, Scientific American **256**, 50–56 (1987).

[65] C. J. Foot: *Atomic Physics*.
Oxford Master Series in Atomic, Optical and Laser Physics. Oxford University Press, Oxford (2005).
ISBN 0-19-850696-1.

[66] H. Uys *et al.*, Physical Review Letters **105**, 200401 (2010).

[67] R. Ozeri *et al.*, Physical Review Letters **95**, 030403 (2005).

[68] H.A. Kramers and W. Heisenberg, Zeitschrift für Physik **31**, 681–708 (1925).

[69] J. van den Brink and M. van Veenendaal, Journal of Physics and Chemistry of Solids **66**, 2145–2149 (2005).

[70] M. Jasperse *et al.*, arXiv:1705.10965v1 [quant-ph] 31 May 2017 (2017).

[71] Th. Udem and F. Riehle, RIVISTA DEL NUOVO CIMENTO (2007).

[72] A. I. Zayed, IEEE Signal Processing Letters **5** (1998).

[73] M. D. Ortigueira, Signal Processing **81**, 581–592 (2001).

[74] D.F.V. James and Jonathan Jerke, Can. J. Phys. **85** (2007).

[75] D. Hayes, Ph.D. thesis, Joint Quantum Institute, University of Maryland Department of Physics and National Institute of Standards and Technology (2012).

[76] Theo Mayer-Kuckuk: *Atomphysik*.
Teubner, Stuttgart (1997).

[77] J. J. Bollinger *et al.*, Physical Review A **31**, 2711–2714 (1985).

[78] Mariusz Puchalski and Krzysztof Pachucki, Physical Review A **79**, 032510 (2009).

[79] C. Langer *et al.*, Physical Review Letters **95**, 060502 (2005).

[80] D. M. Harber *et al.*, Physical Review A **66**, 053616 (2002).

[81] Daniel Adam Steck: *Quantum and Atom optics*.
Department of Physics 1274 University of Oregon (2007).

[82] R. Ozeri *et al.*, Physical Review A **75**, 042329 (2007).

[83] A. Kramida *et al.*, National Institute of Standards and Technology (2017).

[84] A. M. Steane, Physical Review Letters **77**, 793–797 (1996).

[85] G.P. Agrawal: *Nonlinear fiber optics*.
Academic Press Elsevier (2012).
ISBN 978-0-12-397307-8.

[86] M. A. Marangoni *et al.*, Optics Express **15**, 8884–8891 (2007).

[87] C. Rulliere: *Femtosecond Laser Pulses*.
Springer (2003).

[88] Robert W. Boyd: *Nonlinear Optics*.
Elsevier Ltd, Oxford, third edition edition (2008).

[89] B. A. E. Saleh and M. C. Teich: *Fundamentals of Photonics*.
John Wiley & Sons (1991).

[90] A. V. Smith, D. J. Armstrong and W. J. Alford, J. Opt. Soc. Am. B **Vol. 15, No. 1**, 122 ff (1998).

[91] D. Oron *et al.*, Physical Review Letters **Vol 88** (2002).

[92] D. W. McCamant *et al.*, Review of Scientific Instruments **75**, 4971 (2004).

[93] F. Raoult *et al.*, Optics Letters **23** (1998).

[94] H. Luo *et al.*, Optics Express **14**, 10631–10635 (2006).

[95] Guang Xu *et al.*, IEEE Journal of Selected Topics in Quantum Electronics **10**, 174 – 180 (2004).

[96] A. N. Bordenyuk, H. Jayathilake and A. V. Benderskii, J. Phys. Chem. B pages 15941–15949 (2005).

[97] L. J. Richter, T. P. Petralli-Mallow and J. C. Stephenson, Optics Letters **23** (1998).

[98] M.M. Fejer *et al.*, IEEE Journal of Quantum Electronics **28**, 2631 –2654 (1992).

[99] Selcuk Akturk *et al.*, Optics Express **13**, 8642–8661 (2005).

[100] A.V. Smith, AS-Photonics, Albuquerque, USA (2013).

[101] H. Hellwig, J. Liebertz and L. Bohatý, Solid State Communications **109**, 249–251 (1998).

[102] H. Hellwig, J. Liebertz and L. Bohatý, Journal of Applied Physics **88**, 240–244 (2000).

[103] Masood Ghotbi and M. Ebrahim-Zadeh, Optics Express **12**, 6002–6019 (2004).

[104] Z. Zhang *et al.*, Optics Communications **267**, 487–490 (2006).

[105] T. Freegarde and C. Zimemrmann, Optics Communications **199**, 435–446 (2011).

[106] J Hald, Optics Communications **197**, 169–173 (2001).

[107] T. Lang *et al.*, Optics Express **21**, 949–959 (2013).

[108] T. Lang, Ph.D. thesis, Leibniz Universität Hannover, Hannover (2014).

[109] H. Kogelnik and T. Li, Applied Optics **5**, 1550–1567 (1966).

[110] E.A. Sziklas and A.E. Siegman, **14**, 1874–1889 (1975).

[111] H. Lingxiong *et al.*, Journal of Physics D: Applied Physics **42**, 225109 (2009).

[112] S. Akturk *et al.*, Journal of Optics **12** (2010).

[113] D. A. Kleinman and R. C. Miller, Physical Review **148**, 302–312 (1966).

[114] G. D. Boyd and D. A. Kleinman, Journal of Applied Physics **39**, 3597 (1968).

[115] Terence Gerald Mullins, Ph.D. thesis, Albert-Ludwigs-Universität Freiburg, Freiburg (2010).

[116] D. Goswami, Physics Reports **374**, 385–481 (2002).

[117] R. Blatt and C. F. Roos, Nature Physics **8**, 277–284 (2012).

[118] C. Monroe and J. Kim, Science **339**, 1164–1169 (2013).

[119] Ch Schneider, Diego Porras and Tobias Schaetz, Reports on Progress in Physics **75**, 024401 (2012).

[120] Martina Wahnschaffe, Dissertation, Leibniz Universität Hannover, Hannover (2016).

[121] Christopher E. Langer, PhD Thesis, University of Colorado, Boulder, Colorado (2006).

[122] Sebastian Grondkowski, Master's Thesis, Gottfried Wilhelm Leibniz Universität Hannover, Hannover (2014).

[123] Hsiang-Yu Lo *et al.*, Applied Physics B **114**, 17–25 (2013).

[124] A. C. Wilson *et al.*, Applied Physics B **105**, 741–748 (2011).

[125] F. Gebert *et al.*, Optics Express **22**, 15388 (2014).

[126] Yves Colombe *et al.*, Optics Express **22**, 19783–19793 (2014).

[127] U. Warring *et al.*, Physical Review Letters **110**, 173002 (2013).

[128] Valentina Ruseva and Jan Hald, Optics Communications **236**, 219–223 (2004).

[129] E. Peters *et al.*, Optics Express **17**, 9183–9190 (2009).

[130] J. Mizrahi, Ph.D. thesis, University of Maryland (2013).

List of Figures

List of Tables

List of publications

- A.-G. Paschke, G. Zarantonello, H. Hahn, T. Lang, M. Marangoni, C. Manzoni, G. Cerullo, C. Ospelkaus
  Qubit control of $^9Be^+$ ions using a spectrally tailored UV frequency comb
  in preparation for submission

- T. Meiners, M. Niemann, A.-G. Paschke, J. Mielke, A. Idel, K. Voges, M. Borchert, A. Bautista-Salvador, S. Ulmer, C. Ospelkaus
  Towards Quantum Logic Inspired Cooling and Detection for Single (Anti-)Protons
  Conference Proceedings Low Energy Antiprotons - LEAP 2016, Kanazawa (Japan) Physical Society of Japan (accepted)

- T. Meiners, M. Niemann, A.-G. Paschke, M. Borchert, A. Idel, J. Mielke, K. Voges, A. Bautista-Salvador, R. Lehnert, S. Ulmer, C. Ospelkaus
  Towards Sympathetic Laser Cooling and Detection of single (Anti-)Protons
  Proceedings on the 7th meeting on CPT and Lorentz Symmetry, Bloomington, Indiana
  World Scientific, Singapore, 85-88, 2016.

- M. Niemann, A.-G. Paschke, T. Dubielzig, S. Ulmer, C. Ospelkaus
  CPT Test with (anti)proton magnetic moments based on quantum logic cooling and readout
  Proceedings on the 6th meeting on CPT and Lorentz Symmetry, Bloomington, Indiana
  World Scientific, Singapore, 41-44, 2014.

- T. Calmano, A.-G. Paschke, S. Müller, C. Kränkel, G. Huber
  Curved Yb:YAG waveguide lasers, fabricated by femtosecond laser inscription
  Opt.Express, 21(21), 25501-25508, 2013.

- T. Calmano, J. Siebenmorgen, F. Reichert, M. Fechner, A.-G. Paschke, N.-O. Hansen, K. Petermann, G. Huber
  Crystalline $Pr : SrAl_{12}O_{19}$ *waveguide laser in the visible spectral region*
  Opt. Lett, 36(23), 4620-4622, 2011.

- T. Calmano, J. Siebenmorgen, A.-G. Paschke, C. Fiebig, K. Paschke, G. Erbert, K. Petermann, G. Huber
  Diode pumped high power operation of a femtosecond laser inscribed Yb:YAG waveguide laser
  Opt. Materials Expr., 1(3),428-433, 2011.

- T. Calmano, A.-G. Paschke, J. Siebenmorgen, S.T. Friedrich-Thornton, H.Yagi, K. Petermann, G. Huber
  Characterization of an Yb:YAG ceramic waveguide laser, fabricated by the direct femtosecond-laser writing technique
  Appl. Physics B, 103(1),1-4, 2011.

Acknowledgements

Firstly, I would like to express my sincere gratitude to my advisor Prof. Christian Ospelkaus for the extraordinary support and scientific guidance throughout my doctoral research work. It has been an honor to be one of his first PhD students and to be part of the group working in the vibrant trapped-ion business.
Furthermore, I would like to thank my 2nd examiner Prof. Piet O. Schmidt for several constructive scientific discussions and valuable suggestions during the last years.
My sincere thanks also go to Prof. Giulio Cerullo, Dr. Marco Marangoni and Dr. Cristian Manzoni, who provided me the opportunity to join their group as guest researcher and gave access to the research facilities at the Politecnico di Milano.
Special thanks are further directed to Dr. Tino Lang for the support during the expanded application of Chi2D and for the access to Chi3D.
Moreover, I thank all my colleagues for the delightful collaboration and for their exhilarant sense of humor throughout my thesis process. In addition, I particularly thank the group members at PTB for welcoming me and my comb system in their laboratory with special thanks to Giorgio Zarantonello for joyfully joining many extra hours in the lab. Furthermore, I acknowledge the QLEDS-team, Timko Dubielzig and the POMOs for reviewing parts of this thesis.
Finally, I with all my heart thank my parents for their endless love, support and encouragement. My thanks are extended to Lars, my brother and my friends who further completed my personal balance and happiness throughout the years.

Anna-Greta Ursula Kathy Paschke

Born July 19th, 1985
Hannover (Germany)

Research

Feb. 2012 - Sept. 2017 | **Doctoral studies**

Leibniz Universität Hannover

PhD thesis in the group of Prof. Dr. Christian Ospelkaus
Institut für Quantenoptik

- $^{9}Be^{+}$ ion qubit control using an optical frequency comb

University

Oct. 2004 - Oct. 2011 | **Diplom in physics**

Universität Hamburg

Diploma thesis in the group of Prof. Dr. Günter Huber
Institut für Laserphysik

- Waveguiding characteristics of ultrashort-pulse written microstructures in crystalline YAG

School

Aug. 1998 - July 2004 | **Abitur**

Gymnasium Sophienschule, Hannover